Charge Transport through Molecules and Nanoparticles

Insights from Theoretical Studies and Terahertz Spectroscopy

Dissertation

with the aim of achieving a doctoral degree at the Faculty of Mathematics,
Informatics and Natural Sciences, Department of Chemistry,
University of Hamburg

submitted by

Michael Deffner

2020

Contents

Contents

Abstract

Colloidal nanoparticles have the potential to be integrated in various applications such as solar cells, sensors or light-emitting devices due to their electronic and optical properties. An important parameter dictating the particle–particle interactions and thus the charge transport between them is the organic ligand shell, surrounding the particles. Using molecular linkers to connect the particles, the transport and coupling can be precisely tuned for different applications.

Theoretically, the charge transport through such molecules can be described using methods as the Landauer-Büttiker approach, which describes the electron transport through nanostructures and molecules in the coherent tunneling regime. Experimentally, the transport properties are usually studied using scanning tunneling microscopy, mechanically controlled break junctions or on self-assembled monolayers, but such techniques are usually limited to very specific experimental situations and are, e.g., not suited to study ultrafast dynamics of photoexcited charges. In the last years, several new techniques to access such timescales in nanostructures have been established, especially terahertz spectroscopy has proven to be a valuable experimental tool.

The work presented in this thesis aims to explore the applicability of terahertz spectroscopy to measure the electron transport through molecules, without the need of macroscopic electrodes or complicated measures to contact the samples. This was done using experimental schemes with and without optical excitation.

Films of interlinked gold nanoparticles were synthesized using drop casting and layer-by-layer techniques and subsequently studied using terahertz time-domain spectroscopy, without optical excitation. Such materials have been studied in the past with regard to the electron transport properties of the linker molecules, but studies using terahertz spectroscopy are rare. The films of gold nanoparticles synthesized with aliphatic and aromatic molecular linkers showed no indications of losses in the terahertz range while being absorptive in the visible. This indicates no conductivity at terahertz frequencies and poses the question of the applicability of terahertz spectroscopy for the study of the

Abstract

charge transport through molecules in such systems. Classical Monte-Carlo simulations extended by parameters from quantum chemical calculations showed a modification of the low-frequency conductivity of such systems, which could not be validated in the experiments.

Additionally, linked and unlinked $CuInSe_2$ particle films were investigated using optical-pump terahertz-probe spectroscopy to study the dynamics of photoexcited charges. The results, in combination with DC conductivity measurements, showed a change of the hopping transport mechanism depending on the molecular linker. This can potentially be linked to the band alignment of the particles and linker molecules and demonstrates the possibilities of terahertz spectroscopy for studies on photoexcited systems.

To obtain a deeper understanding, the electron transport through molecules was not investigated solely using experimental methods. Inelastic processes in molecular junctions have been studied based on an extension of the Landauer-Büttiker approach, in order to understand the relationship between tunneling pathways in molecules and the strength of electron-phonon interactions of specific vibrations, which are given by the inelastic electron tunneling spectra. A method which is able to calculate the coupling only for selected vibrations was implemented in this work. The findings suggest that tunneling pathways can be traced using inelastic electron tunneling spectroscopy if the molecular vibrations of interest are sufficiently localized.

In total, the idea of using terahertz spectroscopy as a general approach to study charge transport through molecules was proven to be difficult to implement. For the study of the aforementioned ultrafast charge transfer processes it has been demonstrated as a valuable tool, as shown for the $CuInSe_2$ particle films. But using more sophisticated experimental approaches such as the combination of terahertz spectroscopy and scanning probe techniques could enable the study of charge transport through molecules at terahertz frequencies.

Zusammenfassung

Kolloidale Nanopartikel haben aufgrund ihrer elektrischen und optischen Eigenschaften das Potential, in verschiedene Anwendungen wie Solarzellen, Sensoren oder Leuchtquellen integriert zu werden. Einen großen Einfluss, welcher die Wechselwirkungen zwischen den Partikeln und so auch den Elektronentransport bestimmt, hat die organischen Ligandenhülle, welche die Partikel umgibt. Indem molekulare Linker genutzt werden, um die Partikel zu verbinden, können der Transport und die Wechselwirkungen ja nach Anwendung eingestellt werden.

Der Ladungstransport durch solche Moleküle kann theoretisch durch Methoden wie den Landauer-Büttiker Ansatz beschrieben werden, der den Elektronentransport durch Moleküle und Nanostrukturen im Regime des kohärenten Tunnelns beschreibt. Experimentell werden derartige Transportmechanismen z.B. mit Rastertunnelmikroskopen oder mechanisch kontrollierten Bruchkontakten gemessen, aber derartige Methoden sind in der Regel beschränkt auf sehr spezifische Experimente und unter anderem nicht geeignet, um die ultraschnelle Dynamiken von optisch angeregten Ladungsträgern zu untersuchen. In den letzten Jahren wurden jedoch mehrere neue Techniken etabliert, um solche Zeitskalen auflösen zu können, unter anderem hat sich die Terahertzspektroskopie als wertvolle Methode erwiesen.

Im Rahmen dieser Dissertation wurden die Anwendbarkeit von Terahertzspektroskopie untersucht, um den Elektronentransport durch Moleküle zu messen, ohne die Notwendigkeit makroskopische Elektroden anzubringen oder andere komplizierte Methoden die Proben zu kontaktieren. Dabei wurden Experimente sowohl mit als auch ohne optische Anregung durchgeführt.

Vernetzte Gold Nanopartikel Film wurden mit Auftropf- oder Schicht-bei-Schicht-Methoden präpariert und mit Terahertzspektroskopie untersucht. Derartige Proben wurden in der Vergangenheit zwar schon im Hinblick auf den Elektrontransport durch die Linkermoleküle zwischen den Partikeln erforscht, jedoch sind Studien, die Terahertzspektroskopie verwenden, selten. Die Filme mit aliphatischen und aromatischen Linkern zeigten keine

Zusammenfassung

Absorption im Terahertzbereich, während sie Licht im sichtbaren Bereich stark absorbierten. Das deutet darauf hin, dass keine Leitfähigkeit im Terahertzbereich zu messen ist, und es stellt sich die Frage, ob Terahertzspektroskopie geeignet ist, die Transporteigenschaften an solchen Systemen zu messen. Klassische Monte-Carlo Simulationen, die mit Parametern aus quantenchemischen Berechnungen modifiziert wurden, zeigten eine Änderung der niederfrequenten Leitfähigkeit solcher System, was durch die Experimente nicht bestätigt werden konnte.

Zusätzlich wurden verknüpfte und unverknüpfte $CuInSe_2$ Partikelfilme mit Pump-Probe Experimenten untersucht, um das Verhalten von optisch angeregten Partikeln zu untersuchen. Die Ergebnisse, zusammen mit DC Leitfähigkeitsmessungen, zeigten eine Änderung des Hopping-Transportes abhängig vom verwendeten Linker. Diese deutet potentiell auf ein Anpassung der elektronischen Zustände der Partikel und Moleküle hin und demonstriert die Möglichkeiten, mit Terahertzspektroskopie Studien von optisch angeregten System durchzuführen.

Um ein tieferes Verständnis zu gewinnen, wurde der Elektronentransport durch Moleküle nicht allein mit experimentellen Methoden untersucht. Inelastische Prozesse in molekularen Brücken wurden mit einer Erweiterung des Landauer-Büttiker Ansatzes berechnet, um Erkenntnisse über den Zusammenhang zwischen Tunnelpfaden und der Stärke der Wechselwirkung zwischen Elektronen und molekularen Schwingungen zu gewinnen. Dafür wurde eine Methode, diese Wechselwirkungen nur für ausgewählte Schwingungen zu berechnen, neu implementiert. Die Resultate zeigen, dass Tunnelpfade über die Wechselwirkung zwischen den tunnelnden Elektronen und der Molekülschwingungen nachvollziehbar sind, sofern diese ausreichend lokalisiert sind.

Zusammfassend hat sich gezeigt, dass die Idee, Terahertzspektroskopie zur Untersuchung von Ladungstransport durch Moleküle zu nutzen, schwierig umzusetzen ist. Für Studien von ultraschnellen Landungstransferprozessen hat es sich jedoch als wertvolles Tool bewiesen, wie an den Filmen aus $CuInSe_2$ Partikeln gezeigt wurde. Aufwendigere experimentelle Techniken, wie die Kombination von Terahertzspektroskopie und Rastersondenmethoden, könnten jedoch die Untersuchung von Ladungstransport durch Moleküle bei Terahertz-Frequenzen ermöglichen.

1 Introduction

"Things on a very small scale behave like nothing that you have any direct experience about. They do not behave like waves, they do not behave like particles, they do not behave like clouds, or billiard balls, or weights on springs, or like anything that you have ever seen."

Richard P. Feynman, The Feynman Lectures
on Physics, Volume III, p. 1-1

Understanding the transport of charges is one of the most fundamental elements of modern physics, physical chemistry and related branches of science. From electronic devices such as transistors or diodes, to optoelectronic applications like light-emitting diodes or lasers to chemical processes like the reduction and oxidation reactions inside a fuel cell or biological processes like photosynthesis - the key to explain each of these mechanisms is to understand how charges are transferred from one place or state to another.

In 1900, Paul Drude developed a simple model to describe the behavior of an electron by modeling them as tiny particles following a Newtonian equation of motion (EOM). This gave him the possibility to describe the frequency-dependent response of (quasi) free charges, such as the conduction electrons in metals, to an external electric field [1]. Even though this is a very simple approach, it remains powerful and popular until today. But like a lot of classical models, the Drude model has its limits. When the dynamics of charged particles are studied on a meso- or nanoscale, quantum mechanics have to be incorporated into the description. And, as mentioned above in the quote by Richard Feynman, the behavior of particles on small scales is weird. They behave quite differently than we would expect from the macroscopic world determining our daily lives.

To understand the electron movement through matter, it is important to have a closer look at the electron's wave-particle duality, that they behave like particles and waves. Our human language, which is shaped by our daily experience with macroscopic

and relatively slow objects, tries to adapt words we know, such as "particle" or "wave", to describe the behavior of quantum objects and imprinting the meanings we associate with those words.

But in the end an electron, like every other "particle" is both, a wave and a particle. Even though we intuitively view an electron as a tiny ball-like object, it is a scientific fact that it shows the behavior and properties of a wave, e.g. when it penetrates classical barriers and suddenly appears on its other side. This is called tunneling, a fundamental concept to the understanding of quantum mechanics. The tunneling of an electron through a barrier can be explained by describing the electron as a wave packet (Figure 1.1), which is partially reflected and partially transmitted at barrier. The ability of particles to apparently "jump" instantaneously from one side of a barrier to the other (thus, in real space), or from one electronic state to another (thus, in k-space) is the very basic concept which governs the mobility of charges.

Figure 1.1: Reflection and transmission of a wave packet at a barrier in one dimension. Data for the plot was obtained with modified code based on [2]. A measurement following the scattering at the barrier would localize an electron represented by the wave packet on one of the side of the barrier - with a lower but nonzero probability for the right side, indicating a certain chance that the electron has tunneled through the barrier. The arrows denote the wave vector *k* or the propagating direction of the wave packets.
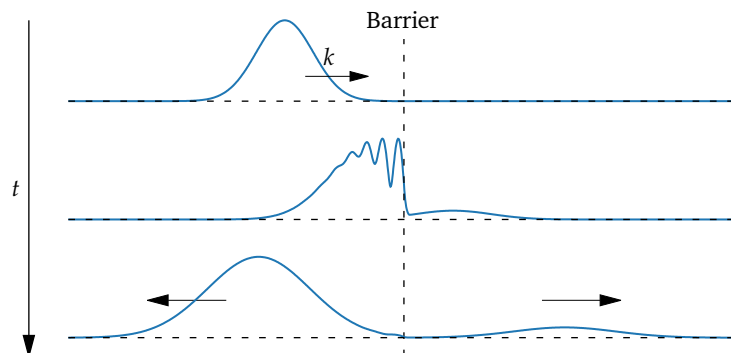
As mentioned above, for many scenarios we do not have to apply quantum mechanical models to describe the conductivity of an object, but can rely on simpler, often (semi-)classical models. But the advent of nanotechnology, new experimental tools and methods and the societal need for technological progress asks for a deeper understanding of the transport mechanisms, which can be used to tailor new and exciting functionalities.

The most apparent field of technology which is dominated by the transport properties of electrons is, of course, electronics. But

before discussing this topic in depth, some other examples should be given to highlight the broad interconnection of this topic.

In solar cells, the energy of a photon is absorbed by an electron, which is transferred to an excited state with higher energy (e.g. the conduction band of a semiconductor). Thus, the electron has moved already in k-space - but it is necessary that it moves in real space as well to extract it from the solar cell and insert it in electrical circuits or store its energy. The same way, the so-called hole, the empty state the excited electrons has left behind and which can be regarded as a positively charged particle, has to be extracted. In silicon semiconductor solar cells, this is done by doping the semiconductor in a controlled way, thus controlling the flow of the electron in the conduction band and the hole in the valence band [3]. Silicon solar cells are the most common type of solar cells. These are the cells on rooftops or large-scale solar power plants. Besides the many types of solar cells employing different crystalline semiconductors, molecules are under study as well, e.g. in Grätzel or organic solar cells [4–6]. These systems have been extensively studied, including studies employing terahertz (THz) spectroscopy, to identify parameters important to improving the charge separation and charge transport after photoexcitation and thus improving the cells' efficiency [7–12].

For biological systems it is also important to understand electron transport, especially for systems that perform photosynthesis. Light-harvesting complexes show surprisingly high efficiency in transferring the energy from the so-called antenna, which absorbs light, to the reaction center, where the energy is used to perform chemical reactions. One example is the Fenna-Matthews-Olson (FMO) complex, for which in 2007 quantum coherence features have been found [13]. Subsequent quantum mechanical simulations have shown several ways of explaining the high efficiency, e.g. in the framework of quantum transport through disordered networks. [14–17]. Biological systems also sometimes show surprisingly efficient long-range electron transfer, e.g. through proteins [18, 19]. Quantum features in biology are still under debate, especially since it is quite complicated to achieve similar coherence times for artificial systems at room temperatures.

The understanding of how electrons move in k as well as in real space shaped our electronic technologies, which may have been the most influential in forming our societies in the last century. One of the most central electronic devices, the transistor, was only enabled by the understanding of the electron mobility in semicon-

ductors and was rewarded with a Nobel price in physics in 1956
[20].

The electronic, and in particular semiconductor, industry has
been driven since then by the miniaturization and improvement
of transistors. Modern computer processors can contain millions
of transistors. But pushing the clock speed of transistors past the
4 GHz mark has been proven to be very difficult (see Figure 1.2).

Figure 1.2: Development of
the single-core frequency and
number of transistor per chip
over the years. Data ob-
tained from [21]. The aver-
age frequency from year 2000
on (2443 MHz) is shown as a
dashed line.
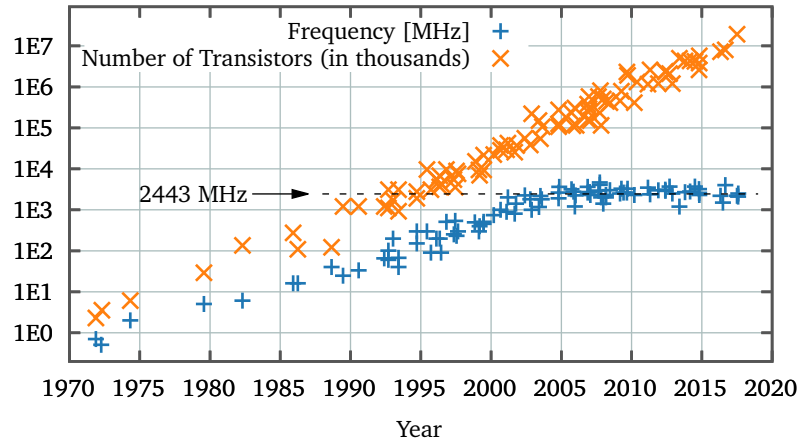
In the past, this frequency speed-up was mostly obtained by re-
ducing the dimensions of the transistors, such as the size of the
gates, which has been more or less constant since Intel has intro-
duced the 45 nm technology in 2007 [22, 23].

Naturally, this scaling down has its limits when it reaches the di-
mensions of atomic bonds or lattice constants [24]. Several other
factors limit the shrinking of the devices, like the onset of quan-
tum tunneling or heat accumulation [22, 24]. Thus, any further
improvements cannot rely on simple changes of the geometry and
dimensions only, but researchers have to look for new materials,
too. IBM, for example, has demonstrated a graphene-based tran-
sistor, which was able to run at 100 GHz [25]

The idea that molecules can act as electronic components came
up around the 50s [26], but what really sparked the field was the
proposal of a single-molecule rectifier by Arieh Aviram & Mark A.
Ratner in Oct. 1974 [27]. This, together with the invention of the
scanning tunneling microscope (STM) in 1983, built the founda-
tions for the field of molecular electronics [28, 29]. Scientific ad-
vances in both theoretical and experimental methods in the last
decades led to discoveries such as molecular switches [30–34],
molecular transistors [35–38] or molecular rectifiers [39–45].
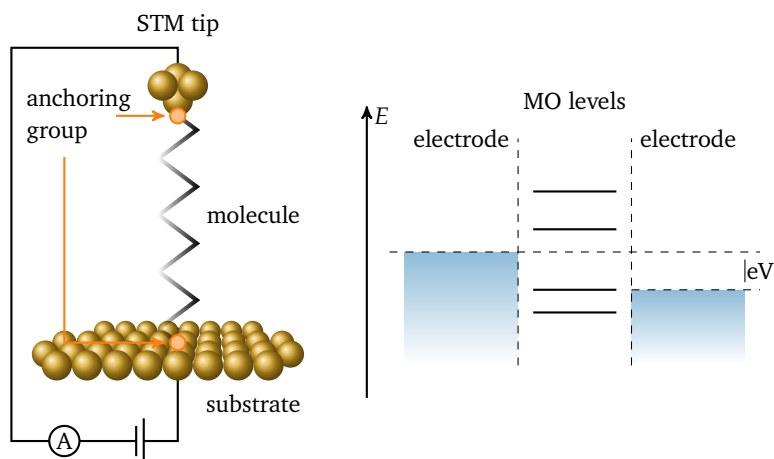
Figure 1.3: The basic picture to understand tunneling transport through molecules. *Left:* Exemplary scheme of a STM setup to measure the conductance of a single molecule. *Right:* Energy diagram for a molecule sandwiched between to electrodes with an applied bias eV, which is visualized by the shifted Fermi levels.

From a theoretical point of view, the Landauer-Büttiker (LB) approach [46, 47] has been successfully established to describe the tunneling transport through short molecules. The way an electron moves through such a molecule is not so different to the picture of a wave packet getting transmitted/reflected by a barrier as shown in Figure 1.1. For structure-property relationships, the electronic structure of the molecule and the electrodes it is connected to have to be taken into account, which was successfully done using density-functional theory (DFT), tight-binding schemes or Hückel methods [46–51]. These or similar approaches have been used to study quantum interference [52–55], inelastic effects [56–64], spin-selective transport [65–68] or aforementioned molecular switches [30, 34, 69–72]. Computer program packages have been developed that can describe transport through molecular junctions, usually in combination with DFT, including TRANSSIESTA [73], QUANTUMATK [74] or our in-house code ARTAIOS [75]. More details and a discussion of the LB approach will be given in Chapter 2.

Experimental techniques have also been developed further [76, 77]. Aside from the already mentioned STM techniques, mechanically controlled break junctions (MC-BJs) as shown in Figure 1.4 are routinely used to measure the conductance of (single) molecules [77–79]. Nanoparticle arrays have also been used, where the conductivity of the array is changed by the molecules connecting the particles [77] - this will be further discussed in Part III. Actually, devices which are using molecules as electronic elements have very recently become commercially available: Overdrive pedals for guitars, which use diodes to artificially clip sinusoidal signals thus altering the spectrum, have been build using molecular rectifiers by the company "Nanolog" [80]. They also sell the molecular junctions as a basic building block for other
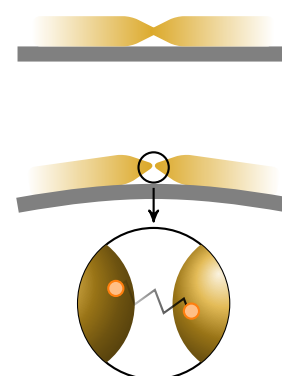
Figure 1.4: Operation of a mechanically controlled break junction (MC-BJ). By bending the the underlying substrate, the gold wire is pulled apart until a gap is formed. In solution, molecules can bridge the gap and the current through the molecules can be measured.

applications.

Molecules offer new and exciting approaches to build electronic devices (as the graphene-based transistor mentioned above). It is tempting to speculate about molecular electronics as a replacement of silicon-based devices, but maybe it is more likely that molecules as electronic elements will enhance and complement silicon-based devices. But molecules as electronic elements are not only interesting in specific devices, they are directly connected to already mentioned fields like organic solar cells, biological processes or other chemical process where, e.g., electron transfer through molecules is involved. Thus, pushing forward the field of molecular electronics should not be justified only by the quest for faster or cheaper electric devices, but also in terms of basic research and the drive to understand the world around us.

In addition to using the charge as an information carrier, it is also possible to use the spin degree of freedom [65–67]. This could potentially increase the information density and also overcome problems concerning heat accumulation or generation by moving charges. Spins can couple via (anti)ferromagnetic coupling, transferring information without the need to actually move an electron (see Figure 1.5). A notable experiment performed by Khajetoorians *et al.* demonstrated the realization of a logic gate based only on the spin interactions of single atoms [81].

To build such spintronic devices, molecules are also of high interest. Molecules can be tailored specifically to promote ferromagnetic or antiferromagnetic coupling. Also, chiral molecules can act as spin valves by promoting a higher transmission probability for electrons with the correct spin or introducing switching capabilities [82–85].

A totally different approach is not only to use electrons, but photons to perform calculations. Light is fast (oscillating in the ~100 Terahertz instead of Gigahertz range as our transistors), but also not so small: In the (human) visible range, wavelengths range from 380 to 740 nm, much more than the typical dimensions of modern electronics. But by using the coupling between light and matter, light can be squeezed into small dimensions, for example by exploiting the properties of plasmons, collective oscillations of free electrons which can couple to light and form a plasmon polariton [86]. These can confine the light field in sub-nanometer dimensions [87, 88]. For so-called plasmonics[1] to play a role for future technology, active control over the plasmon has to be achieved, which has initiated the field of "active plasmonics" [90].
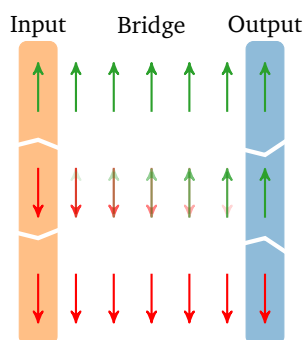
Figure 1.5: Visualization of information transfer by spin flips. The spins are coupled ferromagnetically. Thus, an induced spin flip at the input causes the neighboring spins to flip, until finally the output spin is flipped as well.
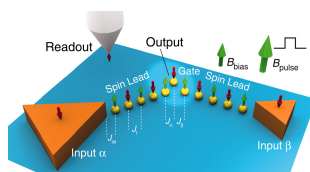
Figure 1.6: All-spin based logic gate. From Khajetoorians, A. A. *et al.* Realizing All-Spin-Based Logic Operations Atom by Atom. *Science* **332,** 1062–1064 (May 2011). Reprinted with permission from AAAS.

[1] A nice article which introduces the idea of plasmonics in a general fashion was written by Harry A. Atwater, published 2007 in the Scientific American [89].

Plasmons can also be used to excite spin currents, thus linking the fields of plasmonics and spintronics [91].

But what do molecules have to do with that? Actually, the interplay between plasmonic excitations and molecular conduction recently has been under study, establishing a field called molecular electronic plasmonics (MEP) [92–95]. Also, many systems of interest for plasmonic applications are colloidal in nature, such as gold nanoparticles (AuNPs), which show a strong plasmonic resonance in the visible range (the electronic and optical properties of AuNPs will be discussed in Chapter 8). The surfaces of the particles are covered with ligands or molecules are used to connect the particles directly to facilitate charge transport. Plasmons of the adjacent particles can couple, which can be tuned by the linking molecules [96]. For larger distances, this coupling can be mostly understood by employing Maxwell's equations, but for small/subnanometer distances, a "charge transfer plasmon" can arise, which stems from quantum tunneling between two particles [95]. Thus, in such systems, optical excitations and electron transport can interact with each other, in such a number of ways that it can hardly be covered here comprehensively. This also asks for new tools to study the properties of such systems. Measurements of electron transport usually happens on slow timescales, even though the microscopic process can be quite fast. Optical processes, on the other hand, are fast, usually in the femtosecond to nanosecond regime. This also asks for new ways to study transport phenomena, since traditional STM or MC-BJ experiments perform DC measurements, without the possibility to access short-lived currents.

One relatively new technique which enables the measurement of the mobility of electrons on a short time scale is THz spectroscopy. There, an electromagnetic pulse is generated, whose frequency is so low (several terahertz) that it can actually move free electrons in real space, thus probing the conductivity of a sample. This can be used to get the conductivity of a sample without the need of contacting it. When it is combined with an optical excitation by a pulsed laser, it can be used to study the conductivity of a photoexcited system on ultrashort timescales ($\sim$ps) [97–99].

A more detailed overview over recent results and achievements in the field of THz spectroscopy will be given in Chapter 5, but it should be mentioned that is has been used to study tunneling currents, most of the experiments have been carried out quite recently and usually performed in STMs, where the high resolution of the STM can combined with the ultrashort temporal resolu-

tion of a THz pulse [100, 101]. It was shown that the tunneling of electrons from the tip to the substrate (or vice-versa) could be controlled by the polarization/carrier-envelope phase (CEP) of a strong THz pulse. Jelic *et al.* performed a similar experiment for a silicon atom [102] and comprehensively discussed the THz-induced band bending and hot electron dynamics. Several other examples involves the vibrational-assisted tunneling[2] induced by a THz pulse or the investigation of the field enhancement [104–106].
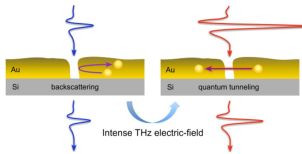
A study which is also of high importance for this thesis was published by Yoshioka *et al.* in 2015 [107]. They investigated the THz response of non-percolated and percolated gold films on Si(100) substrates. By varying the intensity of the THz beam and fitting the obtained data with the Drude-Smith (DS) model, the localization and damping parameters decreased for samples close to the percolation threshold. This implies that the stronger electric fields can make the electrons tunnel from a gold structure to another (see Figure 1.7).

Since THz has been successfully used to study the conductivity and transport mechanisms of nano-sized system, the question arises whether THz spectroscopy can be employed to measure the conductance of molecular junctions, especially in AuNP films where the particles are linked by these molecules? And if yes, can we go a step further and study optical excitations of the particles or the molecules and their effects on the molecular conduction? If so, this would open many possibilities to study new and exciting phenomena, establish new tools to study molecular junctions and maybe even tune the system by the right choice of molecular linker to perform certain tasks, e.g. the extraction of hot carriers generated by a decaying plasmon.

To contribute to this question, this thesis focuses on two aspects. First, using computational tools, inelastic effects in molecular junctions are studied with respect to the identification of tunneling paths through molecules. Unveiling tunneling pathways through molecules can, e.g., answer the question whether electrons follow helical paths in helical structures [108–110]. This work has been published in [111].

Second, several AuNP films connected with molecular linker have been prepared and studied by THz spectroscopy. Parts of this work were published in "Impact of the Crosslinker's Molecular Structure on the Aggregation of Gold Nanoparticles" [112]. These nanoparticle films acted as a model system to study the interactions between THz radiation and linked AuNP. Additionally,

[2] Currents in STMs not induced by THz radiation but plasmons have received a similar attention, see Ref. [103].

Figure 1.7: Schematic drawing for the THz induced tunneling in gold nanostructures. Reprinted with permission from Jelic, V. *et al.* Ultrafast terahertz control of extreme tunnel currents through single atoms on a silicon surface. *Nature Physics* **13**, 591–598 (Feb. 2017). Copyright 2017 American Chemical Society.

semiconducting $CuInSe_2$ particles linked by short molecules have been studied in an collaboration with the group of Horst Weller. The results have been published as "Postdeposition Ligand Exchange Allows Tuning the Transport Properties of Large-Scale $CuInSe_2$ Quantum Dot Solids" [113].

The thesis is organized as follows:

Part 1 - Transport through Nanoscopic Systems discusses the theoretical approach to describe electron transport through nanoscopic systems, in particular molecules in molecular junctions. An introduction into the LB approach in combination with DFT will be given. Results obtained by studying inelastic effects in molecular junctions will be discussed regarding the relation between inelastic effects and tunneling pathways. Additionally, Monte Carlo (MC) simulations for the THz response of AuNP films are presented.

Part 2 - Terahertz Spectroscopy introduces the concept of Terahertz spectroscopy, giving an overview of our setup as well as the techniques to process and extract parameters from the measurements.

Part 3 - Terahertz Spectroscopy of Metallic and Semiconducting Films and Particles discusses THz spectroscopy on thin evaporated gold films, which were used as benchmark measurements, gold nanoparticle films and $CuInSe_2$ quantum dot solids. The optical an electronic properties of AuNPs will be discussed in detail here together with an overview over current research regarding AuNP.

Part I

Electron Transport through Nanoscopic and Molecular Systems

2 Coherent Tunneling

2.1 Tunneling Transport through Molecules

To describe the transport of charges through nanoscale systems like nanoparticles, molecules or vacuum tunneling gaps, models have to account for the quantum nature of the system. Without concepts such as quantum tunneling or the Pauli exclusion principle[3] essential aspects of the charge transport through a molecule can neither be understood nor described. But solving a full quantum-mechanical description of for example a molecular junction is usually not possible or at least highly complex and expensive to calculate. Thus, depending on the size and complexity of the system, different levels of theory or transport approaches have to be used [115].

Different realms of charge transport in nanoscale systems exist. Maybe the most important differentiation to be made is the question whether the transport through specific systems is coherent, so that a specific phase relation between the incoming and outgoing electron wave packet is preserved. The transport through a film of nanoparticles for example usually does not [116]: The electron will stay for a finite amount of time on a particle, will interact with it and hinder further electrons to tunnel onto the particle. This will destroy the coherence, as the phase information is not preserved. In this case, the transport mechanism is usually referred to as "hopping", as the transport path involves several sequential tunneling processes between the input and the output/electrodes (Figure 2.1). This is the dominant transport mechanism e.g. through polymers, metallic nanoparticle arrays or quantum dot solids [77, 116–121]. Depending on the size of the system through which the transport is happening and the strength of the interactions within, an electron also can travel coherently. This is usually fulfilled for short molecules where the highest-occupied molecular orbital (HOMO) and lowest-unoccupied molecular orbital (LUMO) are reasonably far from the Fermi energy and which measured at low temperature. This coherent tunneling transport is again understood best using the idea of a wave packet, which

[3] The Pauli principle states that two identical fermions (elementary particles with half-integer spin) cannot be in the same state of a quantum system at the same time. For a wavefunction Ψ this implies that it has to be antisymmetric with respect to permutation [114].

$$\Psi = \psi_1(r_1)\psi_2(r_2) - \psi_1(r_2)\psi_2(r_1),$$

where $r_{1,2}$ are the spatial and spin coordinates of the fermions.
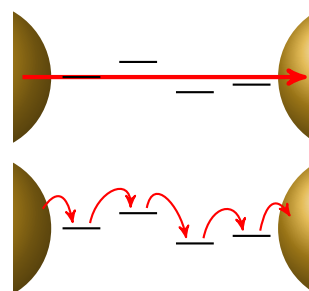
Figure 2.1: Coherent tunneling (top) and hopping transport of electrons from an electrode on the left to the right electrode.

is partially transmitted through a barrier. The transmitted wave has a fixed phase relation to the incident one.

The idea to describe electron transport in nanoscopic systems not on a particle basis but as a wave (or more specific a wave packet) was presented by Rolf Landauer in July 1957 [46]. He established the so-called "Landauer Formula", which connects the conductance G of a system to the transmission

$$G(E, V) = G_0 \sum_n T_n(E, V), \qquad (2.1)$$

where $G_0 = 2e^2/h$ is the quantum of conductance and $T_n(E, V)$ refers the transmission probability for a channel n. e, h are the elementary charge and the Planck constant, respectively. Thus, resistance arises due to scattering/reflection of the electron or wave packet when entering/leaving the system. This so-called Landauer-Büttiker (LB) picture of electron transport is different to, e.g., a classical Drude picture of charge transport, where the resistance arise because of the scattering of electrons inside the junction.

An intuitive way to understand the energy-dependent transmission through a barrier is the analogy of a Fabry-Pérot (FP) etalon. This will also be discussed as a concept for the THz transmission through samples in Chapter 6. Monochromatic light passing through a transparent slab will be reflected internally, that is at the boundaries of the slab. These reflections can interfere with each other constructively or destructively depending on the phase difference, which is governed by the thickness, refractive index, wavelength and transmission angle. Changing the wavelength will result in a change of the transmitted intensity measured at one specific angle behind the FP etalon, thus resulting in an energy-dependent transmission function (Figure 2.2) [122].

To obtain an energy-dependent transmission through a molecular junction using the LB approach, the system is usually divided into electrodes and the central system, as depicted in Figure 2.3 [77, 123, 124]. A variety of purely quantum mechanical features can be derived from this approach, e.g. the occurrence of quantum interference of an electron wave packet [77, 124]. One example is the so-called Aharonov-Bohm effect [125]. There, a magnetic field induces a phase difference into two otherwise equal transmission channels. Depending on the induced phase, they interfere constructively (destructively), which results in a high (low) current through the system. A more detailed discussion the LB
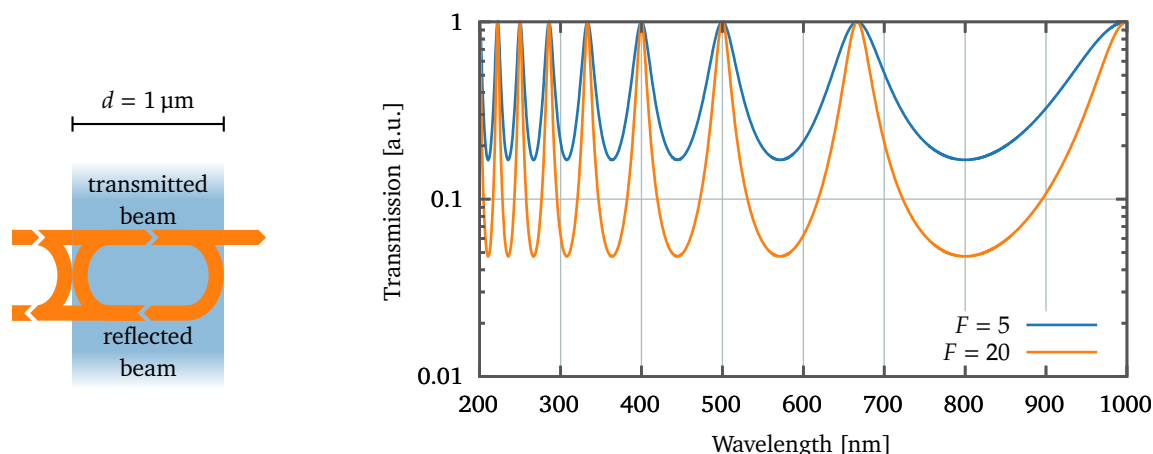
Figure 2.2: Wavelength–dependent transmission of electromagnetic radiation through a FP etalon/interferometer with a thickness of 1 µm at normal incidence. The incoming (from the left) electromagnetic wave is partially reflected and transmitted. The transmitted part undergoes multiple reflections inside the slab which interfere which each other. This leads to a wavelength–dependent transmission pattern due to destructive/constructive interference as shown in the right graph. The data was obtained for a "finesse" of 5 and 20 [122]. The finesse is a measure of quality of a FP etalon and depends on the intensity of the internal reflections.

approach and how it can be used together with DFT to calculate the transport through molecules will be given in the next section.
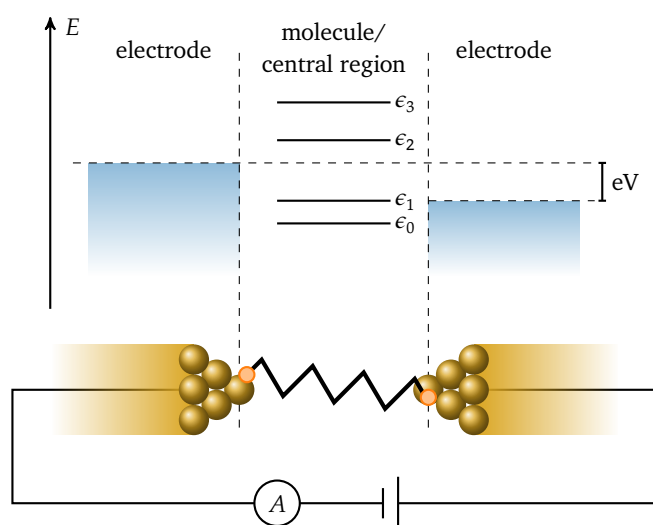
Figure 2.3: Schema of a molecular junction, the partitioning into the central region (e.g. the molecule and parts of the contact region) and the two electrodes and a depiction of the electronic states. The electronic bands of the electrodes are filled up to the Fermi level (blue area), but the respective Fermi levels are shifted by the applied voltage eV. The molecule has discrete electronic states, shown as lines in the central region.

On the experimental side, several techniques exist to measure the transport through molecules[4]. This includes scanning probe techniques such as the STM or conductive atomic-force microscopy (AFM), MC-BJ, lithographic structures, nanoparticle films or self-assembled monolayers (SAMs) [77]

In a typical STM measurement, molecules are deposited on a surface. This can e.g. be done by sublimating or evaporating

[4] When discussing molecular electronics, it is import to distinguish it from the field or "organic electronics". Usually, molecular electronics is regarded as a subfield of the latter, with a focus on much smaller dimensions using more complex or complete models [126].

the molecules in the vacuum chamber of the microscope (or a separate sample preparing chamber) [77]. Then, the surface is scanned with the STM tip until a deposited molecule is identified. This can be approached and an I-V curve can be recorded, which stems from the tunneling current through the molecule. Different techniques to verify the existence of the molecule in the tunneling junction exists, including Raman spectroscopy or inelastic electron tunneling spectroscopy (IETS). The latter will be discussed further in Chapter 3.

MC-BJ experiments use a thin gold wire, which is slowly pulled until it breaks. Right before the rupture of the wire, only a few atoms are connecting the two parts of the wire. Thus, after rupture, two electrodes with atomic-sized tips have been formed. Alternatively, the two electrodes can be formed using, e.g., lithographic methods. When placing this in a solution with linker molecules, the molecules can adsorbate on the electrodes [77]. The distance between the electrodes can be manipulated precisely and changed from a full-contact regime (with direct contact of the electrodes) over a regime where one or several molecules are bridging the gap to a regime without connection between the electrodes. For each distance, the current through the junction can be recorded. This is usually repeated a lot of times, thus collecting the traces of up to several thousand molecules [77].

Another techniques to study the transport through molecules is to prepare extended films of metal nanoparticles which are contacted by two electrodes and replace the particles' stabilizing ligands with conducting linker molecules [127–129]. The bottleneck for electrons which travel through the film from one electrode to the other are the gaps between the particles. The insertion of linker molecules into the gaps thus changes the conductance of the whole film.

These techniques differ in how many molecules take part in the transport. An STM can measure the transport through single molecules, while e.g. measurements involving contacted SAM or also MC-BJ experiments[5] can have several molecules in the tunneling junction [77, 126].

The differences between a "single molecule" and an "ensemble" approach have been described elsewhere [126, 131, 132] and can be summarized as follows. Single molecules are much easier to model theoretically and single-molecule experimental setups are able to measure various properties of the molecular junction, like visualizing the molecular orbitals (MOs) [133] or getting a

[5] In MC-BJ experiments a statistical analysis of the measured conductance can for example be used to differentiate between measurements where only one molecule was bridging the junction or multiple [77, 79, 126, 130].

vibrational footprint via IETS [134]. But due to thermal fluctuations and different bonding motives, the measured results can vary quite strongly and a careful statistical analysis is necessary [79, 135–137]. Also, the integration of single molecule junctions into applications is challenging. "Ensemble" methods are presumably easier to integrate into circuits and provide a more stable electronic response due to the averaging over several molecular junctions. In such systems, more interactions (e.g between the molecules) can occur, which is more difficult to describe.

There are numerous books [77, 115, 124, 138, 139] and reviews [26, 49, 50, 92, 131, 132, 140–146] which give a general introduction to molecular electronics and over the latest developments in research or specific aspects like interaction with light [92]. Especially the books from Elke Scheer and Juan Cuevas and Massimiliano Di Ventra offer a good starting point [77, 124].

2.2 The Landauer-Büttiker Approach

The LB approach describes electron transport with the idea of a barrier, on which an electronic wave packet can be reflected or transmitted with certain probabilities as shown in Figure 1.1. The structure of such a tunneling junction is depicted in Figure 2.3. The incoming electrons enter and leave the junction via the metallic electrodes. A transmitted electron which has been in a state $|l\rangle$ on the left side of the barrier (the left electrode) ends up in some state $|r\rangle$ on the right side of the barrier (the right electrode), with a probability given by the transmission T_{lr}.

For formulas, the following convention regarding the notation of formulas is adapted: Vectors are written in small letters and bold, matrices in capital letters and bold. Functions and operators (as functions) are written upright. Operators can also be written in matrix form, then they will be italic, in capital letters and bold.

By summing over all possible transmission channels, the conductance can be obtained using the Landauer formula (Equation 2.1) [46]. The transmission probabilities can be represented as the so-called scattering matrix $\mathbf{T}$, which contains all transmission probabilities from states on the left side to states on the right side of the scattering region.

The number of electrons at a specific energy is given by the Fermi distribution [147]

$$f_{l,r}(E) = \left(\exp\left(\frac{E - \mu_{l,r}}{k_B T} \right) + 1 \right)^{-1}, \qquad (2.2)$$

where k_B is the Boltzmann constant, T the temperature and $\mu_{l,r}$ the electrochemical potential of the left or right electrode. Without any applied voltage, the number of electrons passing the cen-

tral region from left to right and from right to left should be the same (assuming $T_{ij} = T_{ji}$), thus canceling any current.

By applying a potential, μ_l and μ_r are shifted by $eV = \mu_l - \mu_r$ with respect to each other, as depicted in Figure 2.3. This difference in the Fermi level creates a "window" $(f(E)_L - f(E)_R)$ for electrons with a specific energy to travel only from the left to right electrode, but not the other way (Figure 2.4). This already shows us that the whole system would show no current if the central region had no current-carrying states inside this window.

Figure 2.4: Energy window of current–carrying electrons spanned by $f(E+eV/2)_L - f(E-eV/2)_R$ for a bias voltage of 2 (blue) and 4V (orange). k_{BT} was set to 0.2.
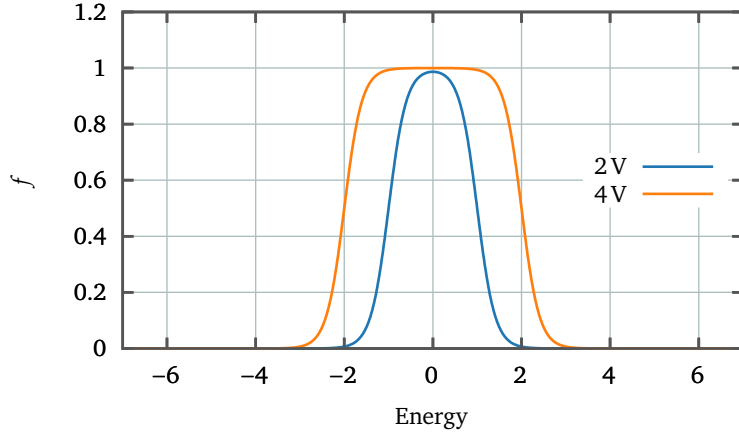
By assuming an energy-dependence of the transmission function $T = \sum_n T_n$ given in Equation (2.1), the current at a specific voltage can be obtained by effectively integrating only over the channels energies which are inside the window spanned by the Fermi functions of the electrodes at that voltage, as given in [46, 47]

$$I = \frac{2e}{h} \int_{-\infty}^{\infty} dE \left[f_l(E + eV/2) - f_l(E - eV/2) \right] T(E). \quad (2.3)$$

As one can see from Equation (2.3), $T(E)$ is the central quantity to be computed in order to obtain the current.

For simple systems, an expression for $T(E)$ can be found analytically, which will be presented below. For more complicated systems, the non-equilibrium Green's function (NEGF) formalism in combination with DFT or other effective single-particle electronic-structure theories can be used.

2.2.1 Transmission through a Single-Level System

The transmission through a single-level system can be derived using the expression for the transmission through a slab. The boundaries of the slab resemble the contacts of the single-level

system with the electrodes. This approach is actually the same as for the FP etalon described above and also for the modeling of a THz pulse passing through a sample, which will be covered in Chapter 6. The total transmission probability is given by [124]

$$T = \frac{T_l T_r}{1 + R_l R_r - 2\sqrt{R_l R_r} \cos \chi} \tag{2.4}$$

$$= \frac{T_l T_r}{\left(1 - \sqrt{R_l R_r}\right)^2 + 2\sqrt{R_l R_r}\left(1 - \cos \chi\right)}, \tag{2.5}$$

where $T_{l,r}$ are the transmission probabilities for the wave to be transmitted into the or out of central region and $R_{l,r} = 1 - T_{l,r}$ are the respective reflection probabilities. χ is the phase the wave accumulates by passing back and forth inside the central region. The total transmission is maximized if $\cos \chi = 1$, thus $\chi = n2\pi$. By assuming $R_l \simeq R_r = 1, T_l \simeq T_r \ll 1$, we can simplify Equation (2.5) to

$$T = \frac{T_l T_r}{\left(1 - \sqrt{(1 - T_l)(1 - T_r)}\right)^2 + 2\left(1 - \cos \chi\right)} \tag{2.6}$$

$$\simeq \frac{T_l T_r}{\left(\frac{T_l + T_r}{2}\right)^2 + 2\left(1 - \cos \chi\right)}, \tag{2.7}$$

where the last step has been performed using a first–order Taylor expansion of $T_{l,r}$[124]. Assuming an energy dependence of the accumulated phase $\chi \to \chi(E)$, we can again perform a second–order Taylor expansion of $\chi(E)$ around an energy ϵ_0, where the transmission is maximized

$$1 - \cos \chi(E) \simeq \frac{1}{2}\left(\frac{\mathrm{d}\chi(E)}{\mathrm{d}E}\right)^2 (E - \epsilon_0)^2 \tag{2.8}$$

and additionally define

$$\Gamma_{l,r} = T_{l,r}\left(\frac{\mathrm{d}\chi(E)}{\mathrm{d}E}\right)^{-1} \Leftrightarrow T_{l,r} = \Gamma_{l,r}\left(\frac{\mathrm{d}\chi(E)}{\mathrm{d}E}\right). \tag{2.9}$$

2 Coherent Tunneling

By inserting Equation (2.8) and (2.9) into Equation (2.7), we obtain

$$T(E) = \frac{\Gamma_l\left(\frac{d\chi(E)}{dE}\right)\Gamma_r\left(\frac{d\chi(E)}{dE}\right)}{\left(\frac{\Gamma_l\left(\frac{d\chi(E)}{dE}\right)+\Gamma_r\left(\frac{d\chi(E)}{dE}\right)}{2}\right)^2 + 2\left(\frac{1}{2}\left(\frac{d\chi(E)}{dE}\right)^2(E-\epsilon_0)^2\right)}$$

$$= \frac{\Gamma_l\Gamma_r\left(\frac{d\chi(E)}{dE}\right)^2}{\left(\frac{d\chi(E)}{dE}\right)^2\left(\frac{\Gamma_l+\Gamma_r}{2}\right)^2 + \left(\frac{d\chi(E)}{dE}\right)^2(E-\epsilon_0)^2}$$

$$= \frac{\Gamma_l\Gamma_r}{\left(\frac{\Gamma_l+\Gamma_r}{2}\right)^2 + (E-\epsilon_0)^2}. \tag{2.10}$$

This is called the "Breit–Wigner" formula, which was first derived for resonances in the interactions of neutron radiation with matter [121, 148]. $\Gamma_{l,r}$ is the coupling between the central region to the left or right electrode. Assuming that the interaction between the left electrode and the central region is the same as the interaction between the right electrode and the central ($\Gamma_{cl} = \Gamma_{cr}$), the formula can be further simplified.

In Figure 2.5, the resulting transmission function is shown, together with the current obtained using Equation (2.3) and the differential conductance $G = dI/dV$.

Figure 2.5: Obtained transmission, current and conductance through a single-level system with $\epsilon_0 = 0.5\,$eV as described in Equation (2.10) for two different coupling strengths between electrodes and the central system. As one can see, the increased coupling leads to a broader transmission peak, which results in an increased current and broader conductance peaks. Effects of the applied voltage on the transmission function are not included here. An applied potential can, e.g., shift the energy ϵ_0.

20
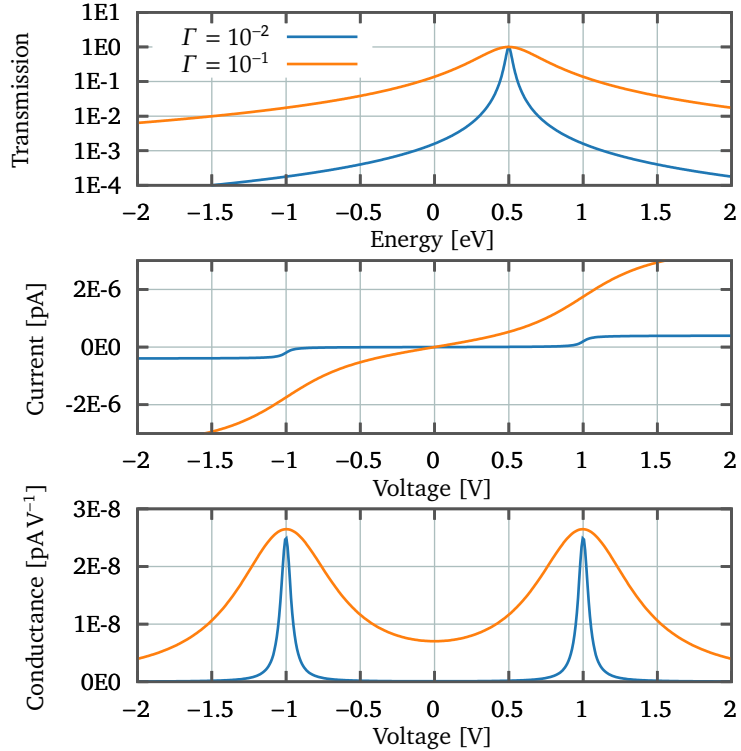
As one can see from Equation (2.10) (and also Figure 2.5), ϵ_0 gives the energy of the peak in the transmission function, while Γ effectively changes the width. In experimental situations, where the data shows a single peak in the conductance, values for ϵ and Γ can be obtained by fitting the model to the data. For multiple resonances at $\epsilon_{0,1,\dots}$ the transmission can be modeled by the sum of several resonances given by Equation (2.10), if they are sufficiently separated in energy [124].

2.2.2 The Non-Equilibrium Green's Function Approach and Density Functional Theory

For more realistic system, it is preferred to obtain an expression of T based on first-principles descriptions or methods. The non-equilibrium Green's function establishes a way to calculate the transport through molecular junctions based on such methods. For these methods, the electronic structure of a junction has to be calculated by solving the Schrödinger equation

$$\mathrm{H}\Psi = E\Psi, \tag{2.11}$$

where Ψ is the wavefunction of the system under study, H is the Hamiltonian operator and E the energy of the system. In the following, the Born-Oppenheimer approximation is made [114]. As a wavefunction for a many-particle system, a Slater determinate can be used, given by

$$\Psi(r_1, r_2, \dots, r_N) = \frac{1}{\sqrt{N!}} \begin{vmatrix} \psi_1(r_1) & \psi_2(r_1) & \dots & \psi_N(r_1) \\ \psi_1(r_2) & \psi_2(r_2) & \dots & \psi_N(r_2) \\ \vdots & \vdots & \ddots & \vdots \\ \psi_1(r_N) & \psi_2(r_N) & \dots & \psi_N(r_N) \end{vmatrix} \tag{2.12}$$

N is the number of electrons, r_i the spatial and spin coordinates of the i-th electron and ψ_i a single-particle function. ψ_i can be represented by a linear combination of atomic orbitals (LCAO), as given by

$$\psi_i = c_{i,1}\phi_{i,1} + c_{i,1}\phi_{i,1} + \dots + c_{i,n}\phi_{i,n} = \sum_j^n c_{i,j}\phi_{i,j}, \tag{2.13}$$

where c_j is a coefficient which weights the contribution of an atomic orbital to the molecular orbital and ϕ_j an atomic orbital, which can be given by Slater or Gaussian-type orbitals [114].

Density Functional Theory

Density Functional Theory (DFT) has been proven as a reliable and efficient approach to describe the electronic structure of molecules or solids [149]. In general, the Hamiltonian H for N electrons in an external potential caused by e.g. the nuclei is given by

$$\text{H} = \underbrace{-\frac{1}{2}\sum_i^N \nabla_i^2}_{\text{T}_e} + \underbrace{\sum_i^N v_{\text{ext}}(\boldsymbol{r}_i)}_{\text{V}_{ne}} + \underbrace{\frac{1}{2}\sum_{i\neq j}^N\sum_i^N \frac{1}{\boldsymbol{r}_i - \boldsymbol{r}_j}}_{\text{V}_{ee}}. \qquad (2.14)$$

The first sum T_e represents the kinetic energy operator for the electrons, the second sum V_{ne} the interaction with the external potential and the third sum V_{ee} represents the Coulomb interactions between the electrons. In this section, atomic units are used so that $e = m_{\text{e}} = \hbar = 4\pi\epsilon_0 = 1$, where e is the elementary charge, m_{e} the mass of an electron, $\hbar$ the reduced Planck constant and ϵ_0 the vacuum permittivity. Additionally, DFT is discussed within the Born-Oppenheimer-regime, thus neglecting the motion of the nuclei. This approximation is reasonable, since the motion of the nuclei is far slower than the motion of the electrons, so that the electrons almost instantaneously react to any change of the nuclei's position.

This system can be solved for example by using a Slater determinant as approximations for the wavefunctions, and then minimizing the systems total energy by varying the expansion coefficients of the Slater determinant. This approach is called Hartree-Fock (HF) theory. HF provides reasonable results for a range of systems, but is still not satisfactory for several, e.g. a simple F_2 molecule is not bound in HF[149]. Post-HF methods are able to improve the results, but usually at a computational cost: HF already scales with the fourth power of the system size, and these post-HF methods perform even worse. Thus, in the mid 1900s there was a need to find a new method with a similar or better accuracy and improved performance, to be able to describe larger systems.

In 1964 and 1965, Hohenberg, Kohn and Sham lead the foundation of density-functional theory (DFT) theory [150, 151]. In contrast to HF theory or other wavefunction–based methods, it assumes that all ground-state properties of an N-electron system are determined by the total ground-state electron density ρ_0. This

assumption reduces the computational cost, since the system co-ordinates are reduced from $4N$ (for wave-function methods/theories) to 3.

In wavefunction-based methods, the external potential v_{ext} defines the wavefunction and thus all properties of interest.

$$v_{ext} \rightarrow \psi \rightarrow \rho, E, ... \qquad (2.15)$$

The first Hohenberg-Kohn theorem states that the external potential and hence the total energy is a unique functional of the electron density. Thus, the scheme above effectively changes[6] to [149]

$$\rho \rightarrow v_{ext} \rightarrow \psi \rightarrow E, \rho ... \qquad (2.16)$$

In that way, the Hamiltonian and thus E can be reformulated to depend on ρ as a fundamental variable. The total energy is then given by

$$E[\rho] = T_e[\rho] + V_{ne}[\rho] + V_{ee}[\rho] \qquad (2.17)$$
$$= F[\rho] + V_{ne}[\rho], \qquad (2.18)$$

where $F[\rho]$ describes the parts which do not depend on v_{ext}. The variational principle is introduced with the second Hohenberg-Kohn theorem, which states that the density ρ', which minimizes the total energy, is the exact ground-state density [150],

$$F[\rho'] + \int v_{ext}\rho' \geq F[\rho] + \int v_{ext}\rho = E_0. \qquad (2.19)$$

Kohn & Sham [151] showed that $F[\rho]$ can be re-ordered into accessible terms and those, which are hard to treat on a theoretical level as

$$F[\rho] = T_{non}[\rho] + J[\rho] + E_{XC}[\rho]. \qquad (2.20)$$

Here, $T_{non}[\rho]$ is the kinetic energy of a non-interacting reference system of Fermions with the same ground-state density as the interacting system and $J[\rho]$ the classic Coulomb interactions between the electrons. $E_{XC}[\rho]$, the exchange-correlation functional, summarizes the non-classical contributions to the kinetic energy and to the electron-electron interactions. Up to this point, DFT is ab-initio, but in order to calculate E_{XC}, approximations have to be introduced.

A set of single-particle equations is obtained, similar to the HF equations [114, 151]. These Kohn-Sham equations are given by

$$h^{KS}\psi_i = \epsilon_i\psi_i, \qquad (2.21)$$

[6] This is not a practical formalism to calculate the desired properties, but more proof that those are contained in ρ.

2 Coherent Tunneling

with h^{KS} as the effective single-particle Hamiltonian

$$h^{KS} = -\frac{1}{2}\nabla^2 + v_{KS} \qquad (2.22)$$

$$\text{with} \quad v_{KS} = v_{\text{ext}} + v_{\text{el}} + \frac{\partial E_{XC}}{\partial \rho}, \qquad (2.23)$$

where v_{el} is the classical Coulomb potential. Thus, instead of solving a many-body Schrödinger equation, DFT yields the properties of interest by solving Equation (2.21) for non-interacting fermions with the same ground-state density as the interacting system [151]. The wavefunction of the non-interacting system is described by a Slater determinant (Expression 2.12), where the single–electron functions are called Kohn-Sham orbitals. This allows to represent the effective single–particle Hamiltonian a local basis and enables partitioning, as will be used in the next section.

The first approximation for E_{XC} was proposed by Kohn & Sham [151]. They applied the local density approximation (LDA) to calculate the exchange-correlation energy based on a uniform electron gas with the density $\rho(r)$ and a uniformly distributed positive background charge [152–154]. An improvement over the LDA approach was to include the first derivative of the density with respect to spatial coordinates. This approach is called generalized gradient approximation (GGA). One of the most popular GGAs is the BP86 functional developed by Becke and Perdew [155, 156].

Another popular functional is B3LYP [157, 158], which mixes a part of Hartree-Fock exchange into the exchange-correlation functional. This group of functionals is called "hybrid functionals".

For further studies, the interested reader is pointed to several reviews discussing latest advances (and also problems) of DFT, e.g. from Burke, Becke, Jones or others [149, 159–163]. A particular amusing review was published by Kieron Burke and coworkers in 2015 [164].

[7] The advanced Green's function is related to the retarded Green's function by $G_{\text{adv}} = G_{\text{ret}}^\dagger$ [115].

[8] The NEGF+DFT approach discussed here describes the transport of non-interacting fermions. For transport of interacting fermions, see, e.g., Ref. [165]

The Non-Equilibrium Green's Function Formalism

To obtain an expression for T using DFT, the definition of the retarded[7] Green's function for an effective single-particle Hamiltonian[8] H [115, 124] is introduced as

$$G(E) = \left[(E + i\eta)\mathbf{1} - H\right]^{-1} \Leftrightarrow \left[(E + i\eta)\mathbf{1} - H\right]G(E) = \mathbf{1}. \qquad (2.24)$$

The Hamiltonian of a molecular junction in a local basis as given in Kohn-Sham DFT can be represented by

$$H = \begin{pmatrix} H_l & V_{lc} & 0 \\ V_{cl} & H_c & V_{cr} \\ 0 & V_{rc} & H_r \end{pmatrix},$$ (2.25)

where $H_{c,l,r}$ describes the electronic structure of the electrodes or central region, while V is the coupling between the central region and the electrodes [123]. Inserting this into the definition of the Green's functions yields

$$\begin{pmatrix} E - H_l & -V_{lc} & 0 \\ -V_{lc}^\dagger & E - H_c & -V_{rc}^\dagger \\ 0 & -V_{rc} & E - H_r \end{pmatrix} \begin{pmatrix} G_l & G_{lc} & 0 \\ G_{cl} & G_c & G_{cr} \\ 0 & G_{rc} & G_r \end{pmatrix} = 1$$ (2.26)

with $E = (E + i\eta)\mathbf{1}$ and $V_{ba} = V_{ab}^\dagger$ [115]. By performing the matrix multiplication, for G_c

$$G_c(E) = [E - H_c - \Sigma_l(E) - \Sigma_r(E)]^{-1}$$ (2.27)

$$\text{with} \quad \Sigma_{l,r}(E) = V_{(l,r)c}^\dagger (E - H_{l,r})^{-1} V_{(l,r)c}$$ (2.28)

$$= V_{(l,r)c}^\dagger G_{l,r} V_{(l,r)c}$$ (2.29)

can be found. Σ is the self-energy representing the interaction of the molecule with the electrode. Additionally, the coupling matrix Γ

$$\Gamma = i(\Sigma - \Sigma^\dagger)$$ (2.30)

can be defined. Following [115, 124], the transmission matrix can then be written as

$$T(E) = \text{tr}\left[\Gamma_{lc}(E)G_c(E)\Gamma_{rc}(E)G_c^\dagger(E)\right].$$ (2.31)

From a DFT calculation of a molecular junction, in principle all entries of the Hamiltonian matrix H can be obtained and thus the current through the junction can be calculated using Equations (2.31) and (2.3). The details of the implementation into ARTAIOS will be presented in the next section. For further information regarding the LB approach or the non-equilibrium Green's function methodology the interested reader may refer to [48, 77, 115, 123, 124, 166].

2.3 Transport Calculations using Artaios

ARTAIOS is a post-processing program for quantum mechanical calculations. As a so-called meta-program, it can interface to third-party programs which perform quantum mechanical calculations and processes the output, thus it can easily profit from latest developments and new features. In contrast to transport programs[9] which include self-consistent field (SCF) schemes such as SIESTA [73], effects of the applied voltage on the electronic structure can not be calculated. But in order to study qualitative trends and perform conceptual analyses, the modular structure of ARTAIOS is preferable. Depending on the type of calculation, it supports GAUSSIAN, TURBOMOLE, ADF or NWCHEM [51, 168, 169]. Aside from transport calculations, it enables the calculation of Heisenberg exchange-spin coupling constants or analysis of local spins [170]. The main purpose of ARTAIOS is the calculation of electron transport properties of molecular junctions, based on the LB approach in combination with the NEGF method. Besides the calculation of the spin-dependent transmission function on the basis of e.g. DFT calculations, the program e.g. allows for an analysis of the local transmissions (atomic decomposition of the transmission to study transmission pathways [168, 171]). Within the scope of this thesis, the program was extended to be able to calculate inelastic electron tunneling (IET) spectra together with the MOVIPAC program package. This will be presented in Chapter 3.

[9] As given in the introduction, other programs which employ the LB approach to calculate transport phenomena include SIESTA/TRANSSIESTA [73], QUANTUMATK [74] or GOLLUM [167].

As input, the output files of an electronic structure calculation as well as an input file which specifies the system has to be provided. From the quantum mechanical calculations, the Hamiltonian/Fock matrix H and the overlap matrix S[10] are the central quantities. As shown before (Equation (2.31) and (2.3), the current through a junction in the LB approach is given by

[10] The overlap matrix is given by the elements $S_{ij} = \langle \psi_i | \psi_j \rangle$ for a non-orthogonal basis, which becomes $S_{ij} = \delta_{ij}$ for an orthogonal basis.

$$I = \frac{e}{h} \int_{-\infty}^{\infty} dE \left[f_l(E + eV/2) - f_l(E - eV/2) \right] T(E),$$

while the transmission matrix as central quantity can be evaluated from by the trace over the retarded Green's functions for the central region and the couplings of the electrodes to the central region

$$T(E) = \text{tr} \left[\boldsymbol{\Gamma}(E) \boldsymbol{G}(E) \boldsymbol{\Gamma}(E) \boldsymbol{G}^\dagger(E) \right]$$

with

$$\boldsymbol{G}_c(E) = \left[\boldsymbol{E} - \boldsymbol{H}_c - \boldsymbol{\Sigma}_l(E) - \boldsymbol{\Sigma}_r(E) \right]^{-1}$$

in an orthogonal and

$$G_c(E) = [ES - H_c - \Sigma_l(E) - \Sigma_r(E)]^{-1} \qquad (2.32)$$

in a non-orthogonal basis. The Hamiltonian matrix H and the overlap matrix S are directly obtained from the quantum mechanical calculations. To calculate Σ, ARTAIOS applies the "wideband" limit by default [115, 172]. Usually the electrodes studied are gold electrodes, which have a relatively constant density of states around the Fermi level. For the Green's functions of the electrodes,

$$G_{l,r} = -i\pi \mathrm{LDOS}^{\mathrm{const}} \delta_{ij} \qquad (2.33)$$

is assumed. For the local density of states of the s-band, $0.036 \, \mathrm{eV}^{-1}$ is used, obtained from DFT calculations for bulk gold [173]. This enables the calculation of the self-energies (Equation 2.29) and consequently the coupling matrices

$$\Gamma = -2\mathrm{Im}(\Sigma). \qquad (2.34)$$

Figure 2.6 summarizes the NEGF formalism to the LB approach and how it is implemented in ARTAIOS.
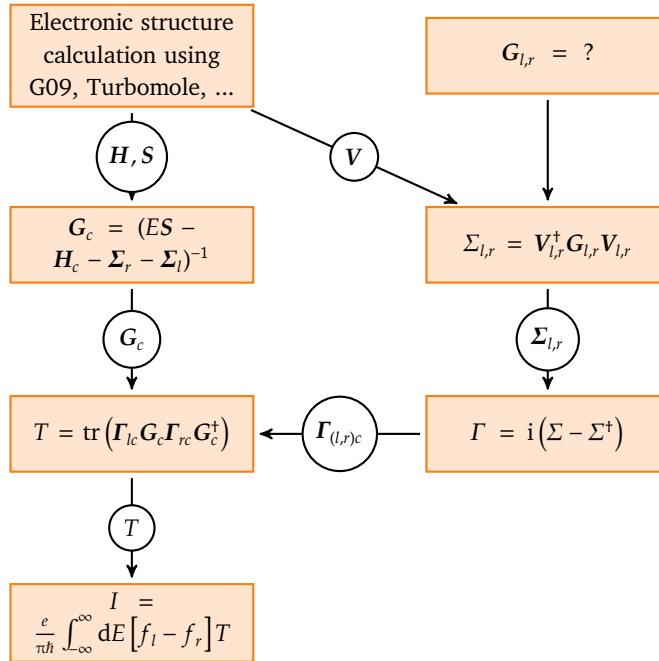
Figure 2.6: Diagramm of the data flow in ARTAIOS to calculate the transmission function T or the current $I(V)$.

In the following, some examples using ARTAIOS to calculate the transport properties of molecular junctions are discussed.

2.3.1 Transmission through a Hydrogen Bridge

Before, the transmission through a simple single-level system was described, which results in a transmission function which has a

Lorentzian shape. The width corresponds to the coupling between the central system and the electrodes, and the position to the energy of the single level. But can similar results be obtained using a first-principles approach, e.g. with DFT in combination with ARTAIOS?

To illustrate the influence of the coupling with a more realistic scenario, transport calculations for a hydrogen bridge are performed. This is a two-level system, which also can be approximated using a sum of two Lorentzians as given by the Breit-Wigner formula. Such a system has been studied experimentally [174] using platin electrodes. Here, gold electrodes are used to be able to apply the wide-band limit implemented in ARTAIOS and to be consistent with later calculations.

The structure of molecular hydrogen is obtained by a structure relaxation using GAUSSIAN 09 (B3LYP/LanL2DZ)[11] [157, 175, 176]. The electrodes are modeled using each a single gold atom (see Figure 2.7). The distance d between the gold atoms and the hydrogen is increased from 1 to 6 Å, thus decreasing the coupling between the electrodes and molecular bridge. Using ARTAIOS, the transmission function is calculated for each d and shown in Figure 2.8 as a heatmap. Here, the breaking of the bonds at a certain distance is disregarded. DFT is not capable of describing this properly, since it models the whole system in a single determinant. But as we are not interested in bond-breaking effects but merely want to study the effect of a changing coupling between the electrodes and the molecule, this is not essential.

$$\text{Au} \overset{d}{\text{———}} \text{H} - \text{H} \overset{d}{\text{———}} \text{Au}$$

Figure 2.7: Structure of the dihydrogen bridge. The distance d is varied from 1 to 6 Å.

11

Figure 2.8: Transmission through a H_2 bridge (depicted above) for different distances displaced as a heat map. When the distance is increasing, the coupling becomes weaker and the broad transmission condenses into sharp peaks. For some points, the transmission exceeds unity, which can be explained with either numerical artifacts or as the contribution from more than one tunneling channels.
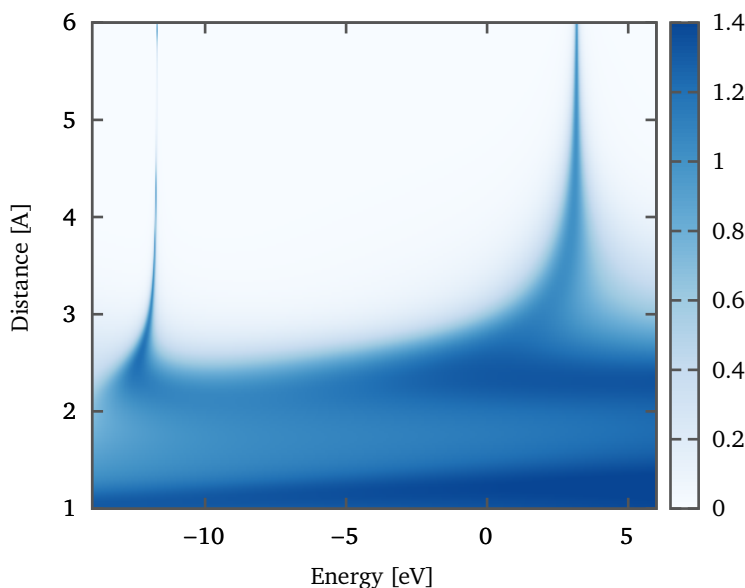
This visualizes how, with decreasing coupling, the transmission

function condenses into two sharp peaks located roughly at the HOMO and LUMO energies of the isolated H_2 (−11.67 eV and 3.14 eV). When the coupling is stronger, shifts and broadening of the peaks are obtained.

A two-level Breit-Wigner model

$$T(E) = \sum_{i=1}^{2} A_i \frac{\Gamma_i^2}{\Gamma_i^2 + (E - \epsilon_i)^2} \tag{2.35}$$

is fitted to the transmission function calculated using ARTAIOS to obtain values for the coupling and the energy levels. Figure 2.9 shows the calculated and fitted transmission functions for two different distances, as well as the values $\Gamma_{1,2}$ and $\epsilon_{1,2}$ extracted from the fit for $d = 2\text{Å}$ to $d = 5\text{Å}$.
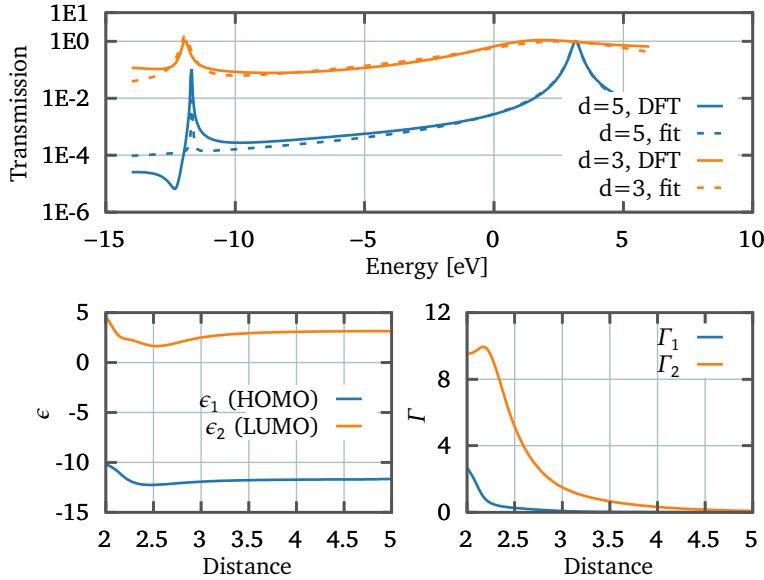
Figure 2.9: *Upper panel:* Calculated (solid line) and fitted (dashed line) transmission function of the hydrogen bridge shown in Figure 2.7 for $d = 3$ Å and $d = 5$ Å. The fit was performed using Equation (2.35). *Lower panel:* The dependency of the the energies $\epsilon_{1,2}$ and the coupling $\Gamma_{1,2}$ on the distance between the electrodes and the hydrogen molecule.

The coupling between the LUMO and the electrodes is much stronger than for the HOMO. Thus, the current would be dominated by tunneling through the LUMO, which indicates electron transport through this H_2 bridge. The main tunneling channel is also determined by the distance of the resonances for ϵ_1, ϵ_2 to the Fermi energy, which is not always easily to determine [177] and can e.g. be estimated using calculations of large gold clusters [178], which yields $E_f = -5.0$ eV. If the HOMO was closer to the Fermi energy and coupled more strongly, the picture would be different and hole transport would be obtained. At close distances ($d \leq 2.5\text{Å}$), the coupling between the molecule and the electrodes becomes very high and signatures of the molecular orbitals cannot be distinguished. But the results should be taken with a grain of salt, since this is a model system and does not represent realistic structures nor a structure, which has been optimized.

2.3.2 Quantum Interference and Tunneling Pathways

To demonstrate the capabilities of Artaios regarding the analysis of local transmission pathways, a phenanthrene junction is investigated, where the thiol anchoring group is attached on one side to the para position, as well as to the two neighboring meta positions. Such structures show a unique property of coherent tunneling transport, quantum interference. This can drastically change the transport properties of a molecular junction, even though the electronic structure might be quite similar [55, 179]. Quantum interference in molecular junctions can be understood as the interference with competing tunneling pathways [180–182][12], thus the understanding and control of tunneling paths enables control over the transport properties of a junction.

[12] But not exclusively, see, e.g. Refs. [52–54, 181, 183–187]

The input structures of the isolated molecules have been relaxed using Gaussian 09, the BP86 correlation functional and the LanL2DZ basis set [155, 156, 175, 176]. Au_9 cluster have been added to mimic the electrodes, with a sulfur-gold distance of 2.85 Å. Transport calculations using Artaios have been performed based on Gaussian 09 single point calculations at the same level of theory.

The Lewis structures and obtained transmission functions are shown in Figure 2.10. The transmission function obtained for the structure with the sulfur anchoring group placed at the *para* position is significantly higher than for the two *meta* positions.

Figure 2.10: *Top:* Lewis structure of the phenanthrene junction, the different colored thiol group on the right side marks the different anchoring positions for the right electrode. *Bottom:* Transmission functions (left) and current (right) obtained for a phenanthrene junction, where the gold clusters were attached to different positions of the ring. The colors of the curves corresponds to the structure with the respectively colored thiol group.
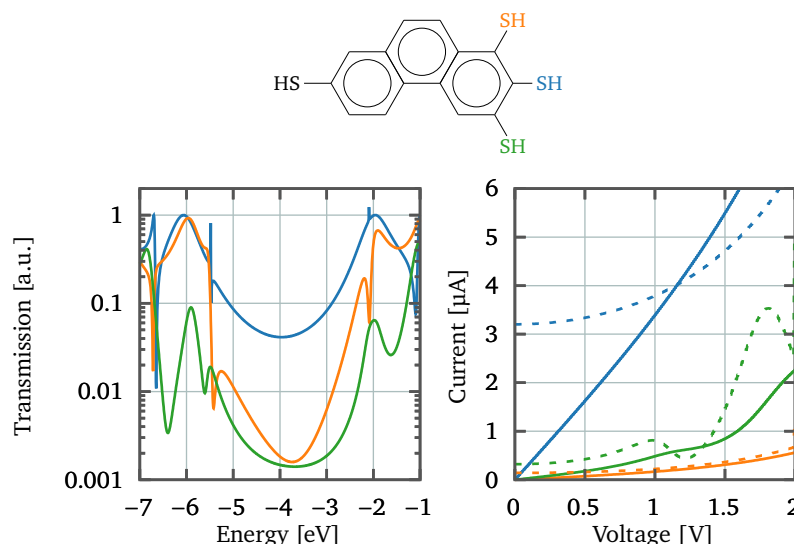
This is a purely quantum mechanical effect and can not be understood by looking at the energy level diagram alone, as the energies of the frontier orbitals vary by less than 0.032 eV for the HOMO

and 0.002 eV for the LUMO. By looking at the local transmissions [168, 171] (Figure 2.11), the reason behind the differences between the transmission functions becomes clear: When the anchoring group is attached at the *para* position, a direct tunneling path through the molecule exists. For the other two placements of anchoring group, ring currents occur. The current which is leaving the system through the anchoring group is significantly lower, since destructive interference between the pathways which lead to the "output" occur. In Figure 2.11, the outgoing currents are not even visualized due to the threshold for the drawn arrows.

These interference features manifest themselves in sharp antiresonances in the transmission function or can decrease the total transmission. Such interference effects can be quite sensitive to external stimuli. This sparked the interest to use molecules showing interference effects to build molecular switches, quantum interference transistors or logic gates [52, 183, 184, 188–191]. The example presented here demonstrate *a)* the effect of quantum interference on the transmission function and thus the transport properties of a molecular junction and *b)* the value of evaluating tunneling pathways as obtained using ARTAIOS. For an in-depth analysis of this class of molecules regarding transport properties and quantum interference refer to Ref. [192].

Figure 2.11: Local transmissions for the three phenanthrene junctions (odered from top to bottom), evaluated at $E_\mathrm{F} = -5$ eV.

The NEGF+DFT approach implemented in ARTAIOS is a powerful tool to study the transport properties of molecular junctions. Two exemplary sytems were studied, a H_2 bridge as a model system to understand the influence of the interactions between the electrodes and the central system, and phenanthrene junctions demonstrating the effects of quantum interference and analysis of tunneling pathways. In the next chapter, the extension of the LB approach to inelastic effects and the implementation into ARTAIOS + MOVIPAC will be discussed. The theoretical approach in ARTAIOS approximates several aspects in the simulation of the transport properties, as the already mentioned wide-band limit for the description of the electrodes. Additionally, electron-electron interactions in the molecular junction are not incorporated. A way to do this would be to use the Meir-Wingreen formula [165]. Self-consistent transport calculations as, e.g., implemented in SIESTA are also capable to describe effects of the electric field over the junction and resulting rectification effects.

2.4 Loosing Coherence: Hopping Transport and Coulomb Blockade

So far, transport has only been discussed in detail in terms of coherent tunneling through a nanoscopic system. But this is not a realistic assumption in all cases. It has been shown that, e.g., with increasing length of a molecular wire, the transport process changes from tunneling to hopping [193–197]. Hopping describes a series of consecutive tunneling events, where coherence is lost. It can be distinguished from coherent tunneling experimentally by the temperature dependence (coherent tunneling has none) or its length dependence.

The regimes of hopping and tunneling transport trough molecules or nanoparticles overlap, as it is not always easy to predict which type of transport a specific system shows [77, 198]. A full discussion of this topic is outside the scope of this work, but in the following some fundamental aspects of incoherent tunneling and the "Coulomb blockade" in comparison with the coherent tunneling model are discussed.

Hopping transport goes along with a finite amount of time a charge stays on a specific site of the bridge or a particle. This can lead to Coulomb repulsion between this charge and any further charges, which can block the current through the system as long the charge is on the particle. This is the so-called Coulomb blockade [121] and shows a typical step-like behavior in the I-V curves (Figure **??**). The conditions for the Coulomb blockade regime are usually weak coupling between the electrodes and the particle and low temperatures ($k_\mathrm{B}T < E_\mathrm{C}$, where E_C is the energy which has to be overcome to charge the particle with one more electron.

The charging energy E_C of particle is given by

$$E_\mathrm{C} = \frac{e^2}{C},\qquad(2.36)$$

where C the capacitance of the particle, which is given for a sphere of radius r as $C = 4\pi\epsilon_0 r$ [199][13]. As long as the applied potential eV is smaller than E_C, no current flows. If the energy is enough to charge the particle, one electron at a time can pass the particle, but no further increase of the current is observed until enough voltage is applied to charge the particle twice. An additional gate voltage can be used to lower or increase the energy needed, which enables the use of devices in the Coulomb blockade regime as single electron transistors. One example was shown by Maeda *et*

---

[13] ϵ_0 refers here to the vacuum permittivity, not to an energy.

al.. A gold nanoparticle connected with a source, a drain and two gates was used to perform logic XOR or NXOR operations [200].
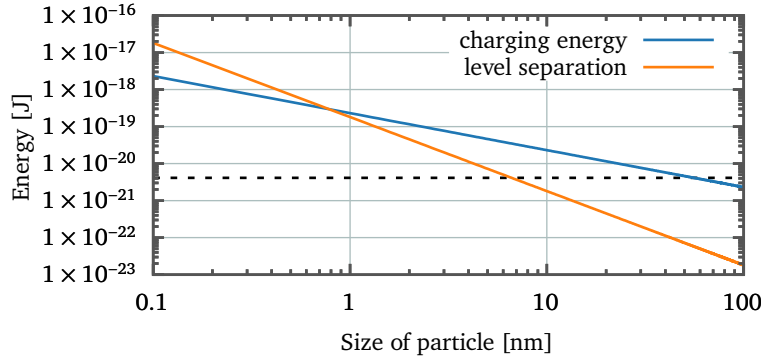
Figure 2.12: Charging energy and level spacing of a particle with respect to its size. The dashed line represents the energy of $k_{\mathrm{B}}298\,\mathrm{K}$, thus the thermal energy at room temperature.

To estimate whether a system is in the incoherent hopping and Coulomb blockade regime or not, one can compare the spacing of the electronic levels of the system with the charging energy. To estimate the spacing between the electronic levels, the expression for energy levels of a particle in a box can be used which is given by

$$E_n = \frac{\hbar^2 \pi^2 n^2}{2 m_{\mathrm{e}} r^2}. \tag{2.37}$$

In Figure 2.12, the size-dependence of the charging energy E_{C} and the energy difference between E_1 and E_2 for a particle in a box are plotted. At particle sizes below 0.8 nm, the spacing between the individual levels is greater than the charging energy. Thus, if the applied potential is big enough to fill the state, the charging energy is already overcome. For particle sizes above 0.8 nm, the spacing of the energy levels is small compared to the charging energy. If the applied potential is high enough to overcome the charging energy, the spacing between the individual does not play a role or can be seen as a continuum.

Interestingly, both regimes (hopping in the Coulomb blockade regime and coherent tunneling) can show similar results for the differential conduction. If, e.g., the Breit-Wigner formula for the transmission function (Expression 2.10) together with Equation (2.3) for the calculation of the current is used, the dI/dV plot shows peaks which correspond to the resonances of the transmission function. Similarly, for a system in the Coulomb blockade regime, the conductance shows peaks when the energy is enough to charge the particle by one more electron (Figure **??**). These peaks are equidistant in energy and separated by the charging

energy E_C, while for a system in the coherent tunneling regime, they are related to the electronic structure of the system.

Hopping transport through nanoparticles as well as molecules has different regimes. At high temperatures, hopping usually occurs from one site to the next, which is called nearest-neighbor hopping [201]. If the temperature becomes lower and/or the disorder in the system increases, hopping can be dominated by the activation energy E_a and not the distance, which leads to variable–range hopping processes [120, 201–203]. More details regarding different types of hopping transport are discussed in Chapter 9.

3 Inelastic Electron Tunneling Spectroscopy and Tunneling Pathways

The following chapter has been published in a modified version as Deffner, M. & Herrmann, C. The Limits of Inelastic Tunneling Spectroscopy for Identifying Transport Pathways. *(preprint, submitted to Chemrxiv)* (Mar. 2020).

The Landauer-Büttiker (LB) approach can not only be used to describe the elastic tunneling transport through molecular junctions. It can also be used to study e.g. heat transport or inelastic processes [142]. Inelastic processes can imprint information about the molecular vibrations of a molecular junction into the current. Also, inelastic processes play an important role in the loss of coherence or dephasing of the tunneling current.

IETS is a technique to study the interplay between tunneling transport and molecular vibrations. Usually, a tunneling electron passes a junction while preserving its energy. If the applied bias and thus the energy of the electron is high enough to excite a molecular vibration, it can also scatter inelastically with the system and transferring (or absorbing) energy to a vibration. Even though the electron can lose a bit of energy, this is notable in the transport by a increase or decrease of the measured current. This can be explained by recalling that the tunneling transport is governed by the tunneling probability for an electron with a specific energy and the number of conduction channels. When the energy is enough to excite a vibration, an additional possibility (or transport channel) is created, thus increasing the current [134]. By calculating the second derivative of the current with respect to the voltage, a peak or dip is obtained at those energies, which correspond to a molecular vibration. Figure 3.1 shows a schematic depiction of this processes.

Experimentally, IET spectra are recorded using STM or MC-BJ setups in combination with lock-in techniques or specific devices, usually at low temperatures [134, 204–206]. This can be used

Figure 3.1: Elastic and inelastic tunneling through a tunneling barrier representing a molecule between two electrodes. $\hbar\omega$ corresponds to the energy of a vibrational quantum. For energies below $\hbar\omega$, just the elastic channel is available. At energies higher or equal to $\hbar\omega$, the inelastic channel is openend which leads to an slight increase of the tunneling current. By calculating the second derivative of the current with respect to the voltage, the IET spectrum is obtained
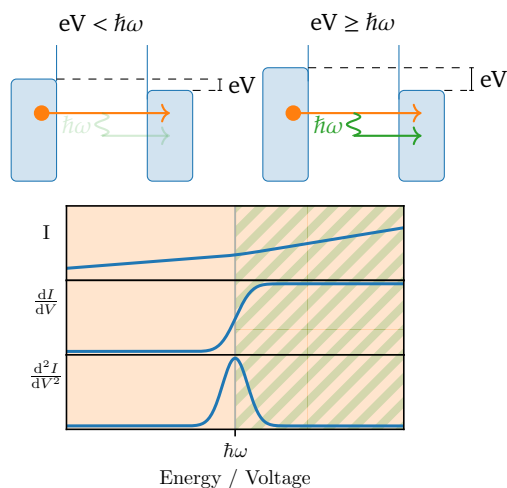
to verify the presence of a molecular in junction or study its conformation [207, 208]. Apart from that, IETS can also be used to study tunneling pathways through molecular junctions. The knowledge of tunneling pathways allows to understand and control the transport through molecules. This has, e.g., been studied in proteins [209–213]. This is also interesting for spin filtering or chiral systems, where pathway analysis can identify whether electrons follow helical paths in helices [108] or in electronically helical structures [109], which can be important for understanding chiral induced spin selectivity [214–234].

On the theoretical side, various techniques like the already mentioned local transmission analysis allows to extract information about tunneling pathways from first–principles calculations [110, 168, 171, 212, 213, 235–241]. This is much more complicated with experimental techniques. One possible approach is to relate the IET spectra and the intensity of specific modes with the tunneling path, since it has been found that the IETS intensity depends on whether the mode is inside or outside the tunneling path [63, 242]. To investigate the feasibility of this idea, we implemented a way to calculate IET spectra into ARTAIOS [75] and MOVIPAC [243] based on the approach developed by Troisi *et al.* [62, 244]. This allows us to use the mode–tracking algorithm in MOVIPAC [243, 245, 246], which can selectively calculate vibrational modes without the need of a full calculation and diagonalization of the Hessian matrix[1]. Especially for molecular junctions, where vibrations of functional groups can potentially be used as a tracer for tunneling pathways, this approach can be beneficial

---

[1]The Hessian matrix contains the second derivatives of the energy with respect to geometry [114].

due to the reduction of calculation time.

In the following, the theoretical approach for the calculation of IET spectra is presented and validated using a set of representative systems. Afterwards, the connection between tunneling pathways and IET spectra is investigated using systems with delocalized and localized vibrations.

3.1 Theoretical Background

For the calculation of the IET spectra, we follow the approach derived by Troisi *et al.* [244], who generalized the theoretical description of the elastic tunneling current through a molecular junction within the coherent tunneling regime [123]. This approach is valid for low bias voltage, low temperatures and the Fermi levels of the electrodes far away from resonances with effective single-particle levels of the molecules. Otherwise, effects such as charging and polaron formation have to be considered [247].

As discussed Section 2.2, the Hamiltonian H_{tot} of the molecular junction contains part describing the electrodes and the central region containing the molecule (or the molecules and parts of the electrodes), as well as the interactions between the subsystems:

$$H_{\text{tot}} = H_{\text{L}} + H_{\text{R}} + H_{\text{C}} + V_{\text{LC}} + V_{\text{RC}},$$

where $H_{\text{L,R,C}}$ is the Hamiltonian of subsystems and V the coupling between the electrodes and the central region. Using a Green's function approach (Section 2.2.2), the so-called transmission function $T(E)$ is obtained as

$$T(E) = \text{tr}\left(\boldsymbol{\Gamma}_{\text{L}}(E)\boldsymbol{G}_{\text{C}}(E)\boldsymbol{\Gamma}_{\text{R}}(E)\boldsymbol{G}_{\text{C}}(E)^{\dagger}\right).$$

This describes the probability of an electron transmitted from one electron to the other for a certain energy. The elastic zero-bias conductance G_{el} is given by

$$G^{\text{el}} = G_0 T(E_{\text{F}}) \tag{3.1}$$

To introduce the electron-vibration coupling, the dependency of the Hamiltonian for the central system on the nuclear coordinates is taken into account ($H_{\text{C}} \rightarrow H_{\text{C}}(Q)$). Now, the Hamiltonian and likewise the expression for $\boldsymbol{G}_{\text{C}}(E)$ depend parametrically on the nuclear coordinates of the molecules. Performing a Taylor expansion of $\boldsymbol{G}(E)$ for a set of vibrational modes $\{Q_\alpha\}$ (using mass-weighted coordinates) around the equilibrium position $\{Q_\alpha\} = 0$,

the first order correction is nonzero only for an initial and final state, which differ by one vibrational quantum [244]. This part (G^α) describes the correction to the elastic current due to the emission (or adsorption) of one vibrational quantum and is given by

$$G_{ij}^\alpha = \frac{\sqrt{(2)}}{2} \left(\frac{\partial G_{ij}(E, \{Q_\alpha\})}{\partial Q_\alpha} \right)_{\{Q_\alpha\}=0}. \qquad (3.2)$$

From this matrix, the IETS intensity $\frac{d^2 I}{dV^2}$ for each mode α can be calculated by [64]

$$W_\alpha = g_0 \text{tr} \left(\boldsymbol{\Gamma}_L(E_F) G_C^\alpha(E_F) \boldsymbol{\Gamma}_R(E_F) G_C^\alpha(E_F)^\dagger \right). \qquad (3.3)$$

Often not the complete IET spectrum is of interest, but only the contribution of some specific vibrations or the fingerprint in a certain energetic region. To be able to address this problem for realistic systems, where the calculation of a complete spectrum would be expensive, we introduce the mode-tracking algorithm described in [245, 246]. To obtain the vibrational normal modes of a molecule within the harmonic approximation, the eigenvalue[14] equation

$$H^{(m)} Q = \lambda Q \qquad (3.4)$$

has to be solved, where $H^{(m)}$ is the Hessian matrix containing the second derivatives of the energy with respect to the mass-weighted nuclear Cartesian coordinates Q. The time-consuming step is not always (depending of the system under study) the diagonalization itself, but can be the calculation of the entries of $H^{(m)}$.

The mode-tracking algorithm does not calculate and diagonalize the full Hessian matrix. Instead, it applies a Davidson, Jacobi-Davidson or Lancos algorithm to perform an iterative subspace diagonalization of the Hessian matrix, based on a set of initial guess modes that may be chosen based on chemical intuition or knowledge on which parts of the system will contribute most to a vibration of interest [243, 245, 248–250].

The normal modes Q_α can be projected onto a set of basis vectors $b_j \in B$ by

$$Q = \sum_j c_j b_j, \qquad (3.5)$$

where $c_j \in C$ contains the expansion coefficients. By choosing an (initially) small basis, approximated normal modes as input guess

[14] The index $_\alpha$ is dropped the following.

are obtained. The (compared to H) small Davidson matrix $\tilde{H}$ can be constructed by

$$\tilde{H} = B^\top H B = B^\top \Sigma. \tag{3.6}$$

The size of $\tilde{H}$ depends on the size of the chosen basis. As shown in [246], Σ can be obtained by numerically calculating the derivatives of the electronic energy along the basis vectors b_j using

$$\Sigma = \left[\frac{\partial}{\partial b_j} \left(\frac{\partial E_{e,i}}{\partial r_A} \right) \right]_0. \tag{3.7}$$

By diagonalizing $\tilde{H}$, $\lambda^{(i)}$ and $C^{(i)}$ are obtained, where the index (i) denotes the iteration step of the algorithm. Thus, the normal modes $Q^{(i)}$ as obtained in that iteration can be constructed. As long as the desired convergence is not reached [249], this process is repeated and new basis vectors are constructed using the residuum vector $r^{(i)}$

$$r^{(i)} = (H - \lambda^{(i)})Q^{(i)}. \tag{3.8}$$

For more details regarding the convergence of the mode-tracking algorithm, see [249].

For the calculation of IET spectra, we combine the mode-tracking algorithm as implemented in MoViPac[243, 245, 246] with our program package Artaios [51, 75].

Our implementation of the IETS calculation into MoViPac is schematically shown in Figure 3.2. First, the initial guess for the modes of interest is generated by AKIRADEFINE. This can be, for instance, a certain stretching mode or all Cartesian displacements of a specific atom. We note that it is also possible to leave out this step and to just calculate the whole spectrum. For the obtained modes, the Green's functions of the distorted structures are calculated using Artaios in a parallel fashion. This is done by the SNFDC algorithm. Afterwards, the derivatives (Equation (3.2)) are calculated by the SNF algorithm, which calls Artaios to calculate the trace in Equation (3.3). These procedures are closely related to the functionalities of the individual programs: The calculation of the IETS intensity given in Equation (3.3) is formally similar to the calculation of the zero-bias conductance in Equation (3.1). The combination of Artaios and AKIRA has several advantages. First, MoViPac and consequently AKIRA is highly parallelizable, while providing full restarting compatibilities. Second, since MoViPac and Artaios are meta-programs which do not perform quantum chemical calculations on their own but interface several electronic structure codes. Third, the

Figure 3.2: Schematic representation of our implementation for the IETS calculation.
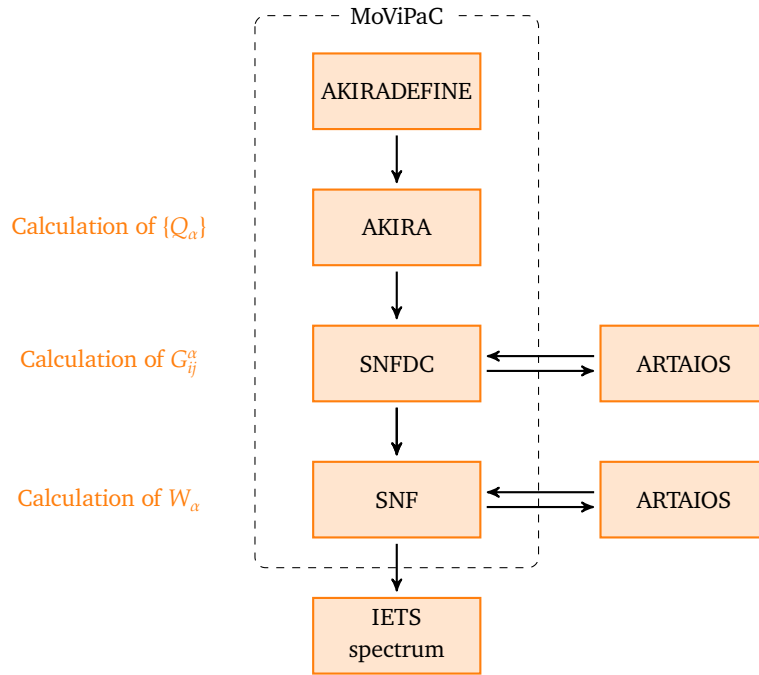
mode-tracking approach can drastically reduce computation time, enabling the study of environmental effects or the influence of the contact geometry on the IETS intensity of a vibrational mode and thus the strength of the electron-vibration.

3.2 Comparison to Previous Experiments and Calculations

In the last years, several groups have presented theoretical approaches to calculate IET spectra and compared them to experimental findings. Some of the most extensively studied molecules are oligophenylene-ethynylene (OPE), oligophenylene-vinylene (OPV) and alkane(di)thiols such as hexadecane-thiol. First measurements were performed by Kushmerick *et al.* in 2004 [251], first-principles calculations of the spectra of these molecules were done e.g. by Troisi & Ratner [64], Kula *et al.* [58] and Paulsson *et al.* [60]. Paulsson *et al.* modeled the junction within periodic boundaries. Troisi & Ratner (in their 2005 paper) and Kula *et al.* used a very similar approach using non-periodic DFT calculations, but they differ in the way they treat the electrodes: The first did not considered electrode-molecule interactions explicitly and calculated the IETS for two chosen "gateway" orbitals, while the latter simulated the IETS for different types of contact structures, such as a gold chain or triangular contacts. Their findings show

that the IETS can be highly sensitive to the contact structure. Several other publications focused on different alkane(di)thiols [252, 253], the effect of functional groups on the IETS of saturated molecules [62], the effect of the electrode separation on the IETS for a single OPE molecule [254] or the interplay between molecular junctions showing interference features and inelastic effects [255, 256].

To validate our implementation, we present calculations of the IET spectra for OPE, OPV and several alkanedithiols. We compare our findings to results by Kushmerick *et al.*, Paulsson *et al.*, Troisi and Ratner and Kula and Lua [58, 60, 64, 251]. To compare the spectra, we did not apply our modetracking approach at this point, but computed the full spectrum instead. The structures of the dithiol molecules are optimized using Gaussian09 [175] in combination with the B3LYP exchange-correlation functional [157] and the LanL2DZ [176] or def2SVP [257, 258] basis set. We chose these settings to be consistent to Kula and Luo [58] (for the aromatic systems) and to [259] for the aliphatic ones. To mimic the electrodes, the terminal hydrogen atoms are stripped and small gold clusters consisting of three gold atoms are attached with an Au-S distance of 2.85 Å as in Refs. [58, 62]. For the calculation of the vibrational modes, the same computational methods have been used as for the structure optimization. The wide-band limit is applied to calculate the self-energies of the electrodes, which should be suitable for our type of calculations [260, 261], but it should be pointed out that Artaios in principle allows for descriptions of the self-energy beyond the wide-band limit. The given intensities are calculated using expression (3.3) and give the second derivative of the current with respect to the applied voltage ($\frac{\mathrm{d}^2 I}{\mathrm{d}V^2}$ vs V) [247]. For OPE and OPV, we calculated the IETS for $E_\mathrm{F} = -0.14\,\mathrm{a.u.} = -3.81\,\mathrm{eV}$ as in [64].

The IET spectra for OPE (Figure 3.3, left) and OPV (Figure 3.3, right) are dominated by only a few vibrations. For OPE, the most dominant modes are the νC$\equiv$C (triple-bond stretching) mode (2289 cm^{-1}), the stretching of the aromatic rings/νC$=$C (double-bond stretching) mode (1624.06 cm^{-1}) and the ν(CS)/ν(CC) modes (1082 cm^{-1}, 1154 cm^{-1}). OPV (Figure 3.3, right) is lacking the carbon-carbon triple-bond, thus the most intense modes are the stretching of the aromatic rings (1620 cm^{-1}), the ν(CS) mode (1086 cm^{-1}) and the ν(CC) mode (1214 cm^{-1}). A combined CC stretching and CH wagging mode at 1383 cm^{-1} can be found, which is not present in OPE. In agreement with previous findings concerning IETS propensity rules, out-of-plane and asymmetric modes contribute only little to the IETS [262–264]: When com-
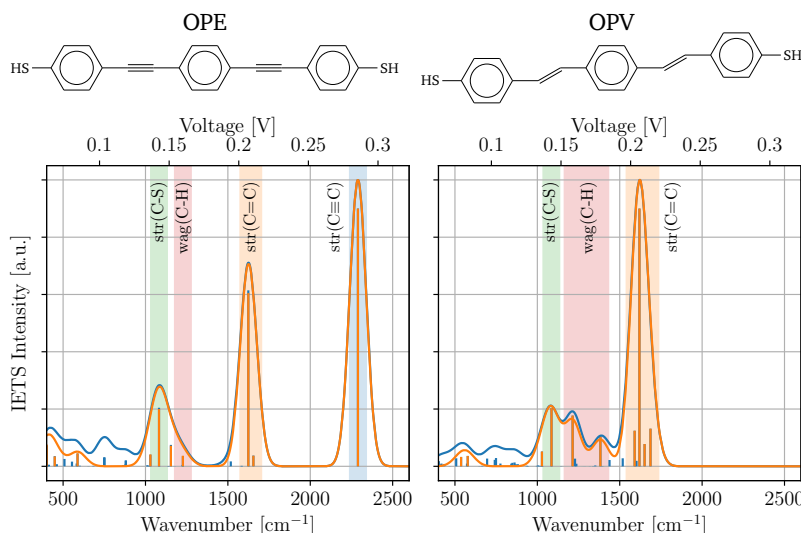
Figure 3.3: Calculated IET spectra for OPE (left) and OPV (right) using B3LYP/LANL2DZ. The lines in blue represent the full spectrum, the orange ones show the 10 most intense vibrations only.

paring the asymmetric and the symmetric stretching mode of the triple-CC bond in OPE, the IETS intensity differs by 6 orders of magnitude. We note that the spectrum can well be reproduced when only considering the 10 most intense normal modes, again supporting the idea of calculating the IETS selectively for specific modes. Aside from aromatic systems, we studied alkane-dithiols
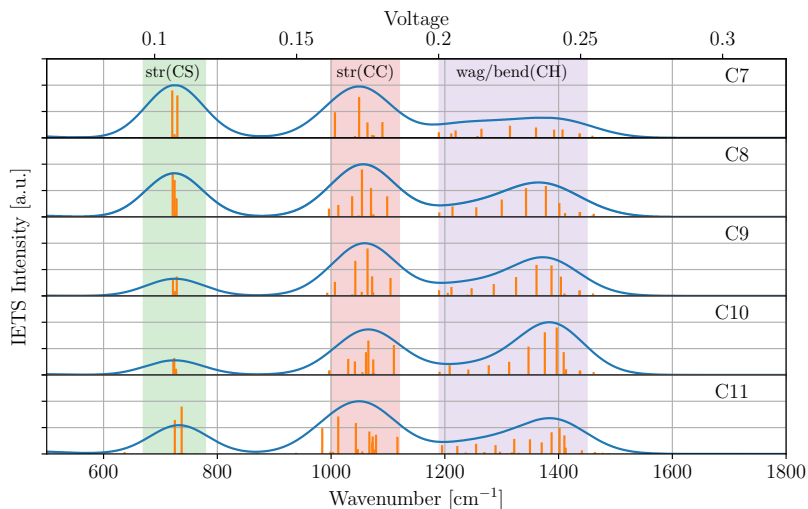
Figure 3.4: IET spectra for alkanedithiols C7 to C11, obtained using B3LYP/def2SVP in stick (orange) representation and broadened by a gaussian broadening of $500\,\mathrm{cm}^{-1}$ (blue).

of different lengths (7 to 11 CH_2 units, labeled as C7, C8, C9, C10 and C11) and compare our findings with previous results. All calculations were performed using B3LYP/def2SVP, and we are again calculating the whole spectrum rather than a few selected vibrations. As Fermi energy we choose $E_F = -3.26\,\mathrm{eV}$ as in [62]. The obtained spectra are shown in Figure 3.4. For all spectra, the following observations can be made: Stretching modes of the carbon–carbon or the carbon-sulfur bonds show a major contribution to the IETS. Additionally, wagging and twisting motions of the CH_2 group give rise to an IETS signal at $1400\,\mathrm{cm}^{-1}$, which

increases with increasing length of the molecule.

Our findings agree with the experimental findings of Kushmerick *et al.* [251] or calculations in [58, 60, 64, 259], but we note that we assign some modes differently. For other cases, similarities are more difficult to find. For example, the frequencies and intensities calculated by Solomon *et al.* [265] for several alkanedithiols are not in total agreement, as in their spectra the CH_2 wagging and twisting modes do not show a high intensity. Other results [62, 259] also deviate from our findings. We attribute this to the nature of IETS: As shown by Kula *et al.* [58], different junction geometries can alter the IET spectrum fundamentally. Frequency-wise well separated and thus easy distinguishable modes like the CC–double– or triple–bond–stretching vibrations in aromatic molecules discussed above are missing, so the effects of conformational differences are not so easily to separate from, for example, employing a somewhat different theoretical approach.

We conclude that our methodology is consistent with measured and calculated IET spectra from the literature within the frames of the introduced approximations. We also point out that for some cases, the IET spectrum can be reproduced with just a few vibrational modes.

3.3 Tracking Tunneling Pathways using IETS

To study the relationship between tunneling pathways and IET spectra, we focus on three different molecular junctions, for which in Lewis structures as shown in Figure 3.5. The first system is an iron(II)porphyrin molecular junction with a CO and an imidazole ligand in a low-spin ground state (Figure 3.5 a)). Such complexes are of high interest for molecular electronics, as they show switching behavior [266–268]. This specific complex was studied in our group before and it was found the the local currents obtained using ARTAIOS usually bypass the central iron atom and the ligands for all energies, except for those close the energies of the iron d orbitals [168]. Thus, we expect the IETS intensity of vibrational modes of the ligands to be low, except for these energies.

The second system is a nitrile–substituted biphenyl junction (Figure 3.5 b)), which was already studied by Troisi & Ratner [262]. The vibrational modes of the nitrile groups are less decoupled of the whole junction compared to the iron(II)porphyrin junction, but should be still differentiable in the frequency-domain.

a)

c)

b)
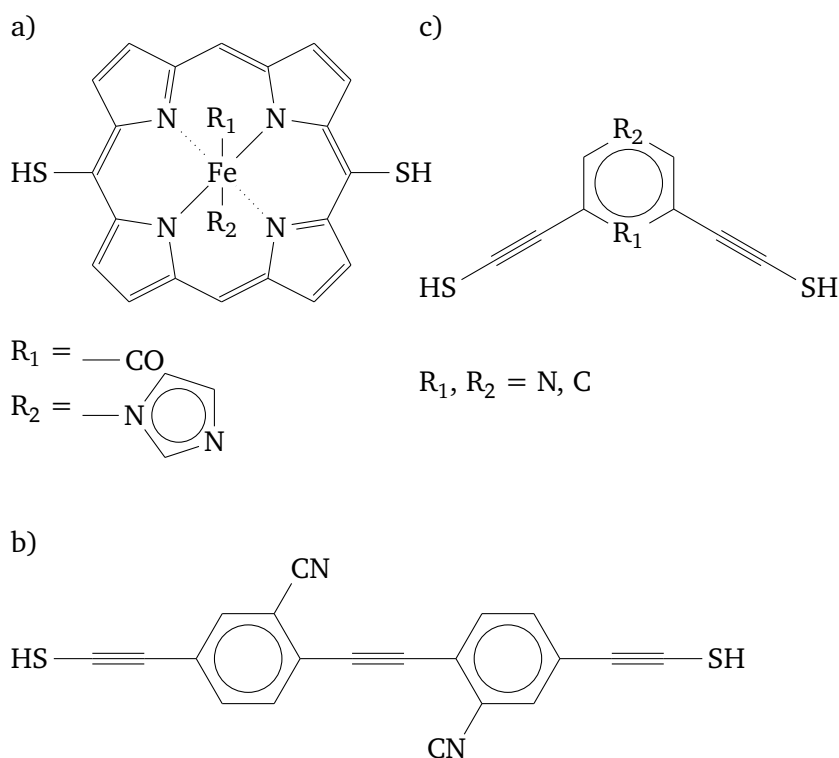
Figure 3.5: Lewis structures of the molecules used to study the relationship between tunneling pathways and IET spectra.

$R_1 = $ —CO

$R_2 = $ —N

$R_1, R_2 = $ N, C

Last, we study a set of meta-substituted benzene/pyridine junctions (Figure 3.5 c)). By the insertion of the nitrogen, tunneling pathways can be altered, so the questions arises whether this can be traced in the IET spectra of these systems. The three system vary in a way the molecular vibrations of interest are coupled to the whole system, thus representing a systematic approach.

3.3.1 Methods

All optimizations of the molecule's structures were performed using Turbomole 6.6, Ahlrichts split-valence triple-ζ basis set with polarization functions on all atoms (def2-TZVP) basis set and the BP86 functional. The resolution-of-identity (RI) approximation as implemented in Turbomole 6.6 was used [155, 156, 257, 258, 269–272]. The convergence criterion of the self-consistent field (SCF) algorithm was a change of energy below 10^{-8} Hartree. The convergence criterion for the structure optimizations was a gradient below 10^{-4} a.u.

To build a molecular junction, after the optimization the terminal hydrogen of the terminal thiol groups are stripped and replaced with small gold cluster (Au$_3$). 2.85 Å was chosen for the sulfur-gold distance. Using the obtained molecular junctions, transport calculations have been performed using ARTAIOS in combination

with Gaussian 09. The LanL2DZ basis set and B3LYP exchange–correlation functional have been used [157, 175, 176]. As described earlier, the wide–band limit has been used for the calculation of the Green's function matrices of the electrodes.

For the analysis of the local transmissions through specific atoms, the local transmission from atom A to all other atoms was summarized and normalized by the total transmission $T(E)$, as given by

$$T_A(E) = \frac{\sum_B |T_{AB}(E)|}{T(E)}. \tag{3.9}$$

This analysis can yield local atomic transmissions higher than the total transmission, since it does not distinguish between local currents which contribute to the total transmission and e.g. ring currents.

The calculation of vibrational modes was performed using MoViPac in combination with Turbomole 6.6, using the same computational settings as for the structure optimization. Depending on the system either a full calculation of the Hessian matrix was performed, or just specific vibrational modes were calculated using the mode-tracking algorithm. Visualizations of selected modes can be found in the Appendix, Section E.

Subsequent IETS calculation were performed as described in Section 3.1, thus a combination of MoViPac and Artaios together with Gaussian 09. As computational settings, again the LanL2DZ basis set and B3LYP exchange-correlation functional have been chosen.

For some systems, a statistical analysis of the contribution of individual atoms to the IET was performed. This was done by summarizing the displacement of each atom for all modes, multiplied with the respective IETS intensity of the modes. This is given by

$$C_A = \sum_{\alpha}^{N_Q} |d_{A,Q_\alpha}| W_\alpha, \tag{3.10}$$

where C_A is the contribution to the IETS of atom A, $|d_{A,Q_\alpha}|$ is the length of the displacement vector of a vibrational mode α and W_α the IETS intensity of that mode.

To artificially "tune" or change the tunneling pathways through a molecule, the IETS here is evaluated at different E_F. From a transport calculation as performed in this thesis, the exact Fermi energy can not easily be obtained [177]. Established approaches are to use the Fermi energy obtained from calculation on relatively

large gold clusters or to take the middle of the HOMO/LUMO energies. Since the exact Fermi energy is not known, it is here used as "quasi-free" parameter, which means we explore the tunneling pathways and IET spectra for probable Fermi energies and compare those, but it should mentioned that this is not directly possible in experiments.

3.3.2 Results and Discussion

Fe(II)Porphyrin

The results for the Fe(II)Porphyrin junction are summarized in Figure 3.6. The local transmission analysis confirms previous results [168]: The local current are bypassing the central iron atom via the organic backbone at most energies. This can be seen in the plot of the local transmissions (Figure 3.6 a)) at $E_F = -5$ eV and also at the energy–resolved plot comparing the local transmissions through a terminal sulfur and the iron atom (Figure 3.6 d)): The normalized transmission through the sulfur atom is close to one at all energies, since the electrons are entering an leaving the system via the thiol groups. The transmission through the Fe (and also the atoms of the coordinated CO) is much lower, but rises for the resonance at $E_F \simeq -6$ eV, which is also visualized by the plot of the local currents in (Figure 3.6 b)).

The stretching mode of the CO ligands serves as a marker for the transmission through the iron atom. The local transmissions through the atoms of the CO following the transmission through the iron atom. This directly translates to the IETS intensity of that mode. Being low for most energies, the intensity rises by more than two orders of magnitude when the electrons tunnel via the central Fe atom.

Since this vibrational mode was calculated using the the mode–tracking algorithm, it demonstrates also the advantage of the chosen approach. Molecular junctions can be relatively large systems because of the inclusion of the electrodes, which makes the calculation of the full Hessian a rather time-costly approach. The calculation of the CO stretching mode using AKIRA took only 6 single-point calculations.

This examples demonstrates how the IETS can be successfully used to track the local current in a molecular junction, at least for a system where the "tracer" vibrational mode is fairly decoupled from the whole system and localized. Situations, where the
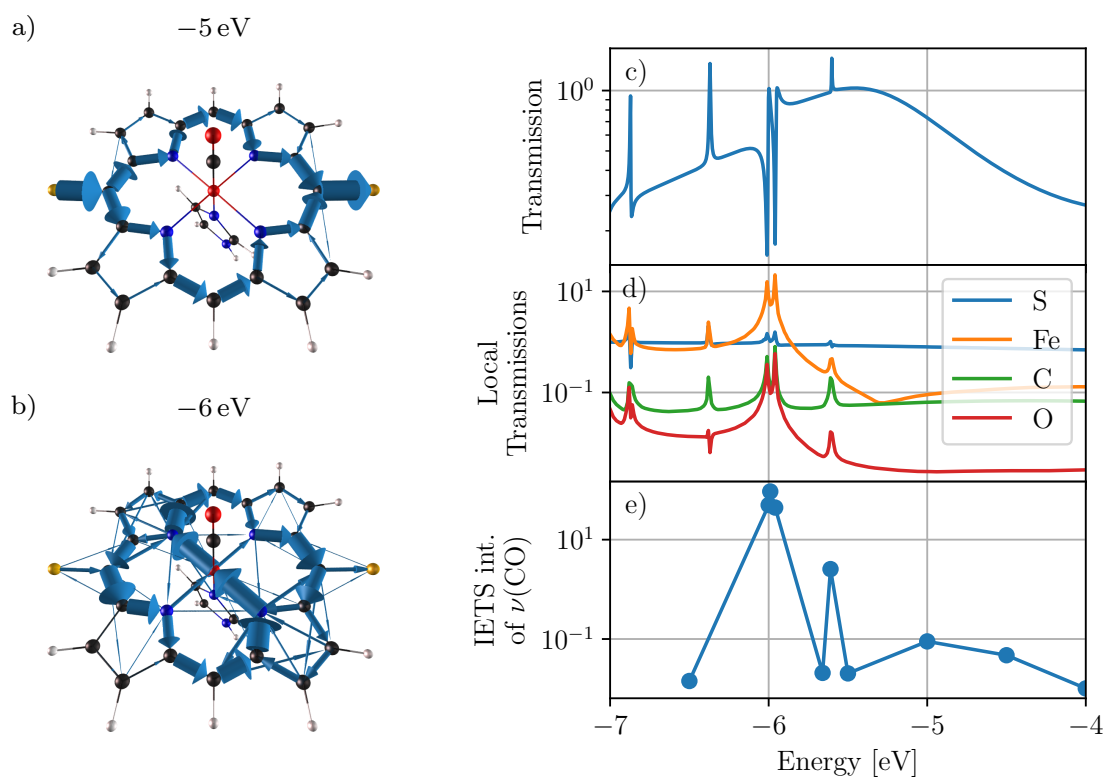
Figure 3.6: Calculated local transmissions at a) −5 and b) −6 eV through the Fe(II)Porphyrin junction. c) shows the transmission function d) the local transmission through selected atoms and c) IETS intensity of the CO stretching mode for different E_{F}. The IETS intensity of the stretching modes follows the local transmissions through the associated atoms (Fe, C, O).

molecular vibrations of a tracer group are more closely connected to the backbone of the molecule are studied in the following.

CN-substituted Biphenyl

In Ref. [262], this CN-substituted biphenyl junction was already investigated and the intensities of the CN stretching vibrations were found to by low, suggesting that the tunneling current is bypassing the the nitrile group. This can be shown analyzing the local transmission through the corresponding atoms (Figure 3.7).
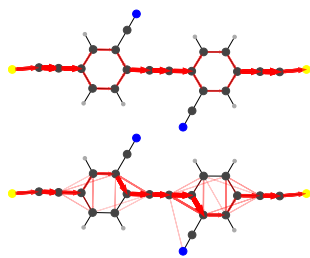
Figure 3.7: Local transmissions through the CN-substituted biphenyl junction obtained at E_F = −5 eV top)and E_F = −7.8 eV. At the upper graph, the is no preference of tunneling pathways through the benzene subunits. At the lower graph, the tunneling current prefers the side of the subunits with the CN groups.

The top panel pf Figure 3.8 shows the total transmission, while the middle panel shows the transmissions through the carbon and nitrogen atom of one nitrile group, as well as the transmission through a carbon atom of the central C≡C bond. The transmission through the central C≡C is nearly one all the time, while the transmission through the atoms of the nitrile groups more than one magnitude lower. This changes only at the resonance associated with destructive interference features. There, the contribution of the nitrile groups becomes comparable to the transmission through the central carbon bond.

The IETS intensities of the stretching vibration of the central C≡C bond (2209 cm^{-1}) is for most energies, at which the spectrum is calculated, much higher than the intensity of the symmetric and asymmetric stretching vibration of the nitrile groups (2242 cm^{-1} and 2241 cm^{-1}). This is in agreement with expectations drawn from propensity rules [262, 273] and the local transmissions. Similar to the results obtained for Fe(II)porphyrin, this changes when the the IETS is evaluated at energies close to interference features (around 7.8 eV). There, the IETS intensity of the nitrile groups becomes comparable or even higher than the intensity of the central C≡C stretching mode.

A similar behavior can be observed at around −1.7 eV. In contrast to the interference feature at 7.8 eV, the IETS intensities are decreased directly at the resonance, but again, in that energy range, the IETS intensity as well as the local transmissions through the respective atoms is increased.

For this system, the statistical analysis given in Equation (3.10) is applied as well. Figure 3.9 shows the calculated values for C_A obtained for calculations performed at different Fermi energies.

For all energies except 7.8 eV, there is a notable dip in the contributions for the atoms of the nitrile groups. But this changes at
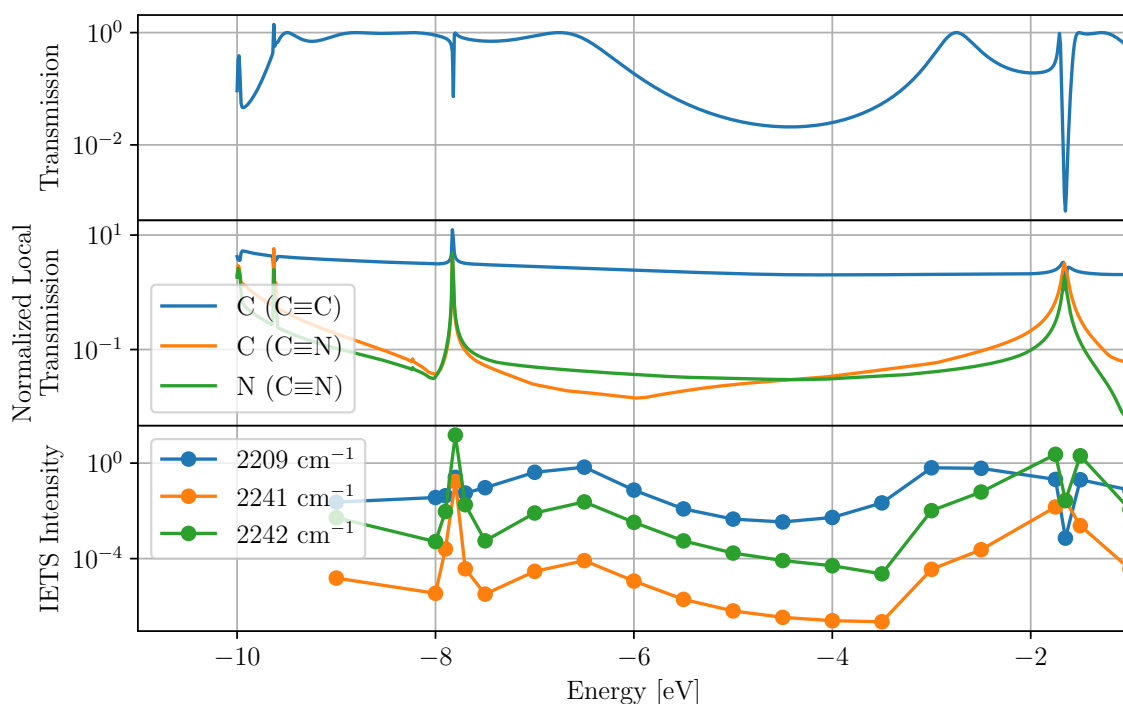
Figure 3.8: *Top:* Transmission through the CN-substituted biphenyl junction. *Middle:* Local transmission through a carbon atom of the central C≡C bond and through the atoms of a C≡N bond. *Bottom:* IETS intensities for the stretching mode of the central C≡C bond as well as the symmetric and antisymmetric stretching vibrations of the CN groups.

7.8 eV, where the calculated contribution becomes similar to the other atoms. The low contribution of, e.g., the sulfur atoms in this plot might be puzzling at first, but this can explained by the wavenumbers of modes they are involved in: The analysis here left out modes with wavenumbers below $500\,\mathrm{cm}^{-1}$, due to the interaction of low-frequency modes and the gold clusters.

The statistical analysis confirms the results obtained analyzing just selected vibrational modes in combination with the local transmissions. In this system, the nitrile groups usually are not within the tunneling path, and consequently are showing a low IETS intensity. When the Fermi energy is artificially shifted close to energies, where the transmission through functional groups is higher, the IETS intensities are increased as well.

Meta–substituted Benzene/Pyridine Junctions

In the example above, the "tracer" vibrations are still relatively localized, even though less than for the Fe(II)porphyrin system. Still, the assumption regarding the relation of tunneling pathways and IETS intensities still holds. In the following, meta-substituted
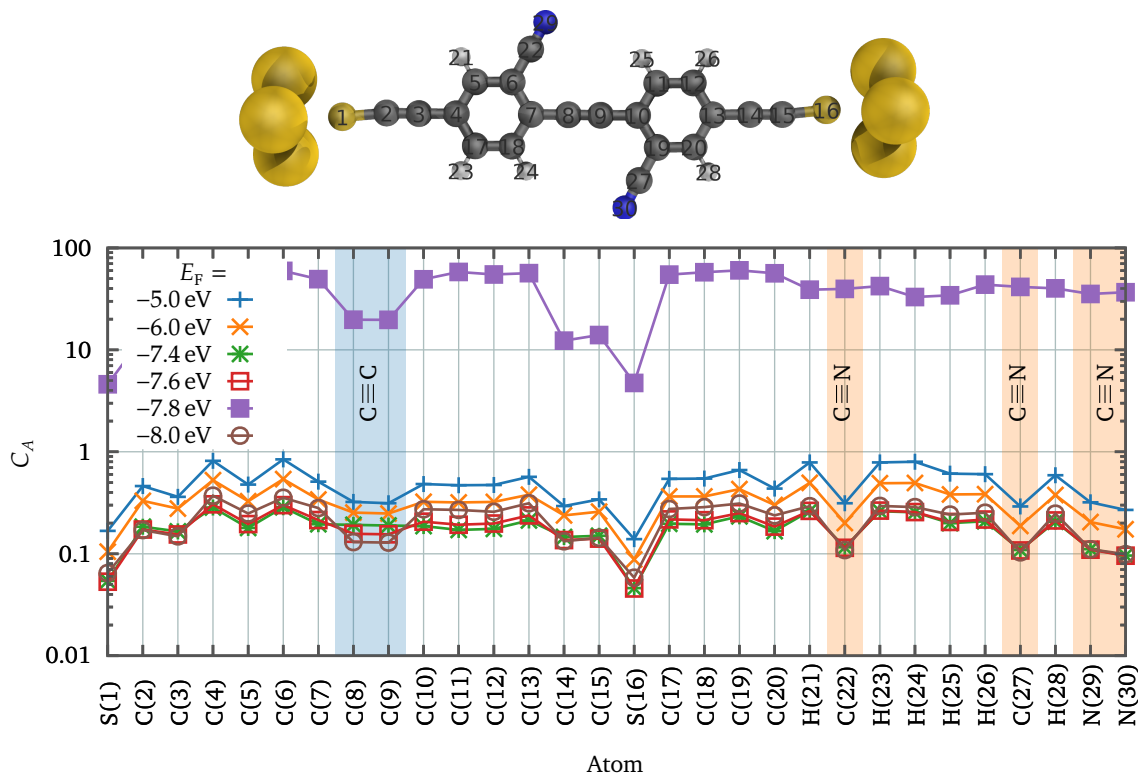
Figure 3.9: Statistical analysis of the contribution of the individual atoms to the IETS spectrum, as given by Equation (3.10). The legend gives the energies, for which the IET spectra have been calculated. At $E_F = -7.8\,\text{eV}$, the relative contributions through the atoms of the nitrile groups are significantly higher.

benzene and pyridine junctions are studied. In such junctions, the transmission is reduced due to destructive interference, but it was shown before that inelastic interactions can be larger than for examples without interference [186, 255, 256]. Figure 3.10 shows the structure, total transmission and transmissions through an atom placed in the shorter and the longer path of the ring.

In the benzene junction, the shorter path is preferred over the longer one at nearly all energies off resonance. But with the insertion of the nitrogen into the lower path (second structure), the transport can be "redirected" to the longer path for energies at around $-4\,\text{eV}$. This is reasonable close to a realistic estimates of the Fermi energy (which is not easily to be determined using the chosen computational approach [177]). Thus, this can be an example for which control over the tunneling path could be achieved. Insertion of the nitrogen atom into the longer path (third structure) mostly reestablish the tunneling preference of the shorter path, except for energies around $-6.2\,\text{eV}$. The following analysis focuses on the second system.

Due to the localized nature of the vibrational modes, it is not possible to relate specific vibrations with the shorter or longer tunnel-
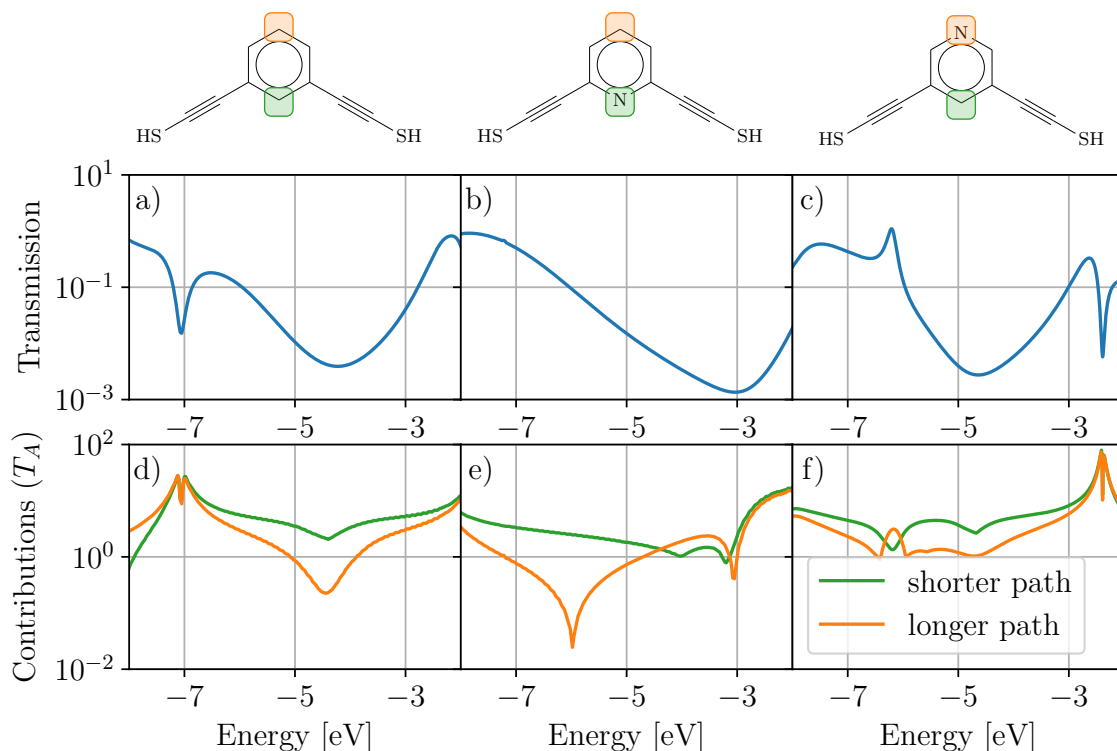
Figure 3.10: Transmission and local transmission through the meta substituted benzene and pyridine junctions.

ing path. Thus, the statistical analysis given in Equation (3.10) is applied. The resulting data is shown in Figure 3.11, alongside with a plot of the local transmission at the energies, for which the IET spectrum was evaluated.

The results are less clear than for the other systems. The is no strong change in the ratios between the contributions for the nitrogen atom in the shorter path and the contribution of the carbon atoms of the longer path. For $E_F = -3.5$ eV, a slight drop of the contributions of the nitrogen atom relatively to the contribution of the carbon atom can be observed. This would be in line with the local transmissions, but the effect is rather small and should be considered with care.

3.3.3 Summary

Summarizing, we could show that the IETS intensities of specific modes can act as a tracer for a tunneling path through molecular junctions, but only if the relevant vibrations are not too delocalized and do not couple to the rest of the molecule.

For the Fe(II)porphyrin, the CO adsorbed onto the central iron atom acted as a tracer for tunneling current through the iron
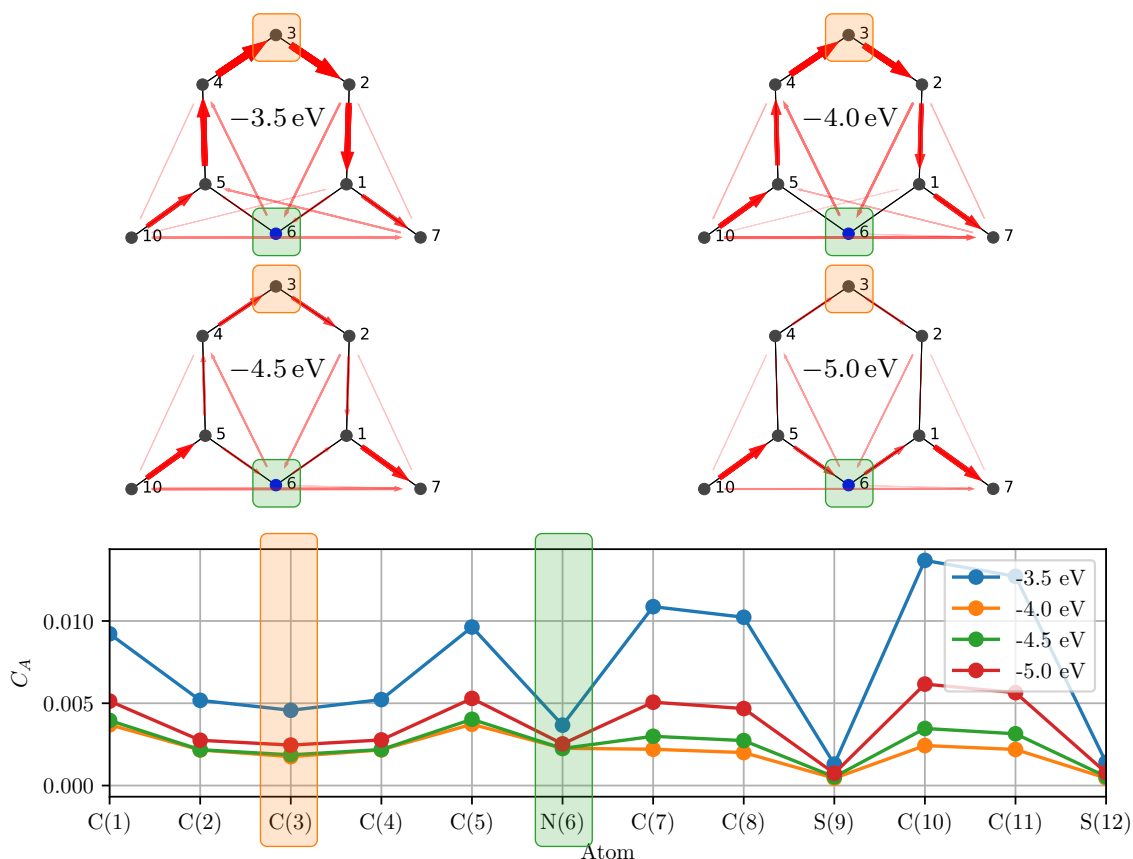
Figure 3.11: *Top:* The local transmissions for four different energies are displayed. The lower the energy, the more the lower tunneling path is preferred, as already shown in Figure 3.10. *Bottom:* The statistical analysis using Equation (3.10) shows no significant changes in the contribution of the individual atoms to the IETS.

atom, which occur at energies close to the iron's d-orbital energies. For the CN-substituted biphenyl junction, the local current through the nitrile groups as well es the intensity of their stretching modes is low compared to, e.g., the IETS intensity of the $C \equiv C$ stretching modes. Close to interference resonances, the local current through the nitrile groups as well as their IETS intensities increase, again demonstrating the relationship between tunneling pathways. For the third system, meta-substituted pyridine, the relationship can not be established. The vibrations including e.g. the nitrogen atom in the shorter tunneling path couple too strongly the rest of the molecule, as that a direct connection between the tunneling path and the IETS intensity of specific vibrational modes could be established.

The results reported here depend on the applied approximations, as the partitioning of the transmission to atomic contributions to obtained local transmissions. Situations, where the current do not follow bonds have been reported [110] and would require more flexible approaches [109, 241, 274] as used in this work.

4 Strategies for Multi-Scale Approaches

4.1 Introduction

One obvious problem when investigating small, nanosized systems in an ab-initio or atomistic way are the size limitations of the chosen approach. DFT can be used to describe a molecular junction as discussed and utilized above, but already for the description of the electrodes, compromises have to be made. To be able to capture the physics of macrosized samples without loosing insight into the "nano dimension" and the underlying quantum mechanical, several orders of magnitudes considering the system size have to be spanned.

This "multiscale modeling" is especially important for going from basic science to real-world applications [275, 276] and also for shifting from a descriptive to a predictive approach. Usually this is done by either incorporating physical regions which are treated on a more complex level of theory into a simpler surrounding (embedding) or by coarse-graining/parametrization, where a coarse-grained model gets its parameters from a more detailed description [277–281].

An example for the first scenario are QM/MM approaches, where a region described by DFT is embedded into a region which is described by a classical force fields (QM/MM) [282–285] (Figure 4.1). This can be improved also by self-learning algorithms or neural networks [286, 287]. Another example for embedding is a solvated molecule which is described by DFT, while the solvent is treated as a simple polarizable field instead of modeling each solvent molecule explicitly.

Density-functional tight-binding (DFTB) approaches are an example where results from a high-level calculation (DFT) are fed into a coarse-grained or conceptually simpler model to be able to describe larger systems [288, 289] (Figure 4.2). Calogero *et al.* used this approach to model the currents induced by a gold tip in huge graphene flakes, where the region where the gold tip and
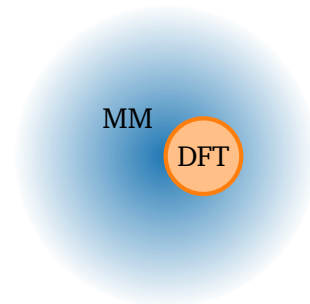
Figure 4.1: Visualization of a QM/MM model.

Figure 4.2: Information flow in a coarse-grained model. High-level calculation for a smaller system yield parameters for a calculation of a bigger system.

the graphene flakes interact are treated with DFT, while the rest of the flake was treated on a tight-binding (TB) level-of-theory [289].

In this work, the interaction of THz radiation with nanoparticle films is studied, where the particles are linked by molecules. The individual linker molecule between two particles can be studied using Artaios, but this neglects the specific interactions of the electromagnetic wave with the particle film and also the AuNP itself. It is highly complicated to tackle this problem completely on a DFT level-of-theory (or similar), but it is important also for a correct description of molecules and particles under illumination of ultrashort optical, UV or X-ray pulses [290–292].

Modeling the interactions of THz radiation with the nanoparticle film including the transport through the molecular junction and, e.g., the polarization and field enhancement effects of the AuNPs on a purely quantum mechanical basis is out of the scope of this work. Instead, we choose the approach of adapting existing models to describe the THz response of materials and add extensions or parameters based on quantum mechanical calculations of molecular junctions.

First, disregarding any interaction or molecules between the particles and disregarding the any size effects of the particles (thus assuming a gold bulk), the response of metals in the THz regime has been successfully modeled using the classical Drude model[1] [1, 293].

Decreasing the thickness of a gold film will eventually lead to thin, isolated gold islands, which starts to resemble a film of AuNPs. The Drude model is at some point not able to describe this system properly, since for DC or low-frequency conductivity is suppressed due to the non-percolated structure of the film (Figure 4.3). To accommodate for this, effective-medium theories (EMTs) could in principle be used to describe a mixture of a metal and an insulator. Interestingly, in Ref. [294] EMTs has been proven not to be very good at describing the THz response, but the Drude-Smith (DS) model performed much better. The DS model is a phenomenological extension of the Drude model to incorporate the quasi-DC/low frequency suppression (see also Chapter 6).

The DS model is criticized for being non–physical [295] but has been established within the THz community simply due to the fact that it is capable of describing a lot of results obtained for

---

[1]Different models to describe and understand the conductivity in the THz range are presented in Section 6.5
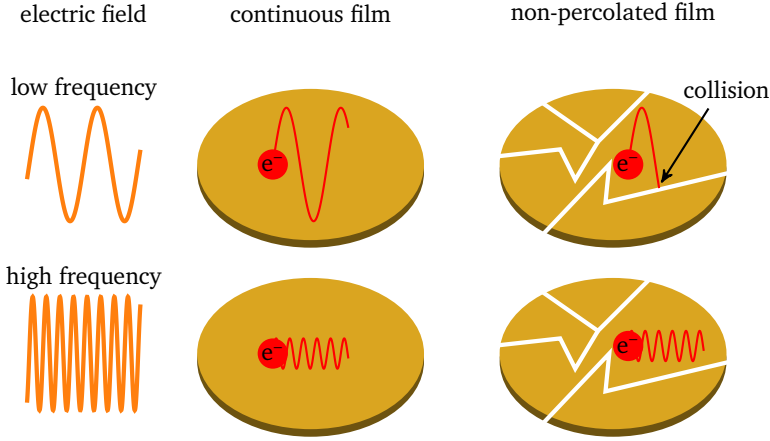
Figure 4.3: Schematic representation of conductivity reduction for low frequencies in non-percolated structures. At low frequencies, the explored space by the electron is larger than for high frequencies. If a structure is smaller than this space, the movement of the electron is hindered and the conductivity becomes lower. At higher frequencies, the explored space is smaller, thus size limitations or boundaries do play a smaller role.

nanomaterials. More insight was obtained by MC simulations performed by Němec *et al.* and Cocker *et al.* [8, 296]: Individual electrons were modeled as classical particles (as in the Drude model) but placed inside a box, which acted as a reflective barrier for the particles. Using this approach, they were able to reproduce a behavior similar to the DS model but on a proper physical basis. Calculations based on first-order pertubative quantum mechanical approach yielded very comparable spectra [297–299]

In the following, the MC approach is adopted to first reproduce the results obtained by Němec *et al.* and Cocker *et al.* [8, 296] which yields a behavior similar to the DS model. Afterwards, an energy-dependent transmission probability is introduced to include the tunneling current through the molecular junctions which connect the particles. The parameters are obtained using the LB ansatz as implemented in ARTAIOS.

4.2 Monte Carlo Conductivity Simulation with Perfectly Transmissive Boundaries

To model a system with perfectly transmissive boundaries, electrons are initialized at a random position inside a box and with a velocity $\vec{v}$ randomly chosen from a Gaussian distribution with a mean of zero and $\sigma = \sqrt{k_B T/m^*}$ (independently for the x and y components) as in [296]. As electron mass the effective mass of electrons in thin gold films is chosen ($m^* = 1m_e$) [300]. The scattering rate τ, the size of the box or particle d and the amplitude E_0 of the incident electromagnetic wave are free parameters. The quality of the simulation depends on the time step Δt (set to 0.1 fs), the number of timesteps (usually $1E6$) and the number

MC simulation

Drude formula

Figure 4.5: Frequency-resolved conductivity obtained for different τ obtained with the MC simulation. All curves are normalized. On the left size, plots of σ using the Drude formula and the same scattering times are shown. The MC simulation are in a very good agreement with the analytical solution. The simulation was performed with $T = 0\,\mathrm{K}$, 100 electrons and $1E6$ time steps.
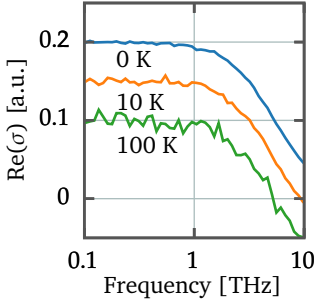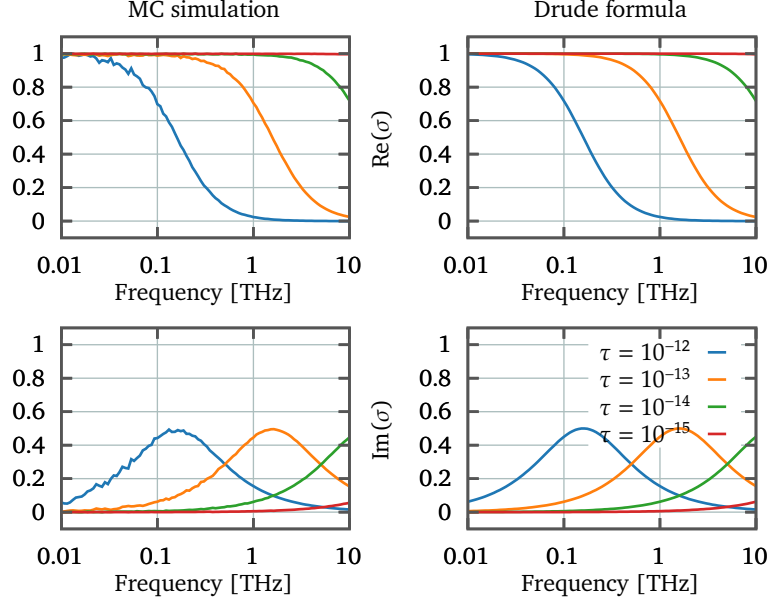
Figure 4.4: Influence of the temperature on the MC simulations. Increasing the temperature leads to more noise. The curves are shifted with respect to each other in along the y axis for visibility.

of electrons. The temperature also effects the noise and thus the quality of the simulation, as shown in the Figure 4.4.

To obtain the frequency resolved conductivity, at each time step n the particles are classically propagated by

$$\boldsymbol{x}_n = \boldsymbol{x}_{n-1} + \boldsymbol{v}_n \Delta t \tag{4.1}$$

$$\text{with} \quad \boldsymbol{v}_n = \boldsymbol{v}_{n-1} + \frac{e\Delta t}{m^*} \boldsymbol{E}_0 \cos\left(2\pi \nu n \Delta t\right). \tag{4.2}$$

This is performed for different frequencies ν of the electromagnetic wave depending on the frequency range of interest. The field has only a nonzero x-component, so any velocity in y-direction is due to scattering. When a particle is scattered with the probability $1/\tau$, its velocity is re-initialized according to the temperature. When a particle reaches the boundary of the box, it is shifted to the other side of the box while preserving its velocity. This effectively creates periodic boundaries and emulates a bulk material.

The conductivity is obtained by using the ratio of the Fourier transformations of the electrons speed and the electric field [296]

$$\sigma(\omega) = \frac{j(\omega)}{E(\omega)} = \frac{\mathscr{F} j(t)}{\mathscr{F} E(t)} \tag{4.3}$$

$$= \frac{\sum_n v_n e^{i\omega 2\pi n \Delta t} \Delta t}{\sum_n E_n e^{i\omega 2\pi n \Delta t} \Delta t}. \tag{4.4}$$

In Figure 4.5, the effect of different scattering times τ is demonstrated. The graph shows the results from the MC simulation as

well as the conductivities calculated with the Drude model. The simualted frequency-resolved conductivities resemble directly the curves obtained with the Drude model. This demonstrates that the MC simulation is able to capture the correct physics and response to the electromagnetic wave.

4.3 Monte Carlo Conductivity Simulation with Perfectly Reflective Boundaries

Similar to the work in [296], now a box with reflective boundaries is simulated. If an electron reaches the boundaries of the box, it is reflected by changing the sign of the corresponding entry of the velocity vector. The rest of the simulation is performed as before.

When the box size is reduced, at some point the confinement starts to play a role and a suppression of the quasi-DC current can be observed. This is happening when the distance the electrons travel becomes comparable to the dimensions of the box. Thus, this effect should depend on the boxsize and the amplitude of the incident electromagnetic radiation.

Figure 4.6 shows the obtained complex conductivity for different box sizes. Depending on the ratio of the box size (and the amplitude of the electromagnetic wave), a suppression of the DC current can be observed. Similar to the DS model, a negative Dip in the imaginary part of the conductivity can be observed if the DC suppression is more than 75 %.
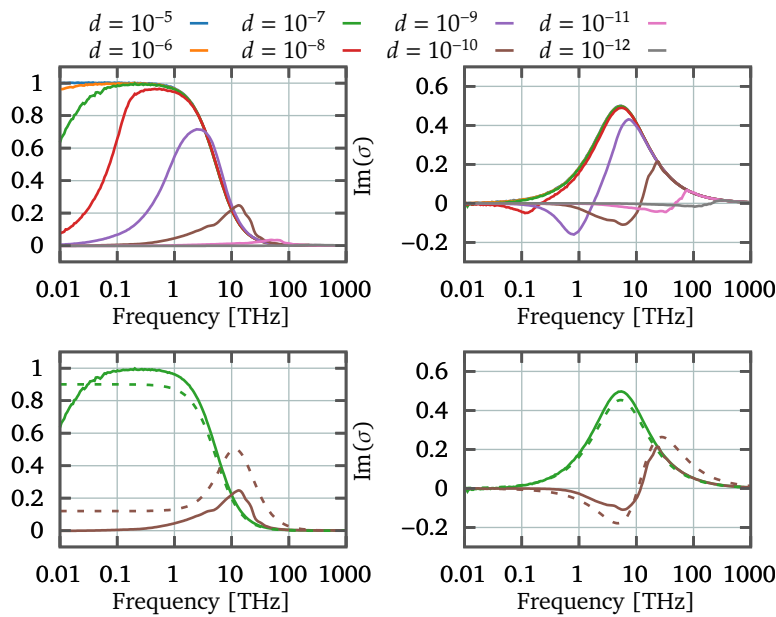
Figure 4.6: MC simulation for different box sizes d from 1×10^{-5} m to 1×10^{-12} m and $\tau = 30 \times 10^{-15}$ s. All curves are normalized to the original (unaffected by the box size) DC conductivity. Fits using the DS model (dashed lines in lower panel) to the imaginary part give a reasonable agreement, but the behavior of the real part can not be captured. Fits of the real part tend to fail at the description of the lower frequencies.

Fitting the curves using the DS model unveil its problems reproducing the low-frequency behavior fully (see Figure 4.6, lower panels). This was also described by Cocker *et al.* [296], who have proposed a modified DS model, which shape resembles the curve obtained by the MC simulations. The results also depend on whether the DS model is fitted against the real, the imaginary or both parts. Fitting the DS model to the imaginary parts obtained from the MC simulation can give reasonable fits for the imaginary part when the quasi–DC current is completely suppressed. In the intermediate regime, no satisfying fits can be obtained.

The suppression of the (real) conductivity for low frequencies is affected by the temperature and the scattering time τ. Shorter scattering times reduce the mean free path and thus the space, which is explored by the electron. This leads to a later onset for the quasi-DC conductivity suppression when decreasing the box-size, as shown in Figure 4.7.

Figure 4.7: Influence of box size and scattering time τ on the conductivity. A shorter scattering time implies a shorter mean free path between two scattering events. Thus, an electron travels less far if scattering time is shorter, therefor the confinement of the movements of the electrons happens at smaller box sizes.
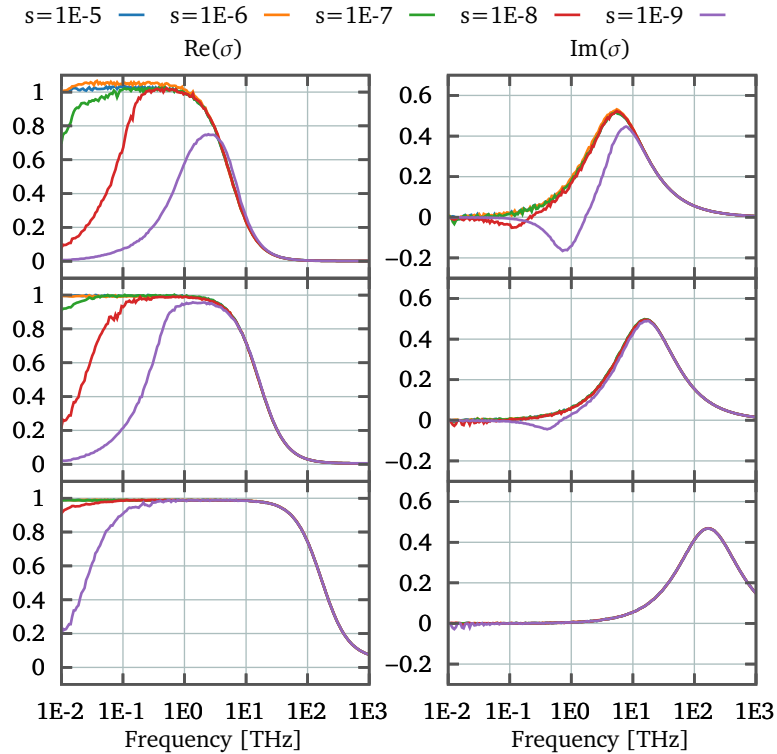
4.4 Modeling Partially Transmissive Boundaries

To introduce partially transmissive boundaries, the simulation is extended by introducing a transmission probability t of the barriers. For $t = 1$, the periodic system in Section 4.2 is obtained, for $t = 0$ the situation in the previous section. Even though the

simulation is performed for classical particles, this adopts the effect of non-classical transport effects like tunneling or hopping between the particles. One way to parameterize t would, e.g., a Simmons model for the tunneling through a vacuum gap [301] with a certain width, corresponding to the distance between the particles.

Simulations performed for electron in a partially transmissive box show, that the introduction of a nonzero transmission probability quickly restores the quasi-DC conductivity. This effectively creates a "plateau" at the region where the conductivity suppression would take place if $t = 0$ (Figure 4.8). For bigger particles (here $d = 10\,\mu m$), the effect is not noticeable, but for smaller particles ($d = 1, 0.1\,nm$)), where the localization effect can be seen, the DC conductivity scales with the transmission probability.
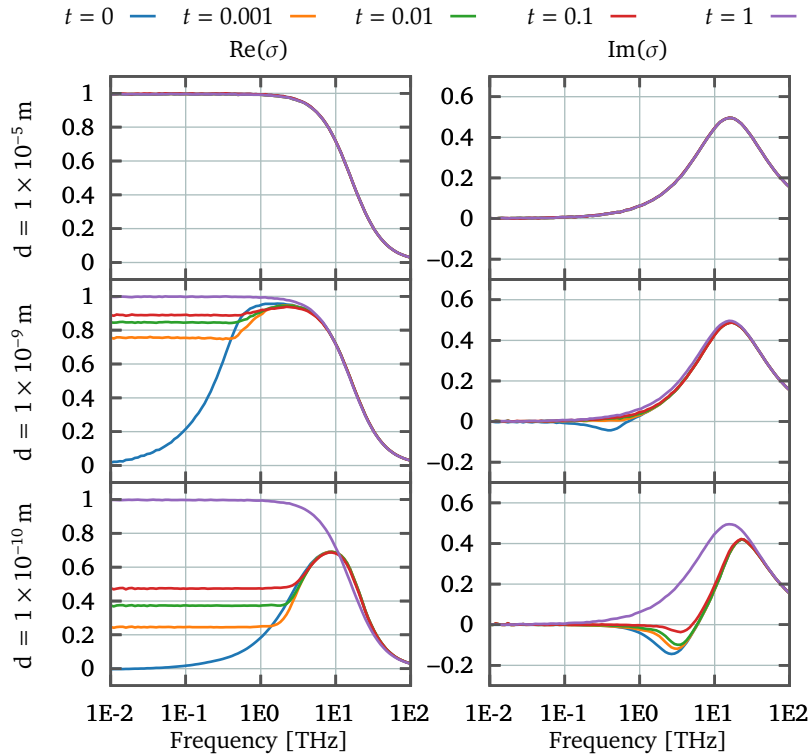
Figure 4.8: Restoration of the quasi-DC current through partially reflective boundaries. For an extended box without any size restrictions, the shape of the conductivity resembles the Drude model. When the box is shrank to sizes affecting the quasi-DC mobility, increasing the transmission probability increases the quasi-DC current. Higher frequencies are not affected by this, since the mean distance traveled by the electrons becomes shorter than the box size.

To emulate an energy dependence of the transmission probability of the barriers, we employ the Breit-Wigner formula (Equation (2.10)) to calculate the transmission $T(E)$.

By choosing appropriate numbers for ϵ_i and Γ_i, the effect of a low or good conducting junction can be emulated. This can, e.g., be done by fitting the Breit-Wigner model to a transmission function obtained with the NEGF+DFT approach, as shown in Section 2.3.

If an electron hits the boundary, the transmission probability is

evaluated according to its speed (and thus kinetic energy) and the formula given above. In Figure 4.9, the effect of an increasing energy separation between two energy levels is explored. The effect is very much similar to the simulations with the simple partially–reflecting border, which are represented by the dashed lines in the Figure. The value for the transmission probability was obtained by taking the zero-bias conductance of the above model.

Figure 4.9: Conductivity obtained from a MC simulation with energy-dependent partially-reflective boundaries. The different energies for ϵ_i are given in the legend. τ was set to 10 fs, the boxsize is 10 nm, the amplitude of the electromagnetic wave is 1E6 and a Γ of 0.01 was chosen.
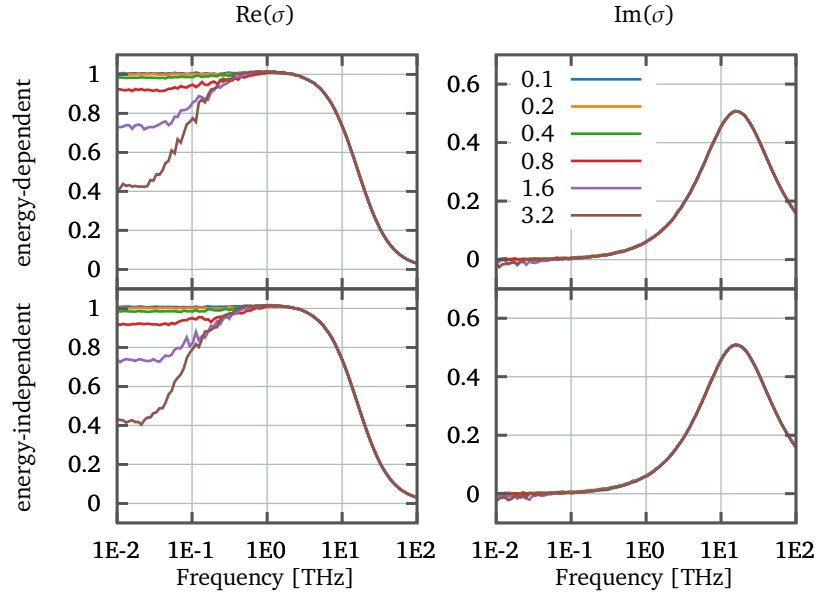
The conductivity curves obtained from simulations seem to be identical with or without energy-dependent transmission. The reason behind this is, that the electron does not reach energies high enough, so that the transmission probability changes significantly from $T(E_\mathrm{F})$. This is also due the limitations of this approach. The Drude model assumes that all electrons participate in charge transport, with a relatively low resulting drift velocity. In reality, transport is provided by only a few electrons close the Fermi edge, but with a high velocity: The Fermi velocity for gold is around $1.4 \times 10^6 \, \mathrm{m \, s^{-1}}$ [147].

Still, this enables to simulate the THz conductivity of particles which are connected by realistic molecular linkers. As they are used later in the experimental part of this thesis, nonane-1,9-dithiol (NON), biphenyl-4,4′-dithiol (BI) and *p*-terphenyl-4,4″-dithiol (TER) are chosen as examples. The transmission function is calculated using the NEGF+DFT approach as implemented in Artaios. The structure optimization of the isolated molecules (NON, BI and TER) was performed using Turbomole 6.6, Ahlrichs split-valence triple-ζ basis set with polarization functions on all atoms (def2-TZVP) basis set and the BP86 functional . We used the resolution-of-identity (RI) approxima-

tion as implemented in Turbomole 6.6 [155, 156, 257, 258, 269–272]. The convergence criterion of the self-consistent field (SCF) algorithm was a change of energy below 10^{-8} Hartree. The convergence criterion for the structure optimizations was a gradient below 10^{-4} a.u. Transport calculations were performed using Gaussian 09, the LanL2DZ basis set with the B3LYP functional [157, 175, 176]. To mimic the gold electrodes, Au_9 clusters were attached to the molecule with a Au-S distance of 2.85 Å while removing the terminal hydrogen atoms. As determined above, the full energy-dependence of the transmission function is not needed, so the transmission probability at the Fermi energy can directly be used. As described above, the exact Fermi energy is not known for our systems. Here, the energetic middle between the frontier orbitals is chosen.

The obtained transmission functions, current-voltage curves and THz conductivities are shown in Figure 4.10. The transmission probabilities of the different molecules leads to different quasi-DC conductivities. The rest of the conductivity is dominated by the scattering. If the scattering is decreased, the mean free path is decreased and the boundary effects become less visible, thus also the effect of transmissive boundaries.

4.5 Summary

This chapter explores the THz conductivity of extended and small systems using numerical MC simulations. The chosen approach is based on work by Cocker *et al.* [296], who tried to understand the lineshapes of the rather unphysical DS model using this classical, numerical approach. This is performed by simulating the propagation of electrons interacting with a classic electric time-dependent field, while having - among others - the scattering rate, the size of the simulation box and the transmission of the box barriers as free parameters. If the boundaries of the box are perfectly transmissive, a periodic system is created which behaves perfectly like the classical Drude model. Suppression of the low-frequency conductivity can be observed when the boundaries become more reflective and the size of the box is in the order of the mean free path of the electrons. The addition of energy-dependent transmission probabilities for the boundaries based on the LB approach can be approximated by feeding $T(E_\mathrm{F})$ into the simulation as a energy-independent transmission probability.
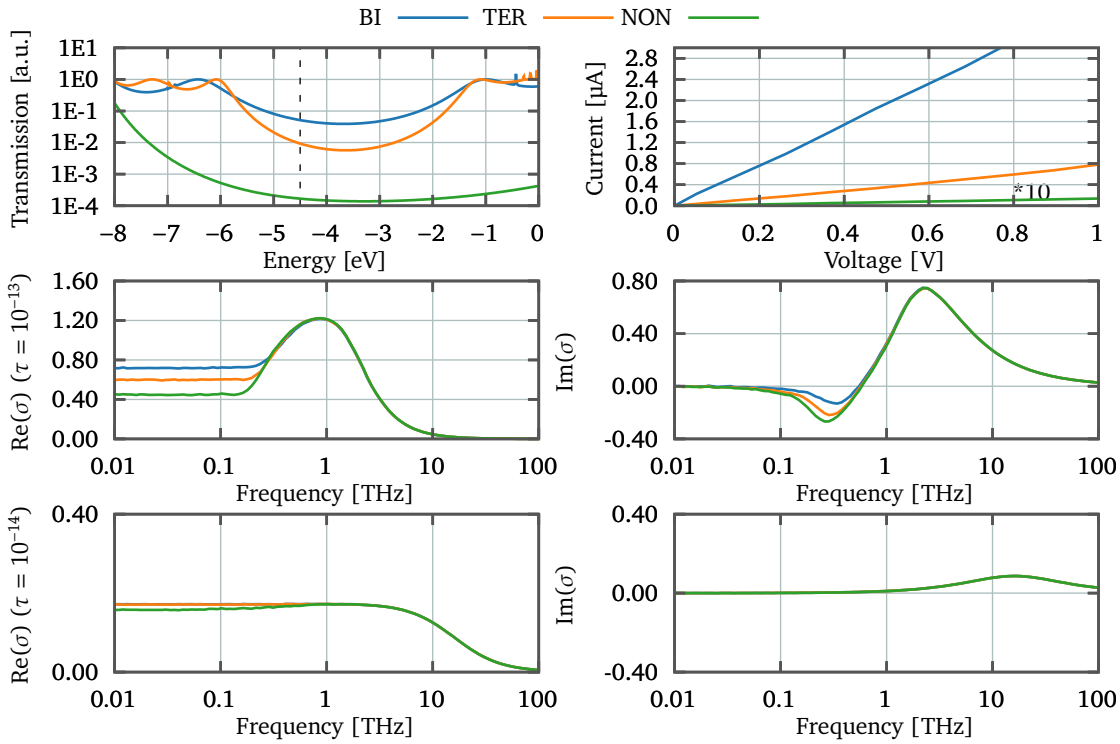
Figure 4.10: Transmission functions, current-voltage curves and THz conductivities for 10 nm sized particles with transmission probabilities obtained from the transmission functions. At the top, the transmission function and the current calculated with ARTAIOS is shown. The dashed line in the first panel visualizes the Fermi energy, at which the current is evaluated. The different transmission probabilities yield different low-frequency conductivities using the MC simulation, but this depends on the scattering time.

Part II

Terahertz Spectroscopy

5 The Design and Principles of a Terahertz Spectrometer

5.1 An Introduction to Terahertz Spectroscopy

Terahertz time-domain spectroscopy (THz-TDS) has been established in the last years as a powerful tool to study the (photo)conductivity, intraband transitions or vibrations for various systems, with the possibility to access picosecond timescales. THz spectroscopy[15] refers to methods which use THz radiation from 0.1 THz up to several tenths of THz, usually generated from by fs laser pulses.

These frequencies have long been difficult to access (also known as "terahertz gap" [302]) since electronic measures cannot be used easily to generate such high frequencies and optical fail as well, since the energy of THz radiation is below room temperature ($\sim$6.045 THz). With the commercial spread of fs laser systems, e.g. non-linear optical effects can be used to generate and detect THz radiation, thus enabling access to the THz range for spectroscopic techniques. One remarkable feature of THz spectroscopy is the ability to measure the oscillating electric field instead of the intensity of the THz field when using schemes like electro-optical sampling [303–305]. This allows for the extraction of material quantities such as the refractive index $\tilde{n}$,

$$\tilde{n} = n_1 + n_2 \mathrm{i} \tag{5.1}$$

$$\leftrightarrow \tilde{\epsilon}_r = \epsilon_{r,1} + \epsilon_{r,2}\mathrm{i} \tag{5.2}$$

$$\leftrightarrow \tilde{\sigma} = \sigma_1 + \sigma_2 \mathrm{i}, \tag{5.3}$$

or in a similar way the complex conductivity $\tilde{\sigma}$ or relative permittivity $\tilde{\epsilon}_r$ without the use of the Kramers–Kronig relation. The THz frequency range is of high interest, as it provides access to the dielectric response of materials as well as the conductivity, thus bridging the fields of electrical engineering and optics. This can also be understood by looking at the relative permittivity or dielectric function ϵ_r of a material [304]

$$\tilde{\epsilon}_r(\omega) = \tilde{\epsilon}_b + \mathrm{i}\frac{\tilde{\sigma}(\omega)}{\omega\epsilon_0}, \tag{5.4}$$

[15] The term "THz spectroscopy" is used here to describe terahertz time-domain spectroscopy (THz-TDS) as well as optical-pump-terahertz-probe spectroscopy (OPTP spectroscopy).
OPTP spectroscopy is sometimes also called TRTS - time-resolved THz spectroscopy.

with $\tilde{\epsilon}_b$ as the response of bound carriers or also lattice vibrations and $\tilde{\sigma}/\omega\epsilon_0$ as the response of free carriers (e.g. electrical conductivity). Which part dominates $\tilde{\epsilon}_r$ depends on the angular frequency ω of the incident electromagnetic radiation. Conventional conductivity experiments probe the response of free charges, since $\tilde{\epsilon}_r \ll \tilde{\sigma}/\omega\epsilon_0$ ($\omega \rightarrow 0$). For optical or infrared experiments, the response of materials is dominated by $\tilde{\epsilon}_b$. The THz regime resembles a transition area from a purely electric to a purely dielectric response [304].

Thus, by analyzing a materials response to THz radiation it is possible to extract the bound carrier response $\tilde{\epsilon}_b$. From this we can then deduct the vibrational footprint of the material which gives access to lower-energetic vibrations as usually accessible via infrared spectrosopy. This can be used to study biological systems like amino acids and peptides [305–313] to e.g. obtain structural information or to detect drugs or explosives [314–316]. It can also be used or resolve the chemical composition of materials [317–320], which is for instance of interest for pharmaceutical applications.

To obtain properties of the (quasi) free charges $\tilde{\sigma}/\omega\epsilon_0$ (second term in Equation (5.4)), THz can be employed to study metallic systems or doped semiconductors [294, 321–324]. In combination with a pump-probe excitation scheme it is possible to investigate the behavior of photoexcited charges [97–99, 325–329]. As described in the introduction, THz spectroscopy can be combined with scanning–probe setups to unite the high spatial resolution of a tip with the temporal resolution of a THz pulse to study e.g. tunneling currents [100, 101, 330].

In recent years more elaborate THz experiments have been performed to study - among others - the interfacial electron transport [331] or ultrafast magnetization/spin dynamics [332–334]. Additionally, chip–based electron–accelerators using THz radiation have been demonstrated [335, 336].

In this chapter, the general layout of a THz spectrometer as well as the layout of the setup used in this thesis is presented. THz generation and detection using ZnTe crystals will be discussed. The chapter afterwards discusses the interaction of the THz beam with layered samples theoretically, together with the most common models to interpret the results. The data extraction routine and its implementation in the `python` library DuoDecim will be presented with a discussion of details like the phase unwrapping problem.

The design principles of THz spectrometer have been extensively discussed in reviews or books [305, 337–340]. Details regarding THz spectroscopy of semiconducting materials have e.g. been reviewed in Refs. [97, 341]. High-power THz sources have been recently discussed by Fülöp *et al.* [342]. Data extraction and interpretation routines (which will be discussed in the next chapter) have been reviewed by James Lloyd-Hughes & Tae-In Jeon for bulk and nanomaterials [295]. The number of books on the topic has substantially increased in the last years [302–304, 343–347].

5.2 Design of a Terahertz Spectrometer

A THz spectrometer, as shown in Figure 5.1, can be divided into three parts: Generation of the THz radiation, interaction area of THz radiation with the sample and the detection and reconstruction of the beam with the detection scheme. Before discussing the generation and detection in detail, some general aspects will be covered.

Spectrometers working in the THz frequency range are usually designed as time–domain spectrometers [302, 304, 305, 326, 344]. Detectors in the visible range use a detection pattern in the frequency–domain by using a grating, which maps the different wavelengths on a CCD. THz spectroscopy measures the signal in the time–domain, which can be easily converted to the frequency–domain by a Fourier transformation [304].

THz radiation can be generated by various techniques, for example by a short-lived current over a photoexcited semiconductor junction (also called optical switch), cherenkov-like radiation in LiNbO$_3$ crystals, optical rectification in ZnTe, frequency mixing in GaSe or air-plasma [304, 337, 338, 342, 347, 348]. All these methods differ in their complexity, generated power or resulting frequency range (Figure 5.2). Here, optical rectification in ZnTe will be used and discussed in detail below.

To guide and focus THz radiation it is difficult to use lenses, since not that many materials exist which combine low losses, moderately high refractive index and low dispersion in the THz range. Commercial THz lenses are usually made of silicon, polytetrafluoroethylene (PTFE) or TPX (polymethylpentene). Silicon lenses are used to collect THz radiation directly after a emitter, but are not suited to collimate or focus an expanded beam. PTFE and TPX are used in commercial systems to focus and collimate THz
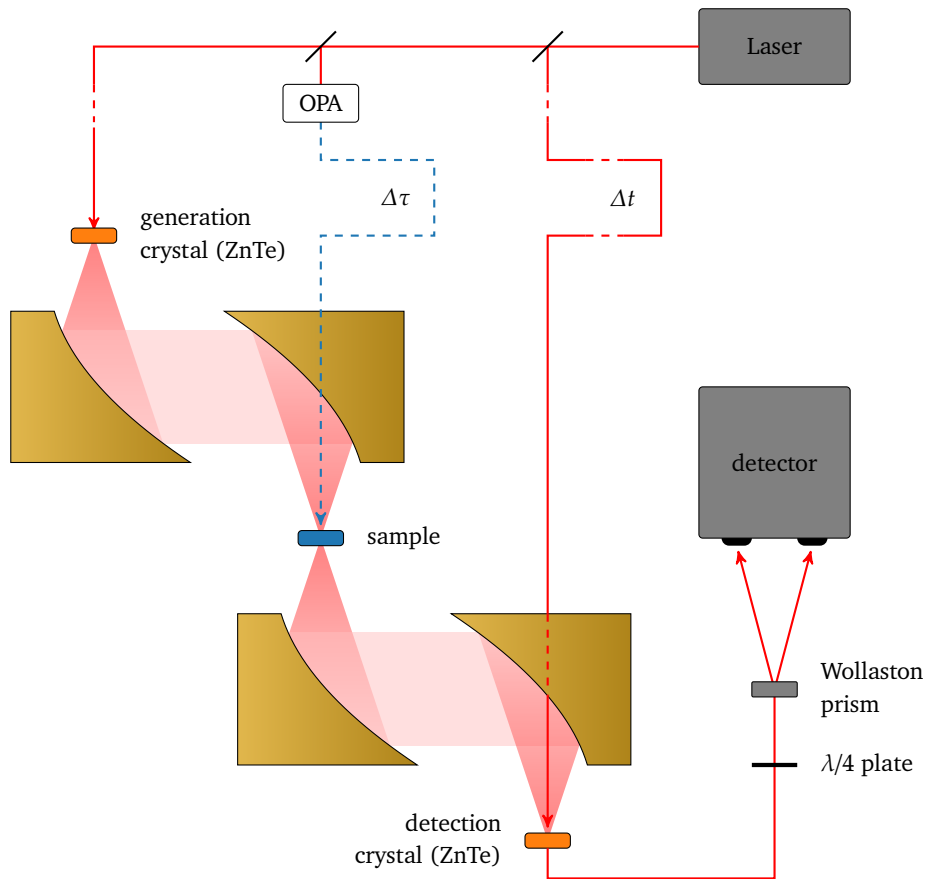
Figure 5.1: General layout of a THz spectrometer. A beam provided by a Ti:Sa laser (800 nm) is focused on a ZnTe crystals, which generates THz radiation by optical rectification. The crystal is placed in the focal point of the first parabolic mirror, which collimates the THz beam. The second mirror focuses the beam on the sample. The sample can be excited by a pump beam of arbitrary wavelength (displayed as the dashed blue line, wavelength provided by the optical parametric amplifier (OPA)) for performing OPTP spectroscopy experiments. The temporal overlap between the THz and the pump beam $\Delta\tau$ is controlled by a mechnical delay stage. The third mirror collimates the beam again, the fourth focuses it into a second ZnTe crystal, where it is overlapped with the detection beam (800 nm). The temporal overlap between the THz and detection beam Δt is controlled by a second delay stage. The electric field of the THz pulse changes the polarization of the detection beam. After the detection beam has passed the crystal, its polarization is measured with a combination of a $\lambda/4$ plate and a Wollaston prism which splits the optical beam into two beams with perpendicular polarization. The intensity of the two polarizations is measured with a balanced photodetector. Not included in this picture is the lock-in detection with the chopper in the generation and pump beams.
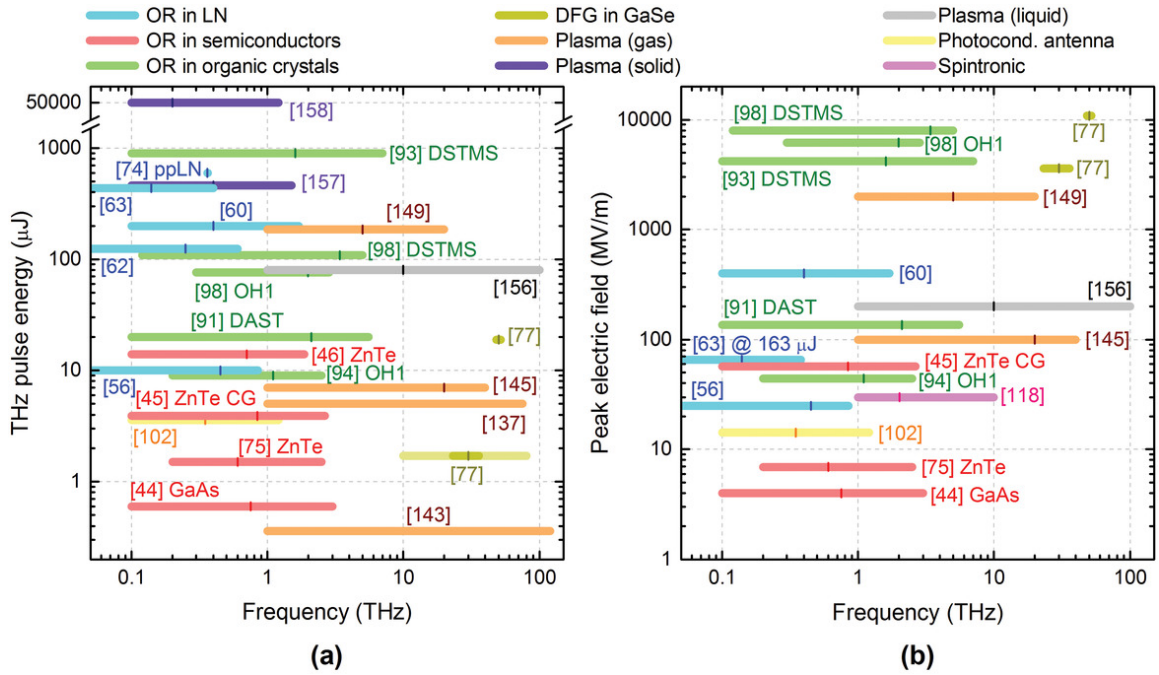
Figure 5.2: Overview of power and frequency range reported for different THz generation schemes. Figure taken from Fülöp, J. A. *et al.* Laser-Driven Strong-Field Terahertz Sources. *Advanced Optical Materials,* 1900681 (Dec. 2019), CC-BY. Please refer to the orginal paper for the references given in the figure. OR refers to optical rectification, DFG to difference–frequency generation.

beams. They have similar refractive indices in the THz range (1.4-1.5) combined with a low dispersion and absorption. The relatively low refractive index makes short focal lengths challenging to obtain.

As an alternative, parabolic off-axis mirrors (Figure 5.3) have been established [344], since their ability to focus and collimate is free of dispersion. Even though the alignment is more challenging than alignment of transmission lenses, they offer an easy way to overlap the THz beam with an optical laser beam in a collinear fashion. This is done by drilling a small hole into the center of the mirror.

Since the duration of THz pulses is in the order of picoseconds, one has to find a detector which can resolve these small time scales. These fast dynamics are challenging to detect with purely electric detectors. Usually, this is overcome by either using the Pockels effects, where the THz field changes the polarization of an optical pulse or by using antennas, where the THz pulse creates a current over a photoexcited semiconductor junction [304]. In both cases, the necessary time resolution is provided by the optical detection beam, which acts as an optical gating. The gating pulse duration is in the order of some tenths of femtoseconds, thus allowing for time-resolved measurements.
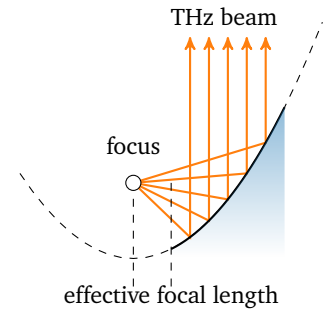
Figure 5.3: Beam path in a off-axis parabolic mirror.

5.3 Terahertz Generation using Optical Rectification

In this work, THz radiation produced by optical rectification in a <110>-cut ZnTe crystal was used. The advantages of using this generation scheme are the alignment tolerances and the broad frequency range of the generated THz pulse. The spectrum is usually dominated by lower frequencies [303]. Optical rectification is a second–order nonlinear effect, that generates quasi-static polarization P by an electromagnetic wave $E = E_0 e^{i\omega t}$ in a crystal [303]. The induced polarization is given by

$$P(t) = \epsilon_0 \left[\chi^{(1)} E(t) + \chi^{(2)} E^2(t) + \chi^{(3)} E^3(t) + ... \right] \qquad (5.5)$$

with $\chi^{(n)}$ as the n-th order susceptibility and $E(t) = E_0(t)e^{-i\omega t}$ as the electric field of the laser pulse. $E_0(t)$ represents the time-varying envelope of the pulse. Since fs laser pulse contains more than one frequency ω, for the electric field, which enters Equation (5.5),

$$E(t) = E_{0,1}(t)e^{-i\omega_1 t} + E_{0,2}(t)e^{-i\omega_2 t} + c.c. \qquad (5.6)$$

can be written. *c.c.* denotes the complex conjugate. For the second–order term $P^{(2)}(t) = \epsilon_0 \chi^{(2)} E^2(t)$, now

$$P^{(2)}(t) = \epsilon_0 \chi^{(2)} [E_{0,1}^2 e^{-i2\omega_1 t} + E_{0,2}^2 e^{-i2\omega_2 t} \qquad (5.7)$$

$$+ 2E_{0,1} E_{0,2} e^{-it(\omega_1 + \omega_2)} \qquad (5.8)$$

$$+ 2E_{0,1} E_{0,2} e^{-it(\omega_1 - \omega_2)} \qquad (5.9)$$

$$+ 2E_{0,1} E_{0,1}^* + 2E_{0,2} E_{0,2}^* + c.c.] \qquad (5.10)$$

is obtained [122]. The first line represents the second–harmonic generation process, the second line the sum–frequency generation and the third line the difference–frequency generation (DFG). Optical rectification corresponds to the special case when $\omega_1 = \omega_2$, thus the DFG term becomes static. But for a laser pulse with a time-varying intensity $E_0(t) = E_0 e^{-2at^2}$, a time-varying polarization

$$|P| \propto |E_0|^2, \qquad (5.11)$$

$$\propto E_0^2 e^{-2at^2} \qquad (5.12)$$

is obtained. This is shown in Figure 5.4. The change of the polarization therefor follows the envelope of the fs laser pulse. This change is effectively a current, which generates electro–magnetic radiation in the THz regime [303].

Figure 5.4: THz generation using optical rectification in ZnTe obtained with an arbitrary puls. The optical pulse induces a polarization in the crystal. The change of the polarization generates the THz pulse, its spectrum can be seen in the right panel. The data plotted here was obtained using an optical pulse of arbitrary frequency and a pulsewidth of 50 fs.

The longer the optical pulse travels in phase with the THz pulse inside the crystal, the higher the intensity of the resulting beam, since more and more THz radiation is generated. The different frequencies of the THz pulse as well as the optical pulse will, however, experience dispersion and propagate at different velocities. This will lead to destructive interference of the generated THz radiation, limiting the thickness of the generation crystal. Using 800 nm laser pulses as provided by Ti:Sa oscillators, this condition can be satisfied using ZnTe crystals, for which THz generation lengths of above a millimeter can be used [303, 349]. The choice of the crystal thickness is always a trade-off between bandwidth and intensity. A thicker crystal leads to a more intense THz pulse, but decreases the intensity of higher frequencies due to destructive interference. Optimization of the phase matching conditions can easily be obtained by rotating the crystal.

5.4 Detection of Terahertz Radiation using Electro-Optical Sampling

The most common technique to detect a THz pulse is to use a second read-out pulse $E_{\text{optical}}(t)$ to scan the THz by changing the temporal delay Δt between the two beams. The measured signal is a convolution of the electric field of the (unknown) THz pulse and the read-out pulse [305],

$$S(t) \propto E_{\text{optical}}(t) \circledast E_{\text{THz}}(t). \tag{5.13}$$

Since the duration of the optical pulse (usually < 100 fs) is much shorter than the THz pulse $\simeq 1 - 5$ ps, the optical pulse can be approximated by a delta function. The convolution in Equation (5.13) can be simplified and the measured signal $S(t)$ is directly proportional to $E_{\text{THz}}(t)$.

Figure 5.5: Electro-optical sampling of a THz pulse (black) using a fs optical pulse (orange). The timing between the two beams is changed and the polarization of the optical beam after the detection crystal is measured.
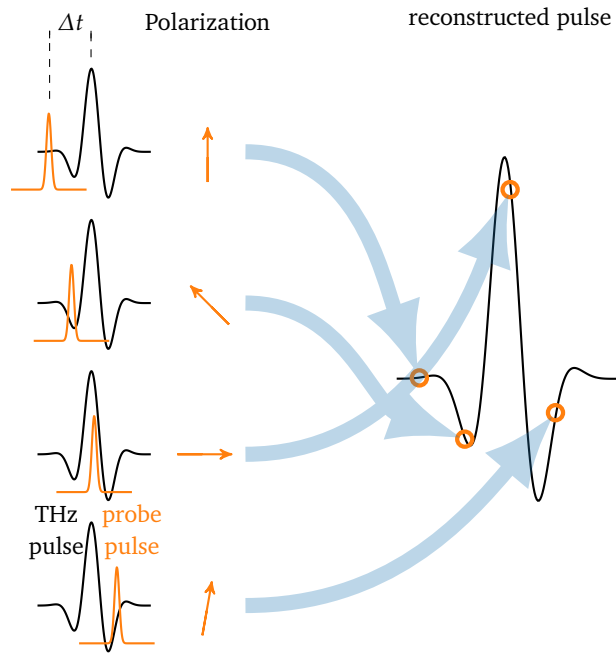
As already depicted in Figure 5.1, scanning of the THz pulse is done using an optical delay line or delay stage. This maps the problem of the temporal resolution to the spatial precision of the delay stage. A 10 fs step Δt translates to $\simeq 1.5\,\mu\text{m}$ delay stage displacement. The whole scanned time window is given by $T = N\Delta t$ (with N as the number of steps), which results in a frequency resolution of $\Delta \nu = 1/T$ and a maximal frequency $\nu_{\text{max}} = 1/\Delta t$.

When the THz passes through a ZnTe (or other non-centrosymmetric crystals such as GaP), it changes or modifies the birefringence of the crystal [304]. Thus, the polarization of an optical beam is altered when being overlapped in space and time with the THz pulse. This change of polarization of the optical read-out pulse can be measured. This is usually done by inserting a quarter-wave plate in the detection beam after the detection crystal. This changes the linear polarization to circular. A Wollaston prism can be used to split the beam according the the polarization into two linearly polarized beams with perpendicular polarization [303–305]. The intensity of these two beams can be measured using a pair of balanced photodiodes. This is usually done with a lock-in amplifier, where the lock-in frequency is set by a chopper, which chops the THz generation. Thus, the measured signal is the difference of the polarization of the optical pulse with and without induced change of polarization due to the THz beam. In that the way, the electric field inside the crystal can be reconstructed.

This idea is illustrated in Figure 5.5. As already mentioned, us-

ing electro-optical sampling the field, not the intensity of the THz pulse can be reconstructed, since the the induced birefringence is proportional to the field, not the intensity. Similar to the generation using non-linear effects, the detection performance is affected by the dispersion the different pulses experience while passing through the crystal. Shorter crystals improve the detected frequency range, but decrease the measured signal [349].
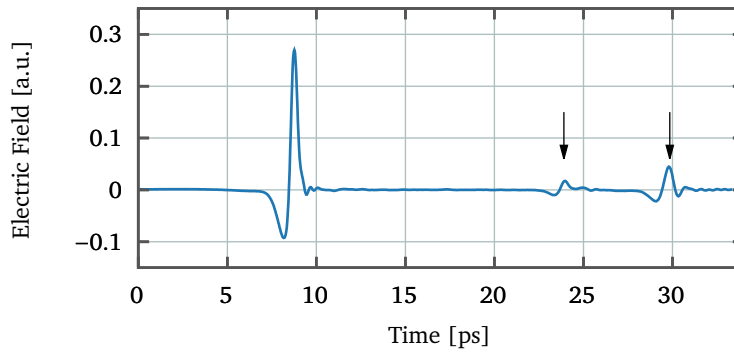
Figure 5.6: Exemplary THz pulse obtained using electro-optical sampling. The arrows mark echos of the main pulse generated in the generation/detection crystals.

Figure 5.6 shows an exemplary THz pulse. The main pulse is followed by smaller pulses, which are echos from internal reflections of the different object in the beam path, here the detection and generation crystals of the setup.

5.5 Some Comments to the Setup Used in this Work

The THz setup used in this thesis is seeded by a Spectra-Physics Spitfire Ace system (2×3W, 35 fs). During the course of the thesis, the system underwent several changes and redesigns, e.g. the generation of THz was changed from focusing the optical beam on a ZnTe crystal to a non-focused THz generation in a large ZnTe slab. This was performed with the intention to increase the THz beam power, while decreasing the frequency range. Bare gold off-axis parabolic mirrors from Edmund Optics were used to guide the THz beam. As balanced photodetectors, the Newport Nirvana balanced optical receiver was chosen, the lock-in detection scheme was realized using a National Instruments data acquisition card together with a ThorLabs chopper. The whole system was controlled by self-written Labview programs, first written by Dr. Shekhar Priyadarshi, later rewritten by the author of this thesis.

When performing OPTP spectroscopy measurements, the optical excitation wavelength is generated by a TOPAS/NirUVVis OPA.

The excitation power can be controlled by variable neutral density filter and a $\lambda/2$ waveplate in a motorized rotating mount together with a polarizing beam splitter.

Assuming a complete realignment is necessary for the setup, the procedure was usually as follows. First, the optical path length was calculated for the generation, detection and optical pump and adjusted to assure a temporal overlap in the sample (for the optical pump) and the detection crystal. Then, the optical beams were aligned with the use of irises as perfectly straight lines. Then, the first mirror pair to collimate and focus the THz beam on the sample is inserted. A first rough alignment is performed to obtain a spot at the sample again, then a diffuser is inserted at the position where the generation crystal is supposed to got. The scattered light is used to optimize the light path to the sample. The same procedure is repeated for the second mirror pair, which collimates the THz beam after the sample and focuses it on the detection crystal. Fine alignments like to optimize the overlap and the beam path into the balanced photodiodes were performed while monitoring the THz pulse shape in the computer.

Since the laser performance, the setup and the detailed alignment changed during the thesis, the shape and spectra of the THz pulses shown here can be quite different from each other.

6 Parameter Extraction and Interpretation

THz measurements provide the time-dependent electric fields of a pulse, which has passed through a sample of interest, and a reference pulse. Using the Fourier transformation $\mathscr{F}$, these can be converted to a spectrum

$$E_{\text{ref}}(t) \xrightarrow{\mathscr{F}} S_{\text{ref}}(\omega), \qquad (6.1)$$

$$E_{\text{sample}}(t) \xrightarrow{\mathscr{F}} S_{\text{sample}}(\omega). \qquad (6.2)$$

From these, the so-called transfer function $H(\omega)$ can be constructed as

$$H(\omega) = \frac{S_{\text{sample}}(\omega)}{S_{\text{ref}}(\omega)}. \qquad (6.3)$$

This transfer function contains all information about the elements in the beam path which affect the propagation of the THz pulse of the sample measurement in comparison to the reference measurement. It is a complex function[16] and can be also expressed in polar form by

$$H(\omega) = |H(\omega)|e^{i\phi(\omega)}, \qquad (6.4)$$

where ϕ is the phase angle of H. To obtain parameters of interest like the refractive index or complex conductivity from the transfer function, an appropriate model for the beam propagation through the sample has to be applied. The complexity of this function can rise substantially depending on number of layers in the sample, the number of multiple reflections and other factors. In most cases, this leads to a non-invertible expression. Thus, the parameters of interest can not be directly calculated from the transfer function. To overcome this problem, approximations can be introduced or numerical schemes have to be employed (Figure 6.1), where an algorithm "tests" a transfer function calculated from a guessed refractive index against the measured transfer function [350–354]. These extraction routines are not straight-forward and hold many pitfalls.

[16] In this section, complex quantities such as the refractive index n will not be labeled using the tilde. Where just the real or imaginary part is used it will be addressed or the notation $a = a_1 + a_2 i$ will be used.
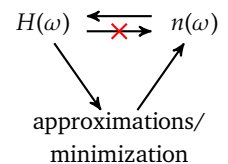
Figure 6.1: Extraction of physical parameters such as the refractive index from the transfer function using approximations and minimization algorithms.

75

The obtained frequency-dependent values for the refractive index or the conductivity are usually analyzed by means of simpler physical models, which give access to physical parameters like scattering times or carrier concentrations. Conceptually simple models like the Drude model or its extension for bound carriers, the Lorentz-Drude model [1] have been applied successfully for the description of various systems [295].

In the following, the theoretical transfer functions for single and double layered samples are given, together with the most common approximation. Afterwards, the most prominent models to explain the frequency dependence of the refractive index or conductivity are discussed. In a last step, the implementation of extraction routines in a `python` library is presented.

In Figure 6.2, examples for the obtained transfer functions for two exemplary systems are shown. In the upper panel, the pulse is delayed by the sample with respect to the original beam. This happens if the real part of the complex refractive index n of the sample is different from the corresponding reference measurement. This phase shift can be directly seen in a nonzero phase of the transfer function. In the lower panel, the THz pulse lost intensity after passing through the sample due to a nonzero imaginary part of n. This leads to a magnitude of the transfer function of less than 1. For realistic samples, both scenarios can happen at the same time and can also show a non-trivial dispersion.

For the Fourier transformation, several aspects have to be considered. Since the recorded pulse can contain later replica of the initial pulse caused by the etalon effect (multiple reflections of the pulse inside the substrate or sample), the Fourier transformation can be done for certain time windows only, thus excluding any etalon-effects on the spectrum.[17] Second, zero-filling (the addition of zeros at the end or the beginning of the data) can be done to artificially increase the spectral resolution of the obtained spectra and reduce any unwanted effects caused by the periodic nature of the Fourier transformation. Third, any occurring DC offset of the pulse has to be removed. Forth, different windows for the Fourier transformation (as an alternative to zero filling, which is effectively a rectangular window) change its result. A study of the effect of different windows on the obtained THz spectra is given in [355].

[17] This is only possible for optically thick samples, where the internal reflections do not overlap with the original pulse.

The changes of a THz (or any optical) pulse with a angular frequency ω, which is passing through a layered system (like a slab), can be described using the Fresnel equations or matrix optics for more complex systems. The beam can be absorbed within the
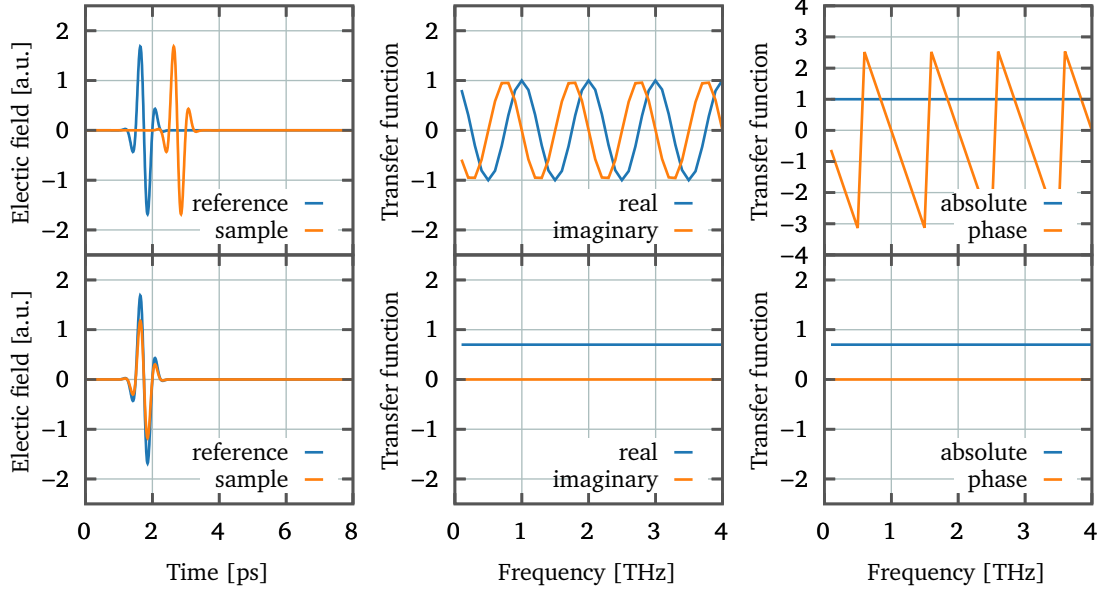
Figure 6.2: Example for the transfer functions for the transmission through two exemplary systems. In the upper row, the pulse is delayed by a material with a nonzero refractive index, but no absorption is happening. In the lower row, the pulse is transmitted through a lossy medium with a refractive index equal 1, so no delay is happening. Note the *wrapped* representation of the phase angle in the top left plot and that the absorption leads to absolute values |H| less than 1.

media, reflected or transmitted at the interfaces. The absorption P, reflection R or transmission T can be described as [122]

$$P_{a,d} = \exp\left(-\frac{i n_a \omega d}{c}\right),$$ (6.5)

$$R_{a,b} = \frac{n_a - n_b}{n_a + n_b},$$ (6.6)

and $$T_{a,b} = \frac{2n_b}{n_a + n_b},$$ (6.7)

where a, b denote two different media, d the thickness of the material, c is the speed of light and $n_{a/b}$ the refractive index of medium a or b. All these quantities can be calculated when the complex refractive index n and the thickness d is known. The transfer function H is defined as

$$E_{\text{out}}(t) = H \circledast E_{\text{in}}(t)$$ (6.8)

$$\rightarrow S_{\text{out}}(\omega) = H S_{\text{in}}(\omega)$$ (6.9)

where E refers to the electric field of the electromagnetic wave in time domain and S refers to the spectrum of the electromagnetic wave. The transfer function convoluted with the incident electromagnetic field results in the output electric field, which gives a multiplication in the frequency domain. When two measurements with and without the sample are performed, the transfer

function for a sample of interest can be calculated by (as given above)

$$H = \frac{S_{\text{sample}}}{S_{\text{reference}}}$$

Thus, by building the appropriate transfer function for a specific system using the Fresnel expressions and inverting it, the complex refractive index can be obtained.

6.1 The Phase-Unwrapping Problem

For the exponential/polar representation of the complex spectrum, phase–unwrapping has to be considered depending on the used extraction algorithms. Phase–unwrapping is the process to unfold the phase ϕ from the range between –180 to 180° to give a continuous line (Figure 6.3). Other way around, phase–wrapping means to fold-back a certain angle to the range from –180 to 180°.
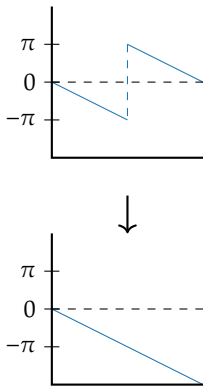
Figure 6.3: Schematic representation of the phase unwrapping.

A simple algorithm to unwrap is to iterate over data points and detect changes between in the phase greater than 2π. If a jump is detected, 2π is subtracted from all following datapoints [356]. Usually, library unwrapping functions as contained in MATLAB or the `python-numpy` library use similar schemes and will also be used in this thesis for (un)wrapping.

The problem of this approach is that it does not perform well with phase noise. This can occur at low signal–to–noise situations, like at very low (≤ 0.1 THz) or high frequencies. The noise can make the unwrapping algorithm detect the phase jump to early or to late, which results in a wrong phase offset starting from that data point to higher frequencies. One way to circumvent that problem is to exclude the areas with insufficient signal–to–noise and extrapolate the phase afterwards by assuming a linear phase [356]. Additionally, the scanning range defines the frequency resolution $\Delta \nu = (N \Delta T)^{-1}$, where N is the number of measured data points and Δt the temporal resolution. Thus, the frequency when a phase jumps occurs can only be determined within the given precision. It is generally advised to examine the resulting transfer function for phase jumps with respect to the noise level.

To detect phase jumps correctly, it is also extremely important to provide the necessary frequency resolution, so that the difference between two datapoints is not always in the same range as the difference obtained by the phase jumps. In Figure 6.4, the problem

is visualized. If the frequency resolution is low, a traditional un-wrapping algorithm has difficulties to distinguish phase disconti-nuities from normal phase steps, since the frequency step between two consecutive steps is so large. Thus, measuring a large tempo-ral window (and remove second reflections by windowing, where appropriate) is important if the phase shift induced by the sample is large.
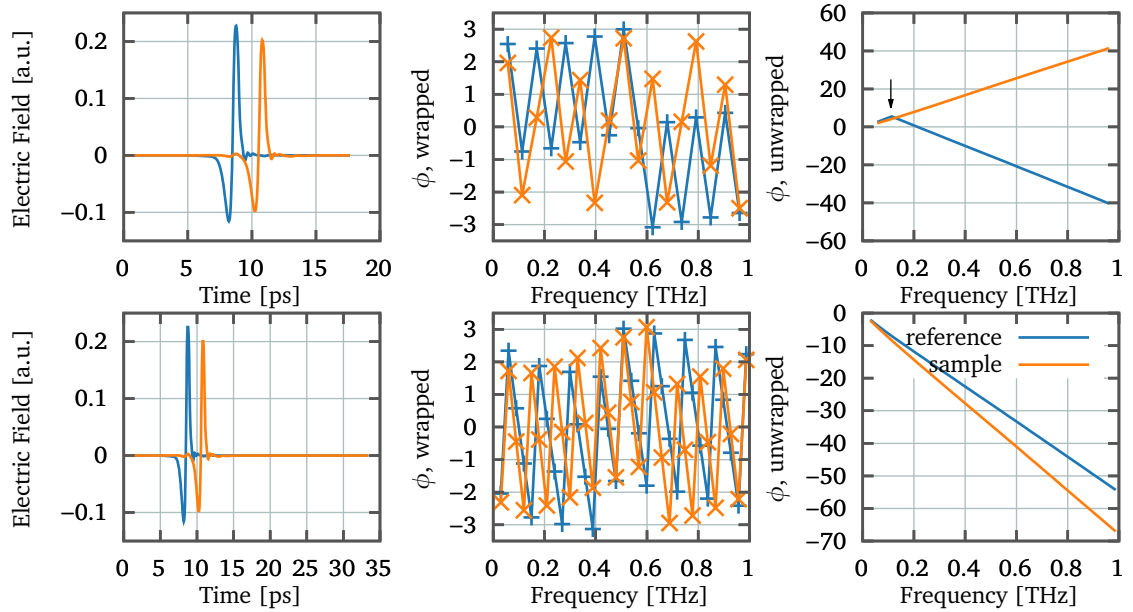
Figure 6.4: Influence of the frequency resolution on the phase unwrapping performance. The top as well as the bottom panels show a "reference" (air) and a "sample" (quartz, $d = 0.5$ mm) measurement. On the top, the signal was cut in time–domain before any internal reflection inside the quartz substrate. In the lower panel, the full temporal scan was used. Both signals were filtered with a Gaussian window filter located at the top of the THz signal and a width of 2 ps. The erroneously detected phase jump for the truncated data is marked by the arrow in the top right panel. From that frequency on, the phase has an incorrect slope. The data extracted with the full data shows more data points between the phase discontinuities, allows the algorithm to correctly identify those.

Peter Uhd Jepsen has written an detailed article about the phase retrieval and unwrapping problem in THz-TDS [357], where he proposes an "informed"unwrapping. In principle, the phase can be calculated by identifying the t_0 of a THz pulse (e.g. by looking for the peak position), and is then given by

$$\phi_0(\nu) = 2\pi\nu t_0. \qquad (6.10)$$

By using this expression as a starting point and testing the ex-tracted phases against it, errors in the in the phase can be cor-rected.

6.2 Transfer Function for a Single-Layer System

Single–layer systems studied by THz spectroscopy can be substrates like quartz or silicon, but also pressed pellets including organic materials or powdered materials. All following derivations are performed under the assumption of plane wave at normal incident at the sample.
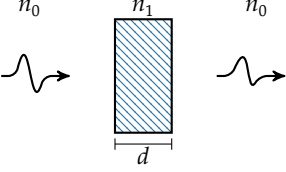
Figure 6.5: Schematic representation of a THz pulse transmitting through a slab with the thickness d.

The incoming beam S_{in} first passes through an infinite amount of air/vacuum (n_0), than gets reflected and/or transmitted on the air/slab interface, passes through the slab while experiencing absorption and dispersion, and finally passing the slab/air interface. This gives

$$S_{\mathrm{sample}} = P_{0,\infty} T_{0,1} P_{1,d} T_{1,0} P_{0,\infty} S_{\mathrm{in}} \tag{6.11}$$

and when the sample is removed (which represents the corresponding "reference" measurement)

$$S_{\mathrm{reference}} = P_0 P_{0,d} P_0 S_{\mathrm{in}} \tag{6.12}$$

For the transfer function, this yields

$$H = \frac{S_{\mathrm{sample}}}{S_{\mathrm{reference}}} = \frac{T_{0,1} P_{1,d} T_{1,0}}{P_{0,d}}. \tag{6.13}$$

When multiple/FP reflections within the slab are considered,

$$H = \frac{T_{0,1} P_{1,d} T_{1,0} \sum_{i=0}^{\infty} \left[R_{1,0} P_{1,d} R_{1,0} P_{1,d} \right]^i}{P_{0,d}} \tag{6.14}$$

$$= \frac{T_{0,1} P_{1,d} T_{1,0}}{P_{0,d}} \left(\frac{1}{1 - (P_{1,d} R_{1,0})^2} \right) \tag{6.15}$$

[18] The geometric series is given by $\sum_{i}^{\infty} a_0 q^i = \frac{a_0}{1-q}$

is obtained, where in the last step the geometric series representation of the sum was used[18]. As already mentioned, this expression is usually not directly invertible, thus one can introduce approximations to obtain an analytically invertible expression or use a numerical approach, which tries to fit $n(\omega)$ to the experimental data.

Analytical Solution for a Thick, Low Absorbing Sample

For an optically thick sample, the FP reflections are separated from the main pulse in the time-domain. This allows to cut the data to remove the need to incorporate those internal reflections in the data extraction routine. In the following, it is also assumed that the absorption in the medium is low.

If the experiment is performed under a dry or nitrogen atmosphere, the refractive index of the surrounding medium can be set to 1. Inserting Expression (6.5), (6.6) and (6.7) into (6.13) yields

$$H(\omega) = \frac{4n}{(1+n)^2} \exp\left(\frac{id\omega}{c}(1-(n_{\text{real}}-in_{\text{imag}}))\right)$$

$$= \frac{4n_1}{(1+n)^2} \underbrace{\exp\left(\frac{id\omega}{c}(1-n_{\text{real}})\right)}_{\text{phase shift by refraction}} \underbrace{\exp\left(\frac{-d\omega}{c}n_{\text{imag}}\right)}_{\text{absorption}}$$

where n is the refractive index of the sample. By comparing the oscillating and non-oscillating parts in

$$H = \underbrace{|H| \exp(i\phi)}_{\text{oscillating}} = \frac{4n_1}{(1+n_1)^2} \underbrace{\exp\left(\frac{id\omega}{c}(1-n_{\text{real}})\right)}_{\text{oscillating}} \exp\left(\frac{-d\omega}{c}n_{\text{imag}}\right),$$

for n_{real} and n_{imag}

$$\exp\left(i\phi\right) = \exp\left(\frac{id\omega}{c}(1-n_{\text{real}})\right)$$

$$\Rightarrow n_{\text{real}} = 1 - \frac{c}{d\omega}\phi \qquad (6.16)$$

and

$$|H| = \frac{4n_1}{(1+n_1)^2} \exp\left(\frac{-d\omega}{c}n_{\text{imag}}\right)$$

$$\Rightarrow n_{\text{imag}} = -\frac{c}{d\omega} \ln\left(\frac{(1+n_{\text{real}})^2}{4n_{\text{real}}}|H|\right) \qquad (6.17)$$

can be found. In the last step n was assumed to be (nearly) real-valued, thus the factor $4n_1/(1+n_1)^2$ is assumed to be real. Thus, the refractive index can be directly calculated from the experimental transfer function using Expression (6.16) and (6.17). This is an effective approximation for common substrate materials, since they are thick enough to host a sample layer and should not show any notable absorption or features in the THz range. The calculated refractive index can also be used as starting point for more elaborate extraction routines.

Numerical approaches

If the approximations performed above are not wanted or applicable, H can not be directly inverted to calculate the refractive index

from the experimental data, but $\tilde{n}(\omega)$ can be found by numerical means. This was first proposed by Duvillaret *et al.* [350] and laid the founding for later extraction routines [351–354]. An arbitrary refractive index is inserted into the transfer functions given in (6.13) or (6.15) and compared against the experimental data. By varying the refractive index, the difference can be minimized and a fitting refractive index be found.

In the case of an optically thick sample, the multiple reflections of the THz beam can be differentiated in time-domain and removed. Inserting the expressions for the transmission (6.7) and propagation (6.5) terms into (6.13) leads to

$$H(\omega) = \frac{\left(\frac{2n_1}{n_0+n_1}\right)\exp\left(-\frac{in_1\omega d}{c}\right)\left(\frac{2n_0}{n_0+n_1}\right)}{\exp\left(-\frac{in_1\omega d}{c}\right)} \tag{6.18}$$

$$= \frac{4n_0 n_1}{(n_0+n_1)^2}\exp\left(\frac{id\omega(n_0-n_1)}{c}\right) \tag{6.19}$$

Due to the $\exp(ix)$ term, this is an oscillatory function with a dependency on the thickness d, which is difficult to fit. As before, n_0 can be set to $1.0 + 0.0i$ assuming the experiment is done in a proper nitrogen/dry air atmosphere. This yields

$$H(\omega) = \frac{4n_1}{(1+n_1)^2}\exp\left(\frac{id\omega}{c}(1-n_1)\right). \tag{6.20}$$

It is important to note that usually algorithms perform better with no oscillatory function in the denominator (Expression (6.18) vs (6.19)), since it gives rise to artifacts and oscillations in the extracted refractive index. The usual approach to solve this problem numerically is to define an error function *Err*

$$M(\omega) = |H_{\text{theory}}(\omega)| - |H_{\text{measurement}}(\omega)| \tag{6.21}$$

$$A(\omega) = \angle H_{\text{theory}}(\omega) - \angle H_{\text{theory}}(\omega) \tag{6.22}$$

$$Err = \sum \left(|M(\omega)| + |A(\omega)|\right) \tag{6.23}$$

as in [352, 353]. Sometimes, the absolute in $M(\omega)$ is replaced by the logarithm of the absolute or the error function is a sum of the squared values [350]. Using a minimization algorithm like `nelder-mead`, *Err* can be minimized to find the correct n_1. This has to be done separately for each frequency. The quality of the fit depends strongly on the parameters for the fitting algorithm, the thickness and the initial guess.

6.3 Transfer Function for a Double-Layer System

Finding a transfer function for a two–layer systems is conceptually similar to the single layer, but treating multiple reflections is more complicated. A system like this can be a sample or a thin film deposited on a substrate. Without considering any multiple reflections, the transmitted beam is given by

$$S_{\text{sample}} = P_{0,\infty} T_{01} P_{1,d_1} T_{12} P_{2,d_2} T_{20} P_{0,\infty} S_{\text{in}} \tag{6.24}$$

and when a bare substrate is placed in the beam

$$S_{\text{reference}} = P_{0,\infty} P_{0,d_1} T_{02} P_{2,d_2} T_{20} P_{0,\infty} S_{\text{in}} \tag{6.25}$$

For the transfer function,

$$H = \frac{S_{\text{sample}}}{S_{\text{reference}}} = \frac{T_{01} P_{1,d_1} T_{12}}{P_{0,d_1} T_{02}} \tag{6.26}$$

$n_0 \qquad n_1 \ n_2 \qquad n_0$

$d_1 \ d_2$

Figure 6.6: Schematic representation of a THz pulse transmitting through two slabs with the thickness d_1 and d_2, as a film deposited on a substrate.

is obtained. By assuming a nitrogen atmosphere and inserting the proper terms for the propagation, reflection and transmissions terms

$$H(\omega) = \frac{2n_1(n_2+1)}{(n_1+1)(n_1+n_2)} \exp\left(\frac{id_1\omega(-n_1+1)}{c}\right) \tag{6.27}$$

is obtained. For a single slab, it is easy to determine whether the inclusion of multiple reflections is important. For a thin slab on a substrate, this might be true for the substrate, but it is difficult to decide for the thin film. Let us assume that the first internal reflection of a THz pulse has to be detected at least 2 ps later than the main pulse so that it can be cut in time-domain, this sets the limit of the materials thickness to 100 µm (assuming a refractive index of 2). In reality, deposited films will likely to be much thinner, so the internal reflection will overlap will the main pulse. The Fabry-Pérot term for the sample is given by

$$FB = \sum_{k=0}^{\infty} \left(R_{1,2} P_{1,d_1} R_{1,0} P_{1,d_1}\right)^k \tag{6.28}$$

$$= \frac{1}{1 - R_{1,2} P_{1,d_1} R_{1,0} P_{1,d_1}}. \tag{6.29}$$

The sum can be resolved since it represents the geometric series. By inserting all the relevant term, for the full transfer function of a two-slab system with multiple reflections in the sample,

$$H(\omega) = \frac{-2.0n_1(n_2+1.0)\exp\left(\frac{id_1\omega(n_1+1)}{c}\right)}{(n1-1.0)(n_1-n_2) - (n_1+1.0)(n_1+n_2)\exp\left(\frac{2.0id_1n_1\omega}{c}\right)} \tag{6.30}$$

is obtained.

In some cases, it might be useful to include the first reflection in the substrate as well, for example when it is clearly differentiable in the time–domain. This can also be used to precisely obtain the thickness of the different layers, as e.g. shown in [358].

Analytic solution for a thin, conducting film on a substrate

An analytical solution for a thin conducting film, which is thinner than the wavelength and the skin depth was first derived by Tinkham [359, 360]. Derivations can also be found in [343] or [361]. This approach has been used to study several kinds of gold films [294, 361, 362]. In a thin conducting film, an electric field E generates a current density $j = \sigma E$, where σ is the complex conductivity. Since the thickness of the layer is assumed to be much smaller than the skin depth, the electric field and thus j can be viewed as uniform in the film. As shown in [361], by looking at the impedance and expressions for transmission/reflection for a transmission to a corresponding circuit, the transfer function

$$H(\omega) = \frac{1 + n_{\text{substrate}}}{1 + n_{\text{substrate}} + Z_0 \sigma(\omega) d} \qquad (6.31)$$

with Z_0 as the impedance of free space is obtained. If d goes to zero, the transmission coefficient (Equation (6.7)) is regained. By inverting Equation (6.31) an expression for the so–called "sheet conductivity" ρ is obtained:

$$\rho = \sigma d = \frac{1}{Z_0} \left(\frac{n_{\text{substrate}}}{H} - n_{\text{substrate}} \right) \qquad (6.32)$$

6.4 Transfer Function for a Optically-Excited System

When OPTP spectroscopy spectroscopy is performed, the THz pulse probes the change of the refractive index caused by the photoexcitation. Usually, it can be assumed that the optical pulse is absorbed in the top layers of the material, thus creating a photoexcited "film" at top of the sample. This also covers scenarios, where a thin, photo–active film is deposited on a photo-inactive substrate (Figure 6.7).

The theoretical background to obtain a transfer function for a photoexcited system was comprehensively reviewed by Joyce *et*

Figure 6.7: Optical-pump and subsequent THz -probe of a photoactive layer on a substrate or a single slab. The optical excitations leads to the same scenario for both situations: A thin, excited layer on an unexcited substrate.

al. [341]. The measured change of the transfer function is given as

$$\frac{\Delta H(\omega)}{H(\omega)} = \frac{\Delta E(\omega)}{E(\omega)} = \frac{E^{\mathrm{on}}(\omega) - E^{\mathrm{off}}(\omega)}{E^{\mathrm{off}}(\omega)}, \qquad (6.33)$$

where $E^{\mathrm{on/off}}(\omega)$ is the spectrum obtained from the THz pulse of the excited/unexcited system. The photoactive layer is usually very thin compared to the wavelength of the THz radiation and the substrate quite thick. Thus, the transfer function can be approximated [341] by

$$H(\omega) = \frac{1 + n_{\mathrm{sub}}}{(1 + n_{\mathrm{sub}}) - \mathrm{i}(n^2 - n_{\mathrm{sub}})\frac{\omega d}{c}}, \qquad (6.34)$$

where n_{sub} is the refractive index of the substrate, n the refractive index of the excited layer and d the thickness of the excited layer. Using $\epsilon = n^2$,

$$\epsilon = \frac{\mathrm{i}c(1 + n_{\mathrm{sub}})}{\omega d}\left(\frac{1}{H(\omega)} - 1\right) - n_{\mathrm{sub}} \qquad (6.35)$$

can be obtained. Using $\epsilon = \epsilon_b + \mathrm{i}\sigma/\omega\epsilon_0$ and assuming a highly conductive sample (thus effectively dropping any background influences ϵ_b),

$$\sigma = \frac{\epsilon_0 c(1 + n_{\mathrm{sub}})}{\omega d}\left(\frac{1}{H(\omega)} - 1\right) \qquad (6.36)$$

is obtained for the photoinduced complex conductivity. Often, instead of the conductivity the "sheet conductivity" $\rho = \sigma d$ is used to circumvent the inclusion of the correct thickness of the photoexcited layer - similar to Equation (6.32).

6.5 Interpretation of the Obtained Parameters

Even though the obtained parameters already give insight into the physical processes, usually it is of interest to compare these with a model, where the obtained values for $\tilde{n}$ or $\tilde{\sigma}$ are connected with physical properties. Often, conceptually simple and (semi)classical models like the Drude model are successfully applied to understand dispersion of the extracted parameters. An overview over the different models can also be found in [295]. Apart from the models described here, effective–medium theories are applied to study in the THz regime [363].

Drude Model

The simplest model to understand the complex conductivity in the THz range is the so-called Drude model [1, 293]. It models the dynamic of a free electron using the EOM

$$\frac{\mathrm{d}^2}{\mathrm{d}t^2}x + \frac{1}{\tau}\frac{\mathrm{d}}{\mathrm{d}t}x = -\frac{e}{m}E(t). \tag{6.37}$$

The conductivity is defined as $\sigma = j/E$ with the current density $j = -eN\dot{x}$, where e is the elementary charge and N the number of electrons. For the stationary case $\ddot{x} = 0$ the so–called Drude DC conductivity is obtained

$$\sigma_{\mathrm{DC}} = \frac{Ne^2\tau}{m^*}, \tag{6.38}$$

where the effective mass m^* has been inserted. By assuming $E(t) = E_0 e^{-\mathrm{i}\omega t}$, for the frequency-dependent conductivity $\sigma_{\mathrm{Drude}}(\tau)$

$$\sigma_{\mathrm{Drude}}(\tau) = \sigma_{\mathrm{DC}}\frac{\tau}{1 - \mathrm{i}\omega\tau} \tag{6.39}$$

[19] Depending on the definition of the plane wave ($e^{-\mathrm{i}\omega t}$ vs. $e^{\mathrm{i}\omega t}$), the sign in the denominator (and thus the sign of the imaginary part) changes. In literature, both definitions are common.

is obtained[19] [293]. Figure 6.8 shows exemplary plots for the Drude conductivity in the THz range. The relative permittivity and consequently the refractive index can be obtained from the Drude conductivity by

$$\epsilon(\omega) = 1 + \frac{\mathrm{i}\sigma(\omega)}{\epsilon_0\omega} \tag{6.40}$$

$$n(\omega) = \sqrt{\epsilon_0(\omega)} \tag{6.41}$$

Figure 6.8: Real (left) and imaginary (right) of the frequency-dependent Drude conductivity for different scattering times τ. The lower panels show the same data, but with a logarithmic x-axis.

Lorentz–Drude/Plasmon Model

By introducing a restoring force to Equation 6.37, the "Drude-oscillator" becomes the "Lorentz-Drude-oscillator", which is also called "Plasmon" model in the literature [295, 364]. This model has been successfully applied to describe e.g. the conductivity of semiconductor nanowires [341]. The EOM

$$\frac{d^2}{dt^2}x + \frac{1}{\tau}\frac{d}{dt}x + \omega_0 x = -\frac{e}{m}E(t), \qquad (6.42)$$

is extended by a term for the restoring force $\omega_0 x$ with the plasmon frequency ω_0. This leads to the expressions for the conductivity $\sigma_{\text{plasmon}}(\omega)$

$$\sigma_{\text{plasmon}}(\omega) = \frac{\tau e^2 N/m}{1 - i\omega\tau(1 - \omega_0^2/\omega^2)}. \qquad (6.43)$$
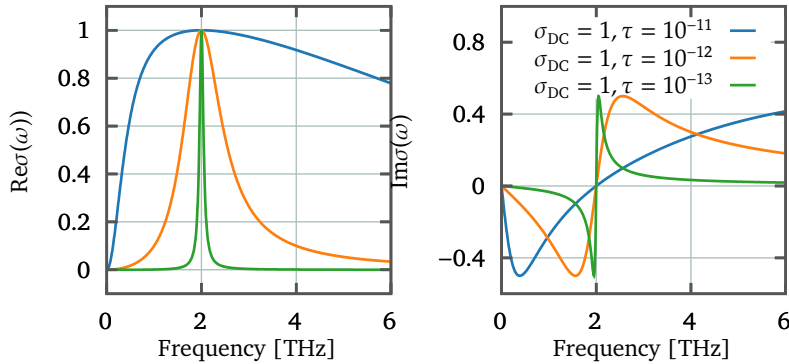
Figure 6.9: Real (left) and imaginary (right) of the frequency-dependent Plasmon conductivity for different scattering times τ and $\omega_0 = 2\,\text{THz}$

The results for different scattering times are visualized in Figure 6.9. By setting ω_0 equal to zero, the Drude model is obtained.

Drude-Smith Model

Another quite famous example in the THz community is the so-called Drude-Smith (DS) model [365]. It is an phenomenological generalization of the Drude model and is used often to describe the conductivity of nanomaterials, but has been criticized often due to the lack of a physical background.

$$\sigma_{DS}(\omega) = \frac{\sigma_{DC}}{1 - i\omega\tau}\left[1 + \sum_{n=1}^{\infty} \frac{c_n}{(1 - i\omega\tau)^n}\right] \tag{6.44}$$

Here, the coefficient c_n represents the fraction of the carrier's original velocity after the n-th scattering event. By assuming just one scattering event and $-1 < c_1 < 0$ (which corresponds to backscattering from particle boundaries or similar),

$$\sigma_{DS}(\omega) = \frac{\sigma_{DC}}{1 - i\omega\tau}\left[1 + \frac{c_1}{1 - i\omega\tau}\right]$$

is obtained. With $c_1 = 0.0$, the DS model reduces to the Drude model again.

Figure 6.10: Real (left) and imaginary (right) of the frequency-dependent Drude–Smith conductivity for different backscattering ratios c_1. *tau* was set to $1E-12$.
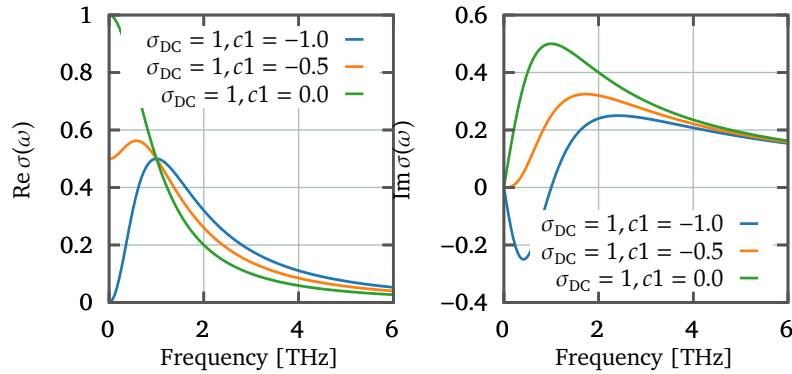
As already mentioned, the physical insight gained by the DS model is limited since its pure phenomenological approach. Also, the truncation of the sum in Expression (6.44) has to be terminated after n = 1, otherwise the model reduces to the Drude model again with modified scattering rates. Several publications tried to address this issue by providing physical explanations for the line shape of the DS model [8, 296]. This is also discussed in Chapter 4. The DS model has been applied especially to nanostructures such as thin films [366–368] or wires [98], graphene or carbon nanotubes [99] or organic materials [10, 369, 370].
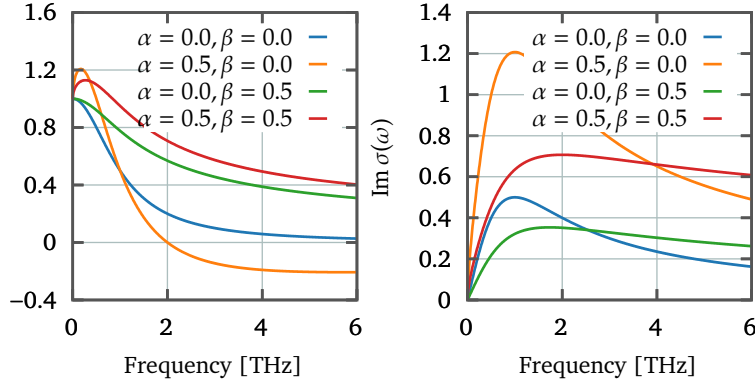
Figure 6.11: Real (left) and imaginary (right) of the frequency-dependent generalized Drude model. τ was set to 1 THz, the other parameters are given in the legend.

Generalized Drude Model

The generalized Drude model is a combination of the Cole–Cole and Cole–Davidson model [371]. This model does not provide insights in the details of the scattering mechanisms, but is a purely phenomenological approach to change the shape of the Drude model [295].

$$\sigma_{\mathrm{GD}}(\omega) = \frac{\sigma_{\mathrm{DC}}}{\left[1 - (\mathrm{i}\omega\tau)^{1-\alpha}\right]^{\beta}} \qquad (6.45)$$

For $\alpha = 0.0, \beta = 1.0$ the Drude model is recovered (see Figure 6.11). It has been applied to describe the conductivity of doped silicon in the THz range [371] or graphene [372].

6.6 Implementation into DuoDecim

The extraction procedures and routines described above have evolved into a python library with the name DuoDecim (from latin "twelve" as an alternative to "tera"). DuoDecim can be used as a standalone program, which extracts the refractive index using an input file, which defines the system, or as a python library to be used in scripts.

Parameter extraction using DuoDecim as a standalone program

To use DuoDecim as a standalone program, the measurement of a reference and a sample has to be provided, for example a measurement of air and a measurement of substrate. An input file defines the parameters for the extraction routines, which are given in Table 6.1. The program supports various extraction routines,
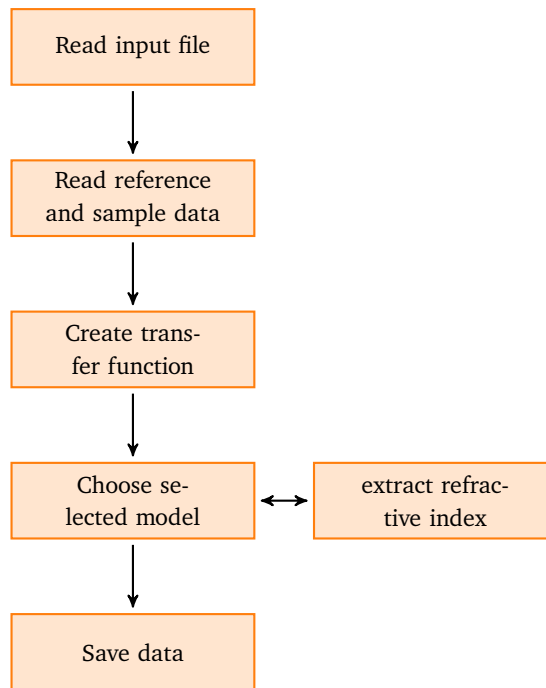
like the analytic calculation of the refractive index using Equation (6.16) and (6.17) or by numerical minimization of Equation (6.23) using the `nelder-mead` algorithm. Alternative routines like the `basinhopping` algorithm from the `scipy.optimize` library or a genetic algorithm can also be included. The program flow of the standalone execution is shown in Figure 6.12.

This offers a simple and convenient way to extract the refractive index for standard measurements.

Usage as a `python` library

Alternatively, the routines can be used as python library and included in other python scripts. This is advised for more complicated scenarios where the intermediate steps (see e.g. Section 6.1) should be done with care. Additionally, it gives access to experimental features. A list of routines in the DUODECIM library is given in Table 6.2. For each routine, the docstring (`help(<function>)`) provides more information about the input and output parameters/variables.

6.6.1 Refractive Index of PTFE in the THz Range

In Figure 6.13, the refractive index for PTFE is shown. The real part of the refractive index is nearly constant and around 1.4, while the imaginary part shows no notable absorption.

Keyword	Default value	Explanation
`$reference`	reference.dat	filename for the reference measurement
`$sample`	sample.dat	filename for the sample measurement
`$nlayer`	1	number of layers - currently only supporting 1 or 2 layers
`$d1`	0.01	thickness of layer 1
`$d2`	0.01	thickness of layer 2 - obsolete if the sample has only one layer
`$guess`	2, 0.01	guess for the refractive index
`$nsub`	1.44, 0.01	refractive index of the substrate for two layer systems
`$nzeros`	0	number of zeros for zero-filling
`$min`	0.1E12	minimum frequency
`$max`	3.5E12	maximum frequency
`$cut`		position, at which the timetrace is cut to remove echos
`$conv`	$\frac{20^{-3}}{\text{speed of light}}$	conversion ratio for the x axis of the measured data to the time-domain
`$analytic`		switches on the analytic parameters extraction based on Equation (6.16) and (6.17), can only be used for single-layered samples
`$numeric`		switch for numerical extraction without FP reflections
`$tinkham`		switch for calculation of conductivity using the Tinkham approximation (Equation (6.32))
`$print_h`		switch to write out the transfer function
`$output`	output	filename for output data
`$overview`		plots an overview of the data and transfer function
`$thickness_coarse`		switch for coarse estimation of sample thickness
`$thickness_fit`		switch for fitting the sample thickness (experimental)

Table 6.1: Parameters in the input file for DuoDecim.

function	Explanation
`fourier`	calculates the Fourier transformation of a THz pulse
`find_transfer`	calculates the transfer function
`optp_extract`	extracted the optical conductivity
`analytic`	extract refractive index for a single slab with the analytic expression
`tinkham`	extract the conductivity using the Tinkham formula

Table 6.2: Routines included in the DuoDecim library.

The extraction was performed for measurement, where any secondary reflections were cut in the time-domain. As an extraction model, the analytic model (Equation (6.16) and (6.16)) and the numeric fitting approach (Section 19) were used. The extracted complex refractive index is nearly identical using the two different techniques.

Figure 6.13: Extracted refractive index for a PTFE chip. The results from the analytical and numeric parameters extraction are almost identical, showing the validity of the assumptions made to obtain Equation (6.16) and (6.17)
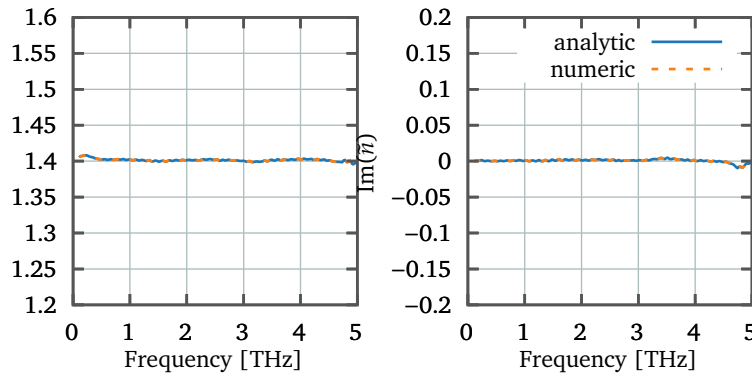
6.6.2 Refractive Index of Quartz in the THz Range

Quartz is a suitable material as a substrate for THz spectroscopy - depending on the way it is synthesized. The terminology is not always clear what quartz is, since the same material can also be named "fused quartz" or "fused silica", depending on the vendor. Quartz substrates for THz studies should have a low OH content, which is usually obtained when the substrate is prepared by melting natural silica grains.

The quartz substrates used in this worked were obtained from plano-em ("Quarzglas GE 124", product number 26016, information about the material can be found under [373]) with a size of $19 \times 19 \times 0.5$ mm.

The refractive index shown in Figure 6.14 is obtained using DuoDecim. The recorded electric field is cut in the time–domain to remove any secondary reflections in the crystals. The analytic (Equation (6.16) and (6.17)) and numeric (see Section 19) extraction methods yield nearly the same refractive index.

The thickness of the material can be measured e.g. using a micrometer screw, but can also be derived from the THz measurements, since the information about the thickness in encoded in the second reflection of the pulse. Figure 6.15 shows the refractive index for different thicknesses, obtained using a numerical approach that includes the second reflection inside the sample.
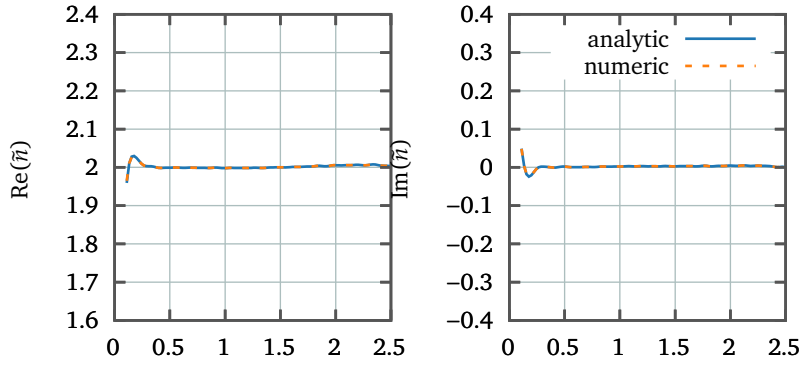
Figure 6.14: Refractive index of quartz, extracted for a thickness of 0.62 mm was used. Quartz exhibits no absorption in the studied frequency range and a refractive index of around 2. The numeric and analytic extraction yield the same results.
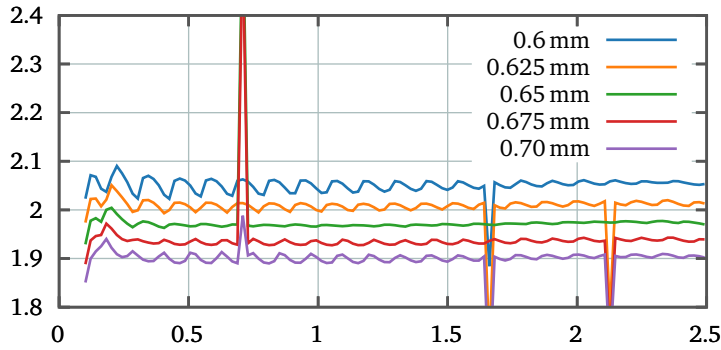
Figure 6.15: Refractive index of quartz for different thicknesses, obtained using the numerical approach including the second reflection in the crystal.

If the thickness given to DuoDecim does not exactly correspond to the real thickness, the extracted refractive index shows oscillations. The occurring spikes can be traced to incorrect phase unwrapping and is here not corrected. Changing the thickness also changes the refractive index slightly.

The dependency of the oscillations on the thickness for which the data is extracted can be used to optimize the thickness, as e.g. proposed in Refs. [350, 351, 353]. This is usually done by calculating the "total variance", that is the summed difference between adjacent data points, or by performing a Fourier transformation of the refractive index and studying the peak which refers to the oscillation. The "total variance" method is also included in DuoDecim, but has to be applied with care. As can be seen in Figure 6.15, the occurrence of spikes can influence the result and overshadowing the oscillations of the refractive index.

Part III

Terahertz Spectroscopy of Metallic and Semiconducting Films and Particles

7 Terahertz Spectroscopy of Thin Gold Films

7.1 Introduction

Even though this work is focused on the transport properties of AuNPs connected with molecules, it is worth to take a step back and look a conceptually simpler system, thin gold films.

When gold is deposited on substrates using physical methods like sputtering or evaporation, it does not instantaneously form a homogeneous layer. First, small nanometer–sized clusters are grown [374, 375]. By depositing more material, a randomly connected network of gold islands is formed, until finally a continuous layer is completed. This transition of an (in a classical sense) isolating to a conducting film is called insulator-to-metal transition (IMT). The percolation threshold describes the amount of deposited material, when a continuous path from one electrode to another can be found. Naturally, the conductivity of such a gold film is changing drastically when crossing the percolation threshold. In order to prevent the formation of islands, a seed/adhesion layer or a silane-activated surface can be used [375–378] (see also Habteyes *et al.* [379] for a study on Au films with both, a Ti adhesion layer and a molecular linker).

Not only the conductivity, also the optical properties change drastically when crossing the percolation threshold. While the optical properties of the initially formed gold islands are similar to gold nanoparticles, as they show a plasmonic absorption band in the visible spectrum (see Section 8.1.1), a continuous film behaves like bulk gold, where the optical properties can be understood with the Drude–model (see Figure 7.2 for $\lambda \geq 1\,\mu m$). Directly at the insulator-to-metal transition, Tu *et al.* found evidence for a dielectric anomaly [324].

Several studies on thin gold films using THz spectroscopy have been performed. Thoman *et al.* [361] studied gold films deposited using a chemical and a physical method. They found for

Figure 7.1: Formation of a solid gold film by evaporation of gold on a substrate. With just a small amount of deposited gold, isolated islands are formed and transport can only happen by tunneling processes between the gold islands (visualized by the dotted red line). When more gold is deposited, at some point a percolated structure is formed, where a continuous path from the bottom to the top is formed. This changes the transport properties of the film from (classically) isolating to metallic. Finally, a continuous film is formed when the islands grow together.
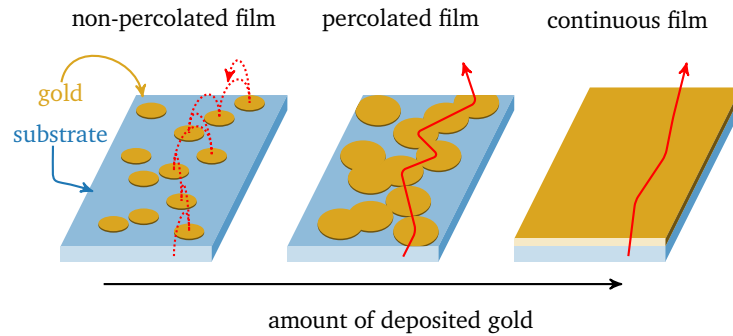
the chemically deposited film a suppression of any secondary reflections inside the sample, thus creating a anti-reflection coating for the THz radiation. Walther *et al.* studied thin gold films at the IMT using THz-TDS [294]. The films showed a flat THz transmission for all thicknesses, but at the percolation threshold at a thickness of 6.4 nm, the transmitted power dropped drastically and also extracted parameters using a Bruggemann EMT and DS fits showed strong deviations. The EMT approach failed to describe the behavior over the percolation transition, while the DS model was able to describe the data properly.

Figure 7.2: Real and imaginary part of the refractive index of gold, as obtained for bulk material [380] and a thin film [381].
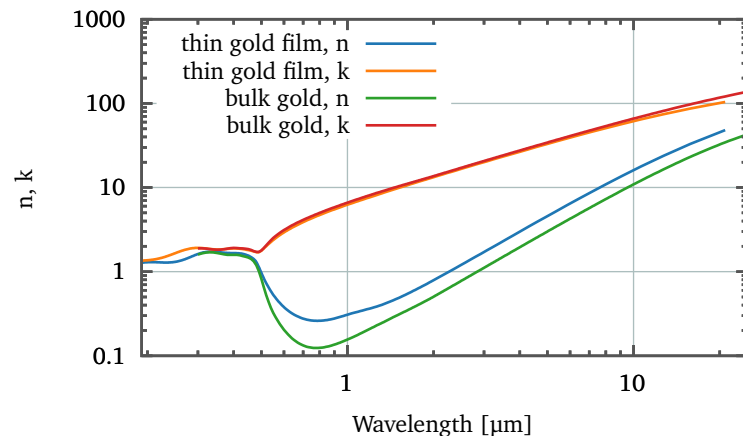
Pre–structured gold films have also been shown to be transparent for THz radiation. In Ref. [362], 65 nm thick films with holes in the range of 100 nm to 300 nm were prepared using lithographic methods. These films showed a strong plasmonic response in the

visible range, while retaining ~ 10% transmission for THz radia-
tion. In the review of Takeda *et al.* [382], several other findings
are summarized. Using the THz transmittance as an indicator,
the percolation threshold for evaporated gold films was found to
be at around 14 nm. Interestingly, the transmittance changed for
THz fields with higher intensities, but this was only found for per-
colated structures. Fits using the DS model showed a decreasing
localization of the electrons with higher THz fields. They con-
cluded that the high fields enabled tunneling between the metal-
lic nanostructures, while for low fields backscattering of the par-
ticles and localization inside the structures occurred [107]. This
is highly relevant for this thesis, since it demonstrates (as already
discussed in the introduction) that tunneling currents in nanos-
tructured materials can be induced and probed using THz spec-
troscopy.

In the following, thin evaporated gold films are studied using UV-
Vis spectroscopy, infrared (IR) spectroscopy and THz-TDS. The
purpose is to get an understanding of THz spectroscopy of small
metallic structures and to demonstrate the data extraction rou-
tines presented in Chapter 6.

7.2 Methods

7.2.1 Film Preparation

Gold films were prepared using a Quorum Q150T coating sys-
tem. As substrates, microscope slides (borosilicate glass,thickness
0.17 mm, purchased from Carl Roth GmbH) and quartz slides
(obtained from plano-em, "Quarzglas GE 124", product number
26016, see [373] for further information) have been used. All
substrates were cleaned first using usually millipore water (MQ),
acetone or isopropanol and toluene. The samples were mounted
(only one sample per time because of the limited space of the de-
vice) on an adhesive pad in the chamber of the coating system.
The chamber was evacuated and the wolfram filament heated up
slowly. The growth rate (monitored with the in-build quartz crys-
tal microbalance) was always kept below 10 nm/m.

7.2.2 Spectroscopy

UV-Vis Spectroscopy

UV-Vis spectroscopy was performed with a Varian Cary 50 Bio in transmission mode. As a reference, an untreated microscope slide has been used. The measurements were repeated several times, the samples have been shifted slightly to average over different places of the sample.

IR Spectroscopy

IR spectroscopy has been performed with a Cary 660 FTIR in transmission mode. As a reference, an untreated microscope slide has been used.

Terahertz Time-Domain Spectroscopy

All samples were investigated in our home-build THz spectrometer. As a reference for the measurements of samples prepared on glass slides, an untreated microscope slide has been used. For samples prepared with quartz substrates, a quartz substrate was used as a reference. All measurements were done under a continuous nitrogen flow to suppress of any absorption lines due to water vapor. Each measurement was repeated several times. The scanning range, time steps and integration time per data point were varied. Data processing and extraction were performed using DuoDecim as described in Chapter 6.

7.3 Results

7.3.1 Gold Films on Glass Substrates

Samples with thickness from 2 nm to 11.8 nm have been prepared. As thickness, the values obtained with the quartz crystal microbalance of the Quorum Q150T coater was used. The data from the UV-Vis and IR measurements are shown in Figure 7.3, along with the absorption determined from the THz measurements. Only for the three thinnest samples THz data is shown, since no transmitted pulse was recorded for the thicker samples. The thinner films ($d = 2, 4$ nm) show a plasmon like feature in the visible range at around 700 nm, with nearly no absorption

at longer wavelengths. In the THz range, these samples are completely transparent. By increasing the thickness slightly to 4.8 nm, the picture is changed completely. The peak in the visible range vanishes and there is absorption over the whole frequency range, increasing with the wavelength. This is the response of a free-electron gas as described by the Drude model.
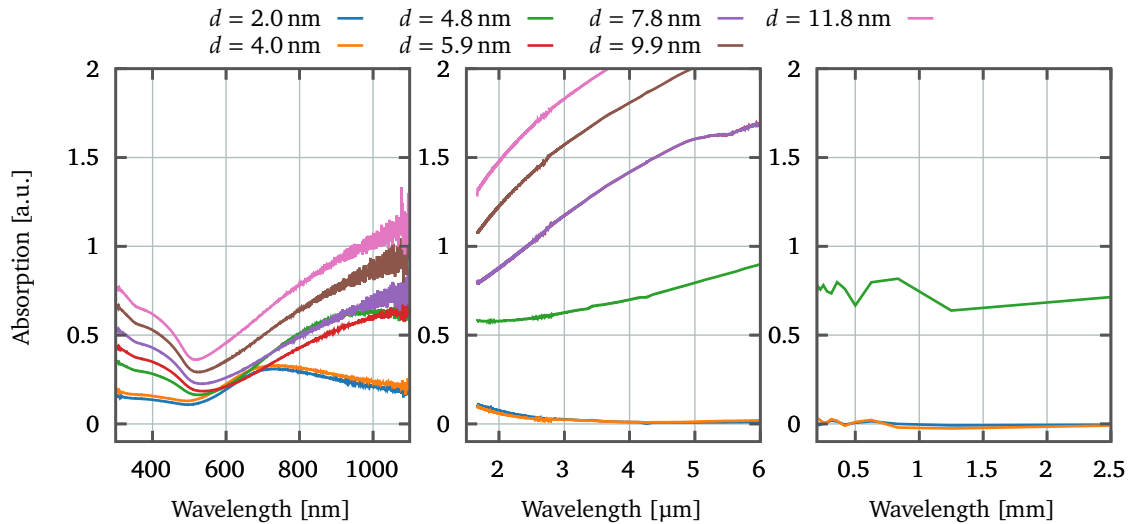
Figure 7.3: Absorption of evaporated gold films for different thicknesses over a broad spectral range. The thin, non–continuous films show a plasmon-like feature in the visible range and no absorption at longer wavelengths. The thicker films show the increasing absorption at longer wavelengths, the typical Drude-like response of a free–electron gas. No normalization of the data has been performed.

According to the spectra, the metal-to-insulator transition (MIT) is happening between a film thickness of 4 nm to 4.8 nm, as the absorption in the THz range is increasing substantially and the optical spectra is changing accordingly from a plasmon to a bulk gold response. This should be taken with a grain of salt, since the film evaporation conditions as the growth rate were not controlled precisely. This can change the structure of the deposited film and thus the percolation threshold.

7.3.2 Gold Films on Quartz Substrates

Additionally to the experiments with gold films on glass slides, films prepared on quartz substrates were investigated using THz spectroscopy. Borosilicate glass is not a suitable substrate in the THz range, thus for an extraction of the conductivity quartz is preferred. Figure 7.4 shows the THz time traces for a measurement of air, of the substrate and of three gold films with thicknesses of 5.3, 10 and 18.2 nm.

Figure 7.4: Thz traces for measurements of air, quartz and three different evaporated gold films on quartz. There is nearly no difference between the measurement of quartz and the two thinner films, the thicker films reduces the THz transmission by around 85%.
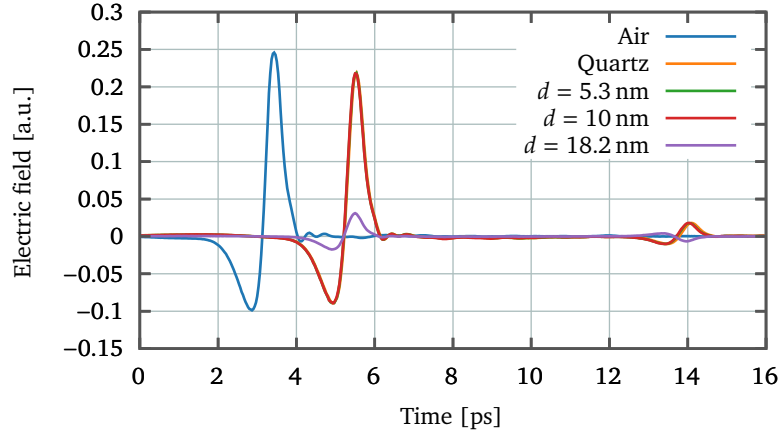
For the sample with a thickness of 18.2 nm, the complex conductivity has been extracted using the Tinkham formula (6.32) and DUODECIM. The refractive index of the substrate is assumed to be $\tilde{n} = 2$ (see section 6.6).
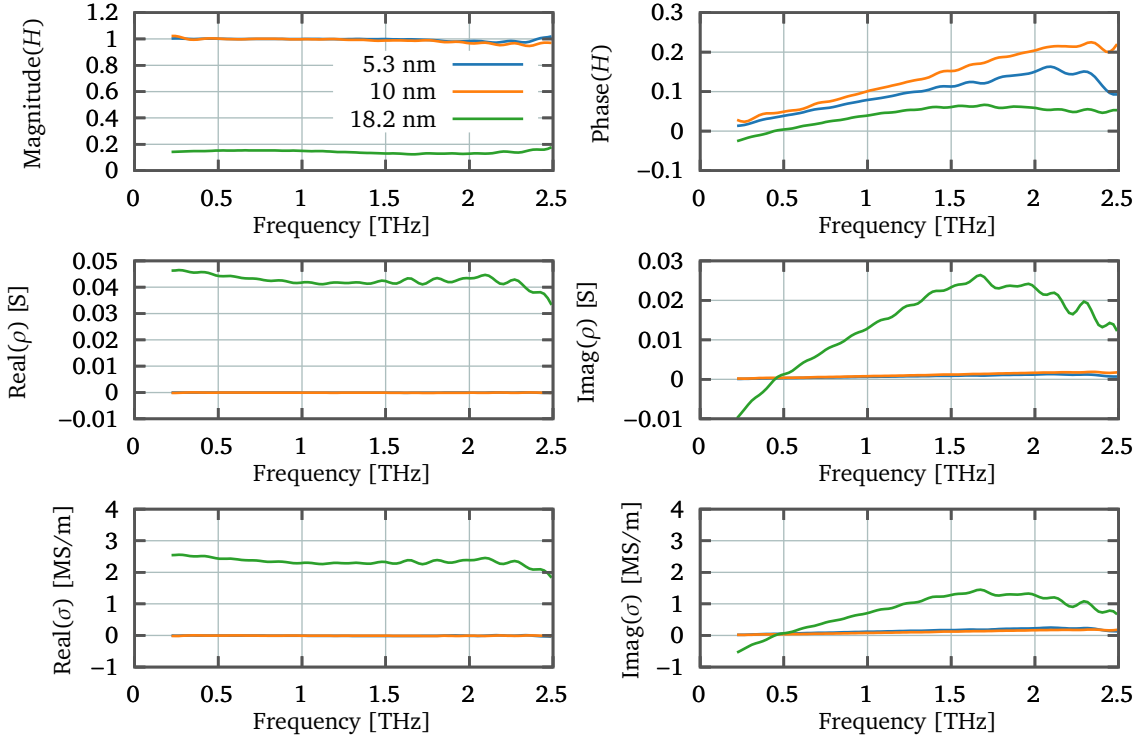
Figure 7.5: Transfer function and Tinkham sheet conductivity for three gold films on quartz with $d = 5.3, 10, 18.2$ nm. The thinner films are transparent in the THz regime, the film with $d = 18.2$ nm shows notable absorption and thus a nonzero real sheet conductivity.

By fitting the conductivity of the thickest film with the Drude model, parameters for σ_0 and τ can be obtained. This was done for five different measurements in the range from 0.1 to 2.5 THz, the obtained values are shown in Table 7.1. This is in the range of other experimental findings, e.g. Olmon *et al.* found a scattering

time of $\tau = 14 \pm 3$ fs for bulk gold and films with a thickness of 200 nm [380]. The negative imaginary conductivity (Figure 7.5) at low frequencies for the 18.2 nm film might be puzzling at first, since this cannot be explained by the Drude model. The extraction at these low frequencies is quite often unreliable and without any zero-filling, these are just two data points. Other analyses often start at e.g. 0.2 THz , disregarding the low frequencies [294].

The conductivity for bulk gold is given around 45.1×10^{-7} S m^{-1} [383], thus the conductivity obtained for the 18.2 nm thin film is about 0.5% of the bulk conductivity. This is in the same range as results for gold films on silicon substrates [294], when comparing samples which have roughly the same transmission of the THz radiation (about 1%). Previous studies on much thicker films (85 nm) found conductivities of about 33% of the bulk conductivity [384].

Table 7.1: Drude parameters for fitting the Tinkham sheet conductivity ρ of a 18.2 nm thin gold film on a quartz substrate in the range from 0.1 to 3 THz. The parameters were obtained for five different measurements of the film.

	σ_0 [kS m^{-1}]	τ [fs]
1	2.53	6.12
2	2.61	11.03
3	3.02	16.84
4	3.33	14.85
5	2.39	16.25

7.4 Summary

These experiments using thin gold films already show a surprising property of metallic nanostructures in the THz regime. Thin, evaporated gold films which show plasmon–like properties in the visible range are transparent in the THz range, as the dielectric function is more likely to be described by a Lorentz-Drude model than a Drude model. Such thin films are not a homogeneous or continuous, but a more alike to gold islands on a substrate. Thicker gold films, which are lacking the plasmon–like feature in the visible range, are blocking THz radiation, as to be expected for a metallic film. This already has several implications for the experiments using films of AuNPs: a) Thin films of metallic nanostructures are likely to be transparent in the THz regime, thus a certain thickness of the sample is relevant. b) Molecular linkers are most probably influencing the (quasi-) DC conductivity of the sample, as already shown in Chapter 4. This can influence the response of the film in the THz regime, depending on the change of the DC conductivity and the scattering parameters of the film.

8 Terahertz Spectroscopy of Gold Nanoparticle Films

8.1 Introduction

In this chapter, the preparation, characterization and THz measurements of gold nanoparticle (AuNP) films prepared by drop casted (or drop cast derived) and layer-by-layer methods is discussed. Following this introduction, the optical and electrical properties of AuNP films will be briefly reviewed and summarized.

AuNPs are more or less knowingly used for centuries, famous examples involve the roman Lycurgus cup, the colored windows of churches from the middle ages or the work of Michael Faraday [96, 385–388]. Gustav Mie presented the Mie theory for the theoretical description of the optical properties of AuNP as early as 1908 [389, 390].

Starting from the pioneering work of Turkevich *et al.* in 1951 [391] regarding the synthesis of AuNP, nowadays a zoo of different methods, techniques or precursors exist to synthesize particles with different sizes, shapes and stabilizing ligands [96]. The ligand shell, which stabilizes the particles and makes them soluble, offers various ways to functionalize the particles. This is valuable for applications for example in biomedicin[20], but the ligands also govern the self-assembly of particles into more or less ordered aggregates or the transport properties [397–403].

But apart from the flexibility of its surface, the most astonishing property of a AuNP is its response to visible light, which is governed by the so-called "plasmon". This manifests in the strong reddish color of AuNP solutions and is the source of basic research interest in AuNPs. A more detailed explanation will be given below.

Numerous reviews which discuss certain aspects of AuNPs have been published. Here, some of them should be mentioned shortly to give the interested reader the opportunity to further studies. Marie-Christine Daniel & Didier Astruc presented in 2004 maybe

[20] From a biomedical point of view, AuNPs are investigated as contrast agents, sensors or a method to deliver heat into a system by optical excitation [96, 392–396].

the most complete review. They present the synthesis of the particles, ligands, film preparation, physical and chemical properties and also applications in, e.g., biology and catalysis [96]. The review of Sardar *et al.* published six years later can be seen as an update [404]. Zabet-Khosousi & Dhirani discussed 2008 the transport mechanisms in nanoparticle assemblies, including AuNPs [116]. A review with a focus on the optoelectronic properties was published in 2015 by Liao *et al.* [129]. In 2017, Kanelidis & Kraus discussed the role of ligands with regard to electronic applications. Summaries regarding hot-electron dynamics can be found in [405–407] or just recently by Kuppe *et al.* [408]. Properties of the surface plasmon resonance in AuNP and various applications are reviewed in [390]. A paper discussing stability issues while preserving the plasmonic properties was published just lately [409].

The following chapter is organized as follows: First, the optical and electronic properties of AuNP and AuNP films will be discussed along with some experimental aspects concerning the synthesis, the film preparation and analytical methods. Afterwards, the experiments (preparation and THz spectroscopy) of drop casted and layer-by-layer prepared films are presented.

The underlying idea of this project is to use the AuNP as a model system, where the sample contains a multitude of molecular junctions: Dithiol linker molecules which are connected to two neighboring particles, acting as "electrodes". This idea has already been exploited for experiments, where the particle film still had to be contacted with macroscopic electrodes [127, 129, 410–412]. This is not required for THz measurements. Basically, five different molecules or scenarios will be studied, as visualized in Figure 8.1.

Figure 8.1: Ligands/linker molecules used in this chapter to build AuNP films. OAm is the stabilizing ligand of the AuNP after the phase transfer (see below for details).

oleylamine (OAm)

biphenyl-4,4′-dithiol (BI),
p-terphenyl-4,4″-dithiol (TER)

nonane-1,9-dithiol (NON)

4,4-thiobisbenzenethiol (THIO)
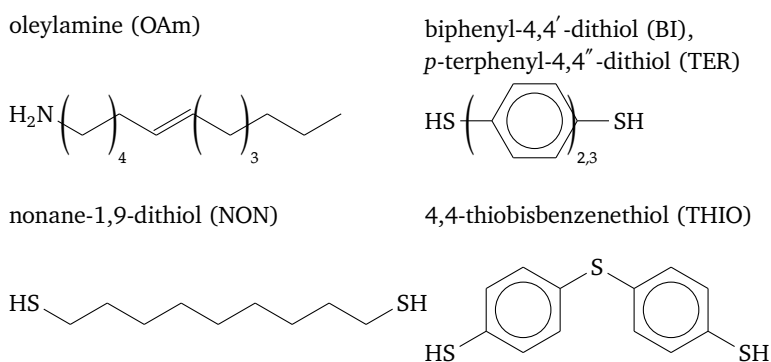
After the phase transfer to toluene (see below for details), OAm is the stabilizing ligand of the particles. NON as a dithiol can link two particles, but is much likely less conductive than the aromatic

linkers (BI, TER). Transport calculations based on the NEGF-DFT approach can be found in Chapter 4. THIO was used in some experiments, as it has a more flexible structure compared to BI and TER due to the sulfur atom in the middle of the molecule.

8.1.1 Optical Properties of Gold Nanoparticles

The optical properties of AuNPs are determined by the plasmon. Plasmons are collective oscillations of free or conduction band electrons. The classical EOM of a free electron gas interacting with a time-varying electromagnetic wave $E(t) = E_0 e^{-i\omega t}$ [293] is given by

$$m_e \frac{d^2 x}{dt^2} + m_e \gamma \frac{dx}{dt} = -eE_0 e^{-i\omega t}. \tag{8.1}$$

m_e is the mass of an electron, γ some damping/scattering rate in the medium and e the elementary charge. This is a second-order differential equation, which can be solved by using the ansatz $x(t) = x_0 e^{-i\omega t}$:

$$-m_e \omega^2 x_0 e^{-i\omega t} - m_e \gamma i\omega x_0 e^{-i\omega t} = -eE_0 e^{-i\omega t} \tag{8.2}$$

$$\Rightarrow x = \frac{eE}{m_e(\omega^2 + i\gamma\omega)} \tag{8.3}$$

$$\Rightarrow P = -\frac{Ne^2 E}{m_e(\omega^2 + i\gamma\omega)} \tag{8.4}$$

We obtain an expression of the polarization $P = -eNx$ of the electron gas, with N as the electron density. By using the definition of the electric displacement

$$D = \epsilon_r \epsilon_0 E \tag{8.5}$$

$$= \epsilon_0 E + P, \tag{8.6}$$

we obtain ϵ_r, the dielectric constant of the electron gas

$$\epsilon_r = 1 - \frac{Ne^2}{\epsilon_0 m_e} \frac{1}{\omega^2 + i\gamma\omega} \tag{8.7}$$

$$= 1 - \frac{\omega_p^2}{\omega^2 + i\gamma\omega} \tag{8.8}$$

$$\text{with} \qquad \omega_p = \sqrt{\frac{Ne^2}{\epsilon_0 m_e}}. \tag{8.9}$$

ω_p is the resonance frequency of the free electron gas. As shown in Figure 8.2, a free electron gas or systems which can be described that way (metals, doped semiconductors) are reflective below the

plasma frequency ω_p [293]. The reflectivity R can be calculated by

$$R = \left| \frac{\tilde{n} - 1}{\tilde{n} + 2} \right|^2 \quad \text{with} \quad \tilde{n} = \sqrt{\epsilon_r}. \tag{8.10}$$

Figure 8.2: Complex refractive index (left) and reflectivity (right) of a free electron gas as described by Equation (8.8) and (8.10).
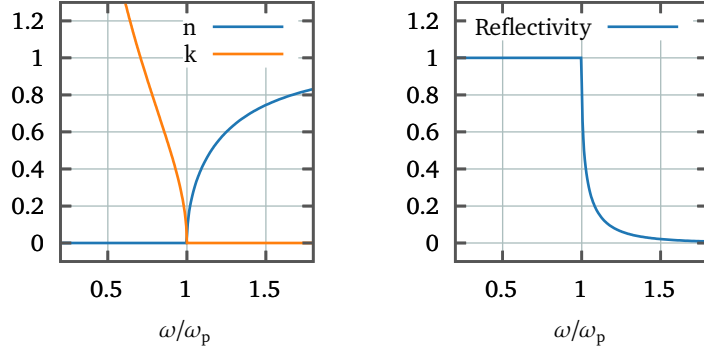
Oscillations of the electron gas at the resonance frequency ω_p can be seen as plasma oscillations, which can be quantized. The associated bosonic quasi-particle is called plasmon [293]. Plasmons inside a bulk material can be measured using electron energy loss spectroscopy (EELS), where the electrons can scatter inelastically and excite a plasmon. Plasmons also exist as surface plasmons, where light can be coupled for example in an attenuated total reflection configuration [413]. These are called "propagating surface plasmon polaritons" [390]. In AuNPs, the plasmon can not propagate. Thus, they are sometimes called "localized surface plasmon". Since the particles are much smaller than the wavelength of the incoming light, the displacement of the electrons against the nuclei can be considered coherent, which is called the quasistatic approximation [390]. Together with the restoring force of the positively charged lattice, this creates a system similar to an harmonic oscillator, which is driven by the external light field. Figure 8.3 visualizes the bulk and surface plasmons as well as their excitation.

An analytic way to calculate the optical properties of AuNPs is the so-called Mie-theory [389], published over 100 years ago. It solves the Maxwell equations for a spherical particle by a multipole expansion of the electromagnetic fields. A full derivation can, e.g., be found in [390]. Using the Mie theory, it is easy to show how the optical spectra change for example due to variations in size (Figure 8.4) or the dielectric surrounding. Alternatively, numerical methods as for example finite-elements methods can also be used to calculate more complex shapes or interactions between particles.
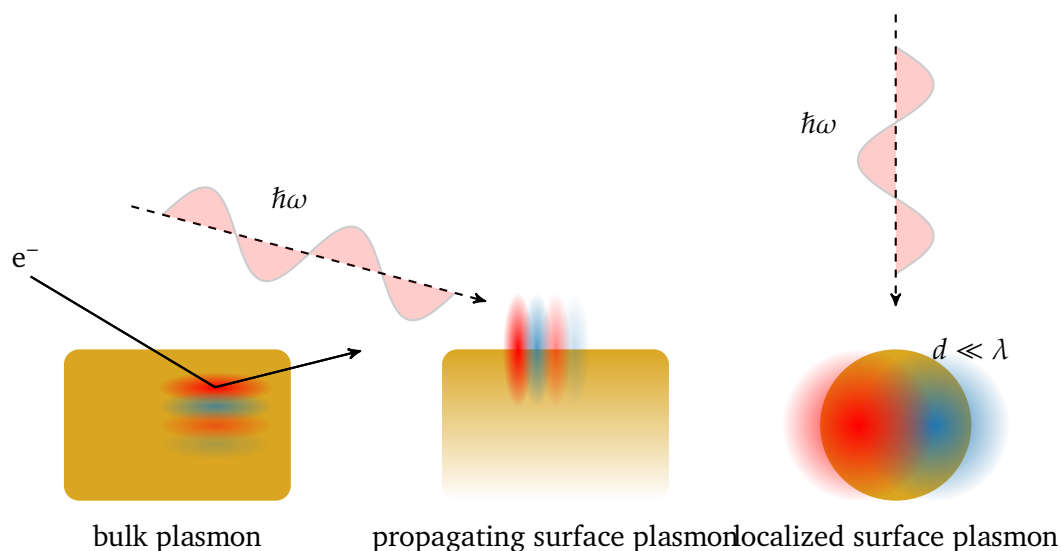
Figure 8.3: Schematic depiction of bulk, surface and localized plasmons. The bulk plasmon is a electron density oscillation inside a gold bulk, which can be probed by EELS. The propagating surface plasmon can be excited with visible light under the right conditions (e.g. using an attenuated total reflection geometry or a grating) on a metal/dielectric interface, such as a gold surface. The excitation of localized surface plasmons can be easily achieved in metal particles with a size smaller than the incident wavelength.

This also makes it clear why AuNP are so appealing for sensor applications: The plasmon is depending sensitively on changes of its local environment, as for example the dielectric constant. This allows for an optical readout of changes of the chemical environment. Also, if another AuNP is close by, the electric fields of the plasmons start to interact, which can lead to a spectral shift of the plasmon or the appearance of additional resonances. The resulting optical changes are highly sensitive to the distance between the particles [414]. The electric field is highly concentrated in the area between the particles, creating a so-called "hotspot" with strong coupling between the plasmon and the incident light [415–418]. This leads to a variety of interesting phenomena, for example just recently, ultra strong light matter coupling could be shown for AuNP films with particle sizes ranging from 30 to 40 nm [419, 420]. AuNP can also be used to build plasmonic wave guides, where light is squeezed into subwavelength dimensions and integrated into photonic circuits [399, 401, 424–426]. Apart from basic research, these unique optical properties are also interesting for applications, since strong fields give rise to an enhancement of Raman signals, which is called surface enhanced Raman spectroscopy (SERS). This can be used to perform measurements on the vibrational footprint of individual molecules or obtain high sensitivities [407, 427–429].
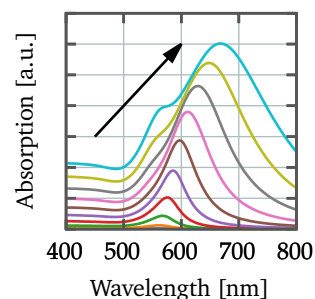
Figure 8.4: Size dependency of the absorption spectra of AuNP as obtained using the Mie theory. The arrow denotes the increasing size of the particles, from 10 nm up to 100 nm. The spectra were obtained using the PyMie-eScatt library [421, 422], as the refractive index of gold data set from Johnson & Christy was used [423]. The refractive index of water as a solvent was set to 1.33 + 0i.

8.1.2 Transport Properties

Aside from their optical properties, AuNP are studied as elements of electronic devices. There, it is crucial to consider the influence of the ligand shell. This shell can create an isolating layer around the AuNP, which electrons have to pass through by tunneling mechanisms.

The electron transport through a AuNP is usually governed by the Coulomb blockade (see Chapter 2): An electron tunnels on a AuNP and charges it. Adding additional electrons on that particle can only be done, if the applied potential gives enough energy to overcome the Coulomb repulsion. Numerous realizations have been published in the last years [199, 430–435], including experiments where fundamental logical operations could be performed: Maeda *et al.* could show that in a device with a source, a drain and two gate electrodes, the output current could be controlled by the voltage of the two gate electrodes (Figure 8.5) [200]. With such a device, XOR or NXOR logic operations could be performed with a single particle. In current electronic circuits, an XOR operation requires several transistors.

Such realizations can be promising candidates for future electronics, but it is still very complicated to integrate an AuNP into a device in a controlled manner. A different approach can be to incorporate AuNPs not as a single particle, but as a film, monolayer or aggregate[21]. This is used to study the basic transport properties of such assemblies, to build sensors or enable printable electronics [116, 397, 436–444]. In such mono- or multilayers, the role of the ligand becomes much more important. By changing for example the length of the ligands, the coupling and transport between two adjacent particles can be precisely controlled. Several studies showed the dependency of the electron transport through such AuNP films on the length of the capping ligands [445, 446] or the electronic structure [117]. Thus, AuNP films with molecular linkers have also been subject to studies of the MIT [447–451]. Depending on the coupling between the particles mediated by the distance [452–456], the size of the particles [457] or type of the molecule [458, 459], AuNP films can be tuned from (classically) isolating to metallic.

To present an example, van der Molen *et al.* demonstrated in 2009 that they could switch the conductance of AuNP films by illumination [127]. They introduced a photochromic diarylethene into the layer, which upon UV illumination could switch to a conjugated form and be switched back using visible light (Figure 8.6). This

Figure 8.5: Logical operations with a single AuNP. Depending on the voltage of the two gate electrodes, the current through the particle could be controlled [200]. Reprinted with permission from Maeda, K. *et al.* Logic Operations of Chemically Assembled Single-Electron Transistor. *ACS Nano* **6**, 2798–2803 (Mar. 2012). Copyright 2012 American Chemical Society.

[21] This is quite similar to the discussion in the field of molecular electronics regarding single-electron or ensemble experiments, see Chapter 2.

demonstrates how the conductivity of a AuNP film can be tuned
and influenced using the molecular linkers between the particles.
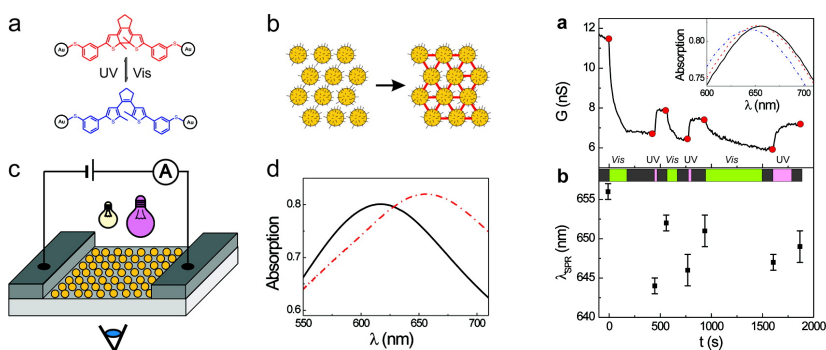
Figure 8.6: Optically switchable transport in AuNP films. Depending on the optical excitation, the molecular switch between the particles can be closed or openend, which changes the optical and electronical properties [127]. Reprinted with permission from van der Molen, S. J. *et al.* Light-Controlled Conductance Switching of Ordered Metal-Molecule-Metal Devices. *Nano Letters* **9,** 76–80 (Jan. 2009). Copyright 2009 American Chemical Society.

The transport properties through AuNP can interact with the optical excitation of the particles. Thus, optoelectronics are of huge interest, since they enable a link between between photonics/plasmonics and electronics and open the way to photonic circuits or sensor applications [460]. Mangold *et al.* demonstrated a bolometric enhancement of the current through AuNP films with alkane linkers [411]. Plasmon induced or enhanced conduction in disordered AuNP linked by prophyrin linkers was shown in [128]. A similar study attributed the increase of the current to the extraction of plasmon-induced hot electrons [461] or showed the plasmon-induced electron transfer through molecules [462]. Resonant photoconductance due to the excitation of the linking molecule was shown for oligo-phenylene-vinylene (OPV) linkers [412] and also discussed theoretically [463, 464]. The aforementioned review by Liao *et al.* discusses additional results and findings [129].

The variety of applications and studies on AuNPs or AuNP films demonstrate that they can be regarded as a general and flexible platform to study basic science, molecular electronics or plasmonics. But to study the transport properties of AuNP or prepared films, the problem of introducing proper electronic contacts has always to be overcome. Therefore, establishing THz spectroscopy as a contactless approach to study transport properties in such systems can pave the way for more possibilities or studies. Especially concerning optoelectronics this is highly interesting, since short-lived timescales of optically excited carriers can be accessed.

8.1.3 Synthesis Techniques

Particle Synthesis

Citrate-stabilized AuNP were used as the starting material for all further experiments. A general discussion regarding synthesis can be found in Daniel & Astruc [96]. The particles used here were obtained using a protocol based on the Turkevich synthesis [391, 465, 466]. The resulting particles are stabilized by citrate in aqueous solution, which can be easily exchanged since they bind only by weak electrostatic interactions. The protocol presented by Schulz *et al.* uses the inverse approach (thus injecting the Au precursor into the hot citrate solution rather than heating the gold precursor solution and adding the citrate agent) and was able to decrease the standard deviation of the particles size below 8% and the reproducibility concerning the size below 3%. This protocol is routinely used to prepare particles for subsequent experiments or reactions in our group, like ligand exchange, phase transfer or seeded growth.

The AuNPs are obtained by a reduction of Tetrachloroauric(III)acid by a citrate buffer (Trisodium citrate dihydrate / citric acid) in the presence of EDTA (ethylenediaminetetraacetate). The reduction of the Tetrachloroauric(III)acid yields the nuclei, which grow to AuNP.

$$C_6H_5O_7^{3-} \rightarrow C_5H_4O_5^{2-} + CO_2 + 2e^- + H^+ \tag{8.11}$$

$$AuCl_4^- \xrightarrow[-4Cl^-]{+3e^-} Au^0 \xrightarrow{\text{particle growth}} AuNP \tag{8.12}$$
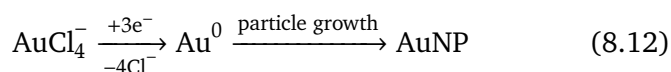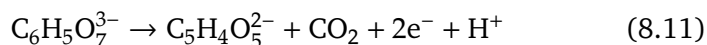
A very elegant aspect for this reaction is that the reducing agent also acts as a stabilizing ligand for the obtained AuNPs. The reaction can be performed with relatively high volumes ($\sim 1\,\text{L}$) and yields concentrations of 3 to 5 nM [466].

Functionalization, Ligand Exchange and Phase Transfer

Functionalization of the AuNP usually involves a ligand exchange reaction. Different binding motives and ligands have been reported, and a multitude can be used: Starting from weak binding of citrate due to electrostatic interactions, via amines, phosphines up to thiols or other ligands including sulfur atoms like dithiocarbamates which can build strong covalent bonds to gold [403, 467].

Especially thiols have been established as robust ligands due to the strength of covalent thiolate-gold bond of around 1.735 to 2.168 eV [468]. The exact binding geometry is not easily to determine, since different bonding motifs exist or a reconstruction of the surface can occur [468–473]. And the thiol-gold bond still continues to surprise: In 2019, Inkpen *et al.* reported physisorbed gold-thiol bonds for connections formed on air, not in solution [474].

New ligands can introduce functionalities, improve the stability of the particles or enables further chemical reactions like cross-linking a polymer shell around the particle or connecting two particles. Also, this can be used to transfer the particles from one phase to another, since the solubility of the particles is mainly determined by the endgroup of the ligands. As already mentioned, the transport properties of prepared films are highly dependent on the nature of the ligand shells [402].

To enable further reactions using ligands which are soluble in organic/unpolar solvents, the AuNPs have to be transferred in the organic phase. The protocol applied here is based on previous work [475, 476], was first applied and published by us in [112] and further improved in [477]. Transferring the AuNPs from the aqueous to an organic phase enables further reactions with molecules which are not solvable in water, for example the aromatic linkers used in this work.
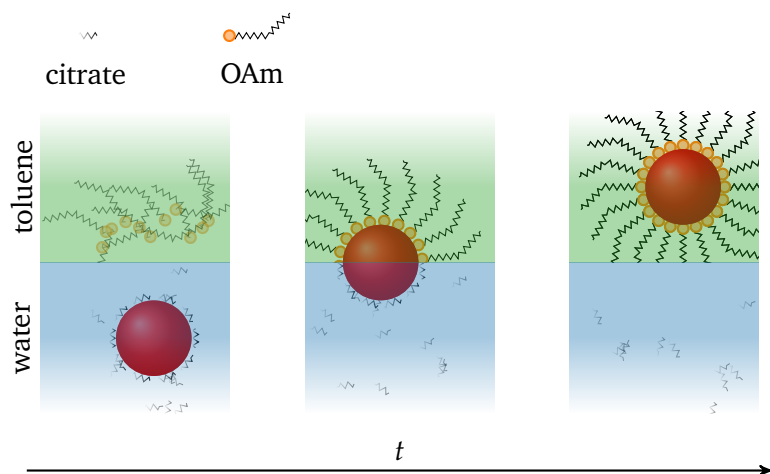
Figure 8.7: Schematic depiction of phase transfer and ligand exchange of citrate-stabilized particles to toluene, accompanied by ligand exchange of citrate with OAm.

Figure 8.7 shows the general scheme of the phase transfer. First, the particles are stabilized by citrate in the aqueous solution. OAm is not soluble in water, but in toluene, the organic phase. At the solvent-solvent interface, however, ligand exchange can take place. This will transfer the particle slowly into the organic phase, replacing the citrate ligand layer with an OAm layer. The reverse reaction is not probable, since the binding of OAm amine groups

is stronger than that of the citrates' carboxylic acids groups. By adding, e.g., ethanol as a phase transfer agent, the reaction yield can be improved since it can act as a cosolvent [477–479].

Film Preparation Techniques

To build films using AuNP, several techniques exists. Numerous efforts have been carried out to present ways to prepare ordered or unordered films on different substrates, using differently sized particles and different kinds of ligands or linkers [95, 401]. Roughly, one can distinguish between two different approaches, even though they are not strictly differentiated. On the one hand, strategies employing self-assembly techniques are used. Usually, this involves slow reaction or evaporation rates, so that order can be established. Examples are the forming of ordered films on liquid-gas or liquid-liquid interfaces, where the solvent slowly evaporates, thus increasing the concentration of particles and forcing them to use the remaining space efficiently, which results in a crystalline structure [397–400, 472, 477, 480–489]. On the other hand, films can be prepared by using chemical reactions, which link particles together. Since this usually happens on relatively fast timescales and the bond prevents further reorientation, these films do not show the same order as the self-assembled ones (but can as in Ref. [490]). These techniques usually use spin-coating or layer-by-layer (LBL) methods, where in an alternating fashion molecular linker and AuNP are bound to a substrate [25, 454, 491–495]. These techniques have the advantage of being able to build films of arbitrary thickness and linker molecules. LBL in combination with spin-coating have been used to build AuNP films which have been utilized as sensor for gases, pressure or strain [440, 442, 496–499]. The molecular linkers, often dithiols, were used for the stable connection of the particles but also to tune the conductivity, either by their length or electronic structure.

An extensive summary over obtained conductivities for films of AuNP (and other particles) prepared by different methods (as the ones mentioned above) and linkers can be found in Ref. [116]. To mention a few examples, the conductivity of films prepared by Liao *et al.* could be reversibly changed by the use of either an thiolated oligo(phenylene ethynylene) (OPE) linker or an 1-octanethiol ligand, which gave sheet resistances in the range of $1 \times 10^7 \, \Omega$ to $1 \times 10^8 \, \Omega$ for the OPE linker and $1 \times 10^9 \, \Omega$ to $1 \times 10^{11} \, \Omega$ for the aliphatic ligand [129]. In Ref. [437], AuNP ($d \simeq 4 \, \text{nm}$) films were prepared by a layer-by-layer
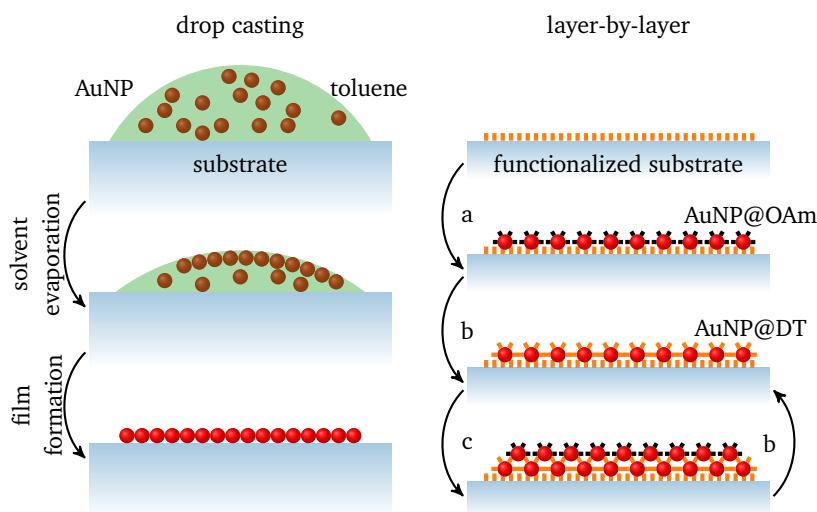
Figure 8.8: Schematic depiction of drop casting (left) and layer-by-layer preparation (right) of AuNP films. *Dropcasting:* A solution of AuNP in toluene is dropped on a substrate. The solvent evaporates, increasing the concentration of the particles until an ordered film is formed. *Layer-by-layer:* AuNP@OAm solution is placed on a functionalized substrate, so that the particles are chemically connected to the substrate (a). Ligand solution with a dithiol (DT) is added, replacing the OAm ligand of the particles (b). Afterwards, the next batch of particles can be added, which are again chemically connected to the previous particle layer (c). Steps b and c are repeated to obtain the desired film thickness.

method with various alkanedithiols, yielding conductivities of $3.73 \times 10^{-2}\,\mathrm{S\,cm^{-1}}$ for hexanedithiol up to $4.81 \times 10^{-5}\,\mathrm{S\,cm^{-1}}$ for hexadecanedithiol at room temperature. In Ref. [500], for particle films with 1,12-dodecanedithiol and TER, conductivities of $7.7 \times 10^{-4}\,\mathrm{S\,cm^{-1}}$ and $6.9 \times 10^{-3}\,\mathrm{S\,cm^{-1}}$ were found.

8.2 Gold Nanoparticle Films Prepared using Drop Casting Methods

The initial ligand transfer to the organic phase and drop casting of our particles into hexagonal closed–packed films was first reported in [112]. The good controllability was later refined and improved to obtain large area coverage [477]. Samples prepared with this technique enabled, e.g., the investigation of collective plasmon properties, known as dark plasmons [419, 420]. The problem with this approach is to link the particles using molecular linkers. This can be done by adding linker solution to the drop casted films, but this also can resolve the film.

An additional approach used here was to place a container on the substrate, which limits the spread of the solution as shown in

Figure 8.9. Thus, the linkers can be added to the AuNP solution and react with the particles while drying. A disadvantage of this approach can be that particles can stick to the container and will not be deposited homogeneously on the substrate due to capillary forces at the edges between the container and the substrate.
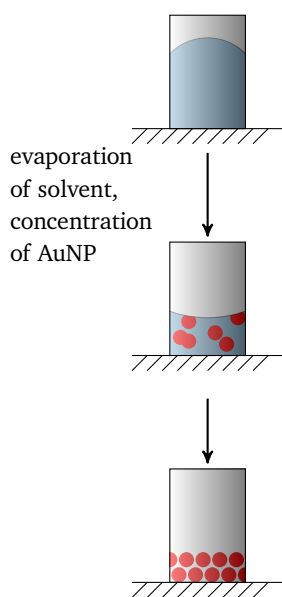
For both approaches, introduction of linker molecules is expected to reduce order in the films, since the chemical bonding can fix a particle at a certain space and limits further rearrangements to optimize the space filling and thus the crystalline structure.

8.2.1 Methods

Direct Drop Cast

Samples using drop cast techniques are prepared by cleaning the substrates with MQ, ethanol and toluene. A drop of a chosen volume of the particle solution is placed on the substrate using an Eppendorf pipette. If the evaporation of the solvent should be slowed down, the samples were placed in a container together with a small flask containing toluene to create a saturated toluene atmosphere.

Drop Cast with Container

The samples were prepared by filling AuNP solution inside the container with a PTFE chip as substrate, with or without additional ligand solution. As a container, cut pipette tips were used, which were pressed on the PTFE substrate ($\varnothing \simeq 7\,\text{mm}$). In the experiments presented here, just TER in toluene as a linker solution was used, except for one test where NON in toluene was tested. Usually, the container was filled only once. In some experiments, particle or ligand solution was added multiple times to build up thicker films.

Table 8.1 gives an overview over the samples which have been prepared using just AuNP@OAm in toluene as particle solution without any additional linkers. As shown in the table, three different concentrations and various volumes have been used. Table 8.2 shows the volumes and concentrations of samples prepared using AuNP@OAm with TER linker solution (and one sample with NON linker solution).

evaporation of solvent, concentration of AuNP

Figure 8.9: Restricted drop casting using a small container.

Sample	AuNP@OAm solution	
	Volume [µL]	Concentration [nmol L^{-1}]
A101	40	27.7
A102	80	27.7
A103	120	27.7
A104	160	27.7
A105	2×80	27.7
A106	4×80	27.7
A107	120	27.7
A108	20	145.6
A109	2×20	145.6
A110	10	145.6
A111	20	145.6
A112	40	145.6
A113	50	26.7
	+ 70	26.7
	$+ 3 \times 100$	26.7

Table 8.1: Overview of sample names and added AuNP solution for the films prepared without any linker molecules.

Sample	AuNP@OAm solution		TER solution	
	Volume [µL]	Concentration [nmol L^{-1}]	Volume [µL]	Concentration [nmol L^{-1}]
A201	80	145.6	10	1
A202	80	27.7	20	1
A203	160	27.7	20	1
A204	160	27.7	20	1
A205	80	27.7	1	1
A206	80	27.7	1	1
A207	120	27.7	20	0.1
A208	120	27.7	20	0.1
A209	2×20	145.6	10	0.1
A210	20	145.6	6	0.1
A211	20	145.6	6	1
A112	50	26.7	5	0.1
	+ 70	26.7	5	0.1
	$+ 3 \times 100$	26.7	5	0.1
			NON solution	
A301	50	26.7	5	0.1
	+ 70	26.7	5	0.1
	$+ 3 \times 100$	26.7	5	0.1

Table 8.2: Overview of sample names and added amounts of particle and linker (*p*-terphenyl-4,4″-dithiol (TER) and nonane-1,9-dithiol (NON)) solution for the preparation of linked particle films.

Terahertz Time-Domain Spectroscopy

All samples were investigated in our home-build THz spectrometer. For each measurement of a sample, measurements of air and a PTFE substrate as a reference were performed. All measurements were done under a continuous nitrogen flow to get rid of any absorption lines due to water vapor. Each measurement was repeated several times. The scanning range, time steps and integration time per data point was varied. Data processing and extraction was performed using DuoDecim as described in Chapter 6.

As a statistical tool to identify and filter out measurements with spikes or high noise, the Jackknife resampling method has been used. A short summary can be found in the appendix (Section D). Basically, the Jackknife method checks each measurement for its influence on the average and standard deviation of all measurements. A measurement with noise increases the standard deviation of the whole set, so by leaving it out, the standard deviation is decreased.

8.2.2 Results and Discussion

Drop Cast with Container

Figure 8.10: Pictures of the samples A104 and A106 prepared using PTFE chips as substrates.
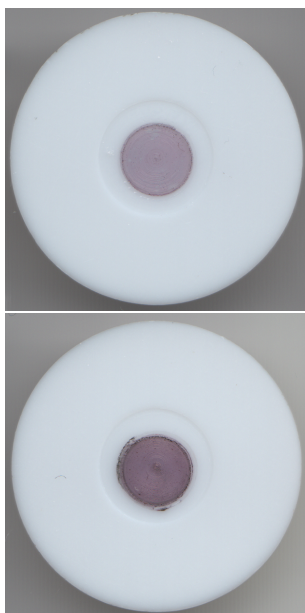
The dried particles formed films on the PTFE substrates (for exemplary pictures see Figure 8.10). Depending on the concentration, the film had either a reddish color or already a golden appearance (samples A108 - A212), which indicates the formation of a thick AuNP layer. At the edge of the tube, irregularities or coffee rings could be observed.

Terahertz Time-Domain Spectroscopy

Since a lot of measurements using the THz -TDS setup have been performed on all samples, not every measurement will be discussed in detail here. Thus, a statistical analysis is given first, identifying samples of interest. A simple visual inspection of the time-domain signals is not possible here, since the differences between reference and sample measurements are very small. Therefore, the mean absolute error (MAE) of the complex spectra is used to calculate the distance between the spectrum of a reference or substrate measurement and the spectrum of a sample.

Afterwards, some chosen samples will be discussed in detail. Additionally, drop casted samples of AuNP with a slightly bigger size of 45 nm will be discussed.

Statistical analysis

In a single measurement session, usually several traces of the THz pulse of a reference and several samples are recorded alternatingly. This is done to be able to compensate for slow drifts in the laser power, since this is affecting the reference and sample measurements equally. If first just the reference is measured several times and afterwards the sample, a different signal for the sample could be obtained due to slow changes of e.g. the laser, which generates the THz pulse [305].

For each single measurement of a session, the complex spectra are calculated using the `python3-numpy` library[22]. Measurements, for which the Jackknife resampling analysis showed a deviation higher than 5% of the total standard deviation, are left out of the following analysis. For each cycle, the MAE[23] of the magnitude and phase between two samples (or sample and reference) is calculated and summed up over the frequency domain from 0.1 to 2.5 THz. Even though usually associated with the calculation of error, the MAE gives in fact a cumulative distance between two curves, which can also be used to measure how similar or close those curves are. Thus, a samples measurement can be compared to the corresponding reference measurement, which is in this case a PTFE chip. The term "cumulative" is used here to refer to the summation over the given frequency range.

Another idea of analyzing the THz measurements statistically would be not to look at the MAE of the spectra, but for example at the correlation of the signals in the time-domain. But this has the drawback that shifts and attenuation are not similarly included, since also an attenuated THz pulse can correlate perfectly with the original one. In Figure 8.11, the frequency-accumulated MAE for the magnitude and the phase of the spectra is given.

For most of the samples, the MAE and thus the distance between complex spectrum of a sample and a measurement of a clean PTFE chip is low. To put these numbers into context, in Table 8.3 the cumulative MAEs are given for shifted or attenuated beams obtained by modified a reference/substrate measurement. This shows, that a shift mostly induces an error into the phase, while an attenuation enters the MAE of the magnitude of the transfer function more strongly.

[22] The polar representation used here of complex numbers $c = Ae^{i\phi}$ is much more useful in terms of analyzing the spectra, since the magnitude and phase directly translate to physical properties. Also, errors or problems concerning the phase unwrapping can not be identified with the Cartesian representation ($c = a + bi$).

[23] The MAE is chosen over the root-mean-square error (RMSE) since the latter has stronger penalty on bigger differences, and here the focus is more on small differences.
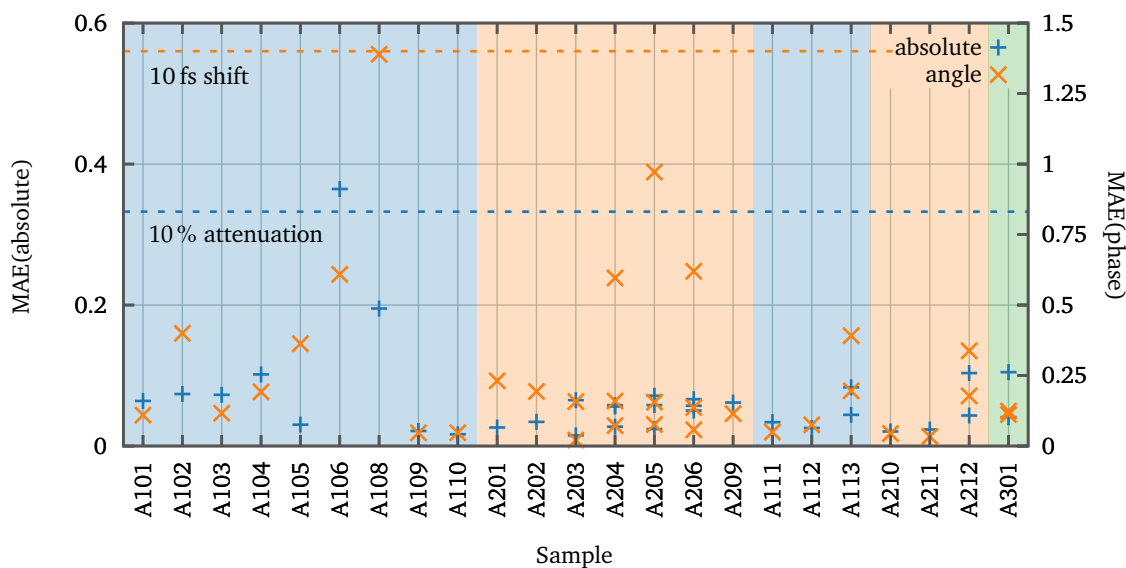
Figure 8.11: Overview of the MAE of the magnitude/absolute and the phase/angle of the spectra for the samples prepared by drop casting. The blue shaded areas include samples which are prepared without any linkers. The orange shaded part includes samples prepared using TER, while the greenish area is a sample prepared with NON. The dashed lines show the calculated MAE for exemplary pulses (see Table 8.3). Multiple points per sample are obtained from measurements which have been performed at a different day.

Table 8.3: Cumulative MAEs for artificial modifications of a THz pulse.

modification	MAE(magnitude)	MAE(phase)
1 % attenuation	0.0334	0.0213
10 % attenuation	0.3325	0.2107
10 fs shift	0.0035	0.1466
100 fs shift	0.0062	1.4000

Sample A106 and A108 show the highest MAE of all samples. A106 was mistakenly prepared using a PTFE chip with a different thickness, thus lacking a corresponding reference measurement which leads to the high MAE.

For a further analysis, Sample A110, A108 and A206 have been chosen. Sample A113, A212 and A301 will also be discussed. These were relatively thick samples prepared the same way using OAm, TER and NON as ligands, enabling a direct comparison. Additionally, a sample prepared by drop casted 45 nm sized AuNPs will be investigated.

A110

The sample A110 has been prepared by adding 10 μL to the container (as depicted in Figure 8.9). Due to the low volume, this resembles a standard drop cast preparation without any constraints of the drop size. The obtained film appeared violet or golden/metallic, depending on the angle of view.

26 measurements have been performed for each sample in an alternating fashion as mentioned earlier. In Figure 8.12 a), the averages of all 26 measurements for a measurements of air, the substrate (PTFE) and AuNP on PTFE (sample A110) are shown. A Jackknife analysis unveils some measurements with higher noise (Figure 8.12 b)). A closer look showed the occurrence of spikes in these measurements.
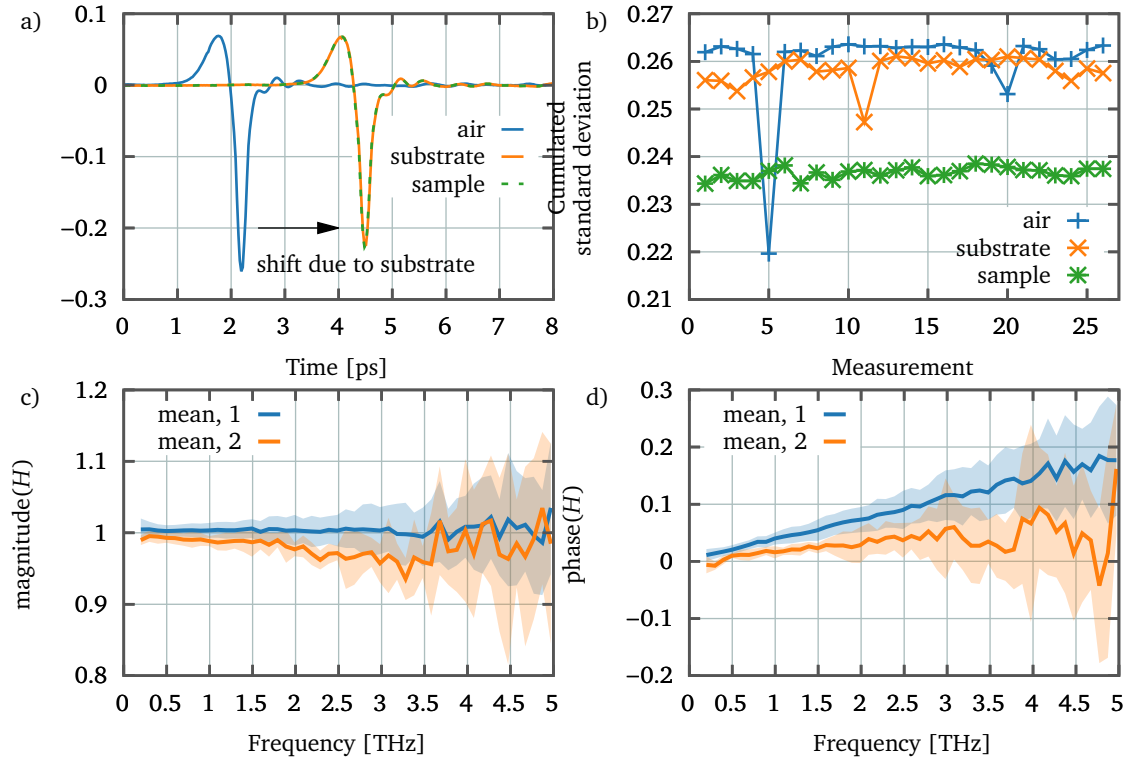
Figure 8.12: a) Measured THz pulses for transmission through air, the substrate (PTFE chip) and the sample (AuNP on PTFE chip, sample A110). Here, the average over 26 measurements taken on a single day in a row is shown. b) Cumulated/summed standard deviation for all measurements with iteratively leaving out one measurement. This gives a hint in which measurement the noise was increased/spikes occurred. c)/d) Obtained magnitude (abs(H)) and phase (ang(H)) of the transfer function, shown for measurements of two consecutive days. The magnitude of the transfer function is nearly one, indicating no absorptive losses in the sample. The phase shows a light slope. This can be referred to a phase shift induced by the AuNP film, but also can be caused by thickness variations. It can also be seen, that the noise is increasing with the frequency, since the power is strongly decreased for frequencies above 2.5 THz In c) and d) the average of the transfer functions obtained in a second set of measurements on another day are shown in red.

The pulse shapes of the reference and sample measurement in Figure 8.12 a) appear to be nearly equal, thus do not allow any conclusion about an influence of the AuNP film on the THz propagation.

In a next step, the transfer functions for the sample can be calculated as described in Chapter 6: For each measurement of substrate and sample, the spectra are calculated, divided and the obtained polar representation (absolute and phase) of the transfer

function is shown in Figure 8.12 c) and d). Measurements showing outliers in the jackknife analysis were left out of the analysis. The data shown here is the average of the sets of measurements performed at two different days. The shaded areas denote the standard deviation.

For the magnitude as well as the phase the standard deviation is increasing with frequency, since the signal-to-noise ratio becomes small at frequencies above 2.5 THz. As can be clearly seen in the transfer function, there is nearly notable absorption in the sample, since the magnitude of the transfer function is flat and nearly equal to 1. The phase shows a slight slope, but this can also be due to thickness variations of the substrate. No data extraction using the Tinkham approximation or the numeric approach is shown here due to the lack of absorption.

This leads to the conclusion, that this particle film is transparent for THz radiation. Any dispersive influence can not be safely determined, since the slight slope observed in the phase was not reproducible and can be caused by various reasons, for example substrate thickness variations.

A108

The statistical analysis of sample A108 (Figure 8.11) shows a relatively high MAE for the magnitude as well as the phase of the transfer function. Figure 8.13 displays the average transfer function (magnitude and phase) as well as the standard deviations (shaded areas). Measurements with a Jackknife deviation of more than 1% were left out of the analysis. The result resembles the results obtained for the sample before: The magnitude is relatively flat and equals to one, which indicates no absorption in the film. The phase slope is in the same range as the sample discussed before and is still below the phase slope induced by a 10 fs shift of the THz pulse.

Figure 8.13: Mean (solid line) and standard deviation (shaded area) for the transfer function obtained for A108. Samples, for which the Jackknife analysis yielded a deviation higher 1% were left out of the analysis.
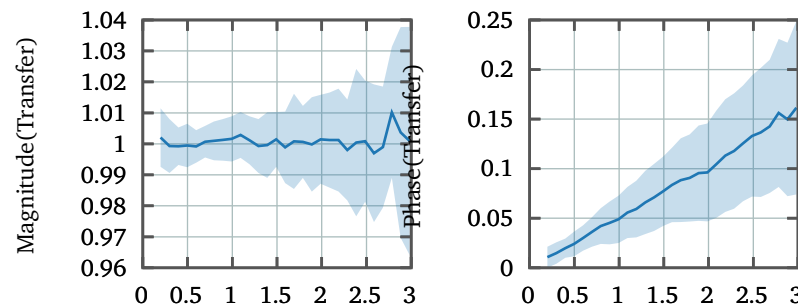
The high MAE shown before can not be reproduced with this analysis. It is most likely that the measurements which have been sorted out by the more strict Jackknife analysis applied here are

responsible for the higher MAE. This could be confirmed with an inspection of the individual THz time traces, which showed spikes for those measurements, which have been sorted out.

A206

Sample A206 was obtained by adding $80\,\mu\text{L}$ of OAm-AuNP in toluene $(27.7\,\text{nmol}\,\text{L}^{-1})$ and $1\,\mu\text{L}$ TER in toluene solution $(1\,\text{nmol}\,\text{L}^{-1})$ to the container. After drying, the film had a violet, nearly black color with a visible metallic radiance when looked at in the right angle.

Measurements have been performed on three different occasions. On each occasion, 20 traces of the THz pulses have been recorded. As before, the transfer function is calculated for each pair of substrate/sample measurements. From these individual transfer functions the mean and the standard deviations for the magnitude and the phase are obtained and shown in Figure (8.14).
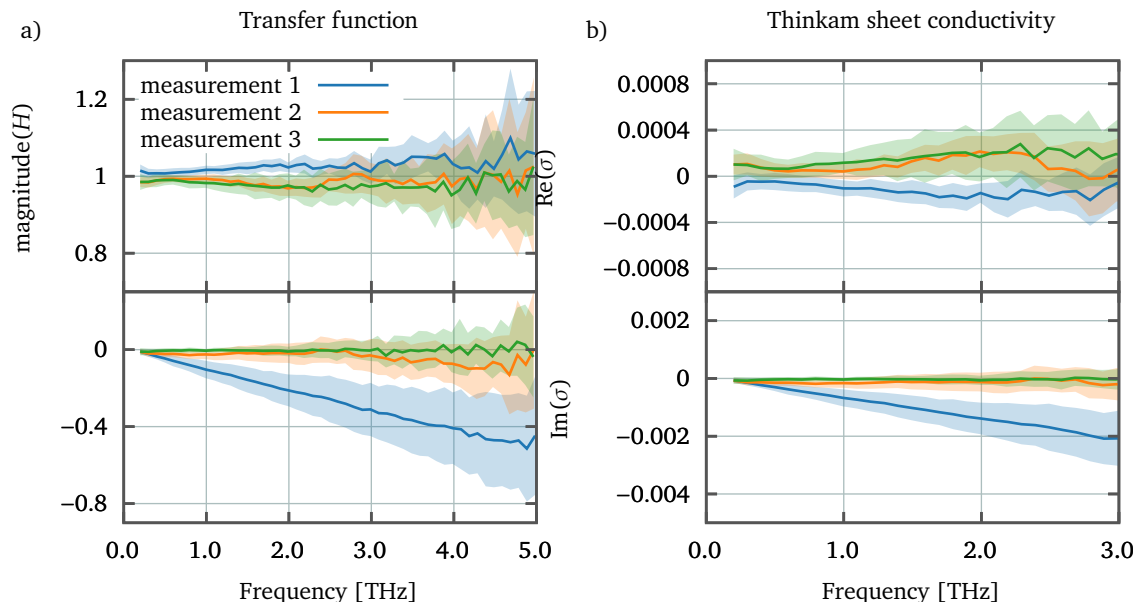
Figure 8.14: Obtained transfer functions for sample A206, from measurements of three consecutive days. The magnitude of the transfer function show a flat response. The phase shows a negative slope for the first measurements, which vanishes for the other measurements. The shaded areas denote the standard deviation (or 1σ interval).

Similarly to the sample studied before, the magnitude of the transfer function indicates no notable absorption. The phase shows a small negative slope for the first set of measurements, which becomes nearly negligible for the measurements which have been performed on following days.

Here, exemplary Tinkham sheet conductivities (see Equation (6.32)) have been extracted using DuoDecim. Since there

is no absorption visible in transfer function, the real conductivity is zero. This is also true for the imaginary part, except for one measurement with the slight slope.

Similar to the sample studied before, the AuNP film apparently does not interact with the THz beam at all, but is completely transparent.

A113, A212, A301

These samples were prepared in the same way, using a total volume of 420 µL of 26.7 nM AuNP@OAm solution. A113 was prepared without the addition of linkers, to A212 in total 15 µL of 0.1 nM TER solution was added. The same amount of NON linker solution was added to A301. The transfer functions obtained for 40 scans per sample are shown in Figure 8.15
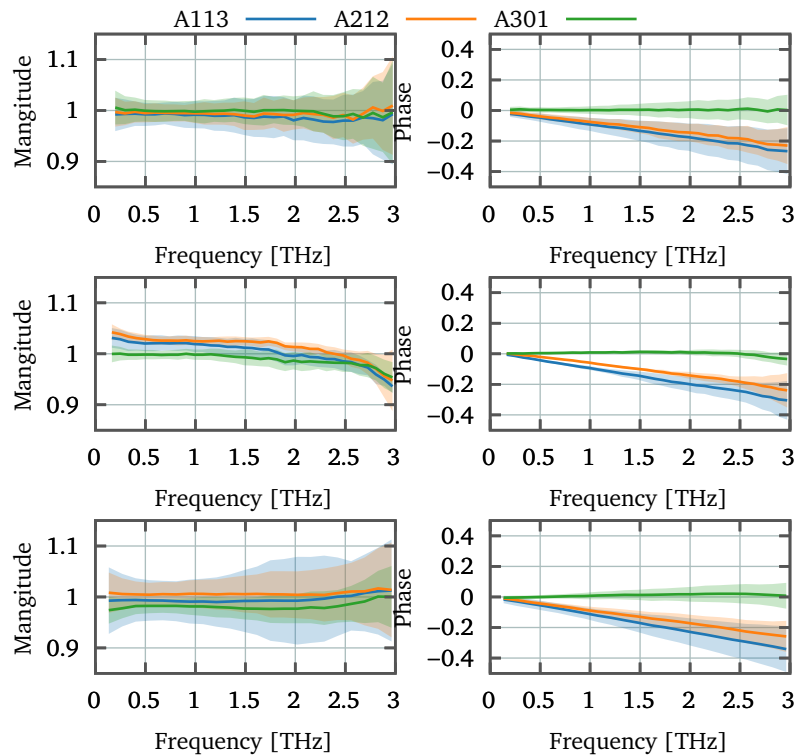
Figure 8.15: Magnitude (left) and phase (right) of the transfer functions for the samples A113, A212 and A301. Data is shown for three repetitions of the measurements. The solid lines represent the averages, the shaded areas the standard deviations.

Similar to previous results, the phase of the transfer function shows a slope for the samples A113 and A212, but not for the sample A301. The magnitude is one and depending on the measurement, the differences between the samples are within their 1σ interval. Thus, no absorption of the samples can be found, which would lead to the real part of the conductivity going to zero. The slope of the phase implies a capacitive response of the particles, but not for the samples with the NON linker. But as mentioned earlier, even though the measurements show a signal with the 1σ
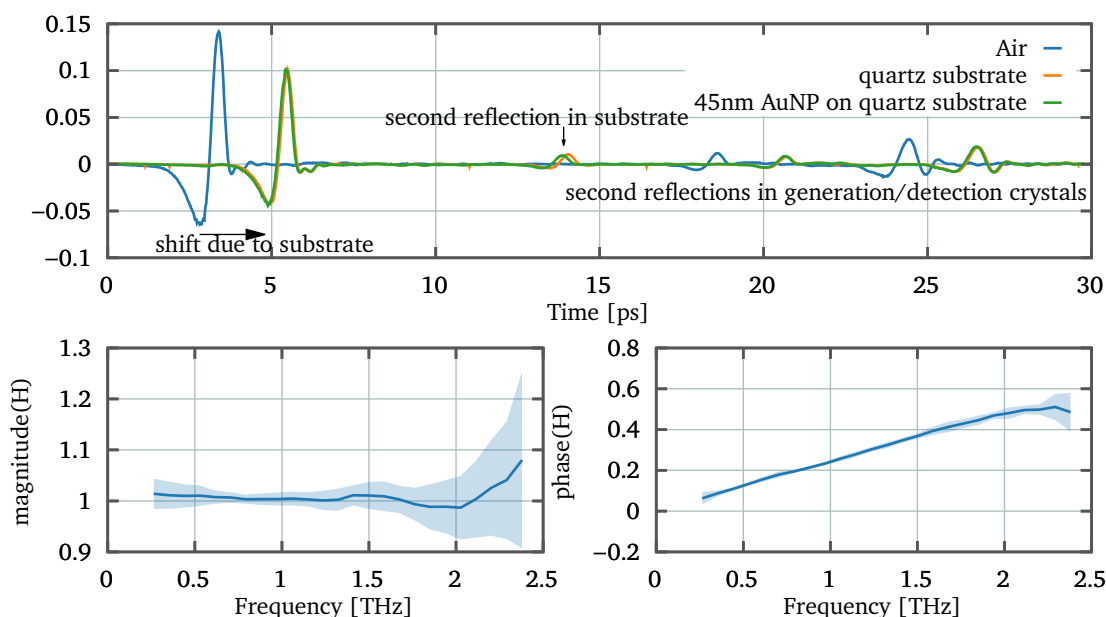
Figure 8.16: Recorded electric fields for a measurement without any sample, a quartz substrate and a quartz substrate with 45 nm-sized AuNP drop casted onto. The refractive index of the substrate causes a noticeable shift of the THz pulse. The small shift between the sample with and without AuNP (more clearly visible for the second reflection) can be due to variations of the substrates thickness.

confidence interval, these changes can not be safely distinguished from influences of substrate thickness variations.

45 nm AuNP

Aside from the 12 nm particles used here, bigger particles have been studied to check whether THz absorption can be achieved. The particles were obtained from Florian Schulz and were prepared by a seeded growth protocol. 10 μL were drop casted on a quartz substrate and measured together with a quartz substrate as a reference and a measurement of air. The obtained electric fields are shown in Figure 8.16 a).

Same as before, there is no absorption visible in the transfer function. The nonzero phase/angle can also be seen in the THz time traces, since there is a slight shift of the samples to earlier times with respect to the reference. This is clearly to identify, when looking at the second reflection in the substrate. This shift can be explained with variations of the substrate thickness.

Summary

Summarizing the results, the drop casted particle films seem to be totally transparent in the THz regime. For every measurement, the magnitude of the transfer function is flat and equal to one, which indicates no absorptive losses. The phase usually shows a slight slope, usually negative. But this signal is too small to be

trusted and to be used as a starting point for further data extraction: For the same sample, the phase changed for measurements performed on subsequent days, e.g. from a negative slope to a slop of almost zero. Also, when compared to the signal by simply shifting the THz pulse by 10 fs (which corresponds roughly to a change of the thickness of 2 µm), all signals in the phase domain are much weaker. The correct thickness of all samples could not be easily obtained. One way to obtain correct thicknesses would be more advanced theoretical approaches as shown e.g. in Ref. [358], but it is unlikely that any signatures of the particles can be obtained, since this only corrects the phase, but doesn't change the lack of absorption features in the magnitude of the transfer functions.
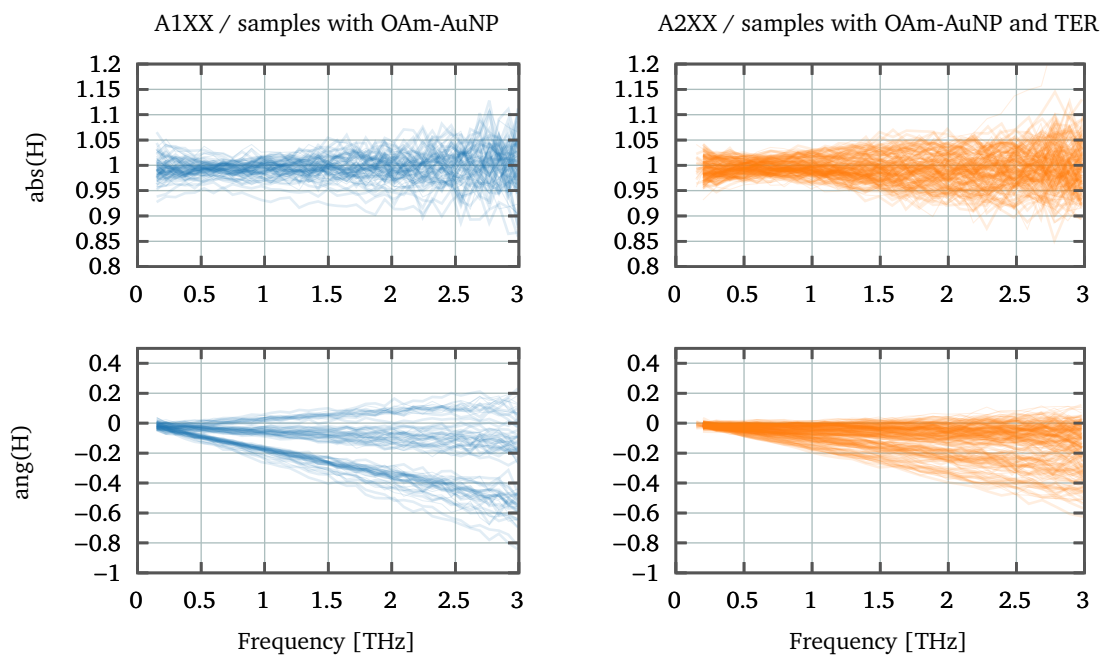
Figure 8.17: Transfer functions for over 2000 measurements on samples without (left) and with (right) molecular linkers.

Figure 8.17 illustrates again the drawn conclusion. It shows the transfer functions of over 2000 measurements for AuNP@OAm and AuNP@TER particle films. The magnitudes scatter around 1, the phase is nearly zero or condenses into slight shifts.

8.3 Gold Nanoparticle Films prepared using a Layer-by-Layer Approach

As an alternative approach, THz studies on AuNP films prepared by layer-by-layer methods have been studied, as already visualized in Figure 8.8. In contrast to the studies performed with drop cast samples on PTFE substrates, a material which enables chemical bonding between the substrate and the particle has to be used. Here, quartz substrates were chosen, since it is a suitable substrate in the THz range (see Section 6.6) and it allows to use the rich possibilities of silane chemistry to functionalize the substrates and bind AuNP as, e.g., in Refs. [117, 448, 454, 501]. Compared to drop casting methods, the layer-by-layer approach can give a better control regarding the thickness of the deposited film, as it is an self-limiting process: Per cycle, only one layer of particles can be deposited until the surface is completely covered. Any further particles cannot bind and would be removed by a subsequent washing step. The preparation of most of the samples studied here is discussed in detail in Ref. [502].

8.3.1 Methods

Materials

The quartz substrates used in this worked were obtained from plano-em ("Quarzglas GE 124", product number 26016, information about the material can be found under [373]) with a size of $19 \times 19 \times 0.5$ mm. biphenyl-4,4′-dithiol (BI)(95%), *p*-terphenyl-4,4″-dithiol (TER)(86%), nonane-1,9-dithiol (NON)(95%), 4,4-thiobisbenzenethiol (THIO)(98%) and oleylamine (OAm)(technical grade) were purchased from Sigma-Aldrich. Ultrapure water (18.2 MΩ cm, Millipore) (MQ) was used for all procedures.

For information regarding the AuNP solution see Section 8.2.

Preparation of LBL Films

The protocol used in this work is based on Ref. [437]. The $19 \times 19 \times 0.5$ mm substrates are broken into smaller, usually four, pieces. The quartz substrates were cleaned by rinsing them with MQ, acetone and/or isopropanol and toluene. Afterwards, they were placed in a plasma cleaner (Harrick Plasma PDC-002). The

chamber was evacuated down to a pressure of 1 mbar, in some cases the chamber was evacuated for up to 15 additional minutes to remove water vapor residues. The substrates were activated by using the "mid" setting for 3 min.

Afterwards, they were either quickly immersed in an (3-Mercaptopropyl)trimethoxysilane (MPTS) in toluene solution or a drop of MPTS was deposited on the substrate. The reaction time was varied for different samples. Afterwards, the functionalized substrates were removed from the solution and washed with toluene.

To add the first particle layer, the samples were immersed into a solution of AuNP@OAm in toluene. The reaction time and concentration of the AuNP solution were varied. To remove unbound particles, the samples were rinsed with toluene afterwards. For the ligand exchange/linking reaction, the samples were placed in a solution of NON, BI, TER or THIO in toluene. The concentration and reaction time were varied. After washing the samples with toluene, the whole procedure was repeated until the desired number of cycles was reached. The exact details of the synthesis can be found in Ref. [502].

Characterization

To obtain the spectrum of the deposited films, UV-Vis spectroscopy was performed using an Agilent Varian Cary 50 Conc, an Agilent Varian Cary 50 Bio or a Perkin Elmer Lambda 25. The measurements were either performed by directly measuring a baseline with a untreated quartz substrate or using a measurement without any sample as a baseline. For the latter, the absorption of the substrate had to be corrected for later. UV-Vis spectra were recorded for different positions of the sample by shifting the sample holder including the sample randomly between the measurements. The measurements could be performed as well between the aforementioned cycles as at the end of the synthesis.

Additionally, same samples were investigated in an optical microscope (Zeiss Axio Scope.A1, A-Plan 40x/0.65 ∞/0.17 lens) to investigate the of the homogeneity and coverage of the sample.

The topology of some samples was investigated using AFM (Digital Instruments (now Bruker) Multimode equipped with a Nanoscope IV controller) and scanning electron microscope (SEM) (ZEISS Gemini LEO-1150). The AFM measurements are

used to determine the thickness of the deposited films. The samples are scratched carefully to remove the film at a certain area. The created step is scanned, the data processed (removal of constant and linear offset) using GWYDDION.

THz Spectroscopy

The procedure of the THz-TDS measurements similar to the procedure described for the drop casted samples (Section 8.2). Up to four samples were mounted in a motorized filterwheel, together with an unprocessed quartz substrate as a reference. One position in the filterwheel was left empty for a reference measurement without any material inside the beam path. Before the measurement, the alignment was usually slightly adjusted to increase the peak THz field intensity, e.g. by optimizing the alignment of the detection beam into the detector. Sometimes, the compressor length of the laser system was tweaked to increase the peak THz field by creating a prechirped pulse.

Subsequently, the filterwheel was mounted in the THz setup, the box surrounding the setup was closed and the system was purged with nitrogen for at least 10, usually 15 min before the first measurement. The measurements were recorded in an alternating fashion (sample 1, sample 2, ..., sample 1, sample 2, ...) to adjust to slow drifts of the system. The scanning range, the scanning steps, the number of data points per scanning step and the number of total measurements were varied.

For the extraction of parameters like the complex conductivity or complex sheet conductivity $\tilde{\sigma}(\omega) = \tilde{\rho}(\omega)/d$, the obtained data was analyzed using DUODECIM.

8.3.2 Results and Discussion

Characterization

Over 30 samples have been measured using THz-TDS and even more have been prepared, e.g. as test experiments for thicker samples. Here, a chosen selection of samples will be discussed which represents different thicknesses and different linker molecules. First, the optical properties and topology of the samples is discussed, then the THz experiments will be reviewed.

Using UV-Vis spectroscopy, the optical properties of the prepared films could be used to study the film growth and thickness as well
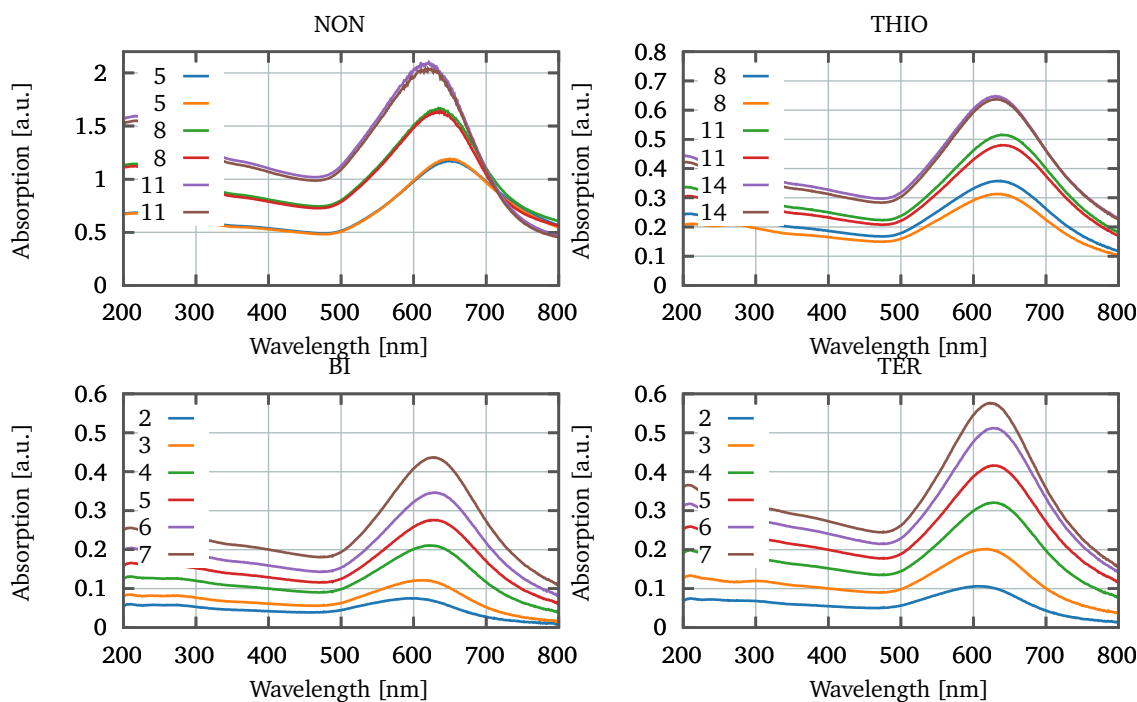
Figure 8.18: UV-Vis spectra obtained for LBL filmes with four different linkers. The number of deposition cycles is given in the respective legends. All samples show an increase of the absorption when more materials is deposited, accompanied with shits of the plasmon resonance.

as the influence of the linker molecules. The increase of deposited AuNP on the substrates directly influence the absorption, while the chosen linker molecules affect the shape, in particular the plasmon resonance. Figure 8.18 shows the absorption in the visible range for samples with different thicknesses and for all four used linker molecules.

According to the spectra, the thickest samples could be obtained using the NON linker. For all samples, the dominating feature is the plasmon peak, indicating intact, non-aggregated particles. Figure 8.19 shows the spectral position of the peak position and the peak value of the plasmon depending on the number of deposition cycles. Interestingly, the peak position of the plasmon first shifts to longer wavelengths due to the coupling of the individual particles, but shifts back to shorter wavelengths if more material is deposited. This was also observed in films prepared by spin-coating layer-by-layer techniques [495].

To obtain information about the film thickness, AFM measurements were performed. Figure 8.20) shows height profiles for the samples obtained with the NON linker discussed above in Figure 8.18. As described in the experimental section, any constant offset or or slope is removed using GWYDDION. Then, the data is averaged along the axis of the edge. For the data shown here,
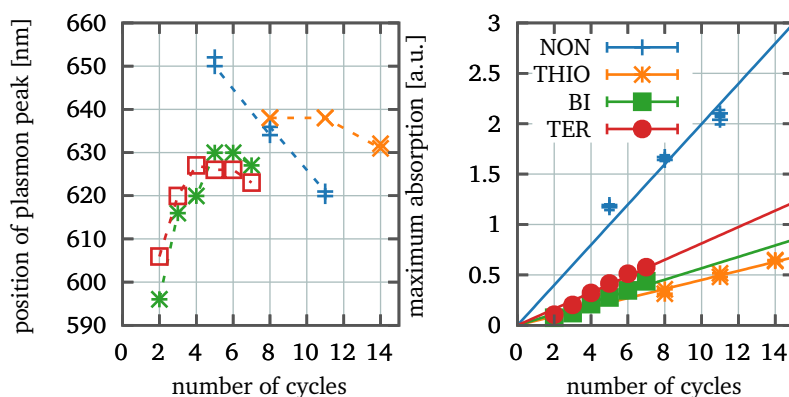
Figure 8.19: *Left:* Wavelength of the plasmon peak with respect to the number of cycles. The dashed line is a guide to the eye. *Right:* Height of the plasmon peak with respect to the number of cycles. The line shows a linear fit $y = mx$, with $m = 0.1997$ for NON, 0.045 for THIO, 0.0566 for BI and 0.08125 for TER. The error-bars concerning the peak height are obtained from measurements of different places of the sample, as described in the methods.

this procedure was repeated for three different areas of the sample. Outliers and peaks in the data can be attributed to larger aggregates and agglomerates, which have also been identified using optical microscopy. For the samples prepared by 5 cycles, a thickness of 47.70 nm is obtained, for 8 cycles 67.33 nm and for 11 cycles 90.4 nm. This corresponds to 8.73 ± 0.56 nm per cycle, so roughly 1.4 cycles are needed to build up a full layer in this case.
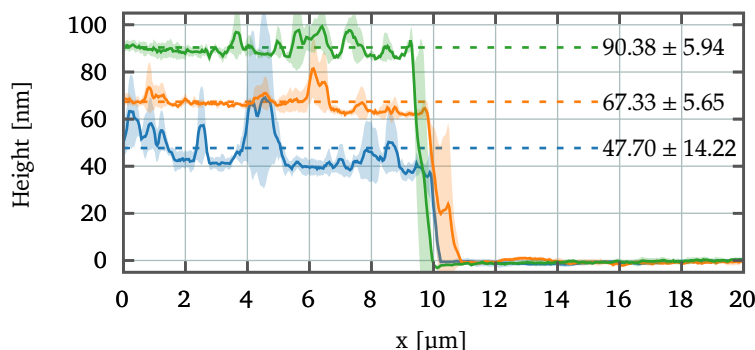
Figure 8.20: Height profiles obtained from AFM measurements for the samples prepared using the NON linker.

Similar analyses were performed for the other samples shown in Figure 8.18 and discussed in detail in Ref. [502].

THz Spectroscopy

Now, the results from the THz spectroscopy of the LBL samples are reviewed. First, a focus will be laid on the aforementioned thick samples prepared using NON. Results using different linkers and the influence of the substrate thickness will be discussed afterwards.

The THz scan of a sample prepared by 8 cycles and the NON linker is shown in Figure 8.21. Panel a) shows the full THz scan for reference and the sample measurement, including reflections in the detection an generation crystals and the reflection inside the quartz substrate (marked with *). In b), the spectrum of both measurements is shown, obtained for the full temporal scan. This explained the ripples in the spectrum, cutting the signal in the time-domain to remove any secondary reflections would yield a smooth spectrum. The transfer function is shown in panel c). The absolute part of the transfer function oscillates around one, while the phase shows a slight slope. This is already quite similar to the studies performed on drop casted samples, as it indicates no losses of the THz radiation by passing through the film. Panel d) shows extracted Tinkham sheet conductivities, obtained for data that was cut in time-domain to remove secondary reflections.
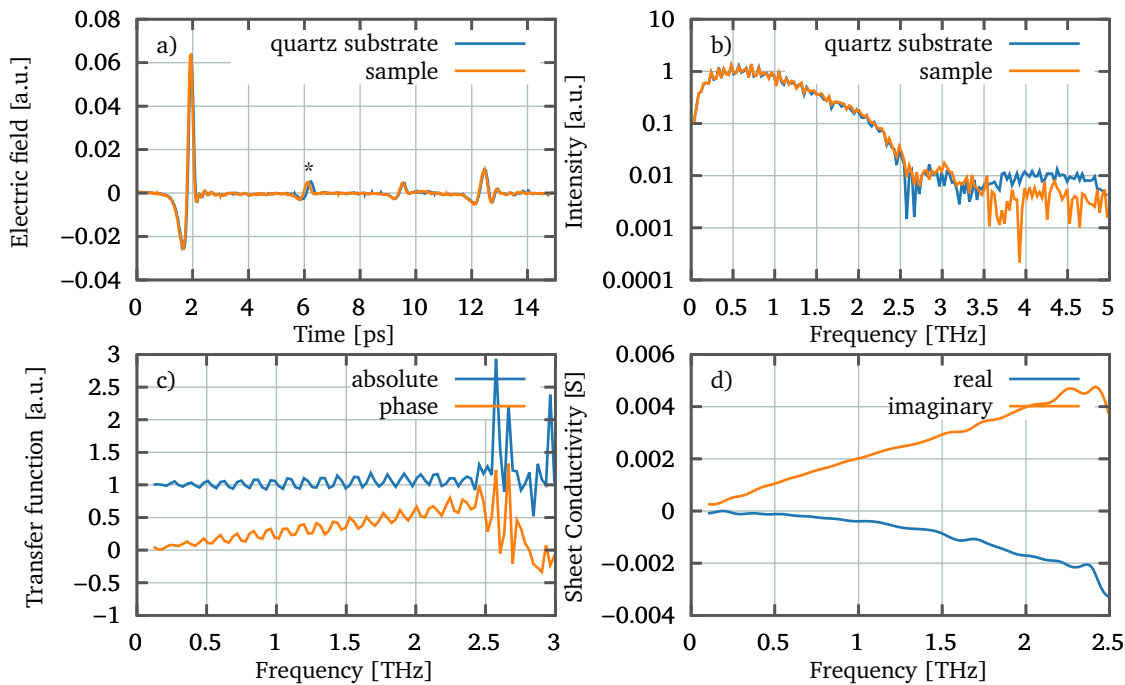
Figure 8.21: a) THz time trace including the second reflection inside the quartz substrate (marked by *) as well the internal reflections inside the generation and detection crystals. b) Spectrum obtained from the full measurement without any zero filling. The ripples are caused by the internal reflections of the THz pulse. c) absolute and phase of the transfer function as obtained from the spectra. The frequency range is restricted to $0 - 3\,\mathrm{THz}$, since the signal beyond $2.5\,\mathrm{THz}$ is too weak. d) Extracted Tinkham sheet conductivity.

For this sample, even though it is rather thick, no absorption could be found, since the magnitude of the transfer function is unity in the trustworthy frequency range. The puzzling aspect is the negative temporal shift of the sample measurement, which can also be seen in the positive slope of the phase of the transfer function. This is difficult to see for the main peak in Figure 8.21, but is visible to see for the second reflection inside the substrate, marked

by * in panel a).

The extracted real sheet conductivity is close to zero. At higher frequencies the obtained value becomes negative, giving a non-physical result. But since the requirements for the Tinkham model are not met, such as an absorbing sample, and there is a notable phase error most probably due to thickness variations of the substrate, this is not surprising.

The major error source regarding the temporal displacement of the pulse is the thickness of the substrates. The difference in thickness is expected to be low for samples/substrates obtained by breaking one substrate, but apparently the variations between the $19 \times 19 \times 0.5$ mm samples can be enough to complicate the analysis. Thus, in the following several substrates are investigated using THz spectroscopy to estimate an error of the optical thickness.

Influence of the Substrate-Thickness Variation

To further study the influence of the varying substrate thicknesses, several substrates are measured using the THz spectrometer. Some of these substrates were taken out of the box, some were cleaned or silanized.

Besides extraction the refractive index together with the thickness as described in Chapter 6, two ways exist to estimate the thickness based on the guess $\tilde{n} \simeq$ const.

Either the time difference Δt between the THz peak of a measurement of air and of a quartz substrate can be compared, or the time $\Delta t'$ between the first pass and the first internal reflection inside the quartz substrate can be analyzed, as visualized in Figure 8.22. For the first case, the thickness d is given by

$$\Delta t = \frac{d}{c_0} - \frac{d}{c_{\text{quartz}}} = d\left(\frac{1}{c_0} - \frac{\tilde{n}_{\text{quartz}}}{c_0}\right)$$

$$\rightarrow d = \frac{c_0 \Delta t}{1 - \tilde{n}_{\text{quartz}}}, \tag{8.13}$$

where $\tilde{n}_{\text{quartz}}$ is the refractive index of quartz and c_0 and c_{quartz} are the speeds of light in vacuum and quartz, respectively. For the second case, the pulse for the first internal reflection travels in the substrate three times the distance as directly transmitted
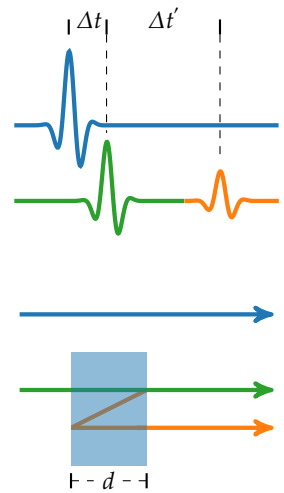
Figure 8.22: Sketch of Δt and $\Delta t'$ to estimate the thickness d of a sample.

pulse. Thus, the thickness is given by

$$\Delta t' = 2\frac{d}{c_{\text{quartz}}} = 2\frac{d\tilde{n}_{\text{quartz}}}{c_0}$$

$$\rightarrow d = \Delta t' \frac{c_0}{2\tilde{n}_{\text{quartz}}}. \tag{8.14}$$

By assuming the the refractive index of quartz to be $\simeq 2 + 0i$, the "substrate thickness error" can be estimated. A random collection of THz measurements of quartz is chosen, d is obtained using booth of the above described methods and the mean and standard deviation is calculated. The results are shown in Figure 8.23.

Figure 8.23: Gaussian distribution of the substrate thickness calculated from the THz measurements for various quartz substrates.
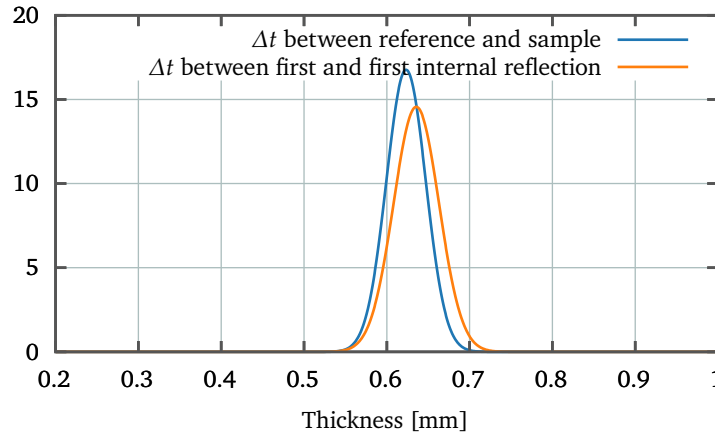
This gives an average optical thickness of 0.6233 (0.6356) mm with an standard deviation of 0.0238 (0.0274) mm, the number in the brackets corresponds to the value obtained by the analysis of the internal reflection. The absolute deviation from the thickness provided by the supplier (0.5 mm) is expected, since the refractive index was approximated in this analysis. The standard deviation nevertheless is much higher as expected and has to be considered for future analysis.

BI and TER

In the following, the results from the THz spectroscopy for the samples prepared using the aromatic linkers are investigated. Here, the calculated transfer functions[24] are directly analyzed and displayed in Figure 8.24. The magnitude of all transfer functions shows no notable absorption below 2.5 THz. Above 2.5 THz, the experiments became less trustworthy since the signal-to-noise ratio is low. The phase is either zero or shows a slight positive slope. This is similar to the results discussed above and is most likely associated with a slightly thinner substrate of some sample compared to the reference measurement.

[24] The transfer functions are obtained with data cut the time-domain signal before any second reflection of the THz pulse.
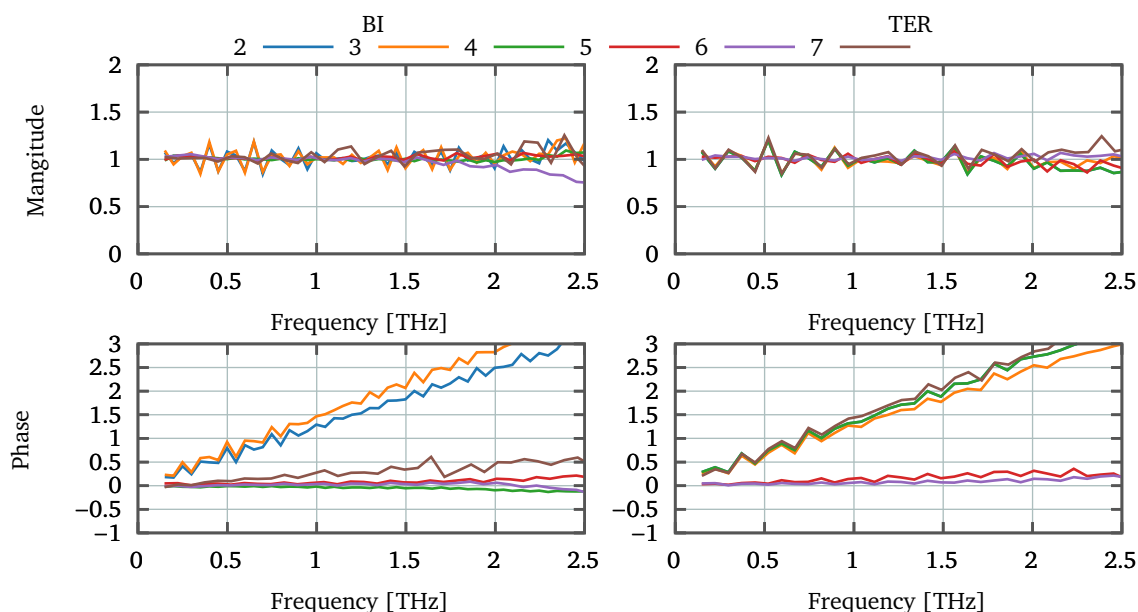
Figure 8.24: Magnitude and phase of the transfer functions for a set of samples prepared using the BI and the TER linker. The magnitude is equal to one for all samples, indicating no absorptive losses of the THz pulse while passing through the AuNP film. The phase of the transfer function is zero for the samples with the presumably same thickness of the substrate for the sample and reference measurement. For the measurements showing a positive slope of the phase, a different substrate thickness can be assumed as the reason. The legend gives the number of cycles for both ligands.

Especially the samples, for which the substrates appear to have the exact same thickness as the quartz substrate which has been used for the reference measurements, show very clearly that there is no notable effect of the particle film on the THz transmission. In other words, there is no measurable conductivity of the samples in the THz frequency range.

8.4 Summary

The prepared samples included thick AuNP layers up to nearly 0.1 μm, optically opaque ones prepared by different methods, different ligands, notable DC conductivity or particle size - the THz transmission was never significantly affected.

Absorptive losses, which would relate to a nonzero real part of the conductivity would be seen in the magnitude of the computed transfer functions, but were never observed within the frequency ranges of trustworthy signal-to-noise.

Any signal which could stem from an phase shift induced by the particle films and thus affecting the imaginary part of the conductivity could not be found, since the uncertainty induced by

the surprisingly high variations of the substrates is so high. Additionally, when the transfer function showed a nonzero phase, a negative phase slope associated with a delay of the THz pulse while passing through the sample could not be observed. This also leads to the conclusion that none of the AuNP films showed a significant conductivity in the THz range.

Additional test experiments using the optical excitation of the AuNP showed a low response on relatively high excitation powers. Even though it is tempting to speculate, that an increased mobility of the hot electrons could been probed by the THz pulse (with surprisingly high lifetimes), it is more likely that the optical pump pulse deposited enough energy in the film to destroy it and slowly turning it into and aggregated or solid sample.

9 Carrier Dynamics of CuInSe$_2$ Quantum Dot Solids

The following chapter has been partially published under Gorris, F. E. S. *et al.* Postdeposition Ligand Exchange Allows Tuning the Transport Properties of Large-Scale CuInSe$_2$ Quantum Dot Solids. *Advanced Optical Materials* **8** (Nov. 2019). The preparatory work described there was performed by Dr. Friederieke Gorris in the group of Prof. Dr. Horst Weller. The OPTP spectroscopy experiments and data processing was done in the group of Dr. Holger Lange by Dr. Shekhar Priyadarshi and Michael Deffner.

Colloidal semiconductor nanoparticles or quantum dots (QDs) feature a size-dependent bandgap [503], in contrast to the metallic particles discussed before. Similar to the ligand shell of AuNPs, the possibility to functionalize the surface of QDs offer many possibilities for applications like solar cells, screens or light sources [504–507]. If the particles are deposited as a well-organized film, the properties of the film can show collective properties, where, e.g., the charge transport properties are not determined by the single particle alone. If the coupling between the particles is strong, the transport mechanism can change from a hopping-type to a band-like transport [120, 508]. Experimentally this is difficult to achieve, since most system show a certain degree of disorder due to size and shape variations of the particles [509].

But even if no band-like transport can be achieved for a specific system, the hopping transport can be improved to obtain high conductivities. By inserting molecular linker into a QD film, the distance between the particles can be decreased and tunneling though the molecule can be more favorable that through-space tunneling from one particle to another [120, 510–513]. Varies hopping models exist, the hopping process is usually governed buy the distance and activation energy between two sites which gives a hopping probability $P \propto \exp{(-2d/a - \Delta E/k_B T)}$ with d as the hopping distance, a the localization length, and ΔE is the activation energy, which depends on the electronic environment [202].

While the distance can relatively easy be tuned using molecular linkers [510–513] to enhance charge transport, a less used approach is to tune the activation energy. This can e.g. be done by tuning the alignment of the molecular orbitals with the band edges of the particle [514, 515] and can also be used to obtain selective hole or electron transport [516, 517].

In the following, $CuInSe_2$ (CIS) quantum dots are investigated using OPTP spectroscopy. CIS quantum dots are promising candidates for various applications since they are less toxic than other types of QDs, as cadmium and lead-based particles. As mentioned before, band-like transport is unlikely to achieve in CIS QD solids, but the influence on the hopping transport of two different molecular linkers, 2-Amino-5-mercapto-1,3,4-thiadiazole (AMTD) and 2,5-Dimercapto-1,3,4-thiadiazole (DMTD) (Figure 9.1) is investigated here.

AMTD
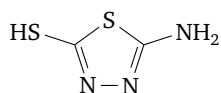
DMTD
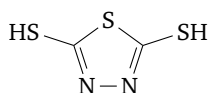
Figure 9.1: Lewis structures of the used linker molecules.
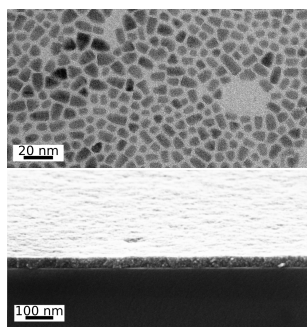
Figure 9.2: TEM micrographs (top) of the particles and SEM pictures of the obtained films (bottom).

Before the discussion of the OPTP spectroscopy results, a brief summary of the experimental results regarding the synthesis and DC transport measurements adopted from [113, 518] is presented. The as-synthesized particles [519] are stabilized by OAm and have a relatively broad size and shape distribution, as shown in Figure 9.2. By repetitive spin-coating, large-area samples (1 mm) could be prepared. The thickness could be controlled by the spin-coating conditions. After the film deposition, the ligand exchange was performed. SEM images of the obtained film is shown in Figure 9.2.

9.1 Methods

For details regarding the synthesis, ligand exchange and transport properties please refer to Ref. [113, 518]. The preparation of the samples for OPTP spectroscopy spectroscopy is shortly summarized here, along with the description of the THz experiments.

In a glovebox with nitrogen atmosphere, 60 mL of the as–synthesized CIS QD solution in n-hexane was given on a PTFE substrate. After drying, the sample was placed in AMTD or DMTD in acetonitrile solution for 12 hour. The samples without any linker molecules was placed the same amount of time in pure acetonitrile. Afterwards, the film was cleaned with acetonitrile and n-hexane.

OPTP spectroscopy experiments were performed in the THz setup described in Chapter 5. Optical excitation was performed using wavelengths of 480, 500, 650, 850 and 1220 nm at 0.5 and

1.2 mW. The obtained data was analyzed using DUODECIM as described in Chapter 6.

9.2 Results and Discussion

9.2.1 Transport Measurements

The DC transport properties are studied in a field-effect transistor geometry. The particle films with the native OAm ligand, AMTD and DMTD all show a linear I-V curve at room temperature (Figure 9.3). The obtained conductivity are 4.7×10^{-5} S cm^{-1} for CIS-OAm, 8.0×10^{-3} S cm^{-1} for CIS-AMTD and 4.3×10^{-2} S cm^{-1} for CIS-DMTD. This is in the same order as polycrystalline CIS films and a similar stoichiometric composition $(1.6 \times 10^{-2}$ S cm$^{-1})$ [520], but lower than the bulk conductivity of 1.5×10^{-1} S cm^{-1} [521]. When going to lower temperatures, the curves became increasingly nonlinear (Figure 9.3). At very low temperatures (10 K) for CIS-OAm and CIS-AMTD no current was observed, while the CIS-DMTD shows a significant current. This already hints to fundamental differences in the charge transport.

By measuring field-dependent I-V-curves, mobilities of 9.4×10^{-5} cm V^{-2} s^{-1} for the CIS-OAm, 1.2×10^{-2} cm V^{-2} s^{-1} for CIS-AMTD and 2.1×10^{-2} cm V^{-2} s^{-1} for CIS-DMTD are obtained. The films exhibit a *p*-type conductivity, in accordance with the literature on the crystal composition [520, 522, 523].
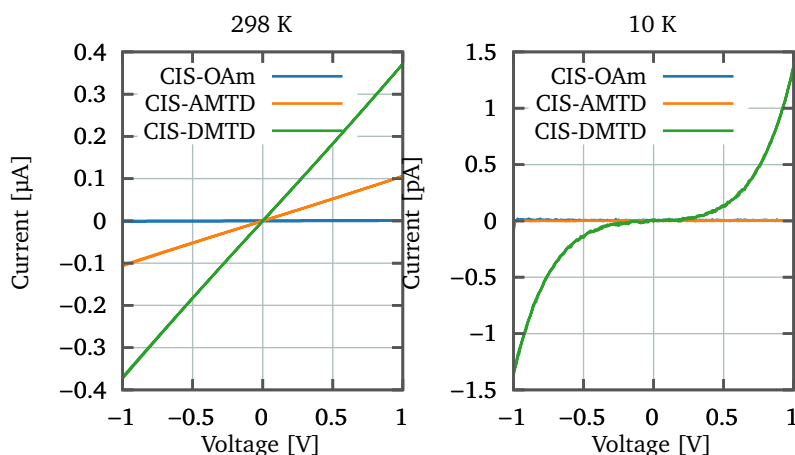
Figure 9.3: I-V curves for CIS-OAm, CIS-ATMD and CIS-DMTD at room temperature (left) and 10 K (right).

By comparing the obtained conductivities with the average distance of the particle obtained by TEM and SAXS analysis, it can be shown that the increase of the conductivity is not due to the simple reduction of the interparticle distance.

Figure 9.4: Conductivity vs. thickness and fit $\sigma = A\exp(-bx)$ The particle-to-particle (center-to-center) distance given here were obtained from SAXS measurements.
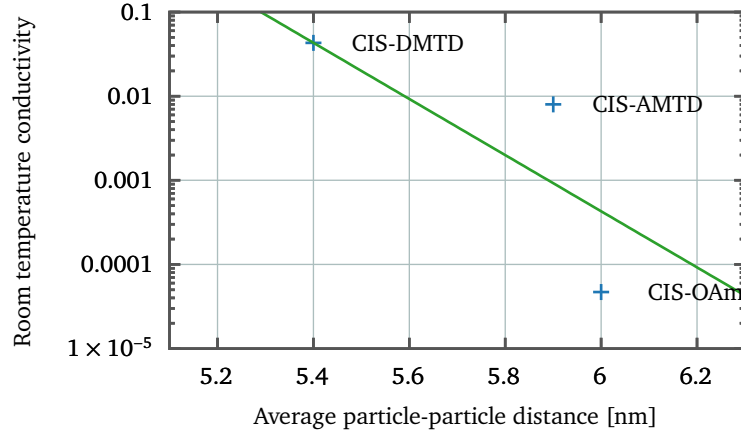
From the temperature dependency conductivity of the particle films conclusion about the exact transport mechanism can be made. For hopping transport, the temperature dependence of the conductivity can in general be described by

$$\sigma(T) = \sigma_0 \exp\left[-\left(\frac{T_0}{T}\right)^\nu\right], \qquad (9.1)$$

with a prefactor σ_0, the activation energy-dependent characteristic temperature T_0 and an exponential factor ν which defines the dominant hopping transport mechanism [203, 524]. If the interparticle distance is relatively homogeneous and the temperature high, electrons will most likely tunnel between adjacent particles. This is called nearest-neighbor hopping with $\nu = 1$. If the disorder of the system increases or the temperature decreases, the activation energy rather than the distance becomes the transport-determining quantity. An electron will not hop to the closest particle, but to a particle where the activation energy is lower. This is called variable-range hopping (VRH) transport [524]. Different types of VRH exists, most notable Mott-VRH [201, 202] and Efros-Shklovski (ES) VRH [525]. The latter includes Coulomb interactions which reduce the density of states (DOS) around the Fermi energy or open up a Coulomb gap and features $\mu = 1/2$.

By plotting $\ln[\mathrm{d}(\ln\sigma)/\mathrm{d}(\ln T)]$ versus $\ln T$, the slope ν can be found using linear fits [526] (Figure 9.5). This gives a hopping parameters of $\nu = 0.51$ for the with CIS-OAm QD solid, $\nu = 0.50$ for CIS-AMTD and $\nu = 0.26$ for CIS-DMTD. Thus, with introducing linker molecules into the QD solid, the transport through the sample can not only be improved, but also the mechanism can be changed: CIS-OAm andCIS-AMTD show a $T^{-1/2}$ temperature dependence of the conductivity. According to the ES-VRH model, this implies that the Coulomb interactions between the carriers are strong or that the DOS at the Fermi edge is low. The DMTD
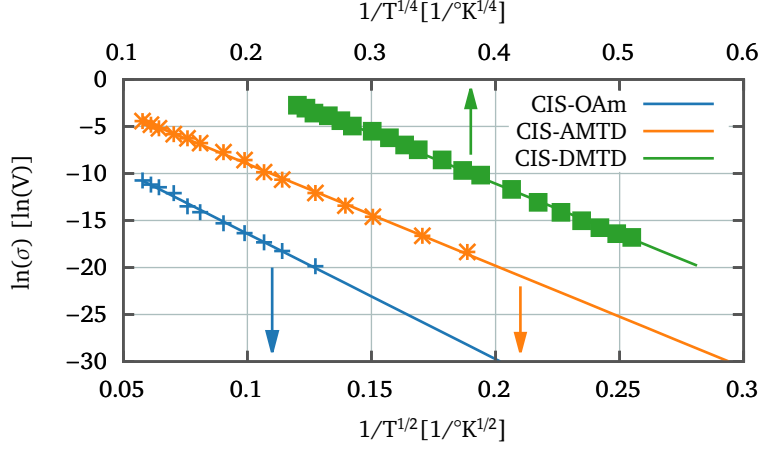
Figure 9.5: Temperature-dependent conductivity for the three CIS QD solids. The arrow show the corresponding x-Axis for the data. For CIS-OAm and CIS-AMTD, the plot of $\ln(\sigma)$ against $1/T^{1/2}$ yields a linear slope, which indicates ES-VRH. For CIS-DMTD, a linear slope is obtained for $\ln(\sigma)$ against $1/T^{1/4}$, which implies Mott-VRH.

linker seems to provide a constant DOS for the holes, since the temperature-dependency $T^{-1/4}$ points towards Mott-VRH. This could also imply, that the frontier orbitals of DMTD align better with the LUMO of the particles and thus improve the hole transport.

9.2.2 Optical-Pump Terahertz-Probe Spectroscopy

To further investigate these differences, OPTP spectroscopy spectroscopy was performed. As described before, THz spectroscopy can be used to study transport properties on a local scale, disregarding the need for contacts and electrodes. By illuminating the sample with an optical light pulse and probing the excited system with a THz pulse, the photoinduced conductivity can be obtained [97, 527].

Figure 9.6 shows exemplary maps of the measured $\Delta E(t, \tau)$ for all three samples excited with 650 nm at 1.2 µJ. In the lower panel, the integrated change of the THz transmission with respect to the time delay τ as obtained by

$$\epsilon(\tau) = \int_t \Delta E(t, \tau)^2 \mathrm{d}t, \tag{9.2}$$

is given, together with triexpoential fits of the curves. This gives access to the carrier recombination times and directly shows the most striking difference between the samples. The recombination of the photocarriers becomes faster for the films prepared with linked particles, with the CIS-DMTD samples showing the fastest decay. Increasing the power of the optical pump from 0.5 to 1.2 µJ per pulse decreases the lifetime of the carriers and changing the dynamics for, e.g., the CIS-OAm system from nearly monoexponential to biexponential. Higher fluences generates more carriers,
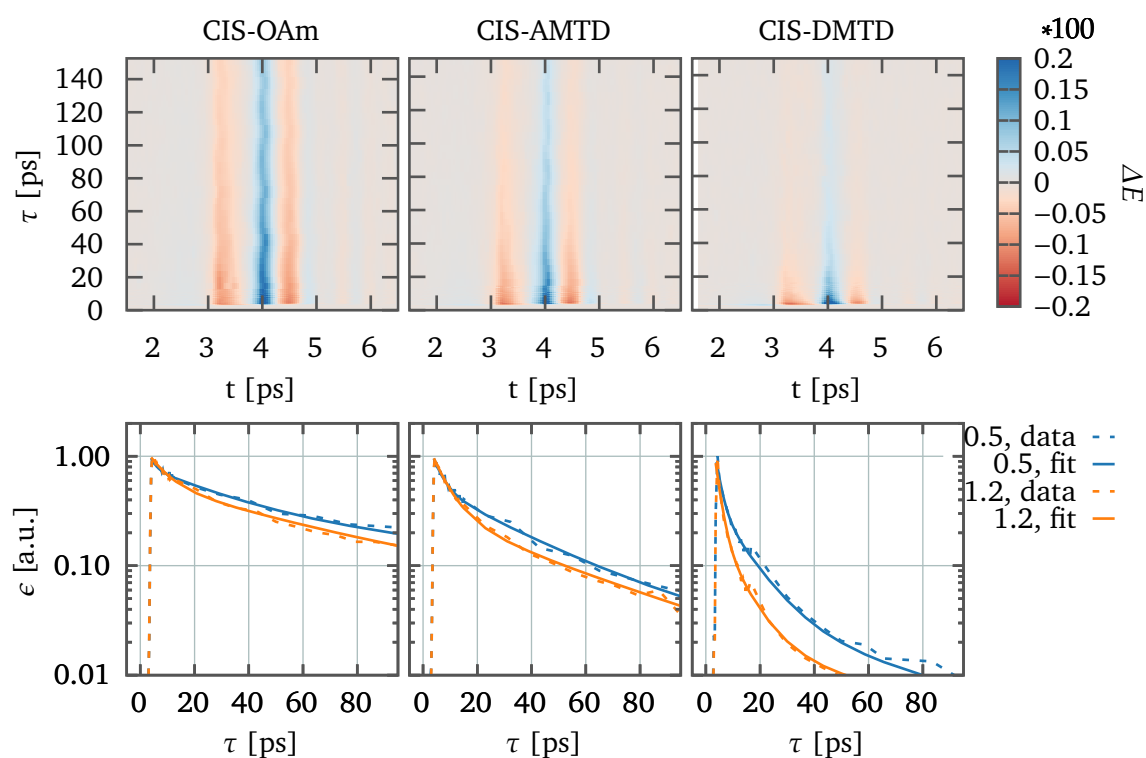
Figure 9.6: *Top row: ΔE maps for all three samples excited with 650 nm and 1.2 µJ. Bottom row:* Change of ΔE, time-integrated and normalized with respect to τ for 0.5 µJ (blue lines) and 1.2 µJ (orange lines) excitation pulse energies. The data is shown in dashed lines, the solid lines represents fits with a triple-exponential decay. The decay dynamics become faster with the insertion of the linker molecules, being the fastest for CIS-DMTD.

which can relax quickly by multicarrier recombination and Auger processes [528]. The samples with the connecting ligands show always an at least biexponential decay, which can be understood by the increased carrier mobility. The increased mobility leads to a higher probability of multicarrier relaxation pathways. This reduction of the lifetimes has the same systematic as the the mobilities obtained by the FET experiments. For the CIS-DMTD sample, no satisfactory fits are obtained using a biexponential decay, so triexponential fits were used. To be consistent, the fits in Figure 9.6 are all performed with triexponential decays. Additionally, fits with biexponetial decays for CIS-OAm and CIS-AMTD and triexponetial decays for CIS-DMTD can be found in the Appendix, Section F.

The photoexcation was performed with different wavelengths, but this does not change the picture substantially. Figure 9.7 gives an overview over the lifetimes obtained for all three samples with 500, 650 and 800 nm. The induced change of the THz transmission was fitted with a triexpoential decay,

$$\epsilon_{\text{fit}}(\tau) = \text{Heavi}(\tau - t_0) \left[A_0 e^{-\frac{\tau - t_0}{\tau_1}} + A_1 e^{-\frac{\tau - t_0}{\tau_2}} + (1 - A_0 - A_1) e^{-\frac{\tau - t_0}{\tau_3}} \right]$$

(9.3)

where Heavi is the Heaviside function to accommodate for the rise. Since the data is normalized to 1, the amplitudes of the three exponential decays are not chosen independently. A triexponential decay model is necessary to obtain sufficiently good fits for the CIS-DMTD model, but very likely to cause overfitting for the CIS-OAm system. Still, it gives the possibility for consistently compare the three samples and visualize the decrease of the lifetimes (see Figure 9.7) for the photogenerated carriers by changing the particles ligand from OAm to AMTD and DMTD.

Using Equation (6.36),

$$\sigma(\tau, \omega) = -\frac{\epsilon_0 c(1 + n_{\text{Substrate}})}{d} \frac{\Delta T(\tau, \omega)}{T(\tau, \omega)},$$

it is possible to extract the photoinduced complex conductivity from the samples. Figure 9.8 shows the conductivity for two representative τ.

All[25] samples show a low real zero-bias conductivity for the photogenerated carriers, but a significant imaginary response, which indicates a dominant role of bound or localized carriers. As we observed no band-like transport in the previous experiments, this is expected: In comparison to band transport, hopping events from

[25] The following part is directly adopted from Gorris, F. E. S. *et al.* Postdeposition Ligand Exchange Allows Tuning the Transport Properties of Large-Scale CuInSe$_2$ Quantum Dot Solids. *Advanced Optical Materials* **8** (Nov. 2019).
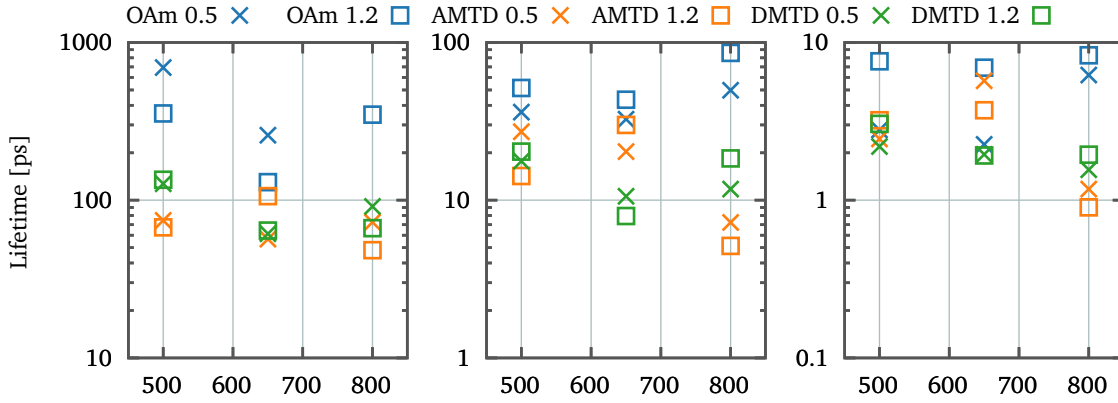
Figure 9.7: Overview over the lifetimes of the photoexcited charges, obtained for triexponential fits of $\epsilon(\tau)$ for different excitation wavelengths and powers. The unlinked sample shows significantly higher lifetimes of the excited carriers. Not included in this picture are the proportions A_X of the individual decays.
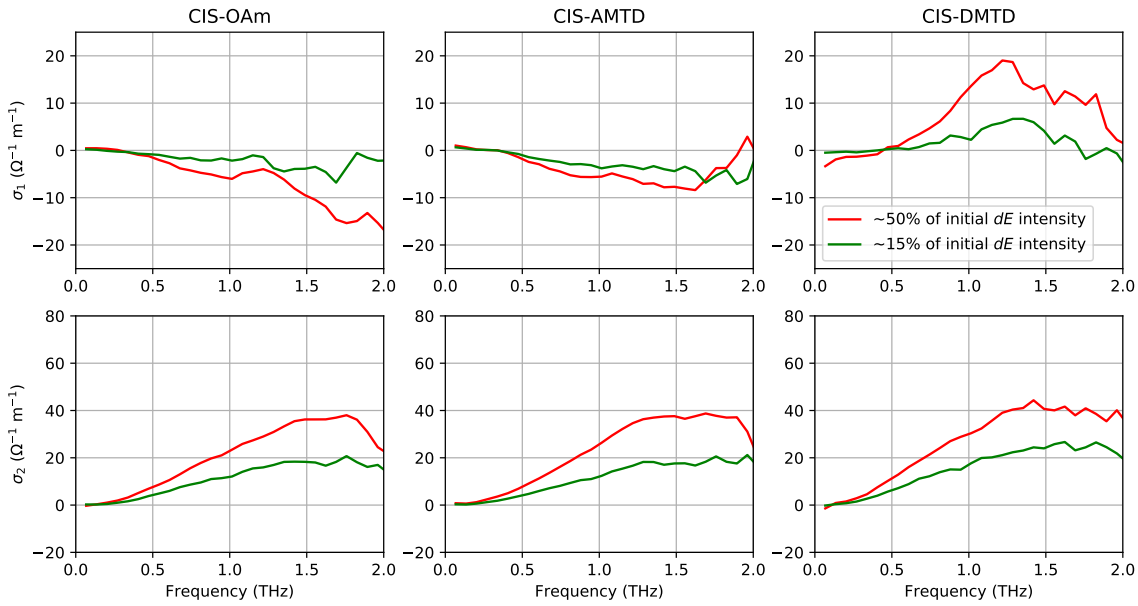
Figure 9.8: Frequency-dependent photoconductivities $\sigma(\omega) = \sigma_1(\omega) + i\sigma_2(\omega)$ obtained for excitation with 1.2 μJ pulse energy at 650 nm. Displayed are data at two representative τ after the fast initial dynamics (compare Figure 9.6 d). The upper panel shows the real part, the lower the imaginary part of the complex conductivity as obtained with Equation (6.36).

particle to particle are rare, thus the overall response of the material is less likely to be Drude-like. For CIS-OAm and CIS-AMTD, the real part of σ becomes negative after photoexcitation. This is a rare observation. Normally, the photoexcitation enhances the conductivity as the concentration of mobile carriers is increased. Negative photoconductivities have been reported earlier for photoexcitation of doped materials. When the interaction of the photogenerated carriers with, for example, intrinsic majority carriers leads to a reduction of the mobility while the relative carrier concentration is almost constant (because of high intrinsic concentrations), a negative differential conductivity can be obtained. For example, in graphene, a negative photoconductivity was observed via OPTP spectroscopy [529, 530]. In the doped high-mobility samples, electron heating increases the carrier scattering rate, without increasing the effective carrier concentration significantly. A net decrease of the photoconductivity was also reported for CdSe nanorods with an electron acceptor molecule. In time-resolved OPTP experiments, after a picosecond trapping of the electrons, the delocalized hole interacts with the Coulomb potential of the reduced electron acceptor. This leads to an effective reduction of the hole mobility in the nanorods [531]. In doped Si nanowires, carriers trapped at dopant ions act as Coulomb scatterers, reducing the mobility [532]. A similar observation was made for p-type $Pb_{1-x}Sn_xTe$ films [533].

The remarkable aspect in case of the CIS QD solids is the dependence of the photoinduced conductivity on the connecting ligands. The ligand exchange is not expected to significantly change the QD's internal structure. In that case, one would also expect stronger changes from CIS-OAm to CIS-AMTD and CIS-DMTD than from CIS-OAm and CIS-AMTD to CIS-DMTD (as observed). Thus, we assume the change from negative to positive conductivity to mostly originate from the general change in the transport process. For another view, the time evolution of the conductivity peaks are plotted in Figure 9.9 a).

The general behavior of CIS-OAm and CIS-AMTD is very similar: a minimum conductivity is reached after $\approx$5 ps and then recovers on timescales of the carrier relaxation time. For CIS-DMTD, the maximum conductivity is reached directly after photoexcitation and also recovers during the carrier lifetime. This difference can be reasoned within the picture obtained from the temperature-dependent studies, schematically displayed in Figure 9.9 b). In CIS QD solids, majority carriers are holes that lead to a significant dark current in all three samples. Photoexcitation generates electron-hole pairs, increasing the carrier concentra-
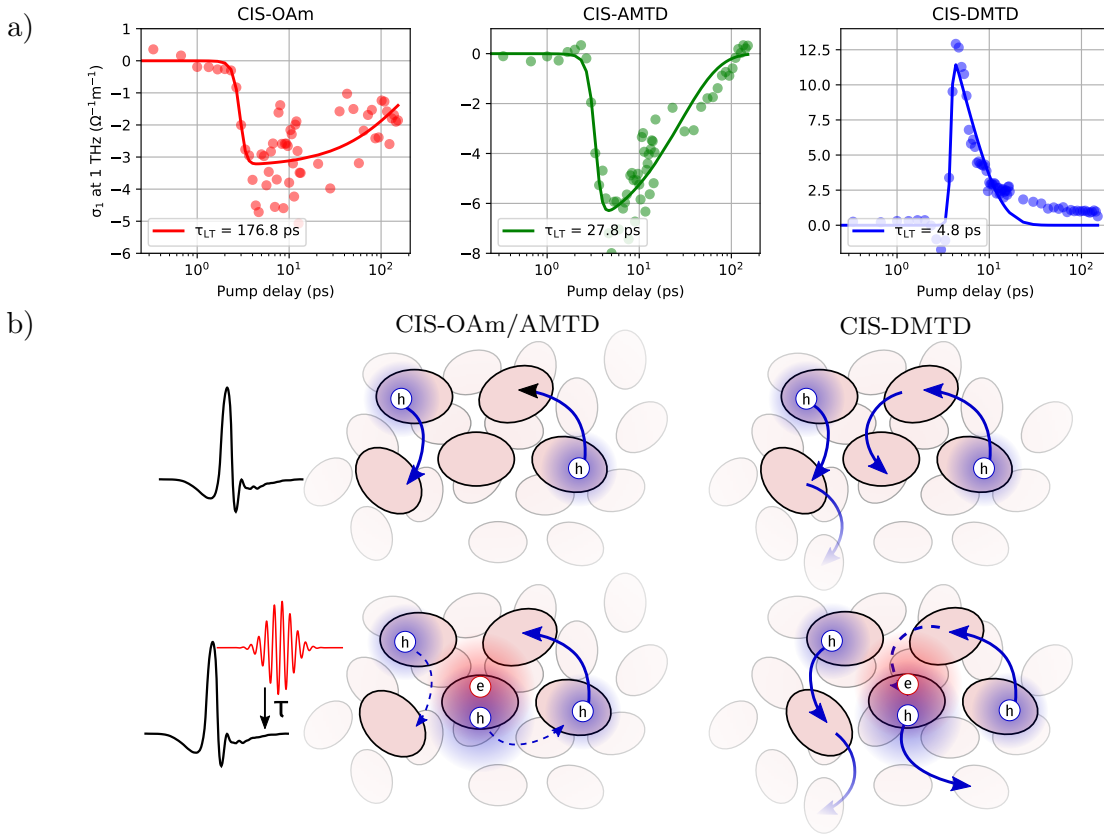
Figure 9.9: a) Time-dependence of the real part of the conductivity σ_1 at the frequency around the maximum value (1 THz). The data (dots) have been fitted with mono-exponential decays (solid line). While for CIS-OAm and CIS-AMTD, this can roughly capture the time evolution, for CIS-DMTD the decay is clearly bi-exponential, as the carrier dynamics. b) Sketch of the proposed effect. Without optical excitation, the movement of the intrinsic carriers (holes) is probed by the THz pulse. Because of efficient M-VRH, holes in CIS-DMTD have a much higher mobility than in CIS-OAm and CIS-AMTD, where the transport is influenced by Coulomb interaction (ES-VRH). Optical excitation generates electron-hole pairs. Trapping leads to localized charges that act on the intrinsic holes by Coulomb interaction. The relative change is more drastic for CIS-OAm and CIS-AMTD than for CIS-DMTD. There, the transport is less influenced by Coulomb interaction and the conductivity gain by the carrier concentration increase outweighs a potential small mobility decrease.

tion. The photogenerated carriers interact with the intrinsic holes via Coulomb interaction. For CIS-OAm and CIS-AMTD Coulomb interactions dominate the hopping probability and the additional carriers increase the hopping activation energy, lowering the carrier mobility. Regarding the amount of intrinsic holes, the net carrier concentration increase is small compared to the decrease in mobility, resulting in the conductivity decrease. This was also observed for other trapped carriers in semiconductor nanostructures, were Coulomb interactions can lead to a carrier localization and reduction of the mobility [531, 532, 534, 535]. For CIS-DMTD, an alignment of the QD VB and the molecules HOMO provides states for an efficient M-VRH transport, leading to a significantly increased mobility of the majority carriers (holes). Under such conditions, the DOS is not significantly altered by additional carriers, so that the hopping probability for M-VRH is almost constant. Changes are but negligible compared to the high intrinsic (dark) mobility. Then, every photogenerated hole leads to an increase in conductivity and the carrier recombination results in a relaxation of this increase, as observed in the experiments. This demonstrates that the type of the hopping mechanisms not only determines the hopping probability (and conductivity), but also alters the system's response to photoexcitation. As the exact mechanism depends on the employed ligands, the strategy of using the ligand's electronic structure to influence the transport is very flexible.

9.3 Summary

In this chapter, the influence of short connecting ligands on the transport in QD solids was investigated. Transport measurements showed an increase of the mobilities by a factor of around 200. This demonstrates, that even though no band–like transport could be achieved, the hopping transport could be tweaked using connecting ligands. Temperature dependent measurements showed a change of the hopping mechanism from ES-VRH for CIS-OAm and CIS-AMTD to Mott-VRH for the highly conductive CIS-DMTD sample.

Using OPTP spectroscopy, a similar picture is obtained. The increase of mobilities lead to a faster recombination of the photoexcited carriers, which can be explained with Auger processes. The extracted frequency-resolved photo–conductivities showed a clear difference between the CIS-OAm/CIS-AMTD and the CIS-DMTD samples. Both are dominated by the capacitive response (thus,

the imaginary part of the conductivity), but the photoinduced carriers lead to a decrease of the real conductivity for the two lower–conducting samples. This we explain by the Coulomb interactions between the intrinsic holes and photoexcited carrier. For the samples which show ES-VRH, this leads to a reduction of the samples' conductivity. For CIS-DMTD, the Mott-VRH already hints towards a lower influence of Coulomb interactions, thus the additional carriers lead to an increase of the conductivity.

10 Conclusion and Outlook

The study of transport mechanisms on the meso- or nanoscale, such as the electron transport through molecules, not only offers an understanding of fundamental quantum mechanical processes but also of the properties of materials on the macroscale. Using theoretical methods such as the Landauer-Büttiker approach (see Chapter 2), the electron transport through molecules can be studied. Experimentally, the study of such molecular junctions is much more complicated, but new technologies like THz spectroscopy can potentially enable an easy experimental access and also give the possibility to study ultrafast processes.

Tunneling pathways in molecular junctions yield a variety of information about the fundamental processes in such systems, like quantum interference or switching behavior, but are difficult to access experimentally. IETS is a promising candidate if the relationship between the IETS intensity of specific vibrational modes and the tunneling pathways can be established. Chapter 3 presents the implementation of the calculation of IET spectra in combination with the mode-tracking algorithm, enabling an efficient way to study the interactions between tunneling electrons and vibrational modes of a molecular junction. Three different systems were studied with regard to tunneling pathways evaluated from local transmissions and IET spectra. The findings suggest that it is possible to track tunneling pathways for systems where the vibrations, which are used as tracers for the tunneling pathways, are sufficiently localized. If a mode couples too strongly with the rest of the molecule, such relations become more and more difficult to establish.

To model the transport properties of electrons in AuNP connected by molecular linkers, numerical simulations (Chapter 4) based on previous work [8, 296] were performed and extended to simulate the influence of linker molecules between particles. The tunneling probability through the molecules connecting the particles was obtained from NEGF+DFT calculations for molecular junctions. The results suggest that the molecules modify the quasi-DC or low-frequency response to THz radiation, with the transmission at the Fermi level as the decisive parameter. Whether this

effect is measurable in experiments depends also on parameters like the scattering rate and field strengths of the THz radiation. Both parameters can shift the frequency range, where the effect is notable, in or out of the experimentally accessible THz window.

Chapters 5 and 6 summarize the experimental design and principles of THz spectroscopy and the data extraction routines. The various methods were implemented in a `python` package, which allows the extraction of physical quantities from THz experiments as a standalone tool or the use as a `python` library.

To experimentally study the conductivity of molecular junctions using THz spectroscopy, thin films were prepared using AuNPs and molecular linkers, creating a network of multiple molecular junctions between the particles (Chapter 8). Two different synthesis strategies were adopted, simple drop casting and layer-by-layer methods.

A variety of samples prepared by the different methods, different thicknesses and different molecular linkers were studied. The samples were without exception transparent in the THz regime, though partially to completely opaque in the visible range. Also, the obtained particle films were much thicker than evaporated gold films, which nearly completely absorbed the THz radiation and have been studied as a benchmark or reference system (Chapter 7). Even though this is interesting for several applications such as transparent electrodes for solar cells or antireflection coatings [361, 362], this poses the question whether THz-TDS is a suitable tool for the study of molecular junctions, or whether the chosen material system is appropriate.

Several examples for which tunneling current could be observed have been reported, e.g. in STM setups [100–102, 330] or thin percolated gold films [382]. In STM setups, the whole experimental situation is much more defined and controllable compared to the experiments demonstrated here. Thus, one possibility to study the conductivity of molecules using THz spectroscopy would be to introduce the molecules in an STM and to perform experiments similar to Ref. [102]. They reported the THz induced tunneling of electrons between an STM tip and individual atoms of a Si surface, but having the molecule in the STM would already enable the measurement of the electron transport, thus spoiling the idea of a simple, contactless way to study the transport properties of molecules. Still, this would shine light on the THz-induced transport processes in the molecules, and may give hints about why for the systems studied in this work no transport could be observed using THz-TDS.

The experiments by Takeda *et al.* [382] are much more similar to the presented ones using AuNP films, but differ in two important aspects. First, they used THz radiation generated in lithium niobate, which yields much higher fields than optical rectification in ZnTe and thus stronger forces acting on the electrons. Second, the gold films they studied can be easily tuned from completely transparent to completely opaque for THz radiation just by changing the thickness of the sample. For the system studied here, the key tuning parameter was the conductivity of the linker molecules. This can not be changed easily to desired values because the chemical conditions for linking as well as the availability of appropriate linker molecules have to be taken into account.

Other studies which investigated the transport properties of molecules did not utilized ground-state THz spectroscopy, but rather optical excitations to study the photo-generated carriers only [328, 329], as presented in Chapter 9. This is a successful approach but also yields different information than THz-TDS spectroscopy, as it studies exclusive photoexcited carriers but not the transport properties of a system which is in its ground-state (with respect to optical excitations).

The study of $CuInSe_2$ quantum dot solids with and without molecular linkers using OPTP films demonstrated that using this approach, it is possible to study the influence of linkers on the transport properties of a macroscopic sample. The sample showed hopping transport, which could be tuned by the choice of the ligands from a Efros-Shklovskii to a Mott-type variable-range hopping transport. This hints at a band alignment which favors hole transport in the samples.

Unveiling the electronic transport processes through individual molecules is a fascinating and promising effort, which is broadly interconnected with the study of, e.g., biological process such as photosynthesis, chemical processes in solar cells or, of course, the development of new electronic or even optoelectronic and spintronic devices. Theoretical and experimental approaches can go hand in hand to explore and push the boundaries of new experimental techniques for the study of such systems, such as the Landauer-Büttiker approach, inelastic electron tunneling spectroscopy and THz spectroscopy.

Bibliography

1. Drude, P. Zur Elektronentheorie der Metalle. *Annalen der Physik* **306,** 566–613. doi:10.1002/andp.19003060312 (1900).

2. VanderPlas, J. *Quantum Python: Animating the Schrodinger Equation* https://jakevdp.github.io/blog/2012/09/05/quantum-python/. 2012.

3. Battaglia, C., Cuevas, A. & Wolf, S. D. High-efficiency crystalline silicon solar cells: status and perspectives. *Energy & Environmental Science* **9,** 1552–1576. doi:10.1039/c5ee03380b (2016).

4. Grätzel, M. Recent Advances in Sensitized Mesoscopic Solar Cells. *Accounts of Chemical Research* **42,** 1788–1798. doi:10.1021/ar900141y (Nov. 2009).

5. Brabec, C. J. *et al.* Polymer-Fullerene Bulk-Heterojunction Solar Cells. *Advanced Materials* **22,** 3839–3856. doi:10.1002/adma.200903697 (Aug. 2010).

6. Facchetti, A. π-Conjugated Polymers for Organic Electronics and Photovoltaic Cell Applications†. *Chemistry of Materials* **23,** 733–758. doi:10.1021/cm102419z (Feb. 2011).

7. Parkinson, P., Lloyd-Hughes, J., Johnston, M. B. & Herz, L. M. Efficient generation of charges via below-gap photoexcitation of polymer-fullerene blend films investigated by terahertz spectroscopy. *Physical Review B* **78.** doi:10.1103/physrevb.78.115321 (Sept. 2008).

8. Němec, H. *et al.* Ultrafast conductivity in a low-band-gap polyphenylene and fullerene blend studied by terahertz spectroscopy. *Physical Review B* **79.** doi:10.1103/physrevb.79.245326 (June 2009).

9. Ponseca, C. S. *et al.* Electron and Hole Contributions to the Terahertz Photoconductivity of a Conjugated Polymer:Fullerene Blend Identified. *The Journal of Physical Chemistry Letters* **3,** 2442–2446. doi:10.1021/jz301013u (Aug. 2012).

10. Jin, Z. *et al.* Ultrafast Terahertz Photoconductivity of Photovoltaic Polymer–Fullerene Blends: A Comparative Study Correlated with Photovoltaic Device Performance. *The Journal of Physical Chemistry Letters* **5,** 3662–3668. doi:`10.1021/jz501890n` (Oct. 2014).

11. Krauspe, P. *et al.* Terahertz short-range mobilities in neat and intermixed regions of polymer:fullerene blends with controlled phase morphology. *Journal of Materials Chemistry A* **6,** 22301–22309. doi:`10.1039/c8ta08061e` (2018).

12. Xue, R., Zhang, J., Li, Y. & Li, Y. Organic Solar Cell Materials toward Commercialization. *Small* **14,** 1801793. doi:`10.1002/smll.201801793` (Aug. 2018).

13. Engel, G. S. *et al.* Evidence for wavelike energy transfer through quantum coherence in photosynthetic systems. *Nature* **446,** 782–786. doi:`10.1038/nature05678` (2007).

14. Scholak, T., Wellens, T. & Buchleitner, A. The optimization topography of exciton transport. *EPL (Europhysics Letters)* **96,** 10001. doi:`10.1209/0295-5075/96/10001` (Aug. 2011).

15. Karafyllidis, I. G. Quantum transport in the FMO photosynthetic light-harvesting complex. *Journal of Biological Physics* **43,** 239–245. doi:`10.1007/s10867-017-9449-4` (Apr. 2017).

16. Walschaers, M., Diaz, J. F.-C., Mulet, R. & Buchleitner, A. Optimally Designed Quantum Transport across Disordered Networks. *Physical Review Letters* **111.** doi:`10.1103/physrevlett.111.180601` (Oct. 2013).

17. Lambert, N. *et al.* Quantum biology. *Nature Physics* **9,** 10–18. doi:`10.1038/nphys2474` (Dec. 2012).

18. Gray, H. B. & Winkler, J. R. Electron tunneling through proteins. *Quarterly Reviews of Biophysics* **36,** 341–372. doi:`10.1017/s0033583503003913` (Aug. 2003).

19. Gray, H. B. & Winkler, J. R. Long-range electron transfer. *Proceedings of the National Academy of Sciences* **102,** 3534–3539. doi:`10.1073/pnas.0408029102` (Feb. 2005).

20. 1956 Nobel Prize in Physics. *Physics Today* **10,** 16–17. doi:`10.1063/1.3060222` (Jan. 1957).

21. Rupp, K. *42 Years of Microprocessor Trend Data* online, avaible at `https://github.com/karlrupp/microprocessor-trend-data`. Feb. 2018.

22. Thompson, S. E. & Parthasarathy, S. Moore's law: the future of Si microelectronics. *Materials Today* **9,** 20–25. doi:`10.1016/s1369-7021(06)71539-5` (June 2006).

23. Intel. Introducing the 45nm Next-Generation Intel®Core™ Microarchitecture (2007).

24. Williams, R. S. What's Next? [The end of Moore's law]. *Computing in Science & Engineering* **19,** 7–13. doi:`10.1109/mcse.2017.31` (Mar. 2017).

25. Lin, M.-H., Chen, H.-Y. & Gwo, S. Layer-by-Layer Assembly of Three-Dimensional Colloidal Supercrystals with Tunable Plasmonic Properties. *Journal of the American Chemical Society* **132,** 11259–11263. doi:`10.1021/ja103722p` (Aug. 2010).

26. Hush, N. S. An Overview of the First Half-Century of Molecular Electronics. *Annals of the New York Academy of Sciences* **1006,** 1–20. doi:`10.1196/annals.1292.016` (Dec. 2003).

27. Aviram, A. & Ratner, M. A. Molecular rectifiers. *Chemical Physics Letters* **29,** 277–283. ISSN: 0009-2614. doi:`10.1016/0009-2614(74)85031-1` (Oct. 1974).

28. Binnig, G. & Rohrer, H. Scanning tunneling microscopy. *Surface Science* **126,** 236–244. doi:`10.1016/0039-6028(83)90716-1` (1983).

29. Binnig, G. & Rohrer, H. Scanning tunneling microscopy—from birth to adolescence. *Reviews of Modern Physics* **59,** 615–625. doi:`10.1103/revmodphys.59.615` (July 1987).

30. Heilemann, M., Margeat, E., Kasper, R., Sauer, M. & Tinnefeld, P. Carbocyanine Dyes as Efficient Reversible Single-Molecule Optical Switch. *Journal of the American Chemical Society* **127,** 3801–3806. doi:`10.1021/ja044686x` (Mar. 2005).

31. Chen, F. *et al.* A Molecular Switch Based on Potential-Induced Changes of Oxidation State. *Nano Letters* **5,** 503–506. doi:`10.1021/nl0478474` (Mar. 2005).

32. Lörtscher, E., Ciszek, J., Tour, J. & Riel, H. Reversible and Controllable Switching of a Single-Molecule Junction. *Small* **2,** 973–977. doi:`10.1002/smll.200600101` (Aug. 2006).

33. Liljeroth, P., Repp, J. & Meyer, G. Current-Induced Hydrogen Tautomerization and Conductance Switching of Naphthalocyanine Molecules. *Science* **317,** 1203–1206. doi:`10.1126/science.1144366` (Aug. 2007).

34. Quek, S. Y. *et al.* Mechanically controlled binary conductance switching of a single-molecule junction. *Nature Nanotechnology* **4,** 230–234. doi:10 . 1038 / nnano . 2009 . 10 (Mar. 2009).

35. Kouwenhoven, L. Single-Molecule Transistors. *Science* **275,** 1896–1897. doi:10.1126/science.275.5308.1896 (Mar. 1997).

36. Liang, W., Shores, M. P., Bockrath, M., Long, J. R. & Park, H. Kondo resonance in a single-molecule transistor. *Nature* **417,** 725–729. doi:10.1038/nature00790 (June 2002).

37. Xu, Xiao, Yang, X., Zang, L. & Tao. Large Gate Modulation in the Current of a Room Temperature Single Molecule Transistor. *Journal of the American Chemical Society* **127,** 2386–2387. doi:10.1021/ja042385h (Mar. 2005).

38. Chen, Z.-Z., Lü, R. & Zhu, B.-f. Effects of electron-phonon interaction on nonequilibrium transport through a single-molecule transistor. *Physical Review B* **71.** doi:10.1103/physrevb.71.165324 (Apr. 2005).

39. Metzger, R. M. *et al.* Unimolecular Electrical Rectification in Hexadecylquinolinium Tricyanoquinodimethanide. *Journal of the American Chemical Society* **119,** 10455–10466. doi:10.1021/ja971811e (Oct. 1997).

40. Elbing, M. *et al.* A single-molecule diode. *Proceedings of the National Academy of Sciences* **102,** 8815–8820. doi:10.1073/pnas.0408888102 (June 2005).

41. Kornyshev, A. A. & Kuznetsov, A. M. A New Type of In Situ Single-Molecule Rectifier. *ChemPhysChem* **7,** 1036–1040. doi:10.1002/cphc.200500685 (May 2006).

42. Díez-Pérez, I. *et al.* Rectification and stability of a single molecular diode with controlled orientation. *Nature Chemistry* **1,** 635–641. doi:10.1038/nchem.392 (Oct. 2009).

43. Yee, S. K. *et al.* Inverse Rectification in Donor–Acceptor Molecular Heterojunctions. *ACS Nano* **5,** 9256–9263. doi:10.1021/nn203520v (Oct. 2011).

44. Tawfik, S. A., Cui, X. Y., Ringer, S. P. & Stampfl, C. Communication: Electrical rectification of C59N: The role of anchoring and doping sites. *The Journal of Chemical Physics* **144,** 021101. doi:10.1063/1.4940142 (Jan. 2016).

45. Valdiviezo, J. & Palma, J. L. Molecular Rectification Enhancement Based On Conformational and Chemical Modifications. *The Journal of Physical Chemistry C* **122,** 2053–2063. doi:10.1021/acs.jpcc.7b12780 (Jan. 2018).

46. Landauer, R. Spatial Variation of Currents and Fields Due to Localized Scatterers in Metallic Conduction. *IBM Journal of Research and Development* **1,** 223–231. doi:`10.1147 /rd.13.0223` (July 1957).

47. Büttiker, M., Imry, Y., Landauer, R. & Pinhas, S. Generalized many-channel conductance formula with application to small rings. *Physical Review B* **31,** 6207–6215. ISSN: 0163-1829. doi:`10.1103/physrevb.31.6207` (May 1985).

48. Xue, Y., Datta, S. & Ratner, M. A. First-principles based matrix Green's function approach to molecular electronic devices: general formalism. d. *Chemical Physics* **281,** 151–170. ISSN: 0301-0104. doi:`10.1016/s0301-0104(02)004 46-9` (Aug. 2002).

49. Nitzan, A. & Ratner, M. A. Electron Transport in Molecular Wire Junctions. *Science* **300,** 1384–1389. ISSN: 1095-9203. doi:`10.1126/science.1081572` (May 2003).

50. Lindsay, S. & Ratner, M. Molecular Transport Junctions: Clearing Mists. *Advanced Materials* **19,** 23–31. doi:`10.100 2/adma.200601140` (Jan. 2007).

51. Herrmann, C., Solomon, G. C., Subotnik, J. E., Mujica, V. & Ratner, M. A. Ghost transmission: How large basis sets can make electron transport calculations worse. *The Journal of Chemical Physics* **132,** 024103. ISSN: 0021-9606. doi:`10.1 063/1.3283062` (Jan. 2010).

52. Markussen, T., Stadler, R. & Thygesen, K. S. The Relation between Structure and Quantum Interference in Single Molecule Junctions. *Nano Letters* **10,** 4260–4265. doi:`1 0.1021/nl101688a` (Oct. 2010).

53. Solomon, G. C. *et al.* Understanding quantum interference in coherent molecular conduction. *The Journal of Chemical Physics* **129,** 054701. doi:`10.1063/1.2958275` (Aug. 2008).

54. Solomon, G. C. in *Cross Conjugation* 397–412 (Wiley-VCH Verlag GmbH & Co. KGaA, Apr. 2016). doi:`10.1002/9783 527671182.ch11`.

55. Garner, M. H. *et al.* Permethylation Introduces Destructive Quantum Interference in Saturated Silanes. *Journal of the American Chemical Society* **141,** 15471–15476. doi:`10.10 21/jacs.9b06965` (Sept. 2019).

56. Jiang, J., Kula, M., Lu, W. & Luo, Y. First-Principles Simulations of Inelastic Electron Tunneling Spectroscopy of Molecular Electronic Devices. *Nano Letters* **5,** 1551–1555. ISSN: 1530-6992. doi:`10.1021/nl050789h` (Aug. 2005).

57. Jiang, J., Kula, M. & Luo, Y. A generalized quantum chemical approach for elastic and inelastic electron transports in molecular electronics devices. *J. Chem. Phys.* **124,** 034708. ISSN: 0021-9606. doi:10.1063/1.2159490 (2006).

58. Kula, M., Jiang, J. & Luo, Y. Probing Molecule–Metal Bonding in Molecular Junctions by Inelastic Electron Tunneling Spectroscopy. *Nano Lett.* **6,** 1693–1698. ISSN: 1530-6992. doi:10.1021/nl060951w (Aug. 2006).

59. Long, D. P. & Troisi, A. Inelastic Electron Tunneling Spectroscopy of Alkane Monolayers with Dissimilar Attachment Chemistry to Gold. *Journal of the American Chemical Society* **129,** 15303–15310. ISSN: 1520-5126. doi:10.1021/ja074970z (Dec. 2007).

60. Paulsson, M., Frederiksen, T. & Brandbyge, M. Inelastic Transport through Molecules: Comparing First-Principles Calculations to Experiments. *Nano Lett.* **6,** 258–262. ISSN: 1530-6992. doi:10.1021/nl052224r (Feb. 2006).

61. Ségerie, A., Liégeois, V. & Champagne, B. Inelastic Electron Tunneling of C 60 on Gold Surfaces from First-Principles Calculations. *The Journal of Physical Chemistry C* **119,** 803–818. ISSN: 1932-7455. doi:10.1021/jp5103093 (Jan. 2015).

62. Troisi, A. Inelastic electron tunnelling in saturated molecules with different functional groups: correlations and symmetry considerations from a computational study. *J. Phys.: Condens. Matter* **20,** 374111. ISSN: 1361-648X. doi:10.1088/0953-8984/20/37/374111 (Aug. 2008).

63. Troisi, A. *et al.* Tracing electronic pathways in molecules by using inelastic tunneling spectroscopy. *Proceedings of the National Academy of Sciences* **104,** 14255–14259. ISSN: 1091-6490. doi:10.1073/pnas.0704208104 (Aug. 2007).

64. Troisi, A. & Ratner, M. A. Modeling the inelastic electron tunneling spectra of molecular wire junctions. *Physical Review B* **72.** ISSN: 1550-235X. doi:10.1103/physrevb.72.033408 (July 2005).

65. Žutić, I., Fabian, J. & Sarma, S. D. Spintronics: Fundamentals and applications. *Reviews of Modern Physics* **76,** 323–410. doi:10.1103/revmodphys.76.323 (Apr. 2004).

66. Wolf, S. A., Chtchelkanova, A. Y. & Treger, D. M. Spintronics—A retrospective and perspective. *IBM Journal of Research and Development* **50,** 101–110. doi:10.1147/rd.501.0101 (Jan. 2006).

67. Seneor, P., Bernand-Mantel, A. & Petroff, F. Nanospintronics: when spintronics meets single electron physics. *Journal of Physics: Condensed Matter* **19,** 165222. doi:`10.1088/0953-8984/19/16/165222` (Apr. 2007).

68. Herrmann, C., Groß, L., Voigt, B. A., Shil, S. & Steenbock, T. in *Atomic- and Nanoscale Magnetism* 117–136 (Springer International Publishing, 2018). doi:`10.1007/978-3-319-99558-8_6`.

69. Gutierrez, R. *et al.* Theory of an all-carbon molecular switch. *Physical Review B* **65.** doi:`10.1103/physrevb.65.113410` (Feb. 2002).

70. Li, J., Speyer, G. & Sankey, O. F. Conduction Switching of Photochromic Molecules. *Physical Review Letters* **93.** doi:`10.1103/physrevlett.93.248302` (Dec. 2004).

71. Hofmeister, C. *et al.* Switching the conductance of a molecular junction using a proton transfer reaction. *Journal of Molecular Modeling* **20.** doi:`10.1007/s00894-014-2163-2` (Mar. 2014).

72. Schlicke, H. & Herrmann, C. Controlling Molecular Conductance: Switching Off π Sites through Protonation. *ChemPhysChem* **15,** 4011–4018. doi:`10.1002/cphc.201402561` (Oct. 2014).

73. Soler, J. M. *et al.* The SIESTA method for ab initio order-N materials simulation. *Journal of Physics: Condensed Matter* **14,** 2745–2779. doi:`10.1088/0953-8984/14/11/302` (Mar. 2002).

74. Smidstrup, S. *et al.* QuantumATK: an integrated platform of electronic and atomic-scale modelling tools. *Journal of Physics: Condensed Matter* **32,** 015901. doi:`10.1088/1361-648x/ab4007` (Oct. 2019).

75. Deffner, M. *et al. ARTAIOS - a transport code for postprocessing quantum chemical electronic structure calculations* 2009-2017.

76. Akkerman, H. B. & de Boer, B. Electrical conduction through single molecules and self-assembled monolayers. *Journal of Physics: Condensed Matter* **20,** 013001. doi:`10.1088/0953-8984/20/01/013001` (Dec. 2007).

77. Cuevas, J. C. & Scheer, E. *Molecular Electronics: An Introduction to Theory and Experiment* 2nd (eds Reed, M., Reed, M., Reed, M. & Reed, M.) (World Scientific, Singapore, 2017).

78. Xu, B. Measurement of Single-Molecule Resistance by Repeated Formation of Molecular Junctions. *Science* **301,** 1221–1223. doi:`10.1126/science.1087481` (Aug. 2003).

79. Xiang, D., Jeong, H., Lee, T. & Mayer, D. Mechanically Controllable Break Junctions for Molecular Electronics. *Advanced Materials* **25,** 4845–4867. doi:`10.1002/adma.2013 01589` (Aug. 2013).

80. *Nanolog Audio Inc.* `https://www.nanologaudio.com`.

81. Khajetoorians, A. A., Wiebe, J., Chilian, B. & Wiesendanger, R. Realizing All-Spin-Based Logic Operations Atom by Atom. *Science* **332,** 1062–1064. doi:`10.1126/science.12 01725` (May 2011).

82. Takayama, K., Matsuda, K. & Irie, M. Photoswitching of the Magnetic Interaction between a Copper(II) Ion and a Nitroxide Radical by Using a Photochromic Spin Coupler. *Chemistry - A European Journal* **9,** 5605–5609. doi:`10.100 2/chem.200305154` (Nov. 2003).

83. Escribano, A., Steenbock, T., Stork, C., Herrmann, C. & Heck, J. Why Are Dithienylethene-Linked Biscobaltocenes so Hard to Photoswitch? *ChemPhysChem* **18,** 596–609. doi:`10.1002/cphc.201601146` (Feb. 2017).

84. Matsuda, K. & Irie, M. Photochromism of Diarylethenes with Two Nitronyl Nitroxides: Photoswitching of an Intramolecular Magnetic Interaction. *Chemistry - A European Journal* **7,** 3466. doi:`10.1002/1521-3765(20010817)7:1 6<3466::aid-chem3466>3.0.co;2-x` (Aug. 2001).

85. Herrmann, C. in *Chemical Modelling* 43–70 (Royal Society of Chemistry). doi:`10.1039/9781788010719-00043`.

86. Barnes, W. L., Dereux, A. & Ebbesen, T. W. Surface plasmon subwavelength optics. *Nature* **424,** 824–830. doi:`10.1038 /nature01937` (Aug. 2003).

87. Stockman, M. I. *et al.* Roadmap on plasmonics. *Journal of Optics* **20,** 043001. doi:`10.1088/2040-8986/aaa114` (Mar. 2018).

88. Iranzo, D. A. *et al.* Probing the ultimate plasmon confinement limits with a van der Waals heterostructure. *Science* **360,** 291–295. doi:`10.1126/science.aar8438` (Apr. 2018).

89. Atwater, H. A. The Promise of PLASMONICS. *Scientific American sp* **17,** 56–63. doi:`10.1038/scientificameri can0907-56sp` (Sept. 2007).

90. Jiang, N., Zhuo, X. & Wang, J. Active Plasmonics: Principles, Structures, and Applications. *Chemical Reviews* **118,** 3054–3099. doi:`10.1021/acs.chemrev.7b00252` (Sept. 2017).

91. Uchida, K. *et al.* Generation of spin currents by surface plasmon resonance. *Nature Communications* **6.** doi:`10.1038/ncomms6910` (Jan. 2015).

92. Galperin, M. & Nitzan, A. Molecular optoelectronics: the interaction of molecular conduction junctions with light. *Physical Chemistry Chemical Physics* **14,** 9421. doi:`10.1039/c2cp40636e` (2012).

93. Wang, T. & Nijhuis, C. A. Molecular electronic plasmonics. *Applied Materials Today* **3,** 73–86. doi:`10.1016/j.apmt.2016.03.001` (June 2016).

94. Du, W. *et al.* On-chip molecular electronic plasmon sources based on self-assembled monolayer tunnel junctions. *Nature Photonics* **10,** 274–280. doi:`10.1038/nphoton.2016.43` (Mar. 2016).

95. Lacroix, J.-C., Martin, P. & Lacaze, P.-C. Tailored Surfaces/Assemblies for Molecular Plasmonics and Plasmonic Molecular Electronics. *Annual Review of Analytical Chemistry* **10,** 201–224. doi:`10.1146/annurev-anchem-061516-045325` (June 2017).

96. Daniel, M.-C. & Astruc, D. Gold nanoparticles: assembly, supramolecular chemistry, quantum-size-related properties, and applications toward biology, catalysis, and nanotechnology. *Chemical reviews* **104,** 293–346. doi:`10.1021/cr030698` (2004).

97. Ulbricht, R., Hendry, E., Shan, J., Heinz, T. F. & Bonn, M. Carrier dynamics in semiconductors studied with time-resolved terahertz spectroscopy. *Reviews of Modern Physics* **83,** 543–586. doi:`10.1103/revmodphys.83.543` (June 2011).

98. Ulbricht, R., Kurstjens, R. & Bonn, M. Assessing Charge Carrier Trapping in Silicon Nanowires Using Picosecond Conductivity Measurements. *Nano Letters* **12,** 3821–3827. doi:`10.1021/nl3017835` (June 2012).

99. Jensen, S. A. *et al.* Ultrafast Photoconductivity of Graphene Nanoribbons and Carbon Nanotubes. *Nano Letters* **13,** 5925–5930. doi:`10.1021/nl402978s` (Nov. 2013).

100. Cocker, T. L. *et al.* An ultrafast terahertz scanning tunnelling microscope. *Nature Photonics* **7,** 620–625. doi:`10.1038/nphoton.2013.151` (July 2013).

101. Shigekawa, H. in *Compendium of Surface and Interface Analysis* 749–753 (Springer Singapore, 2018). doi:`10.1007/978-981-10-6156-1_120`.

102. Jelic, V. *et al.* Ultrafast terahertz control of extreme tunnel currents through single atoms on a silicon surface. *Nature Physics* **13,** 591–598. doi:`10.1038/nphys4047` (Feb. 2017).

103. Liu, S., Wolf, M. & Kumagai, T. Plasmon-Assisted Resonant Electron Tunneling in a Scanning Tunneling Microscope Junction. *Physical Review Letters* **121.** doi:`10.1103/physrevlett.121.226802` (Nov. 2018).

104. Du, S., Yoshida, K., Zhang, Y., Hamada, I. & Hirakawa, K. Terahertz dynamics of electron–vibron coupling in single molecules with tunable electrostatic potential. *Nature Photonics* **12,** 608–612. doi:`10.1038/s41566-018-0241-1` (Sept. 2018).

105. Yoshioka, K. *et al.* Tailoring Single-Cycle Near Field in a Tunnel Junction with Carrier-Envelope Phase-Controlled Terahertz Electric Fields. *Nano Letters* **18,** 5198–5204. doi:`10.1021/acs.nanolett.8b02161` (July 2018).

106. Yoshida, S. *et al.* Subcycle Transient Scanning Tunneling Spectroscopy with Visualization of Enhanced Terahertz Near Field. *ACS Photonics* **6,** 1356–1364. doi:`10.1021/acsphotonics.9b00266` (May 2019).

107. Yoshioka, K. *et al.* Terahertz-Field-Induced Nonlinear Electron Delocalization in Au Nanostructures. *Nano Letters* **15,** 1036–1040. doi:`10.1021/nl503916t` (Jan. 2015).

108. Tsuji, Y. & Hoffmann, R. Helical Oligoenes: Conformations, Bond Alternation, and Competing Through-Bond and Through-Space Transmission. *Chem. Eur. J.* **22,** 4878–4888 (2016).

109. Garner, M. H., Jensen, A., Hyllested, L. O. H. & Solomon, G. C. Helical orbitals and circular currents in linear carbon wires. *Chem. Sci.* **10,** 4598–4608 (2019).

110. Jensen, A., Garner, M. H. & Solomon, G. C. When Current Does Not Follow Bonds: Current Density in Saturated Molecules. *The Journal of Physical Chemistry C* **123,** 12042–12051. doi:`10.1021/acs.jpcc.8b11092` (Apr. 2019).

111. Deffner, M. & Herrmann, C. The Limits of Inelastic Tunneling Spectroscopy for Identifying Transport Pathways. *(preprint, submitted to Chemrxiv).* doi:`10.26434/chemrxiv.11954403.v1` (Mar. 2020).

112. Deffner, M., Schulz, F. & Lange, H. Impact of the Crosslinker's Molecular Structure on the Aggregation of Gold Nanoparticles. *Zeitschrift für Physikalische Chemie* **231.** ISSN: 0942-9352. doi:10.1515/zpch-2016-0865 (Jan. 2017).

113. Gorris, F. E. S. *et al.* Postdeposition Ligand Exchange Allows Tuning the Transport Properties of Large-Scale CuInSe$_2$ Quantum Dot Solids. *Advanced Optical Materials* **8.** doi:10.1002/adom.201901058 (Nov. 2019).

114. Attila Szabo, N. S. O. *Modern Quantum Chemistry* 480 pp. ISBN: 0486691861 (Dover Publications Inc., Jan. 1, 1996).

115. Ryndyk, D. A. *Theory of Quantum Transport at Nanoscale* (Springer-Verlag GmbH, Dec. 8, 2015).

116. Zabet-Khosousi, A. & Dhirani, A.-A. Charge Transport in Nanoparticle Assemblies. *Chemical Reviews* **108,** 4072–4124. doi:10.1021/cr0680134 (2008).

117. Wessels, J. M. *et al.* Optical and Electrical Properties of Three-Dimensional Interlinked Gold Nanoparticle Assemblies. *Journal of the American Chemical Society* **126,** 3349–3356. doi:10.1021/ja0377605 (Mar. 2004).

118. Jaiswal, M. & Menon, R. Polymer electronic materials: a review of charge transport. *Polymer International* **55,** 1371–1384. doi:10.1002/pi.2111 (2006).

119. Tessler, N., Preezant, Y., Rappaport, N. & Roichman, Y. Charge Transport in Disordered Organic Materials and Its Relevance to Thin-Film Devices: A Tutorial Review. *Advanced Materials* **21,** 2741–2761. doi:10.1002/adma.200803541 (May 2009).

120. Guyot-Sionnest, P. Electrical Transport in Colloidal Quantum Dot Films. *The Journal of Physical Chemistry Letters* **3,** 1169–1175. doi:10.1021/jz300048y (Apr. 2012).

121. Heikkila, T. T. *The Physics of Nanoelectronics: Transport and Fluctuation Phenomena at Low Temperatures (Oxford Master Series in Physics)* ISBN: 9780199592449 (Oxford University Press, 2013).

122. Hecht, E. *Optics* ISBN: 020111609X (Addison-Wesley Pub. Co, Reading, Mass, 1987).

123. Mujica, V., Kemp, M. & Ratner, M. A. Electron conduction in molecular wires. I. A scattering formalism. *J. Chem. Phys.* **101,** 6849. ISSN: 0021-9606. doi:10.1063/1.468314 (1994).

124. Ventra, M. D. *Electrical Transport in Nanoscale Systems* ISBN: 9780511755606 (Cambridge University Press, 2010).

125. Aharonov, Y. & Bohm, D. Significance of Electromagnetic Potentials in the Quantum Theory. *Physical Review* **115,** 485–491. doi:`10.1103/physrev.115.485` (Aug. 1959).

126. McCreery, R. L., Yan, H. & Bergren, A. J. A critical perspective on molecular electronic junctions: there is plenty of room in the middle. *Phys. Chem. Chem. Phys.* **15,** 1065–1081. doi:`10.1039/c2cp43516k` (2013).

127. Van der Molen, S. J. *et al.* Light-Controlled Conductance Switching of Ordered Metal-Molecule-Metal Devices. *Nano Letters* **9,** 76–80. doi:`10.1021/nl802487j` (Jan. 2009).

128. Banerjee, P. *et al.* Plasmon-Induced Electrical Conduction in Molecular Devices. *ACS Nano* **4,** 1019–1025. doi:`10.1021/nn901148m` (Jan. 2010).

129. Liao, J. *et al.* Ordered nanoparticle arrays interconnected by molecular linkers: electronic and optoelectronic properties. *Chemical Society Reviews* **44,** 999–1014. doi:`10.1039/c4cs00225c` (2015).

130. Lörtscher, E., Weber, H. B. & Riel, H. Statistical Approach to Investigating Transport through Single Molecules. *Physical Review Letters* **98.** doi:`10.1103/physrevlett.98.176807` (Apr. 2007).

131. McCreery, R. L. Molecular Electronic Junctions. *Chemistry of Materials* **16,** 4477–4496. doi:`10.1021/cm049517q` (Nov. 2004).

132. McCreery, R. L. & Bergren, A. J. Progress with Molecular Electronic Junctions: Meeting Experimental Challenges in Design and Fabrication. *Advanced Materials* **21,** 4303–4322. doi:`10.1002/adma.200802850` (Nov. 2009).

133. Repp, J., Meyer, G., Stojković, S. M., Gourdon, A. & Joachim, C. Molecules on Insulating Films: Scanning-Tunneling Microscopy Imaging of Individual Molecular Orbitals. *Physical Review Letters* **94.** doi:`10.1103/physrevlett.94.026803` (Jan. 2005).

134. Reed, M. A. Inelastic electron tunneling spectroscopy. *Materials Today* **11,** 46–50. ISSN: 1369-7021. doi:`10.1016/s1369-7021(08)70238-4` (Nov. 2008).

135. Hong, W. *et al.* An MCBJ case study: The influence of π-conjugation on the single-molecule conductance at a solid/liquid interface. *Beilstein Journal of Nanotechnology* **2,** 699–713. doi:`10.3762/bjnano.2.76` (Oct. 2011).

136. Reuter, M. G., Hersam, M. C., Seideman, T. & Ratner, M. A. Signatures of Cooperative Effects and Transport Mechanisms in Conductance Histograms. *Nano Letters* **12,** 2243–2248. doi:`10.1021/nl204379j` (Apr. 2012).

137. Makk, P. *et al.* Correlation Analysis of Atomic and Single-Molecule Junction Conductance. *ACS Nano* **6,** 3411–3423. doi:`10.1021/nn300440f` (Mar. 2012).

138. Datta, S. *Electronic Transport in Mesoscopic Systems* doi:`10.1017/cbo9780511805776` (Cambridge University Press, Sept. 1995).

139. Cuniberti, G. *Introducing molecular electronics* ISBN: 3540279946 (Springer, Berlin New York, 2005).

140. Reed, M. Molecular-scale electronics. *Proceedings of the IEEE* **87,** 652–658. doi:`10.1109/5.752520` (Apr. 1999).

141. Bourgoin, J.-P. in *Lecture Notes in Physics* 105–124 (Springer Berlin Heidelberg, 2001). doi:`10.1007/3-540-45532-9_6`.

142. Aradhya, S. V. & Venkataraman, L. Single-molecule junctions beyond electronic transport. *Nature Nanotechnology* **8,** 399–410. doi:`10.1038/nnano.2013.91` (June 2013).

143. Nichols, R. J. & Higgins, S. J. Single-Molecule Electronics: Chemical and Analytical Perspectives. *Annual Review of Analytical Chemistry* **8,** 389–417. doi:`10.1146/annurev-anchem-071114-040118` (July 2015).

144. Su, T. A., Neupane, M., Steigerwald, M. L., Venkataraman, L. & Nuckolls, C. Chemical principles of single-molecule electronics. *Nature Reviews Materials* **1.** doi:`10.1038/natrevmats.2016.2` (Feb. 2016).

145. Vilan, A., Aswal, D. & Cahen, D. Large-Area, Ensemble Molecular Electronics: Motivation and Challenges. *Chemical Reviews* **117,** 4248–4286. doi:`10.1021/acs.chemrev.6b00595` (Feb. 2017).

146. Xin, N. *et al.* Concepts in the design and engineering of single-molecule electronic devices. *Nature Reviews Physics* **1,** 211–230. doi:`10.1038/s42254-019-0022-x` (Feb. 2019).

147. Neil W. Ashcroft, N. M. *Solid State Physics* 848 pp. ISBN: 0030839939 (Cengage Learning, Inc, Jan. 2, 1976).

148. Breit, G. & Wigner, E. Capture of Slow Neutrons. *Physical Review* **49,** 519–531. doi:10.1103/physrev.49.519 (Apr. 1936).

149. Becke, A. D. Perspective: Fifty years of density-functional theory in chemical physics. *Journal of Chemical Physics* **140,** 18A301. ISSN: 1089-7690. doi:10.1063/1.4869598 (May 2014).

150. Hohenberg, P. & Kohn, W. Inhomogeneous Electron Gas. *Phys. Rev.* **136,** B864–B871. ISSN: 0031-899X. doi:10.1103/physrev.136.b864 (Nov. 1964).

151. Kohn, W. & Sham, L. J. Self-Consistent Equations Including Exchange and Correlation Effects. *Phys. Rev.* **140,** A1133–A1138. ISSN: 0031-899X. doi:10.1103/physrev.140.a1133 (Nov. 1965).

152. Vosko, S. H., Wilk, L. & Nusair, M. Accurate spin-dependent electron liquid correlation energies for local spin density calculations: a critical analysis. *Canadian Journal of Physics* **58,** 1200–1211. ISSN: 1208-6045. doi:10.1139/p80-159 (Aug. 1980).

153. Perdew, J. P. & Zunger, A. Self-interaction correction to density-functional approximations for many-electron systems. *Phys. Rev. B* **23,** 5048–5079. ISSN: 0163-1829. doi:10.1103/physrevb.23.5048 (May 1981).

154. Perdew, J. P. & Wang, Y. Accurate and simple analytic representation of the electron-gas correlation energy. *Phys. Rev. B* **45,** 13244–13249. ISSN: 1095-3795. doi:10.1103/physrevb.45.13244 (June 1992).

155. Perdew, J. P. Density-functional approximation for the correlation energy of the inhomogeneous electron gas. *Phys. Rev. B* **33,** 8822–8824. ISSN: 0163-1829. doi:10.1103/physrevb.33.8822 (June 1986).

156. Becke, A. D. Density-functional exchange-energy approximation with correct asymptotic behavior. *Phys. Rev. A* **38,** 3098–3100. ISSN: 0556-2791. doi:10.1103/physreva.38.3098 (Sept. 1988).

157. Becke, A. D. Density-functional thermochemistry. III. The role of exact exchange. *The Journal of Chemical Physics* **98,** 5648. ISSN: 0021-9606. doi:10.1063/1.464913 (1993).

158. Lee, C., Yang, W. & Parr, R. G. Development of the Colle-Salvetti correlation-energy formula into a functional of the electron density. *Phys. Rev. B* **37,** 785–789. ISSN: 0163-1829. doi:10.1103/physrevb.37.785 (Jan. 1988).

159. Burke, K. Perspective on density functional theory. *The Journal of Chemical Physics* **136,** 150901. doi:`10.1063/1.4704546` (Apr. 2012).

160. Jones, R. Density functional theory: Its origins, rise to prominence, and future. *Reviews of Modern Physics* **87,** 897–923. doi:`10.1103/revmodphys.87.897` (Aug. 2015).

161. Huang, P. & Carter, E. A. Advances in Correlated Electronic Structure Methods for Solids, Surfaces, and Nanostructures. *Annual Review of Physical Chemistry* **59,** 261–290. doi:`10.1146/annurev.physchem.59.032607.093528` (May 2008).

162. Koentopp, M., Chang, C., Burke, K. & Car, R. Density functional calculations of nanoscale conductance. *Journal of Physics: Condensed Matter* **20,** 083203. doi:`10.1088/0953-8984/20/8/083203` (Feb. 2008).

163. Su, N. Q. & Xu, X. Development of New Density Functional Approximations. *Annual Review of Physical Chemistry* **68,** 155–182. doi:`10.1146/annurev-physchem-052516-044835` (May 2017).

164. Pribram-Jones, A., Gross, D. A. & Burke, K. DFT: A Theory Full of Holes? *Annual Review of Physical Chemistry* **66,** 283–304. doi:`10.1146/annurev-physchem-040214-121420` (2015).

165. Meir, Y. & Wingreen, N. S. Landauer formula for the current through an interacting electron region. *Physical Review Letters* **68,** 2512–2515. doi:`10.1103/physrevlett.68.2512` (Apr. 1992).

166. Williams, A. R., Feibelman, P. J. & Lang, N. D. Green's-function methods for electronic-structure calculations. *Physical Review B* **26,** 5433–5444. doi:`10.1103/physrevb.26.5433` (Nov. 1982).

167. edon. GOLLUM: a next-generation simulation tool for electron, thermal and spin transport. *New Journal of Physics* **16,** 093029. doi:`10.1088/1367-2630/16/9/093029` (Sept. 2014).

168. Herrmann, C., Solomon, G. C. & Ratner, M. A. Local Pathways in Coherent Electron Transport through Iron Porphyrin Complexes: A Challenge for First-Principles Transport Calculations. *The Journal of Physical Chemistry C* **114,** 20813–20820. doi:`10.1021/jp107147x` (Oct. 2010).

169. Herrmann, C., Solomon, G. C. & Ratner, M. A. Organic Radicals As Spin Filters. *Journal of the American Chemical Society* **132,** 3682–3684. doi:10.1021/ja910483b (Mar. 2010).

170. Steenbock, T., Tasche, J., Lichtenstein, A. I. & Herrmann, C. A Green's-Function Approach to Exchange Spin Coupling As a New Tool for Quantum Chemistry. *Journal of Chemical Theory and Computation* **11,** 5651–5664. ISSN: 1549-9626. doi:10.1021/acs.jctc.5b00349 (Dec. 2015).

171. Solomon, G. C., Herrmann, C., Hansen, T., Mujica, V. & Ratner, M. A. Exploring local currents in molecular junctions. *Nature Chemistry* **2,** 223–228. ISSN: 1755-4349. doi:10.1038/nchem.546 (Feb. 2010).

172. Verzijl, C. J. O., Seldenthuis, J. S. & Thijssen, J. M. Applicability of the wide-band limit in DFT-based molecular transport calculations. *The Journal of Chemical Physics* **138,** 094102. doi:10.1063/1.4793259 (Mar. 2013).

173. Papaconstantopoulos, D. A. *Handbook of the Band Structure of Elemental Solids* ISBN: 9781441982643 (Springer-Verlag GmbH, Nov. 10, 2014).

174. Smit, R. H. M. *et al.* Measurement of the conductance of a hydrogen molecule. *Nature* **419,** 906–909. doi:10.1038/nature01103 (Oct. 2002).

175. Frisch, M. J. *et al. Gaussian 09 Revision A.1* Gaussian Inc. Wallingford CT 2009.

176. Hay, P. J. & Wadt, W. R. Ab initio effective core potentials for molecular calculations. Potentials for the transition metal atoms Sc to Hg. *The Journal of Chemical Physics* **82,** 270–283. doi:10.1063/1.448799. eprint: http://dx.doi.org/10.1063/1.448799 (1985).

177. Xue, Y., Datta, S. & Ratner, M. A. Charge transfer and "band lineup" in molecular electronic devices: A chemical and numerical interpretation. *The Journal of Chemical Physics* **115,** 4292–4299. doi:10.1063/1.1391253 (Sept. 2001).

178. Pauly, F., Viljas, J. K., Cuevas, J. C. & Schön, G. Density-functional study of tilt-angle and temperature-dependent conductance in biphenyl dithiol single-molecule junctions. *Phys. Rev. B* **77.** doi:10.1103/physrevb.77.155312 (Apr. 2008).

179. Guédon, C. M. *et al.* Observation of quantum interference in molecular charge transport. *Nature Nanotechnology* **7,** 305–309. doi:10.1038/nnano.2012.37 (Mar. 2012).

180. Hansen, T., Solomon, G. C., Andrews, D. Q. & Ratner, M. A. Interfering pathways in benzene: An analytical treatment. *The Journal of Chemical Physics* **131,** 194704. doi:10.1063/1.3259548 (2009).

181. Kocherzhenko, A. A., Grozema, F. C. & Siebbeles, L. D. A. Charge Transfer Through Molecules with Multiple Pathways: Quantum Interference and Dephasing. *The Journal of Physical Chemistry C* **114,** 7973–7979. doi:10.1021/jp9117216 (Apr. 2010).

182. Li, Y., Yu, X., Zhen, Y., Dong, H. & Hu, W. Two-Pathway Viewpoint to Interpret Quantum Interference in Molecules Containing Five-Membered Heterocycles: Thienoacenes as Examples. *The Journal of Physical Chemistry C* **123,** 15977–15984. doi:10.1021/acs.jpcc.9b03177 (June 2019).

183. Stafford, C. A., Cardamone, D. M. & Mazumdar, S. The quantum interference effect transistor. *Nanotechnology* **18,** 424014. doi:10.1088/0957-4484/18/42/424014 (Sept. 2007).

184. Ke, S.-H., Yang, W. & Baranger, H. U. Quantum-Interference-Controlled Molecular Electronics. *Nano Letters* **8,** 3257–3261. doi:10.1021/nl8016175 (Oct. 2008).

185. Chen, S. *et al.* Interference and Molecular Transport - A Dynamical View: Time-Dependent Analysis of Disubstituted Benzenes. *The Journal of Physical Chemistry Letters* **5,** 2748–2752. ISSN: 1948-7185. doi:10.1021/jz5007143 (Aug. 2014).

186. Salhani, C. *et al.* Inelastic electron tunneling spectroscopy in molecular junctions showing quantum interference. *Physical Review B* **95.** doi:10.1103/physrevb.95.165431 (Apr. 2017).

187. Gunasekaran, S., Greenwald, J. E. & Venkataraman, L. Visualizing Quantum Interference in Molecular Junctions. *Nano Letters.* doi:10.1021/acs.nanolett.0c00605 (Mar. 2020).

188. Cardamone, D. M., Stafford, C. A. & Mazumdar, S. Controlling Quantum Transport through a Single Molecule. *Nano Letters* **6,** 2422–2426. doi:10.1021/nl0608442 (Nov. 2006).

189. Andrews, D. Q., Solomon, G. C., Duyne, R. P. V. & Ratner, M. A. Single Molecule Electronics: Increasing Dynamic Range and Switching Speed Using Cross-Conjugated Species. *Journal of the American Chemical Society* **130,** 17309–17319. doi:10.1021/ja804399q (Dec. 2008).

190. Renaud, N. *et al.* A NOR–AND quantum running gate molecule. *Chemical Physics Letters* **472,** 74–79. doi:10.1016/j.cplett.2009.02.071 (Apr. 2009).

191. Markussen, T., Schiötz, J. & Thygesen, K. S. Electrochemical control of quantum interference in anthraquinone-based molecular switches. *The Journal of Chemical Physics* **132,** 224104. doi:10.1063/1.3451265 (June 2010).

192. Liu, H. *et al.* Nonequilibrium Green's function study on the electronic structure and transportation behavior of the conjugated molecular junction: Terminal connections and intramolecular connections. *The Journal of Chemical Physics* **130,** 244501. doi:10.1063/1.3151682 (June 2009).

193. Hines, T. *et al.* Transition from Tunneling to Hopping in Single Molecular Junctions by Measuring Length and Temperature Dependence. *Journal of the American Chemical Society* **132,** 11658–11664. doi:10.1021/ja1040946 (Aug. 2010).

194. Lu, Q. *et al.* From Tunneling to Hopping: A Comprehensive Investigation of Charge Transport Mechanism in Molecular Junctions Based on Oligo(p-phenylene ethynylene)s. *ACS Nano* **3,** 3861–3868. doi:10.1021/nn9012687 (Nov. 2009).

195. Choi, S. H. *et al.* Transition from Tunneling to Hopping Transport in Long, Conjugated Oligo-imine Wires Connected to Metals. *Journal of the American Chemical Society* **132,** 4358–4368. doi:10.1021/ja910547c (Mar. 2010).

196. Zhao, X. *et al.* Oligo(aryleneethynylene)s with Terminal Pyridyl Groups: Synthesis and Length Dependence of the Tunneling-to-Hopping Transition of Single-Molecule Conductances. *Chemistry of Materials* **25,** 4340–4347. doi:10.1021/cm4029484 (Oct. 2013).

197. Smith, C. E. *et al.* Length-Dependent Nanotransport and Charge Hopping Bottlenecks in Long Thiophene-Containing π-Conjugated Molecular Wires. *Journal of the American Chemical Society* **137,** 15732–15741. doi:10.1021/jacs.5b07400 (Dec. 2015).

198. Kröncke, S. & Herrmann, C. Designing Long-Range Charge Delocalization from First-Principles. *Journal of Chemical Theory and Computation* **15,** 165–177. doi:10.1021/ac s.jctc.8b00872 (Nov. 2018).

199. Pluchery, O., Caillard, L., Dollfus, P. & Chabal, Y. J. Gold Nanoparticles on Functionalized Silicon Substrate under Coulomb Blockade Regime: An Experimental and Theoretical Investigation. *The Journal of Physical Chemistry B* **122,** 897–903. doi:10.1021/acs.jpcb.7b06979 (Nov. 2017).

200. Maeda, K. *et al.* Logic Operations of Chemically Assembled Single-Electron Transistor. *ACS Nano* **6,** 2798–2803. doi:1 0.1021/nn3003086 (Mar. 2012).

201. Mott, N. F. Conduction in non-crystalline materials: III. Localized states in a pseudogap and near extremities of conduction and valence bands. *Philosophical Magazine* **19,** 835–852. ISSN: 1478-6435. doi:DOI:10.1016/0022-3093 (68)90002-1 (1969).

202. Yu, D., Wang, C., Wehrenberg, B. L. & Guyot-Sionnest, P. Variable Range Hopping Conduction in Semiconductor Nanocrystal Solids. *Physical Review Letters* **92,** 216802. doi:10.1103/PhysRevLett.92.216802 (2004).

203. Liu, H., Pourret, A. & Guyot-Sionnest, P. Mott and Efros-Shklovskii variable range hopping in CdSe quantum dots films. *ACS Nano* **4,** 5211–5216. ISSN: 19360851. doi:10.1 021/nn101376u (2010).

204. Jaklevic, R. C. & Lambe, J. Molecular Vibration Spectra by Electron Tunneling. *Physical Review Letters* **17,** 1139–1140. ISSN: 0031-9007. doi:10.1103/physrevlett.17.1139 (Nov. 1966).

205. Chalmers, J. & Griffiths, P. *Handbook of vibrational spectroscopy Handbook of Vibrational Spectroscopy* **Bd. 1.** ISBN: 9780471988472 (J. Wiley, 2002).

206. Zandvliet, H. J. & van Houselt, A. Scanning Tunneling Spectroscopy. *Annual Review of Analytical Chemistry* **2,** 37–55. ISSN: 1936-1335. doi:10.1146/annurev-anchem-060 908-155213 (July 2009).

207. Lin, L.-L., Wang, C.-K. & Luo, Y. Inelastic Electron Tunneling Spectroscopy of Gold-Benzenedithiol-Gold Junctions: Accurate Determination of Molecular Conformation. *ACS Nano* **5,** 2257–2263. ISSN: 1936-086X. doi:10.1021/nn10 3522k (Mar. 2011).

208. Lin, L., Jiang, J. & Luo, Y. Elastic and inelastic electron transport in metal–molecule(s)–metal junctions. **47,** 167–187. ISSN: 1386-9477. doi:10.1016/j.physe.2012.10.017 (2013).

209. Ullmann, G. M. & Kostic, N. M. Electron-Tunneling Paths in Various Electrostatic Complexes between Cytochrome c and Plastocyanin. Anisotropy of the Copper-Ligand Interactions and Dependence of the Iron–Copper Electronic Coupling on the Metalloprotein Orientation. *J. Am. Chem. Soc.* **117,** 4766–4774 (1995).

210. Balabin, I. A. & Onuchic, J. N. Dynamically Controlled Protein Tunneling Paths in Photosynthetic Reaction Centers. *Science* **290,** 114–117 (2000).

211. Jasaitis, A., Johansson, M. P., Wikstrom, M., Vos, M. H. & Verkhovsky, M. I. Nanosecond electron tunneling between the hemes in cytochrome bo3. *Proc. Nat. Acad. Sci.* **104,** 20811–20814 (2007).

212. Beratan, D. N. & Balabin, I. A. Heme–copper oxidases use tunneling pathways. *Proc. Nat. Acad. Sci.* **105,** 403–404 (2008).

213. Balabin, I. A., Hu, X. & Beratan, D. N. Exploring Biological Electron Transfer Pathway Dynamics with the Pathways Plugin for VMD. *J. Comput. Chem.* **33,** 906–910 (2012).

214. Rai, D., Hod, O. & Nitzan, A. Circular Currents in Molecular Wires. *The Journal of Physical Chemistry C* **114,** 20583–20594 (2010).

215. Xie, Z. *et al.* Spin Specific Electron Conduction through DNA Oligomers. *Nano Lett.* **11,** 4652–4655 (2011).

216. Göhler, B. *et al.* Spin selectivity in electron transmission through self-assembled monolayers of double-stranded DNA. *Science* **331,** 894–897 (2011).

217. Gutierrez, R., Diaz, E., Naaman, R. & Cuniberti, G. Spin-selective transport through helical molecular systems. *Phys. Rev. B* **85,** 081404 (2012).

218. Gutierrez, R. *et al.* Modeling Spin Transport in Helical Fields: Derivation of an Effective Low-Dimensional Hamiltonian. *J. Phys. Chem. C* **117,** 22276–22284 (2013).

219. Mishra, D. *et al.* Spin-dependent electron transmission through bacteriorhodopsin embedded in purple membrane. *Proc. Natl. Acad. Sci.* **110,** 14872–14876 (2013).

220. Zwang, T. J., Hürlimann, S., Hill, M. G. & Barton, J. K. Helix-Dependent Spin Filtering through the DNA Duplex. *J. Am. Chem. Soc.* **138,** 15551–15554 (2016).

221. Guo, A.-M. & Sun, Q.-f. Spin-Selective Transport of Electrons in DNA Double Helix. *Phys Rev. Lett.* **108,** 218102 (2012).

222. Guo, A.-M. & Sun, Q.-F. Spin-dependent electron transport in protein-like single-helical molecules. *Proc. Natl. Acad. Sci.* **111,** 11658–11662 (2014).

223. Kettner, M. *et al.* Spin Filtering in Electron Transport Through Chiral Oligopeptides. *J. Phys. Chem. C* **119,** 14542–14547 (2015).

224. Varela, S., Mujica, V. & Medina, E. Effective spin–orbit couplings in an analytical tight-binding model of DNA: spin filtering and chiral spin transport. *Phys. Rev. B* **93,** 155436 (2016).

225. Kiran, V. *et al.* Helicenes — A New Class of Organic Spin Filter. *Adv. Mater.* **28,** 1957–1962 (2016).

226. Aragones, A. C. *et al.* Measuring the Spin-Polarization Power of a Single Chiral Molecule. *small* **13,** 1602519 (2017).

227. Kettner, M. *et al.* Chirality-Dependent Electron Spin Filtering by Molecular Monolayers of Helicenes. *J. Phys. Chem. Lett.* **9,** 2025–2030 (2018).

228. Varela, S., Mujica, V. & Medina, E. Spin-orbit Coupling Modulation in DNA by Mechanical Deformations. *Chimia* **72,** 411–417 (2018).

229. Maslyuk, V. V., Gutierrez, R., Dianat, A., Mujica, V. & Cuniberti, G. Enhanced Magnetoresistance in Chiral Molecular Junctions. *J. Phys. Chem. Lett.* **9,** 5453–5459 (2018).

230. Zöllner, M. S., Varela, S., Medina, E., Mujica, V. & Herrmann, C. Chiral-Induced Spin Selectivity: A Symmetry Analysis of Electronic Transmission. ChemRxiv, DOI: 10.26434/chemrxiv.8325248.v2 (2019).

231. Dhakal, U. & Rai, D. Circular current and induced force in a molecular ring junction. *J. Phys.: Condens. Matter* **31,** 125302 (2019).

232. Naaman, R., Paltiel, Y. & Waldeck, D. H. Chiral molecules and the electron spin. *Nature Reviews* **3,** 250–260 (2019).

233. Abendroth, J. M. *et al.* Spin-Dependent Ionization of Chiral Molecular Films. *J. Am. Chem. Soc.* **141,** 3863–3874 (2019).

234. Varela, S., Zambrano, I., Mujica, V., Berche, B. & Medina, E. Spin-orbit interaction and spin selectivity for tunneling electron transfer in DNA. to be submitted (2019).

235. Todorov, T. N. Tight-binding simulation of current-carrying nanostructures. *J. Phys.: Condens. Matter* **14,** 3049–3084 (2002).

236. Pecchia, A. & Carlo, A. D. Atomistic theory of transport in organic and inorganic nanostructures. *Rep. Prog. Phys.* **67,** 1497–1561 (2004).

237. Ernzerhof, M., Bahmann, H., Goyer, F., Zhuang, M. & Rocheleau, P. Electron Transmission through Aromatic Molecules. *J. Chem. Theory Comput.* **2,** 1291–1297 (2006).

238. Sai, N., Bushong, N., Hatcher, R. & di Ventra, M. Microscopic current dynamics in nanoscale junctions. *Phys. Rev. B* **75,** 15410–115418 (2007).

239. Solomon, G. C., Herrmann, C. & Ratner, M. A. Molecular Electronic Junction Transport: Some Pathways and Some Idea. *Top. Curr. Chem.* **313,** 1–38 (2012).

240. Hansen, T., Solomon, G. C. & Hansen, T. Interatomic inelastic current. *The Journal of Chemical Physics* **146,** 092322. doi:10.1063/1.4975320 (Mar. 2017).

241. Pohl, V., Steinkasserer, L. E. M. & Tremblay, J. C. Imaging Time-Dependent Electronic Currents through a Graphene-Based Nanojunction. *The Journal of Physical Chemistry Letters* **10,** 5387–5394. doi:10.1021/acs.jpclett.9b01732 (Aug. 2019).

242. Troisi, A. & Ratner, M. A. Inelastic insights for molecular tunneling pathways: Bypassing the terminal groups. *Physical Chemistry Chemical Physics* **9,** 2421. ISSN: 1463-9084. doi:10.1039/b702377d (2007).

243. Weymuth, T. *et al.* M O V I P AC: Vibrational spectroscopy with a robust meta-program for massively parallel standard and inverse calculations. *Journal of Computational Chemistry* **33,** 2186–2198. ISSN: 0192-8651. doi:10.1002/jcc.23036 (June 2012).

244. Troisi, A., Ratner, M. A. & Nitzan, A. Vibronic effects in off-resonant molecular wire conduction. *J. Chem. Phys.* **118,** 6072. ISSN: 0021-9606. doi:10.1063/1.1556854 (2003).

245. Reiher, M. & Neugebauer, J. A mode-selective quantum chemical method for tracking molecular vibrations applied to functionalized carbon nanotubes. *The Journal of Chemical Physics* **118,** 1634–1641. ISSN: 1089-7690. doi:10.1063/1.1523908 (Jan. 2003).

246. Herrmann, C., Neugebauer, J. & Reiher, M. Finding a needle in a haystack: direct determination of vibrational signatures in complex systems. *New Journal of Chemistry* **31,** 818. ISSN: 1369-9261. doi:10.1039/b618769m (2007).

247. Galperin, M., Ratner, M. A. & Nitzan, A. Molecular transport junctions: vibrational effects. *Journal of Physics: Condensed Matter* **19,** 103201. doi:10.1088/0953-8984/19/10/103201 (2007).

248. Davidson, E. R. The iterative calculation of a few of the lowest eigenvalues and corresponding eigenvectors of large real-symmetric matrices. *Journal of Computational Physics* **17,** 87–94 (1975).

249. Reiher, M. & Neugebauer, J. Convergence characteristics and efficiency of mode-tracking calculations on preselected molecular vibrations. *Physical Chemistry Chemical Physics* **6,** 4621. doi:10.1039/b406134a (2004).

250. Herrmann, C., Neugebauer, J. & Reiher, M. QM/MM vibrational mode tracking. *Journal of Computational Chemistry* **29,** 2460–2470. ISSN: 1096-987X. doi:10.1002/jcc.20988 (Oct. 2008).

251. Kushmerick, J. G. *et al.* Vibronic Contributions to Charge Transport Across Molecular Junctions. *Nano Lett.* **4,** 639–642. ISSN: 1530-6992. doi:10.1021/nl049871n (Apr. 2004).

252. Wang, W., Lee, T., Kretzschmar, I. & Reed, M. A. Inelastic Electron Tunneling Spectroscopy of an Alkanedithiol Self-Assembled Monolayer. *Nano Letters* **4,** 643–646. doi:10.1021/nl049870v (Apr. 2004).

253. Hihath, J., Bruot, C. & Tao, N. Electron−Phonon Interactions in Single Octanedithiol Molecular Junctions. *ACS Nano* **4,** 3823–3830. ISSN: 1936-086X. doi:10.1021/nn100470s (July 2010).

254. Frisenda, R., Perrin, M. L. & van der Zant, H. S. J. Probing the local environment of a single OPE3 molecule using inelastic tunneling electron spectroscopy. *Beilstein Journal of Nanotechnology* **6,** 2477–2484. ISSN: 2190-4286. doi:10.3762/bjnano.6.257 (Dec. 2015).

255. Lykkebo, J., Gagliardi, A., Pecchia, A. & Solomon, G. C. Strong Overtones Modes in Inelastic Electron Tunneling Spectroscopy with Cross-Conjugated Molecules: A Prediction from Theory. *ACS Nano* **7**, 9183–9194. doi:10.1021/nn4037915 (Oct. 2013).

256. Lykkebo, J., Gagliardi, A., Pecchia, A. & Solomon, G. C. IETS and quantum interference: Propensity rules in the presence of an interference feature. *The Journal of Chemical Physics* **141**, 124119. doi:10.1063/1.4896234 (Sept. 2014).

257. Weigend, F. & Ahlrichs, R. Balanced basis sets of split valence, triple zeta valence and quadruple zeta valence quality for H to Rn: Design and assessment of accuracy. *Physical Chemistry Chemical Physics* **7**, 3297. ISSN: 1463-9084. doi:10.1039/b508541a (2005).

258. Weigend, F. Accurate Coulomb-fitting basis sets for H to Rn. *Physical Chemistry Chemical Physics* **8**, 1057. doi:10.1039/b515623h (2006).

259. Kim, Y., Hellmuth, T. J., Bürkle, M., Pauly, F. & Scheer, E. Characteristics of Amine-Ended and Thiol-Ended Alkane Single-Molecule Junctions Revealed by Inelastic Electron Tunneling Spectroscopy. *ACS Nano* **5**, 4104–4111. ISSN: 1936-086X. doi:10.1021/nn200759s (May 2011).

260. Viljas, J. K., Cuevas, J. C., Pauly, F. & Häfner, M. Electron-vibration interaction in transport through atomic gold wires. *Physical Review B* **72.** doi:10.1103/physrevb.72.245415 (Dec. 2005).

261. Lü, J.-T. *et al.* Efficient calculation of inelastic vibration signals in electron transport: Beyond the wide-band approximation. *Physical Review B* **89.** doi:10.1103/physrevb.89.081405 (Feb. 2014).

262. Troisi, A. & Ratner, M. A. Propensity rules for inelastic electron tunneling spectroscopy of single-molecule transport junctions. *J. Chem. Phys.* **125**, 214709. ISSN: 0021-9606. doi:10.1063/1.2390698 (2006).

263. Gagliardi, A. *et al.* A priorimethod for propensity rules for inelastic electron tunneling spectroscopy of single-molecule conduction. *Physical Review B* **75.** doi:10.1103/physrevb.75.174306 (May 2007).

264. Paulsson, M., Frederiksen, T., Ueba, H., Lorente, N. & Brandbyge, M. Unified Description of Inelastic Propensity Rules for Electron Transport through Nanoscale Junctions. *Physical Review Letters* **100.** doi:`10.1103/physrevlett.1 00.226604` (June 2008).

265. Solomon, G. C. *et al.* Understanding the inelastic electron-tunneling spectra of alkanedithiols on gold. *The Journal of Chemical Physics* **124,** 094704. doi:`10.1063/1.2166362` (Mar. 2006).

266. Auwärter, W. *et al.* A surface-anchored molecular four-level conductance switch based on single proton transfer. *Nature Nanotechnology* **7,** 41–46. doi:`10.1038/nnano.2011.211` (Dec. 2011).

267. Saito, S. & Osuka, A. Expanded Porphyrins: Intriguing Structures, Electronic Properties, and Reactivities. *Angewandte Chemie International Edition* **50,** 4342–4373. doi:`1 0.1002/anie.201003909` (Apr. 2011).

268. Stuyver, T., Perrin, M., Geerlings, P., Proft, F. D. & Alonso, M. Conductance Switching in Expanded Porphyrins through Aromaticity and Topology Changes. *Journal of the American Chemical Society* **140,** 1313–1326. doi:`10.1021/jacs.7b09464` (Jan. 2018).

269. Ahlrichs, R., Bär, M., Häser, M., Horn, H. & Kölmel, C. Electronic structure calculations on workstation computers: The program system turbomole. *Chemical Physics Letters* **162,** 165–169. ISSN: 0009-2614. doi:`10.1016/0009-2614(89)85118-8` (Oct. 1989).

270. Schäfer, A., Huber, C. & Ahlrichs, R. Fully optimized contracted Gaussian basis sets of triple zeta valence quality for atoms Li to Kr. *The Journal of Chemical Physics* **100,** 5829–5835. doi:`10.1063/1.467146` (Apr. 1994).

271. Weigend, F., Häser, M., Patzelt, H. & Ahlrichs, R. RI-MP2: optimized auxiliary basis sets and demonstration of efficiency. *Chemical Physics Letters* **294,** 143–152. ISSN: 0009-2614. doi:`10.1016/s0009-2614(98)00862-8` (Sept. 1998).

272. Ahlrichs, R. *Turbomole* 2009.

273. Troisi, A. & Ratner, M. A. Molecular Transport Junctions: Propensity Rules for Inelastic Electron Tunneling Spectra. *Nano Lett.* **6,** 1784–1788. ISSN: 1530-6992. doi:`10.1021 /nl0609394` (Aug. 2006).

274. Sai, N., Bushong, N., Hatcher, R. & Ventra, M. D. Microscopic current dynamics in nanoscale junctions. *Physical Review B* **75.** doi:10.1103/physrevb.75.115410 (Mar. 2007).

275. Ghosh, S. K. Density functional theory and multiscale materials modeling. *Bulletin of Materials Science* **26,** 3–12. doi:10.1007/bf02712781 (Jan. 2003).

276. Marzari, N. The frontiers and the challenges. *Nature Materials* **15,** 381–382. doi:10.1038/nmat4613 (Mar. 2016).

277. Huang, P. & Carter, E. A. Self-consistent embedding theory for locally correlated configuration interaction wave functions in condensed matter. *The Journal of Chemical Physics* **125,** 084102. doi:10.1063/1.2336428 (Aug. 2006).

278. Jacob, C. R., Neugebauer, J. & Visscher, L. A flexible implementation of frozen-density embedding for use in multilevel simulations. *Journal of Computational Chemistry* **29,** 1011–1018. doi:10.1002/jcc.20861 (2008).

279. Gomes, A. S. P., Jacob, C. R. & Visscher, L. Calculation of local excitations in large systems by embedding wave-function theory in density-functional theory. *Physical Chemistry Chemical Physics* **10,** 5353. doi:10.1039/b805739g (2008).

280. Gomes, A. S. P. & Jacob, C. R. Quantum-chemical embedding methods for treating local electronic excitations in complex chemical systems. *Annual Reports Section "C" (Physical Chemistry)* **108,** 222. doi:10.1039/c2pc90007f (2012).

281. Jacob, C. R. & Neugebauer, J. Subsystem density-functional theory. *Wiley Interdisciplinary Reviews: Computational Molecular Science* **4,** 325–362. doi:10.1002/wcms.1175 (July 2014).

282. Ng, T. Y., Yeak, S. H. & Liew, K. M. Coupling ofab initio-density functional theory and molecular dynamics for the multiscale modeling of carbon nanotubes. *Nanotechnology* **19,** 055702. doi:10.1088/0957-4484/19/05/055702 (Jan. 2008).

283. Rapacioli, M., Spiegelman, F., Scemama, A. & Mirtschink, A. Modeling Charge Resonance in Cationic Molecular Clusters: Combining DFT-Tight Binding with Configuration Interaction. *Journal of Chemical Theory and Computation* **7,** 44–55. doi:10.1021/ct100412f (Dec. 2010).

284. Hofer, T. S. & Tirler, A. O. Combining 2d-Periodic Quantum Chemistry with Molecular Force Fields: A Novel QM/MM Procedure for the Treatment of Solid-State Surfaces and Interfaces. *Journal of Chemical Theory and Computation* **11,** 5873–5887. doi:10.1021/acs.jctc.5b00548 (Nov. 2015).

285. Hofer, T. S. & de Visser, S. P. Editorial: Quantum Mechanical/Molecular Mechanical Approaches for the Investigation of Chemical Systems – Recent Developments and Advanced Applications. *Frontiers in Chemistry* **6.** doi:10.3389/fchem.2018.00357 (Sept. 2018).

286. Shen, L., Wu, J. & Yang, W. Multiscale Quantum Mechanics/Molecular Mechanics Simulations with Neural Networks. *Journal of Chemical Theory and Computation* **12,** 4934–4946. doi:10.1021/acs.jctc.6b00663 (Sept. 2016).

287. Zhang, Y.-J., Khorshidi, A., Kastlunger, G. & Peterson, A. A. The potential for machine learning in hybrid QM/MM calculations. *The Journal of Chemical Physics* **148,** 241740. doi:10.1063/1.5029879 (June 2018).

288. Kubař, T. & Elstner, M. Coarse-Grained Time-Dependent Density Functional Simulation of Charge Transfer in Complex Systems: Application to Hole Transfer in DNA. *The Journal of Physical Chemistry B* **114,** 11221–11240. doi:10.1021/jp102814p (Sept. 2010).

289. Calogero, G., Papior, N., Koleini, M., Larsen, M. H. L. & Brandbyge, M. Multi-scale approach to first-principles electron transport beyond 100 nm. *Nanoscale* **11,** 6153–6164. doi:10.1039/c9nr00866g (2019).

290. Ruggenthaler, M. *et al.* Quantum-electrodynamical density-functional theory: Bridging quantum optics and electronic-structure theory. *Physical Review A* **90.** doi:10.1103/physreva.90.012508 (July 2014).

291. Ruggenthaler, M., Tancogne-Dejean, N., Flick, J., Appel, H. & Rubio, A. From a quantum-electrodynamical light–matter description to novel spectroscopies. *Nature Reviews Chemistry* **2.** doi:10.1038/s41570-018-0118 (Mar. 2018).

292. Philip, T. M. & Gilbert, M. J. Theory of AC quantum transport with fully electrodynamic coupling. *Journal of Computational Electronics* **17,** 934–948. doi:10.1007/s10825-018-1191-z (May 2018).

293. Fox, M. *Optical Properties of Solids* 416 pp. ISBN: 0199573379 (Oxford University Press, Mar. 25, 2010).

294. Walther, M. *et al.* Terahertz conductivity of thin gold films at the metal-insulator percolation transition. *Physical Review B* **76.** doi:10.1103/physrevb.76.125408 (Sept. 2007).

295. Lloyd-Hughes, J. & Jeon, T.-I. A Review of the Terahertz Conductivity of Bulk and Nano-Materials. *Journal of Infrared, Millimeter, and Terahertz Waves* **33,** 871–925. doi:10.1007/s10762-012-9905-y (May 2012).

296. Cocker, T. L. *et al.* Microscopic origin of the Drude-Smith model. *Physical Review B* **96.** doi:10.1103/physrevb.96.205439 (Oct. 2017).

297. Pushkarev, V. *et al.* Quantum behavior of terahertz photoconductivity in silicon nanocrystals networks. *Physical Review B* **95.** doi:10.1103/physrevb.95.125424 (Mar. 2017).

298. Ostatnický, T., Pushkarev, V., Němec, H. & Kužel, P. Quantum theory of terahertz conductivity of semiconductor nanostructures. *Physical Review B* **97.** doi:10.1103/physrevb.97.085426 (Feb. 2018).

299. Ostatnický, T. Linear THz conductivity of nanocrystals. *Optics Express* **27,** 6083. doi:10.1364/oe.27.006083 (Feb. 2019).

300. Szczyrbowski, J. A new simple method of determining the effective mass of an electron or the thickness of thin metal films. *Journal of Physics D: Applied Physics* **19,** 1257–1263. doi:10.1088/0022-3727/19/7/015 (July 1986).

301. Simmons, J. G. Generalized Formula for the Electric Tunnel Effect between Similar Electrodes Separated by a Thin Insulating Film. *Journal of Applied Physics* **34,** 1793–1803. doi:10.1063/1.1702682 (June 1963).

302. Lee, Y.-S. *Principles of Terahertz Science and Technology* (Springer-Verlag GmbH, Mar. 2, 2009).

303. *Terahertz Spectroscopy and Imaging* (eds Peiponen, K.-E. *et al.*) doi:10.1007/978-3-642-29564-5 (Springer Berlin Heidelberg, 2013).

304. Coutaz, J.-L., Garet, F. & Wallace, V. P. *Principles of Terahertz Time-Domain Spectroscopy* 622 pp. ISBN: 9814774561 (Pan Stanford Publishing Pte Ltd, Dec. 14, 2018).

305. Neu, J. & Schmuttenmaer, C. A. Tutorial: An introduction to terahertz time domain spectroscopy (THz-TDS). *Journal of Applied Physics* **124,** 231101. doi:10.1063/1.5047659 (Dec. 2018).

306. Brucherseifer, M. *et al.* Label-free probing of the binding state of DNA by time-domain terahertz sensing. *Applied Physics Letters* **77,** 4049–4051. doi:10.1063/1.1332415 (Dec. 2000).

307. Korter, T. *et al.* Terahertz spectroscopy of solid serine and cysteine. *Chemical Physics Letters* **418,** 65–70. doi:10.1016/j.cplett.2005.10.097 (Jan. 2006).

308. King, M. D., Hakey, P. M. & Korter, T. M. Discrimination of Chiral Solids: A Terahertz Spectroscopic Investigation ofl- anddl-Serine. *The Journal of Physical Chemistry A* **114,** 2945–2953. doi:10.1021/jp911863v (Mar. 2010).

309. Williams, M. R. C., Aschaffenburg, D. J., Ofori-Okai, B. K. & Schmuttenmaer, C. A. Intermolecular Vibrations in Hydrophobic Amino Acid Crystals: Experiments and Calculations. *The Journal of Physical Chemistry B* **117,** 10444–10461. doi:10.1021/jp406730a (Aug. 2013).

310. Samanta, N., Mahanta, D. D. & Mitra, R. K. Collective hydration dynamics of guanidinium chloride solutions and its possible role in protein denaturation: a terahertz spectroscopic study. *Phys. Chem. Chem. Phys.* **16,** 23308–23315. doi:10.1039/c4cp03273j (Sept. 2014).

311. Yu, B. *et al.* Torsional Vibrational Modes of Tryptophan Studied by Terahertz Time-Domain Spectroscopy. *Biophysical Journal* **86,** 1649–1654. doi:10.1016/s0006-3495(04)74233-2 (Mar. 2004).

312. Neu, J., Nemes, C. T., Regan, K. P., Williams, M. R. C. & Schmuttenmaer, C. A. Exploring the solid state phase transition in dl-norvaline with terahertz spectroscopy. *Physical Chemistry Chemical Physics* **20,** 276–283. doi:10.1039/c7cp05479c (2018).

313. Zang, Z. *et al.* Temperature- and pH-dependent protein conformational changes investigated by terahertz dielectric spectroscopy. *Infrared Physics & Technology* **98,** 260–265. doi:10.1016/j.infrared.2019.03.021 (May 2019).

314. Shen, Y. C. *et al.* Detection and identification of explosives using terahertz pulsed spectroscopic imaging. *Applied Physics Letters* **86,** 241116. doi:10.1063/1.1946192 (June 2005).

315. Lu, M. *et al.* Detection and identification of illicit drugs using terahertz imaging. *Journal of Applied Physics* **100,** 103104. doi:10.1063/1.2388041 (Nov. 2006).

316. Allis, D. G., Prokhorova, D. A. & Korter, T. M. Solid-State Modeling of the Terahertz Spectrum of the High Explosive HMX. *The Journal of Physical Chemistry A* **110,** 1951–1959. doi:10.1021/jp0554285 (Feb. 2006).

317. Ajito, K. & Ueno, Y. THz Chemical Imaging for Biological Applications. *IEEE Transactions on Terahertz Science and Technology* **1,** 293–300. doi:10.1109/tthz.2011.2159562 (Sept. 2011).

318. Schirmer, M. *et al.* Biomedical applications of a real-time terahertz color scanner. *Biomedical Optics Express* **1,** 354. doi:10.1364/boe.1.000354 (Aug. 2010).

319. Hu, B. B. & Nuss, M. C. Imaging with terahertz waves. *Optics Letters* **20,** 1716. doi:10.1364/ol.20.001716 (Aug. 1995).

320. Watanabe, Y. *et al.* Component spatial pattern analysis of chemicals using terahertz spectroscopic imaging. *Applied Physics Letters* **83,** 800–802. doi:10.1063/1.1595132 (July 2003).

321. Van Exter, M. & Grischkowsky, D. Carrier dynamics of electrons and holes in moderately doped silicon. *Physical Review B* **41,** 12140–12149. doi:10.1103/physrevb.41.12140 (June 1990).

322. Grischkowsky, D., Keiding, S., van Exter, M. & Fattinger, C. Far-infrared time-domain spectroscopy with terahertz beams of dielectrics and semiconductors. *Journal of the Optical Society of America B* **7,** 2006. doi:10.1364/josab.7.002006 (Oct. 1990).

323. Katzenellenbogen, N. & Grischkowsky, D. Electrical characterization to 4 THz of N- and P-type GaAs using THz time-domain spectroscopy. *Applied Physics Letters* **61,** 840–842. doi:10.1063/1.107762 (Aug. 1992).

324. Tu, J. J., Homes, C. C. & Strongin, M. Optical Properties of Ultrathin Films: Evidence for a Dielectric Anomaly at the Insulator-to-Metal Transition. *Physical Review Letters* **90.** doi:10.1103/physrevlett.90.017402 (Jan. 2003).

325. Averitt, R. D. & Taylor, A. J. Ultrafast optical and far-infrared quasiparticle dynamics in correlated electron materials. *Journal of Physics: Condensed Matter* **14,** R1357–R1390. doi:10.1088/0953-8984/14/50/203 (Dec. 2002).

326. Beard, M. C., Turner, G. M. & Schmuttenmaer, C. A. Terahertz Spectroscopy. *The Journal of Physical Chemistry B* **106,** 7146–7159. doi:10.1021/jp020579i (July 2002).

327. Schmuttenmaer, C. A. Exploring Dynamics in the Far-Infrared with Terahertz Spectroscopy. *Chemical Reviews* **104,** 1759–1780. doi:10.1021/cr020685g (Apr. 2004).

328. Negre, C. F. A. *et al.* Efficiency of Interfacial Electron Transfer from Zn-Porphyrin Dyes into TiO_2 - Correlated to the Linker Single Molecule Conductance. *The Journal of Physical Chemistry C* **117,** 24462–24470. ISSN: 1932-7455. doi:10.1021/jp408738b (Oct. 2013).

329. Jiang, J. *et al.* Direct Interfacial Electron Transfer from High-Potential Porphyrins into Semiconductor Surfaces: A Comparison of Linkers and Anchoring Groups. *The Journal of Physical Chemistry C* **122,** 13529–13539. doi:10.1021/acs.jpcc.7b12405 (Feb. 2018).

330. Yoshioka, K. *et al.* Real-space coherent manipulation of electrons in a single tunnel junction by single-cycle terahertz electric fields. *Nature Photonics* **10,** 762–765. doi:10.1038/nphoton.2016.205 (Nov. 2016).

331. Ma, E. Y. *et al.* Recording interfacial currents on the subnanometer length and femtosecond time scale by terahertz emission. *Science Advances* **5,** eaau0073. doi:10.1126/sciadv.aau0073 (Feb. 2019).

332. Seifert, T. S. *et al.* Femtosecond formation dynamics of the spin Seebeck effect revealed by terahertz spectroscopy. *Nature Communications* **9.** doi:10.1038/s41467-018-05135-2 (July 2018).

333. Němec, P., Fiebig, M., Kampfrath, T. & Kimel, A. V. Antiferromagnetic opto-spintronics. *Nature Physics* **14,** 229–241. doi:10.1038/s41567-018-0051-x (Mar. 2018).

334. Olejník, K. *et al.* Terahertz electrical writing speed in an antiferromagnetic memory. *Science Advances* **4,** eaar3566. doi:10.1126/sciadv.aar3566 (Mar. 2018).

335. Nanni, E. A. *et al.* Terahertz-driven linear electron acceleration. *Nature Communications* **6.** doi:10.1038/ncomms9486 (Oct. 2015).

336. Zhang, D. *et al.* Segmented terahertz electron accelerator and manipulator (STEAM). *Nature Photonics* **12,** 336–342. doi:10.1038/s41566-018-0138-z (Apr. 2018).

337. Lewis, R. A. A review of terahertz sources. *Journal of Physics D: Applied Physics* **47,** 374001. doi:`10.1088/002 2-3727/47/37/374001` (Aug. 2014).

338. Hangyo, M., Tani, M. & Nagashima, T. Terahertz Time-Domain Spectroscopy of Solids: A Review. *International Journal of Infrared and Millimeter Waves* **26,** 1661–1690. doi:`10.1007/s10762-005-0288-1` (Nov. 2005).

339. Holland, D. B. *Design, Construction, and Applications of a High-Resolution Terahertz Time-Domain Spectrometer* PhD thesis (2014).

340. Jepsen, P., Cooke, D. & Koch, M. Terahertz spectroscopy and imaging - Modern techniques and applications. *Laser & Photonics Reviews* **5,** 124–166. doi:`10.1002/lpor.2010 00011` (Oct. 2010).

341. Joyce, H. J., Boland, J. L., Davies, C. L., Baig, S. A. & Johnston, M. B. A review of the electrical properties of semiconductor nanowires: insights gained from terahertz conductivity spectroscopy. *Semiconductor Science and Technology* **31,** 103003. doi:`10.1088/0268-1242/31/10/103003` (Sept. 2016).

342. Fülöp, J. A., Tzortzakis, S. & Kampfrath, T. Laser-Driven Strong-Field Terahertz Sources. *Advanced Optical Materials,* 1900681. doi:`10.1002/adom.201900681` (Dec. 2019).

343. *Millimeter and Submillimeter Wave Spectroscopy of Solids* (ed Grüner, G.) doi:`10.1007/bfb0103417` (Springer Berlin Heidelberg, 1998).

344. *Terahertz Spectroscopy* 360 pp. ISBN: 0849375258 (Taylor & Francis Inc, Dec. 22, 2007).

345. Rostami, A., Rasooli, H. & Baghban, H. *Terahertz Technology* doi:`10.1007/978-3-642-15793-6` (Springer Berlin Heidelberg, 2011).

346. Lewis, R. A. *Terahertz Physics* 302 pp. ISBN: 1107018579 (Cambridge University Press, July 4, 2014).

347. Nuss, M. C. & Orenstein, J. in *Topics in Applied Physics* 7–50 (Springer Berlin Heidelberg). doi:`10.1007/bfb0103419`.

348. Ferguson, B. & Zhang, X.-C. Materials for terahertz science and technology. *Nature Materials* **1,** 26–33. doi:`10.1038/n mat708` (Sept. 2002).

349. Leitenstorfer, A., Hunsche, S., Shah, J., Nuss, M. C. & Knox, W. H. Detectors and sources for ultrabroadband electro-optic sampling: Experiment and theory. *Applied Physics Letters* **74,** 1516–1518. doi:10.1063/1.123601 (Mar. 1999).

350. Duvillaret, L., Garet, F. & Coutaz, J.-L. A reliable method for extraction of material parameters in terahertz time-domain spectroscopy. *IEEE Journal of Selected Topics in Quantum Electronics* **2,** 739–746. doi:10.1109/2944.571775 (1996).

351. Duvillaret, L., Garet, F. & Coutaz, J.-L. Highly precise determination of optical constants and sample thickness in terahertz time-domain spectroscopy. *Applied Optics* **38,** 409. doi:10.1364/ao.38.000409 (Jan. 1999).

352. Dorney, T. D., Baraniuk, R. G. & Mittleman, D. M. Material parameter estimation with terahertz time-domain spectroscopy. *Journal of the Optical Society of America A* **18,** 1562. doi:10.1364/josaa.18.001562 (July 2001).

353. Pupeza, I., Wilk, R. & Koch, M. Highly accurate optical material parameter determination with THz time-domain spectroscopy. *Optics Express* **15,** 4335. doi:10.1364/oe.15.004335 (2007).

354. Scheller, M. Data Extraction from Terahertz Time Domain Spectroscopy Measurements. *Journal of Infrared, Millimeter, and Terahertz Waves* **35,** 638–648. doi:10.1007/s10762-014-0053-4 (Jan. 2014).

355. Vázquez-Cabo, J. *et al.* Windowing of THz time-domain spectroscopy signals: A study based on lactose. *Optics Communications* **366,** 386–396. doi:10.1016/j.optcom.2015.12.069 (May 2016).

356. Withayachumnankul, W. & Naftaly, M. Fundamentals of Measurement in Terahertz Time-Domain Spectroscopy. *Journal of Infrared, Millimeter, and Terahertz Waves* **35,** 610–637. doi:10.1007/s10762-013-0042-z (Dec. 2013).

357. Jepsen, P. U. Phase Retrieval in Terahertz Time-Domain Measurements: a "how to" Tutorial. *Journal of Infrared, Millimeter, and Terahertz Waves* **40,** 395–411. ISSN: 1866-6906. doi:10.1007/s10762-019-00578-0 (Apr. 2019).

358. Krewer, K. L. *et al.* Accurate terahertz spectroscopy of supported thin films by precise substrate thickness correction. *Optics Letters* **43,** 447. doi:10.1364/ol.43.000447 (Jan. 2018).

359. Tinkham, M. Energy Gap Interpretation of Experiments on Infrared Transmission through Superconducting Films. *Physical Review* **104,** 845–846. doi:`10.1103/physrev.104.845` (Nov. 1956).

360. Glover, R. E. & Tinkham, M. Transmission of Superconducting Films at Millimeter-Microwave and Far Infrared Frequencies. *Physical Review* **104,** 844–845. doi:`10.1103/physrev.104.844` (Nov. 1956).

361. Thoman, A., Kern, A., Helm, H. & Walther, M. Nanostructured gold films as broadband terahertz antireflection coatings. *Physical Review B* **77.** doi:`10.1103/physrevb.77.195405` (May 2008).

362. Krewer, K. L. *et al.* Large area conductive nanoaperture arrays with strong optical resonances and spectrally flat terahertz transmission. *Applied Physics Letters* **111,** 021107. doi:`10.1063/1.4992131` (July 2017).

363. Kužel, P. & Němec, H. Terahertz conductivity in nanoscaled systems: effective medium theory aspects. *Journal of Physics D: Applied Physics* **47,** 374005. doi:`10.1088/0022-3727/47/37/374005` (Aug. 2014).

364. Nienhuys, H.-K. & Sundström, V. Influence of plasmons on terahertz conductivity measurements. *Applied Physics Letters* **87,** 012101. doi:`10.1063/1.1977213` (July 2005).

365. Smith, N. Classical generalization of the Drude formula for the optical conductivity. *Physical Review B* **64.** doi:`10.1103/physrevb.64.155106` (Sept. 2001).

366. Cocker, T. L. *et al.* Terahertz conductivity of the metal-insulator transition in a nanogranular VO2 film. *Applied Physics Letters* **97,** 221905. doi:`10.1063/1.3518482` (Nov. 2010).

367. Titova, L. V. *et al.* Ultrafast percolative transport dynamics in silicon nanocrystal films. *Physical Review B* **83.** doi:`10.1103/physrevb.83.085403` (Feb. 2011).

368. Cooke, D. G., Meldrum, A. & Jepsen, P. U. Ultrabroadband terahertz conductivity of Si nanocrystal films. *Applied Physics Letters* **101,** 211107. doi:`10.1063/1.4767145` (Nov. 2012).

369. Ai, X. *et al.* Photoinduced Charge Carrier Generation in a Poly(3-hexylthiophene) and Methanofullerene Bulk Heterojunction Investigated by Time-Resolved Terahertz Spectroscopy†. *The Journal of Physical Chemistry B* **110,** 25462–25471. doi:`10.1021/jp065212i` (Dec. 2006).

370. Cunningham, P. D. & Hayden, L. M. Carrier Dynamics Resulting from Above and Below Gap Excitation of P3HT and P3HT/PCBM Investigated by Optical-Pump Terahertz-Probe Spectroscopy. *The Journal of Physical Chemistry C* **112,** 7928–7935. doi:`10.1021/jp711827g` (Apr. 2008).

371. Willis, K. J., Hagness, S. C. & Knezevic, I. A generalized Drude model for doped silicon at terahertz frequencies derived from microscopic transport simulation. *Applied Physics Letters* **102,** 122113. doi:`10.1063/1.4798658` (Mar. 2013).

372. Sule, N., Willis, K. J., Hagness, S. C. & Knezevic, I. Terahertz-frequency electronic transport in graphene. *Physical Review B* **90.** doi:`10.1103/physrevb.90.045431` (July 2014).

373. TED PELLA. *Technical Information about GE 124 Quartz Material* `https://www.tedpella.com/histo_html/GE124-Quartz.htm`.

374. Norrman, S., Andersson, T., Granqvist, C. G. & Hunderi, O. Optical properties of discontinuous gold films. *Physical Review B* **18,** 674–695. doi:`10.1103/physrevb.18.674` (July 1978).

375. Kossoy, A. *et al.* Optical and Structural Properties of Ultrathin Gold Films. *Advanced Optical Materials* **3,** 71–77. doi:`10.1002/adom.201400345` (Sept. 2014).

376. Dunaway, D. J. & McCarley, R. L. Scanning Force Microscopy Studies of Enhanced Metal Nucleation: Au Vapor Deposited on Self-Assembled Monolayers of Substituted Silanes. *Langmuir* **10,** 3598–3606. doi:`10.1021/la00022a037` (Oct. 1994).

377. Pattier, B., Bardeau, J.-F., Edely, M., Gibaud, A. & Delorme, N. Cheap and Robust Ultraflat Gold Surfaces Suitable for High-Resolution Surface Modification. *Langmuir* **24,** 821–825. doi:`10.1021/la702777k` (Feb. 2008).

378. Stec, H. M., Williams, R. J., Jones, T. S. & Hatton, R. A. Ultrathin Transparent Au Electrodes for Organic Photovoltaics Fabricated Using a Mixed Mono-Molecular Nucleation Layer. *Advanced Functional Materials* **21,** 1709–1716. doi:`10.1002/adfm.201002021` (Mar. 2011).

379. Habteyes, T. G. *et al.* Metallic Adhesion Layer Induced Plasmon Damping and Molecular Linker as a Nondamping Alternative. *ACS Nano* **6,** 5702–5709. doi:`10.1021/nn301885u` (June 2012).

380. Olmon, R. L. *et al.* Optical dielectric function of gold. *Physical Review B* **86.** doi:`10.1103/physrevb.86.235147` (Dec. 2012).

381. Ciesielski, A. *et al.* Evidence of germanium segregation in gold thin films. *Surface Science* **674,** 73–78. doi:`10.1016/j.susc.2018.03.020` (Aug. 2018).

382. Takeda, J., Yoshioka, K., Minami, Y. & Katayama, I. Nanoscale electron manipulation in metals with intense THz electric fields. *Journal of Physics D: Applied Physics* **51,** 103001. doi:`10.1088/1361-6463/aaa8c7` (Feb. 2018).

383. Gatesman, A. J., Giles, R. H. & Waldman, J. High-precision reflectometer for submillimeter wavelengths. *Journal of the Optical Society of America B* **12,** 212. doi:`10.1364/josab.12.000212` (Feb. 1995).

384. Laman, N. & Grischkowsky, D. Terahertz conductivity of thin metal films. *Applied Physics Letters* **93,** 051105. doi:`10.1063/1.2968308` (Aug. 2008).

385. Freestone, I., Meeks, N., Sax, M. & Higgitt, C. The Lycurgus cup—a roman nanotechnology. *Gold bulletin* **40,** 270–277 (2007).

386. Helcher, H. H. Aurum Potabile oder Gold Tinstur. *J. Herbord Klossen, Breslau and Leipzig* (1718).

387. Ostwald, W. Zur Geschichte des kolloiden Goldes. *Colloid & Polymer Science* **4,** 5–14 (1909).

388. Faraday, M. X. The Bakerian Lecture. —Experimental relations of gold (and other metals) to light. *Philosophical Transactions of the Royal Society of London* **147,** 145–181. doi:`10.1098/rstl.1857.0011` (Jan. 1857).

389. Mie, G. Beiträge zur Optik trüber Medien, speziell kolloidaler Metallösungen. *Annalen der Physik* **330,** 377–445. doi:`10.1002/andp.19083300302` (1908).

390. Amendola, V., Pilot, R., Frasconi, M., Maragò, O. M. & Iatì, M. A. Surface plasmon resonance in gold nanoparticles: a review. *Journal of Physics: Condensed Matter* **29,** 203002. doi:`10.1088/1361-648x/aa60f3` (Apr. 2017).

391. Turkevich, J., Stevenson, P. C. & Hillier, J. A study of the nucleation and growth processes in the synthesis of colloidal gold. *Discuss. Faraday Soc.* **11,** 55. doi:`10.1039/df9511100055` (1951).

392. Ghosh, P., Han, G., De, M., Kim, C. K. & Rotello, V. M. Gold nanoparticles in delivery applications. *Advanced Drug Delivery Reviews* **60.** Inorganic Nanoparticles in Drug Delivery, 1307–1315. ISSN: 0169-409X. doi:`https://doi.org/10.1016/j.addr.2008.03.016` (2008).

393. Murphy, C. J. *et al.* Gold Nanoparticles in Biology: Beyond Toxicity to Cellular Imaging. *Accounts of Chemical Research* **41,** 1721–1730. doi:`10.1021/ar800035u` (Dec. 2008).

394. Saha, K., Agasti, S. S., Kim, C., Li, X. & Rotello, V. M. Gold Nanoparticles in Chemical and Biological Sensing. *Chemical Reviews* **112,** 2739–2779. doi:`10.1021/cr2001178` (May 2012).

395. Austin, L. A., Kang, B. & El-Sayed, M. A. Probing molecular cell event dynamics at the single-cell level with targeted plasmonic gold nanoparticles: A review. *Nano Today* **10,** 542–558. doi:`10.1016/j.nantod.2015.07.005` (Oct. 2015).

396. Fabrizio, E. D. *et al.* Roadmap on biosensing and photonics with advanced nano-optical methods. *Journal of Optics* **18,** 063003. doi:`10.1088/2040-8978/18/6/063003` (May 2016).

397. Bethell, D., Brust, M., Schiffrin, D. & Kiely, C. From monolayers to nanostructured materials: an organic chemist's view of self-assembly. *Journal of Electroanalytical Chemistry* **409,** 137–143. doi:`10.1016/0022-0728(96)04533-0` (June 1996).

398. Bishop, K. J. M., Wilmer, C. E., Soh, S. & Grzybowski, B. A. Nanoscale Forces and Their Uses in Self-Assembly. *Small* **5,** 1600–1630. doi:`10.1002/smll.200900358` (July 2009).

399. Klinkova, A., Choueiri, R. M. & Kumacheva, E. Self-assembled plasmonic nanostructures. *Chemical Society Reviews* **43,** 3976. doi:`10.1039/c3cs60341e` (2014).

400. Boles, M. A., Engel, M. & Talapin, D. V. Self-Assembly of Colloidal Nanocrystals: From Intricate Structures to Functional Materials. *Chemical Reviews* **116,** 11220–11289. doi:`10.1021/acs.chemrev.6b00196` (Aug. 2016).

401. Gwo, S., Chen, H.-Y., Lin, M.-H., Sun, L. & Li, X. Nanomanipulation and controlled self-assembly of metal nanoparticles and nanocrystals for plasmonics. *Chemical Society Reviews* **45,** 5672–5716. doi:`10.1039/c6cs00450d` (2016).

402. Kanelidis, I. & Kraus, T. The role of ligands in coinage-metal nanoparticles for electronics. *Beilstein Journal of Nanotechnology* **8,** 2625–2639. doi:10.3762/bjnano.8.263 (2017).

403. Heuer-Jungemann, A. *et al.* The Role of Ligands in the Chemical Synthesis and Applications of Inorganic Nanoparticles. *Chemical Reviews* **119,** 4819–4880. doi:10.1021/acs.chemrev.8b00733 (Mar. 2019).

404. Sardar, R., Funston, A. M., Mulvaney, P. & Murray, R. W. Gold Nanoparticles: Past, Present, and Future. *Langmuir* **25,** 13840–13851. doi:10.1021/la9019475 (Dec. 2009).

405. Link, S. & El-Sayed, M. A. Shape and size dependence of radiative, non-radiative and photothermal properties of gold nanocrystals. *International Reviews in Physical Chemistry* **19,** 409–453. doi:10.1080/01442350050034180 (July 2000).

406. Hashimoto, S., Werner, D. & Uwada, T. Studies on the interaction of pulsed lasers with plasmonic gold nanoparticles toward light manipulation, heat management, and nanofabrication. *Journal of Photochemistry and Photobiology C: Photochemistry Reviews* **13,** 28–54. doi:10.1016/j.jphotochemrev.2012.01.001 (Mar. 2012).

407. Gieseking, R. L., Ratner, M. A. & Schatz, G. C. in *Frontiers of Plasmon Enhanced Spectroscopy Volume 1* 1–22 (2016). doi:10.1021/bk-2016-1245.ch001. eprint: https://pubs.acs.org/doi/pdf/10.1021/bk-2016-1245.ch001.

408. Kuppe, C., Rusimova, K. R., Ohnoutek, L., Slavov, D. & Valev, V. K. "Hot" in Plasmonics: Temperature-Related Concepts and Applications of Metal Nanostructures. *Advanced Optical Materials* **8,** 1901166. doi:10.1002/adom.201901166 (Nov. 2019).

409. Kang, H. *et al.* Stabilization of Silver and Gold Nanoparticles: Preservation and Improvement of Plasmonic Functionalities. *Chemical Reviews* **119,** 664–699. doi:10.1021/acs.chemrev.8b00341 (Oct. 2018).

410. Liao, J., Bernard, L., Langer, M., Schönenberger, C. & Calame, M. Reversible Formation of Molecular Junctions in 2D Nanoparticle Arrays. *Advanced Materials* **18,** 2444–2447. doi:10.1002/adma.200601001 (Sept. 2006).

411. Mangold, M. A., Weiss, C., Calame, M. & Holleitner, A. W. Surface plasmon enhanced photoconductance of gold nanoparticle arrays with incorporated alkane linkers. *Applied Physics Letters* **94,** 161104. doi:`10.1063/1.3116148` (Apr. 2009).

412. Mangold, M. A., Calame, M., Mayor, M. & Holleitner, A. W. Resonant Photoconductance of Molecular Junctions Formed in Gold Nanoparticle Arrays. *Journal of the American Chemical Society* **133,** 12185–12191. doi:`10.1021/ja204240v` (Aug. 2011).

413. Maier, S. A. *Plasmonics: Fundamentals and Applications* (Springer-Verlag GmbH, May 16, 2007).

414. Lange, H. *et al.* Tunable Plasmon Coupling in Distance-Controlled Gold Nanoparticles. *Langmuir* **28,** 8862–8866. doi:`10.1021/la3001575` (Mar. 2012).

415. Genov, D. A., Sarychev, A. K., Shalaev, V. M. & Wei, A. Resonant Field Enhancements from Metal Nanoparticle Arrays. *Nano Letters* **4,** 153–158. doi:`10.1021/nl0343710` (Jan. 2004).

416. Jung, H., Cha, H., Lee, D. & Yoon, S. Bridging the Nanogap with Light: Continuous Tuning of Plasmon Coupling between Gold Nanoparticles. *ACS Nano* **9,** 12292–12300. doi:`10.1021/acsnano.5b05568` (Oct. 2015).

417. Mondes, V. *et al.* Plasmonic electric near-field enhancement in self-organized gold nanoparticles in macroscopic arrays. *Applied Physics B* **122.** doi:`10.1007/s00340-016-6412-1` (May 2016).

418. Manjavacas, A., Zundel, L. & Sanders, S. Analysis of the Limits of the Near-Field Produced by Nanoparticle Arrays. *ACS Nano* **13,** 10682–10693. doi:`10.1021/acsnano.9b05031` (Sept. 2019).

419. Mueller, N. S. *et al.* Dark Interlayer Plasmons in Colloidal Gold Nanoparticle Bi- and Few-Layers. *ACS Photonics* **5,** 3962–3969. doi:`10.1021/acsphotonics.8b00898` (Oct. 2018).

420. Mueller, N. S. *et al.* Direct optical excitation of dark plasmons for hot electron generation. *Faraday Discussions* **214,** 159–173. doi:`10.1039/c8fd00149a` (2019).

421. Sumlin, B. *PyMieScatt: A Mie computational package with visualization capabilities* https://github.com/bsumlin/PyMieScatt.

422. Sumlin, B. J., Heinson, W. R. & Chakrabarty, R. K. Retrieving the aerosol complex refractive index using PyMieScatt: A Mie computational package with visualization capabilities. *Journal of Quantitative Spectroscopy and Radiative Transfer* **205,** 127–134. doi:`10.1016/j.jqsrt.2017.10.012` (Jan. 2018).

423. Johnson, P. B. & Christy, R. W. Optical Constants of the Noble Metals. *Physical Review B* **6,** 4370–4379. doi:`10.1103/physrevb.6.4370` (Dec. 1972).

424. Maier, S. A. *et al.* Local detection of electromagnetic energy transport below the diffraction limit in metal nanoparticle plasmon waveguides. *Nature Materials* **2,** 229–232. doi:`10.1038/nmat852` (Mar. 2003).

425. Krenn, J. R. Nanoparticle waveguides: Watching energy transfer. *Nature Materials* **2,** 210–211. doi:`10.1038/nmat865` (Apr. 2003).

426. Wei, H., Wang, Z., Tian, X., Käll, M. & Xu, H. Cascaded logic gates in nanophotonic plasmon networks. *Nature Communications* **2,** 387. doi:`10.1038/ncomms1388` (July 2011).

427. Dasary, S. S. R., Singh, A. K., Senapati, D., Yu, H. & Ray, P. C. Gold Nanoparticle Based Label-Free SERS Probe for Ultrasensitive and Selective Detection of Trinitrotoluene. *J. Am. Chem. Soc.* **131,** 13806–13812. doi:`10.1021/ja905134d` (Sept. 2009).

428. Xie, W., Walkenfort, B. & Schlücker, S. Label-Free SERS Monitoring of Chemical Reactions Catalyzed by Small Gold Nanoparticles Using 3D Plasmonic Superstructures. *Journal of the American Chemical Society* **135,** 1657–1660. ISSN: 1520-5126. doi:`10.1021/ja309074a` (Feb. 2013).

429. Kubackova, J., Fabriciova, G., Miskovsky, P., Jancura, D. & Sanchez-Cortes, S. Sensitive Surface-Enhanced Raman Spectroscopy (SERS) Detection of Organochlorine Pesticides by Alkyl Dithiol-Functionalized Metal Nanoparticles-Induced Plasmonic Hot Spots. *Analytical Chemistry* **87,** 663–669. doi:`10.1021/ac503672f` (Dec. 2014).

430. Thelander, C. *et al.* Gold nanoparticle single-electron transistor with carbon nanotube leads. *Applied Physics Letters* **79,** 2106–2108. doi:`10.1063/1.1405154` (Sept. 2001).

431. Ray, V. *et al.* CMOS-compatible fabrication of room-temperature single-electron devices. *Nature Nanotechnology* **3,** 603–608. doi:`10.1038/nnano.2008.267` (Sept. 2008).

432. Khondaker, S. I., Luo, K. & Yao, Z. The fabrication of single-electron transistors using dielectrophoretic trapping of individual gold nanoparticles. *Nanotechnology* **21,** 095204. doi:`10.1088/0957-4484/21/9/095204` (Feb. 2010).

433. Yamaguchi, H. *et al.* A photoresponsive single electron transistor prepared from oligothiophene molecules and gold nanoparticles in a nanogap electrode. *Applied Physics Letters* **96,** 103117. doi:`10.1063/1.3359424` (Mar. 2010).

434. Noguchi, Y. *et al.* Photoresponses in Gold Nanoparticle Single-Electron Transistors with Molecular Floating Gates. *Japanese Journal of Applied Physics* **52,** 110102. doi:`10.7567/jjap.52.110102` (Nov. 2013).

435. Bitton, O., Gutman, D. B., Berkovits, R. & Frydman, A. Multiple periodicity in a nanoparticle-based single-electron transistor. *Nature Communications* **8.** doi:`10.1038/s41467-017-00442-6` (Sept. 2017).

436. Brust, M., Bethell, D., Kiely, C. J. & Schiffrin, D. J. Self-Assembled Gold Nanoparticle Thin Films with Nonmetallic Optical and Electronic Properties. *Langmuir* **14,** 5425–5429. doi:`10.1021/la980557g` (Sept. 1998).

437. Joseph, Y. *et al.* Self-Assembled Gold Nanoparticle/Alkanedithiol Films: Preparation, Electron Microscopy, XPS-Analysis, Charge Transport, and Vapor-Sensing Properties. *The Journal of Physical Chemistry B* **107,** 7406–7413. doi:`10.1021/jp030439o` (July 2003).

438. Schmid, G. & Simon, U. Gold nanoparticles: assembly and electrical properties in 1–3 dimensions. *Chem. Commun.,* 697–710. doi:`10.1039/b411696h` (2005).

439. Wu, Y., Li, Y., Liu, P., Gardner, S. & Ong, B. S. Studies of Gold Nanoparticles as Precursors to Printed Conductive Features for Thin-Film Transistors. *Chemistry of Materials* **18,** 4627–4632. doi:`10.1021/cm0611643` (Sept. 2006).

440. Vossmeyer, T., Stolte, C., Ijeh, M., Kornowski, A. & Weller, H. Networked Gold-Nanoparticle Coatings on Polyethylene: Charge Transport and Strain Sensitivity. *Advanced Functional Materials* **18,** 1611–1616. doi:`10.1002/adfm.200701509` (June 2008).

441. Anto, B. T., Sivaramakrishnan, S., Chua, L.-L. & Ho, P. K. H. Hydrophilic Sparse Ionic Monolayer-Protected Metal Nanoparticles: Highly Concentrated Nano-Au and Nano-Ag "Inks" that can be Sintered to Near-Bulk Conductivity at 150 °C. *Advanced Functional Materials* **20,** 296–303. doi:`10.1002/adfm.200901336` (Jan. 2010).

442. Olichwer, N., Leib, E. W., Halfar, A. H., Petrov, A. & Voss-meyer, T. Cross-Linked Gold Nanoparticles on Polyethylene: Resistive Responses to Tensile Strain and Vapors. *ACS Applied Materials & Interfaces* **4,** 6151–6161. doi:`10.1021/am301780b` (Nov. 2012).

443. Abulikemu, M. *et al.* In Situ Synthesis of Self-Assembled Gold Nanoparticles on Glass or Silicon Substrates through Reactive Inkjet Printing. *Angewandte Chemie International Edition* **53,** 420–423. doi:`10.1002/anie.201308429` (Dec. 2013).

444. Kamyshny, A. & Magdassi, S. Conductive Nanomaterials for Printed Electronics. *Small* **10,** 3515–3535. doi:`10.1002/smll.201303000` (Jan. 2014).

445. Wuelfing, W. P., Green, S. J., Pietron, J. J., Cliffel, D. E. & Murray, R. W. *Electronic Conductivity of Solid-State, Mixed-Valent, Monolayer-Protected Au Clusters* 2000. doi:`10.1021/ja002367`.

446. Wuelfing, W. P. & Murray, R. W. Electron Hopping through Films of Arenethiolate Monolayer-Protected Gold Clusters. *The Journal of Physical Chemistry B* **106,** 3139–3145. doi:`10.1021/jp013987f` (Mar. 2002).

447. Trudeau, P.-E., Orozco, A., Kwan, E. & Dhirani, A.-A. Competitive transport and percolation in disordered arrays of molecularly-linked Au nanoparticles. *The Journal of Chemical Physics* **117,** 3978–3981. doi:`10.1063/1.1495838` (Aug. 2002).

448. Trudeau, P.-E., Escorcia, A. & Dhirani, A.-A. Variable single electron charging energies and percolation effects in molecularly linked nanoparticle films. *The Journal of Chemical Physics* **119,** 5267–5273. doi:`10.1063/1.1597871` (Sept. 2003).

449. Quinn, A. J. & Redmond, G. Artificial atom solids based on metal nanocrystals: Formation and electrical properties. *Progress in Solid State Chemistry* **33,** 263–277. doi:`10.1016/j.progsolidstchem.2005.11.048` (Jan. 2005).

450. Dunford, J. L., Suganuma, Y., Dhirani, A.-A. & Statt, B. Quasilocalized hopping in molecularly linked Au nanoparticle arrays near the metal-insulator transition. *Physical Review B* **72.** doi:`10.1103/physrevb.72.075441` (Aug. 2005).

451. Beloborodov, I. S., Lopatin, A. V., Vinokur, V. M. & Efetov, K. B. Granular electronic systems. *Reviews of Modern Physics* **79,** 469–518. doi:10.1103/revmodphys.79.469 (Apr. 2007).

452. Musick, M. D., Keating, C. D., Keefe, M. H. & Natan, M. J. Stepwise Construction of Conductive Au Colloid Multilayers from Solution. *Chemistry of Materials* **9,** 1499–1501. doi:10.1021/cm970087w (July 1997).

453. Markovich, G., Collier, C. P. & Heath, J. R. Reversible Metal-Insulator Transition in Ordered Metal Nanocrystal Monolayers Observed by Impedance Spectroscopy. *Physical Review Letters* **80,** 3807–3810. doi:10.1103/physrevlett.80.3807 (Apr. 1998).

454. Musick, M. D. *et al.* Metal Films Prepared by Stepwise Assembly. 2. Construction and Characterization of Colloidal Au and Ag Multilayers. *Chemistry of Materials* **12,** 2869–2881. doi:10.1021/cm990714c (Oct. 2000).

455. Brust, M. & Kiely, C. J. Some recent advances in nanostructure preparation from gold and silver particles: a short topical review. *Colloids and Surfaces A: Physicochemical and Engineering Aspects* **202,** 175–186. doi:10.1016/s0927-7757(01)01087-1 (Apr. 2002).

456. Zabet-Khosousi, A., Trudeau, P.-E., Suganuma, Y., Dhirani, A.-A. & Statt, B. Metal to Insulator Transition in Films of Molecularly Linked Gold Nanoparticles. *Physical Review Letters* **96.** doi:10.1103/physrevlett.96.156403 (2006).

457. Snow, A. W. & Wohltjen, H. Size-Induced Metal to Semiconductor Transition in a Stabilized Gold Cluster Ensemble. *Chemistry of Materials* **10,** 947–949. doi:10.1021/cm970794p (Apr. 1998).

458. Ahn, H., Chandekar, A., Kang, B., Sung, C. & Whitten, J. E. Electrical Conductivity and Vapor-Sensing Properties of ω-(3-Thienyl)alkanethiol-Protected Gold Nanoparticle Films. *Chemistry of Materials* **16,** 3274–3278. doi:10.1021/cm049794x (Aug. 2004).

459. Jiang, C.-W., Ni, I.-C., Tzeng, S.-D. & Kuo, W. Anderson localization in strongly coupled gold-nanoparticle assemblies near the metal–insulator transition. *Applied Physics Letters* **101,** 083105. doi:10.1063/1.4747322 (Aug. 2012).

460. Liang, Z., Sun, J., Jiang, Y., Jiang, L. & Chen, X. Plasmonic Enhanced Optoelectronic Devices. *Plasmonics* **9,** 859–866. doi:10.1007/s11468-014-9682-7 (Feb. 2014).

461. Conklin, D. *et al.* Exploiting Plasmon-Induced Hot Electrons in Molecular Electronic Devices. *ACS Nano* **7,** 4479–4486. doi:10.1021/nn401071d (Apr. 2013).

462. Sprague-Klein, E. A. *et al.* Observation of Single Molecule Plasmon-Driven Electron Transfer in Isotopically Edited 4,4ʹ-Bipyridine Gold Nanosphere Oligomers. *Journal of the American Chemical Society* **139,** 15212–15221. doi:10.1021/jacs.7b08868 (Oct. 2017).

463. Li, G.-Q., Schreiber, M. & Kleinekathöfer, U. Coherent laser control of the current through molecular junctions. *Europhysics Letters (EPL)* **79,** 27006. doi:10.1209/0295-5075/79/27006 (July 2007).

464. Viljas, J. K., Pauly, F. & Cuevas, J. C. Photoconductance of organic single-molecule contacts. *Physical Review B* **76.** doi:10.1103/physrevb.76.033403 (July 2007).

465. Zhao, P., Li, N. & Astruc, D. State of the art in gold nanoparticle synthesis. *Coordination Chemistry Reviews* **257,** 638–665. doi:10.1016/j.ccr.2012.09.002 (Feb. 2013).

466. Schulz, F. *et al.* Little Adjustments Significantly Improve the Turkevich Synthesis of Gold Nanoparticles. *Langmuir* **30,** 10779–10784. ISSN: 1520-5827. doi:10.1021/la503209b (Sept. 2014).

467. Al-Johani, H. *et al.* The structure and binding mode of citrate in the stabilization of gold nanoparticles. *Nature Chemistry* **9,** 890–895. doi:10.1038/nchem.2752 (Mar. 2017).

468. Pensa, E. *et al.* The Chemistry of the Sulfur–Gold Interface: In Search of a Unified Model. *Accounts of Chemical Research* **45,** 1183–1192. doi:10.1021/ar200260p (Mar. 2012).

469. Molina, L. & Hammer, B. Theoretical study of thiol-induced reconstructions on the Au(111) surface. *Chemical Physics Letters* **360,** 264–271. doi:10.1016/s0009-2614(02)00841-2 (July 2002).

470. Whetten, R. L. & Price, R. C. Nano-Golden Order. *Science* **318,** 407–408. doi:10.1126/science.1150176 (Oct. 2007).

471. Maksymovych, P., Voznyy, O., Dougherty, D. B., Sorescu, D. C. & Yates, J. T. Gold adatom as a key structural component in self-assembled monolayers of organosulfur molecules on Au(111). *Progress in Surface Science* **85,** 206–240. doi:10.1016/j.progsurf.2010.05.001 (May 2010).

472. Vericat, C., Vela, M. E., Benitez, G., Carro, P. & Salvarezza, R. C. Self-assembled monolayers of thiols and dithiols on gold: new challenges for a well-known system. *Chemical Society Reviews* **39,** 1805. doi:10.1039/b907301a (2010).

473. Häkkinen, H. The gold–sulfur interface at the nanoscale. *Nature Chemistry* **4,** 443–455. doi:10.1038/nchem.1352 (May 2012).

474. Inkpen, M. S. *et al.* Non-chemisorbed gold–sulfur binding prevails in self-assembled monolayers. *Nature Chemistry* **11,** 351–358. doi:10.1038/s41557-019-0216-y (2019).

475. Karg, M. *et al.* Versatile Phase Transfer of Gold Nanoparticles from Aqueous Media to Different Organic Media. *Chemistry – A European Journal* **17,** 4648–4654. doi:10.1002/chem.201003340 (Mar. 2011).

476. Kumar, A., Joshi, H., Pasricha, R., Mandale, A. & Sastry, M. Phase transfer of silver nanoparticles from aqueous to organic solutions using fatty amine molecules. *Journal of Colloid and Interface Science* **264,** 396–401. doi:10.1016/s0021-9797(03)00567-8 (Aug. 2003).

477. Schulz, F., Tober, S. & Lange, H. Size-Dependent Phase Transfer Functionalization of Gold Nanoparticles To Promote Well-Ordered Self-Assembly. *Langmuir* **33,** 14437–14444. doi:10.1021/acs.langmuir.7b03600 (Dec. 2017).

478. Yang, J., Lee, J. Y., Deivaraj, T. & Too, H.-P. A highly efficient phase transfer method for preparing alkylamine-stabilized Ru, Pt, and Au nanoparticles. *Journal of Colloid and Interface Science* **277,** 95–99. doi:10.1016/j.jcis.2004.03.074 (Sept. 2004).

479. Han, S. & Balasubramanian, R. Multidentate Ionic Surfactant Mediated Extraction and Dispersion of Gold Nanoparticles in Organic Solvents. *Langmuir* **30,** 9063–9070. doi:10.1021/la501661s (July 2014).

480. Lin, S., Li, M., Dujardin, E., Girard, C. & Mann, S. One-Dimensional Plasmon Coupling by Facile Self-Assembly of Gold Nanoparticles into Branched Chain Networks. *Advanced Materials* **17,** 2553–2559. ISSN: 1521-4095. doi:10.1002/adma.200500828 (Oct. 2005).

481. Love, J. C., Estroff, L. A., Kriebel, J. K., Nuzzo, R. G. & Whitesides, G. M. Self-Assembled Monolayers of Thiolates on Metals as a Form of Nanotechnology. *Chemical Reviews* **105,** 1103–1170. doi:10.1021/cr0300789 (Apr. 2005).

482. Shevchenko, E. V., Talapin, D. V., Kotov, N. A., O'Brien, S. & Murray, C. B. Structural diversity in binary nanoparticle superlattices. *Nature* **439,** 55–59. doi:`10.1038/nature04414` (Jan. 2006).

483. Bigioni, T. P. *et al.* Kinetically driven self assembly of highly ordered nanoparticle monolayers. *Nature Materials* **5,** 265–270. doi:`10.1038/nmat1611` (Mar. 2006).

484. Fernandes, R., Li, M., Dujardin, E., Mann, S. & Kanaras, A. G. Ligand-mediated self-assembly of polymer-enveloped gold nanoparticle chains and networks. *Chemical Communications* **46,** 7602. ISSN: 1364-548X. doi:`10.1039/c0cc03033c` (2010).

485. Grzelczak, M., Vermant, J., Furst, E. M. & Liz-Marzán, L. M. Directed Self-Assembly of Nanoparticles. *ACS Nano* **4,** 3591–3605. doi:`10.1021/nn100869j` (June 2010).

486. Baranov, D., Manna, L. & Kanaras, A. G. Chemically induced self-assembly of spherical and anisotropic inorganic nanocrystals. *Journal of Materials Chemistry* **21,** 16694–16703 (2011).

487. Abbas, A., Tian, L., Kattumenu, R., Halim, A. & Singamaneni, S. Freezing the self-assembly process of gold nanocrystals. *Chemical Communications* **48,** 1677–1679 (2012).

488. Luo, D., Yan, C. & Wang, T. Interparticle Forces Underlying Nanoparticle Self-Assemblies. *Small* **11,** 5984–6008. doi:`10.1002/smll.201501783` (Oct. 2015).

489. Gong, J. *et al.* Shape-dependent ordering of gold nanocrystals into large-scale superlattices. *Nature Communications* **8.** doi:`10.1038/ncomms14038` (Jan. 2017).

490. Yanagida, S., Nishiyama, S., Sakamoto, K., Fudouzi, H. & Miki, K. Formation of Uniform and High-Coverage Monolayer Colloidal Films of Midnanometer-Sized Gold Particles over the Entire Surfaces of 1.5-in. Substrates. *Langmuir* **33,** 9954–9960. doi:`10.1021/acs.langmuir.7b02788` (Sept. 2017).

491. Higashi, N., Takagi, T. & Koga, T. Layer-by-layer fabrication of well-packed gold nanoparticle assemblies guided by a β-sheet peptide network. *Polymer Journal* **42,** 95–99. doi:`10.1038/pj.2009.311` (Jan. 2010).

492. Liu, Z., Bai, L., Zhao, G. & Liu, Y. Sandwich-like layer-by-layer assembly of gold nanoparticles with tunable SERS properties. *Beilstein Journal of Nanotechnology* **7,** 1028–1032. doi:`10.3762/bjnano.7.95` (July 2016).

493. Kawasaki, H. *et al.* Layer-by-Layer Self-Assembled Mutilayer Films of Gold Nanoparticles for Surface-Assisted Laser Desorption/Ionization Mass Spectrometry. *Analytical Chemistry* **80,** 7524–7533. doi:`10.1021/ac800789t` (Oct. 2008).

494. Hicks, J. F., Seok-Shon, Y. & Murray, R. W. Layer-by-Layer Growth of Polymer/Nanoparticle Films Containing Monolayer-Protected Gold Clusters. *Langmuir* **18,** 2288–2294. doi:`10.1021/la0156255` (Mar. 2002).

495. Schlicke, H. *et al.* Freestanding films of crosslinked gold nanoparticles prepared via layer-by-layer spin-coating. *Nanotechnology* **22,** 305303. doi:`10.1088/0957-4484/22/30/305303` (June 2011).

496. Schlicke, H., Leib, E. W., Petrov, A., Schröder, J. H. & Vossmeyer, T. Elastic and Viscoelastic Properties of Cross-Linked Gold Nanoparticles Probed by AFM Bulge Tests. *The Journal of Physical Chemistry C* **118,** 4386–4395. doi:`10.1021/jp4091969` (Feb. 2014).

497. Schlicke, H. *et al.* Freestanding Membranes of Cross-Linked Gold Nanoparticles: Novel Functional Materials for Electrostatic Actuators. *ACS Applied Materials & Interfaces* **7,** 15123–15128. doi:`10.1021/acsami.5b02691` (July 2015).

498. Schlicke, H., Rebber, M., Kunze, S. & Vossmeyer, T. Resistive pressure sensors based on freestanding membranes of gold nanoparticles. *Nanoscale* **8,** 183–186. doi:`10.1039/c5nr06937h` (2016).

499. Schlicke, H. *et al.* Cross-Linked Gold-Nanoparticle Membrane Resonators as Microelectromechanical Vapor Sensors. *ACS Sensors* **2,** 540–546. doi:`10.1021/acssensors.6b00831` (Mar. 2017).

500. Joseph, Y. *et al.* Vapor Sensitivity of Networked Gold Nanoparticle Chemiresistors: Importance of Flexibility and Resistivity of the Interlinkage. *The Journal of Physical Chemistry C* **111,** 12855–12859. doi:`10.1021/jp072053+`. eprint: `https://doi.org/10.1021/jp072053+` (2007).

501. Abdelrahman, A. I., Mohammad, A. M., Okajima, T. & Ohsaka, T. Fabrication and Electrochemical Application of Three-Dimensional Gold Nanoparticles: Self-Assembly. *The Journal of Physical Chemistry B* **110,** 2798–2803. doi:`10.1021/jp056238x` (Feb. 2006).

502. Runge, D. *Layer-by-Layer Synthese homogener und großflächiger dithiol-vernetzter Goldnanopartikelfilme mit definierten Schichtdicken* MA thesis (University of Hamburg, 2019).

503. Brus, L. E. Electron-electron and electron-hole interactions in small semiconductor crystallites: The size dependence of the lowest excited electronic state. *The Journal of Chemical Physics* **80,** 4403–4409. ISSN: 0021-9606. doi:10.1063/1.447218 (1984).

504. Shirasaki, Y., Supran, G. J., Bawendi, M. G. & Bulović, V. Emergence of colloidal quantum-dot light-emitting technologies. *Nature Photonics* **7,** 13–23. ISSN: 1749-4893. doi:10.1038/nphoton.2012.328 (2013).

505. Carey, G. H. *et al.* Colloidal Quantum Dot Solar Cells. *Chemical Reviews* **115,** 12732–12763. ISSN: 0009-2665. doi:10.1021/acs.chemrev.5b00063 (2015).

506. Boles, M. A., Ling, D., Hyeon, T. & Talapin, D. V. The surface science of nanocrystals. en. *Nature Materials* **15,** 141–153. ISSN: 1476-4660. doi:10.1038/nmat4526 (2016).

507. Uhl, A. R. *et al.* Solution-Processed Low-Bandgap CuIn(S,Se)2 Absorbers for High-Efficiency Single-Junction and Monolithic Chalcopyrite-Perovskite Tandem Solar Cells. *Advanced Energy Materials* **8,** 1801254. ISSN: 1614-6840. doi:10.1002/aenm.201801254 (2018).

508. Talgorn, E. *et al.* Unity quantum yield of photogenerated charges and band-like transport in quantum-dot solids. *Nature Nanotechnology* **6,** 733–739. doi:10.1038/nnano.2011.159 (Sept. 2011).

509. Whitham, K. *et al.* Charge transport and localization in atomically coherent quantum dot solids. en. *Nature Materials* **15,** 557–563. doi:10.1038/nmat4576 (2016).

510. Liu, Y. *et al.* Dependence of Carrier Mobility on Nanocrystal Size and Ligand Length in PbSe Nanocrystal Solids. *Nano Letters* **10,** 1960–1969. ISSN: 1530-6984. doi:10.1021/nl101284k (2010).

511. Fafarman, A. T. *et al.* Thiocyanate-Capped Nanocrystal Colloids: Vibrational Reporter of Surface Chemistry and Solution-Based Route to Enhanced Coupling in Nanocrystal Solids. *Journal of the American Chemical Society* **133,** 15753–15761. ISSN: 0002-7863. doi:10.1021/ja206303g (2011).

512. Lauth, J. *et al.* Virtually Bare Nanocrystal Surfaces: Significantly Enhanced Electrical Transport in CuInSe$_2$ and CuIn$_{1-x}$Ga$_x$Se$_2$ Thin Films upon Ligand Exchange with Thermally Degradable 1-Ethyl-5-Thiotetrazole. *Advanced Functional Materials* **24,** 1081–1088. ISSN: 1616-3028. doi:10.1002/adfm.201301957 (2014).

513. Carey, G. H., Levina, L., Comin, R., Voznyy, O. & Sargent, E. H. Record Charge Carrier Diffusion Length in Colloidal Quantum Dot Solids via Mutual Dot-To-Dot Surface Passivation. *Advanced Materials* **27,** 3325–3330 (2015).

514. Scheele, M. *et al.* PbS Nanoparticles Capped with Tetrathiafulvalenetetracarboxylate: Utilizing Energy Level Alignment for Efficient Carrier Transport. *ACS Nano* **8,** 2532–2540. ISSN: 1936-0851. doi:10.1021/nn406127s (2014).

515. Ray, N., Staley, N. E., Grinolds, D. D. W., Bawendi, M. G. & Kastner, M. A. Measuring Ligand-Dependent Transport in Nanopatterned PbS Colloidal Quantum Dot Arrays Using Charge Sensing. *Nano Letters* **15,** 4401–4405. ISSN: 1530-6984 (2015).

516. André, A. *et al.* Electron-Conducting PbS Nanocrystal Superlattices with Long-Range Order Enabled by Terthiophene Molecular Linkers. *ACS Applied Materials & Interfaces* **10,** 24708–24714. ISSN: 1944-8244. doi:10.1021/acsami.8b06044 (2018).

517. Liu, J., Huang, X., Wang, F. & Hong, W. Quantum Interference Effects in Charge Transport through Single-Molecule Junctions: Detection, Manipulation, and Application. *Accounts of Chemical Research* **52,** 151–160. ISSN: 0001-4842. doi:10.1021/acs.accounts.8b00429 (2019).

518. Gorris, F. E. S. *Ladungstransporteigenschaften von thiadiazol-funktionalisierten Kupferindiumselenidnanokristalldünnschichten* ger. PhD thesis (Universität Hamburg, Von-Melle-Park 3, 20146 Hamburg, 2018).

519. Panthani, M. G. *et al.* Synthesis of CuInS$_2$, CuInSe$_2$, and Cu(In$_x$Ga$_{1-x}$)Se$_2$ (CIGS) Nanocrystal "Inks" for Printable Photovoltaics. *Journal of the American Chemical Society* **130,** 16770–16777. doi:10.1021/ja805845q. eprint: https://doi.org/10.1021/ja805845q (2008).

520. Firoz Hasan, S. M., Subhan, M. A. & Mannan, K. M. The optical and electrical properties of copper indium di-selenide thin films. *Optical Materials* **14,** 329–336. doi:Doi:10.1016/s0925-3467(00)00006-9 (2000).

521. Shaban, H. T., Mobarak, M. & Nassary, M. M. Characterization of CuInSe$_2$ single crystal. *Physica B: Condensed Matter* **389,** 351–354. ISSN: 09214526. doi:10.1016/j.physb.2006.07.016 (2007).

522. Zhang, S. B., Wei, S.-H., Zunger, A. & Katayama-Yoshida, H. Defect physics of the CuInSe$_2$ chalcopyrite semiconductor. *Physical Review B* **57,** 9642–9656. doi:10.1103/PhysRevB.57.9642 (1998).

523. Draguta, S., McDaniel, H. & Klimov, V. I. Tuning Carrier Mobilities and Polarity of Charge Transport in Films of CuInSexS2–x Quantum Dots. *Advanced Materials* **27,** 1701–1705 (2015).

524. Kang, M. S., Sahu, A., Norris, D. J. & Frisbie, C. D. Size- and temperature-dependent charge transport in PbSe nanocrystal thin films. *Nano Letters* **11,** 3887–3892. ISSN: 15306984. doi:10.1021/nl2020153 (2011).

525. Efros, A. L. & Shklovskii, B. I. Coulomb gap and low temperature conductivity of disordered systems. *Journal of Physics C: Solid State Physics* **8,** L49–L51. ISSN: 0022-3719. doi:10.1088/0022-3719/8/4/003 (1975).

526. Zabrodskii, A. G. & Zinov'eva, K. N. Low-temperature conductivity and metal-insulator transition in compensate n-Ge. *Sov. Phys. JETP* **59,** 425–433 (1984).

527. Kužel, P. & Němec, H. Terahertz Spectroscopy of Nanomaterials: a Close Look at Charge-Carrier Transport. *Advanced Optical Materials,* 1900623. doi:10.1002/adom.201900623 (June 2019).

528. Gao, Y., Sandeep, C. S. S., Schins, J. M., Houtepen, A. J. & Siebbeles, L. D. A. Disorder strongly enhances Auger recombination in conductive quantum-dot solids. en. *Nature Communications* **4.** ISSN: 2041-1723. doi:10.1038/ncomms3329 (2013).

529. Lu, J., Liu, H. & Sun, J. Negative terahertz photoconductivity in 2D layered materials. en. *Nanotechnology* **28,** 464001. ISSN: 0957-4484, 1361-6528. doi:10.1088/1361-6528/aa8c28 (2017).

530. Jnawali, G., Rao, Y., Yan, H. & Heinz, T. F. Observation of a Transient Decrease in Terahertz Conductivity of Single-Layer Graphene Induced by Ultrafast Optical Excitation. en. *Nano Letters* **13,** 524–530. ISSN: 1530-6984, 1530-6992. doi:10.1021/nl303988q (2013).

531. Yang, Y. *et al.* Direct Observation of Photoexcited Hole Localization in CdSe Nanorods. en. *ACS Energy Letters* **1,** 76–81. ISSN: 2380-8195, 2380-8195. doi:10.1021/acsenerg ylett.6b00036 (2016).

532. Baek, E. *et al.* Negative Photoconductance in Heavily Doped Si Nanowire Field-Effect Transistors. *Nano Letters* **17,** 6727–6734. ISSN: 1530-6984. doi:10.1021/acs.nano lett.7b02788 (2017).

533. Tavares, M. a. B. *et al.* Investigation of negative photoconductivity in p-type Pb1-xSnxTe film. *Applied Physics Letters* **110,** 042102. ISSN: 0003-6951. doi:10.1063/1.4974539 (2017).

534. Lui, C. H. *et al.* Trion-Induced Negative Photoconductivity in Monolayer MoS_2. *Phys. Rev. Lett.* **113,** 166801. doi:10.1 103/PhysRevLett.113.166801 (16 Oct. 2014).

535. Han, Y. *et al.* Switching from Negative to Positive Photoconductivity toward Intrinsic Photoelectric Response in InAs Nanowire. *ACS Applied Materials & Interfaces* **9,** 2867–2874. ISSN: 1944-8244. doi:10.1021/acsami.6b13775 (2017).

536. Ziemann, E. A. *et al.* Extended Threefold-Symmetric Second-Harmonic-Generation Chromophores Based on 1,3,5-Trisubstituted Benzene Complexes. *European Journal of Inorganic Chemistry* **2015.** doi:10.1002/ejic.2015 00689 (Aug. 2015).

537. Stegmann, T. *et al.* Current vortices in aromatic carbon molecules. *Physical Review B* **102.** doi:10.1103/physrev b.102.075405 (Aug. 2020).

538. James, G. *An introduction to statistical learning : with applications in R* ISBN: 9781461471387 (Springer, New York, NY, 2013).

List of Figures

List of Tables

List of Abbreviations

DMTD 2,5-Dimercapto-1,3,4-thiadiazole

AMTD 2-Amino-5-mercapto-1,3,4-thiadiazole

THIO 4,4-thiobisbenzenethiol

TER p-terphenyl-4,4$''$-dithiol

AFM atomic-force microscopy

BI biphenyl-4,4$'$-dithiol

CEP carrier-envelope phase

CIS $CuInSe_2$

DOS density of states

DFT density-functional theory

DS Drude-Smith

EMT effective-medium theory

EELS electron energy loss spectroscopy

EOM equation of motion

FP Fabry-Pérot

GGA generalized gradient approximation

AuNP gold nanoparticle

HF Hartree-Fock

HOMO highest-occupied molecular orbital

IETS inelastic electron tunneling spectroscopy

IET inelastic electron tunneling

IR infrared

IMT insulator-to-metal transition

LB Landauer-Büttiker

LBL layer-by-layer

List of Abbreviations

LED light-emitting diode

LDA local density approximation

LUMO lowest-unoccupied molecular orbital

MAE mean absolute error

MC-BJ mechanically controlled break junction

MIT metal-to-insulator transition

MQ millipore water

MO molecular orbital

MC Monte Carlo

MPTS (3-Mercaptopropyl)trimethoxysilane

ND neutral density

NEGF non-equilibrium Green's function

NON nonane-1,9-dithiol

OAm oleylamine

OPV oligo-phenylene-vinylene

OPA optical parametric amplifier

OPTP spectroscopy optical-pump-terahertz-probe spectroscopy

PTFE polytetrafluoroethylene

QD quantum dot

RMSE root-mean-square error

SEM scanning electron microscope

STM scanning tunneling microscope

SAM self-assembled monolayer

SCF self-consistent field

SERS surface enhanced Raman spectroscopy

THz-TDS terahertz time-domain spectroscopy

THz terahertz

TB tight-binding

VRH variable-range hopping

Acknowledgments

Finally, me deepest respect goes to the people, who fight for change in science, who campaign for free access to scientific results, gender equality or an improvement of working conditions in academia.

Apart from university, many people supported and helped me such as my partner Sarah Köver, my family and my friends. It is not possible to fully acknowledge everybody who has supported, encouraged or helped me in that time, so if I failed to mention you so far: Thank you.

Appendix

A List of Publications

- Ziemann, E. A. *et al.* Extended Threefold-Symmetric Second-Harmonic-Generation Chromophores Based on 1,3,5-Trisubstituted Benzene Complexes. *European Journal of Inorganic Chemistry* **2015** (Aug. 2015)

- Deffner, M. *et al.* Impact of the Crosslinker's Molecular Structure on the Aggregation of Gold Nanoparticles. *Zeitschrift für Physikalische Chemie* **231.** ISSN: 0942-9352 (Jan. 2017)

- Stegmann, T. *et al.* Current vortices in aromatic carbon molecules. *Physical Review B* **102** (Aug. 2020)

- Gorris, F. E. S. *et al.* Postdeposition Ligand Exchange Allows Tuning the Transport Properties of Large-Scale $CuInSe_2$ Quantum Dot Solids. *Advanced Optical Materials* **8** (Nov. 2019)

- Deffner, M. & Herrmann, C. The Limits of Inelastic Tunneling Spectroscopy for Identifying Transport Pathways. *(preprint, submitted to Chemrxiv)* (Mar. 2020)

B Conference Contributions

Towards reality in modeling of molecular electronics in San Sebastian (Spain), May 2016: Poster with the title "ARTAIOS - A transport code for post-processing quantum chemical electronic structure calculations"

DPG Spring Meeting in Dresden, March 2017: Poster with the title "Electron transport in Nanoparticle Networks"

CUI Winterschool on Rügen, February 2017: Talk with the title "Electron Transport in Nanoparticle Networks"

Transport at the Nanoscale: Molecules, Graphene and more in Cuernavaca (Mexico), March 2019: Talk and poster with the title "Efficient Calculation of Vibrational IET Spectra in Molecular Junctions"

Watoc in Munich, August/September 2017: Poster with the title "Efficient Calculation of Vibrational IET Spectra in Molecular Junctions"

CUI Winterschool in Karpacz (Poland), March 2018: Talk with the title "Efficient calculation of Inelastic Electron Tunneling Spectra"

Workshop "Plasmonics" in Wittenberge, March 2019: Talk with the title "Terahertz Spectroscopy on Thin Films of Metallic Nanoparticles"

DPG Spring Meeting in Regensburg, March/April 2019: Talk with the title "Carrier Dynamics in CuInSe$_2$ QD Solids studied by THz Spectrocopy"

C List of Chemicals

chemical	symbols	hazard statements (H…)	precautionary statements (P…)
2-propanol		225-319-336	210-261-305 + 351 + 338
(3-mercaptopropyl) trimethoxysilane		302-317-411	273-280
4,4′-thiobisbenzenethiol		315-319-335	261-305 + 351 + 338
nonane-1,9-dithiol		315-319-335	261-305 + 351 + 338
acetone		225-319-336	210-233-261-280-303 + 361 + 353-370 + 378
biphenyl-4,4′-dithiol		302-413	-
p-terphenyl-4,4″-dithiol		302-319-410	301 + 312 + 330-305 + 351 + 338
ethanol		225-319	210-233-280-303 + 361 + 353-337 + 313-370 + 378
oleylamine		302-304-314-335-373-410	260-280-301 + 310-303 + 361 + 353-304 + 340 + 310-305 + 351 + 338
toluene		225-304-315-336-361d-373	210-260-280-301 + 310-370 + 378-403 + 235

Table 1: GHS information for the chemicals used in this work.

Table 2: All H, EUH, and P Statements.

Identifier	Statement
H200	Unstable explosives.
H201	Explosive; mass explosion hazard.
H202	Explosive, severe projection hazard.
H203	Explosive; fire, blast or projection hazard.
H204	Fire or projection hazard.
H205	May mass explode in fire.
H220	Extremely flammable gas.
H221	Flammable gas.
H222	Extremely flammable aerosol.
H223	Flammable aerosol.
H224	Extremely flammable liquid and vapour.
H225	Highly flammable liquid and vapour.
H226	Flammable liquid and vapour.
H228	Flammable solid.
H240	Heating may cause an explosion.
H241	Heating may cause a fire or explosion.
H242	Heating may cause a fire.
H250	Catches fire spontaneously if exposed to air.
H251	Self-heating: may catch fire.
H252	Self-heating in large quantities; may catch fire.
H260	In contact with water releases flammable gases which may ignite spontaneously.
H261	In contact with water releases flammable gases.
H270	May cause or intensify fire; oxidiser.
H271	May cause fire or explosion; strong oxidiser.
H272	May intensify fire; oxidiser.
H280	Contains gas under pressure; may explode if heated.
H281	Contains refrigerated gas; may cause cryogenic burns or injury.
H290	May be corrosive to metals.
H300	Fatal if swallowed.

Identifier	Statement
H301	Toxic if swallowed.
H302	Harmful if swallowed.
H304	May be fatal if swallowed and enters airways.
H310	Fatal in contact with skin.
H311	Toxic in contact with skin.
H312	Harmful in contact with skin.
H314	Causes severe skin burns and eye damage.
H315	Causes skin irritation.
H317	May cause an allergic skin reaction.
H318	Causes serious eye damage.
H319	Causes serious eye irritation.
H330	Fatal if inhaled.
H331	Toxic if inhaled.
H332	Harmful if inhaled.
H334	May cause allergy or asthma symptoms or breathing difficulties if inhaled.
H335	May cause respiratory irritation.
H336	May cause drowsiness or dizziness.
H340	May cause genetic defects. ⟨*state route of exposure if it is conclusively proven that no other routes of exposure cause the hazard*⟩
H341	Suspected of causing genetic defects. ⟨*state route of exposure if it is conclusively proven that no other routes of exposure cause the hazard*⟩
H350	May cause cancer. ⟨*state route of exposure if it is conclusively proven that no other routes of exposure cause the hazard*⟩
H351	Suspected of causing cancer. ⟨*state route of exposure if it is conclusively proven that no other routes of exposure cause the hazard*⟩
H360	May damage fertility or the unborn child. ⟨*state specific effect if known*⟩ ⟨*state route of exposure if it is conclusively proven that no other routes of exposure cause the hazard*⟩

Identifier	Statement
H361	Suspected of damaging fertility or the unborn child. ⟨*state specific effect if known*⟩ ⟨*state route of exposure if it is conclusively proven that no other routes of exposure cause the hazard*⟩
H362	May cause harm to breast-fed children.
H370	Causes damage to organs ⟨*or state all organs affected, if known*⟩. ⟨*state route of exposure if it is conclusively proven that no other routes of exposure cause the hazard*⟩
H371	May cause damage to organs ⟨*or state all organs affected, if known*⟩. ⟨*state route of exposure if it is conclusively proven that no other routes of exposure cause the hazard*⟩
H372	Causes damage to organs ⟨*or state all organs affected, if known*⟩ through prolonged or repeated exposure. ⟨*state route of exposure if it is conclusively proven that no other routes of exposure cause the hazard*⟩
H373	May cause damage to organs ⟨*or state all organs affected, if known*⟩ through prolonged or repeated exposure. ⟨*state route of exposure if it is conclusively proven that no other routes of exposure cause the hazard*⟩
H400	Very toxic to aquatic life.
H410	Very toxic to aquatic life with long lasting effects.
H411	Toxic to aquatic life with long lasting effects.
H412	Harmful to aquatic life with long lasting effects.
H413	May cause long lasting harmful effects to aquatic life.
H350i	May cause cancer by inhalation.
H360F	May damage fertility.
H360D	May damage the unborn child.
H361f	Suspected of damaging fertility.
H361d	Suspected of damaging the unborn child.
H360FD	May damage fertility. May damage the unborn child.

Identifier	Statement
H361fd	Suspected of damaging fertility. Suspected of damaging the unborn child.
H360Fd	May damage fertility. Suspected of damaging the unborn child.
H360Df	May damage the unborn child. Suspected of damaging fertility.
EUH001	Explosive when dry.
EUH006	Explosive with or without contact with air.
EUH014	Reacts violently with water.
EUH018	In use may form flammable/explosive vapour-air mixture.
EUH019	May form explosive peroxides.
EUH044	Risk of explosion if heated under confinement.
EUH029	Contact with water liberates toxic gas.
EUH031	Contact with acids liberates toxic gas.
EUH032	Contact with acids liberates very toxic gas.
EUH066	Repeated exposure may cause skin dryness or cracking.
EUH070	Toxic by eye contact.
EUH071	Corrosive to the respiratory tract.
EUH059	Hazardous to the ozone layer.
EUH201	Contains lead. Should not be used on surfaces liable to be chewed or sucked by children.
EUH201A	Warning! contains lead.
EUH202	Cyanoacrylate. Danger. Bonds skin and eyes in seconds. Keep out of the reach of children.
EUH203	Contains chromium (VI). May produce an allergic reaction.
EUH204	Contains isocyanates. May produce an allergic reaction.
EUH205	Contains epoxy constituents. May produce an allergic reaction.
EUH206	Warning! Do not use together with other products. May release dangerous gases (chlorine).

Identifier	Statement
EUH207	Warning! Contains cadmium. Dangerous fumes are formed during use. See information supplied by the manufacturer. Comply with the safety instructions.
EUH208	Contains ⟨*name of sensitising substance*⟩. May produce an allergic reaction.
EUH209	Can become highly flammable in use.
EUH209A	Can become flammable in use.
EUH210	Safety data sheet available on request.
EUH401	To avoid risks to human health and the environment, comply with the instructions for use.
P101	If medical advice is needed, have product container or label at hand.
P102	Keep out of reach of children.
P103	Read label before use.
P201	Obtain special instructions before use.
P202	Do not handle until all safety precautions have been read and understood.
P210	Keep away from heat/sparks/open flames/ hot surfaces. — No smoking.
P211	Do not spray on an open flame or other ignition source.
P220	Keep/Store away from clothing/…/combustible materials.
P221	Take any precaution to avoid mixing with combustibles …
P222	Do not allow contact with air.
P223	Keep away from any possible contact with water, because of violent reaction and possible flash fire.
P230	Keep wetted with …
P231	Handle under inert gas.
P232	Protect from moisture.
P233	Keep container tightly closed.
P234	Keep only in original container.
P235	Keep cool.

Identifier	Statement
P240	Ground/bond container and receiving equipment.
P241	Use explosion-proof electrical/ventilating/lighting/… equipment.
P242	Use only non-sparking tools.
P243	Take precautionary measures against static discharge.
P244	Keep reduction valves free from grease and oil.
P250	Do not subject to grinding/shock/…/friction.
P251	Pressurized container: Do not pierce or burn, even after use.
P260	Do not breathe dust/fume/gas/mist/vapours/spray.
P261	Avoid breathing dust/fume/gas/mist/vapours/spray.
P262	Do not get in eyes, on skin, or on clothing.
P263	Avoid contact during pregnancy/while nursing.
P264	Wash … thoroughly after handling.
P270	Do not eat, drink or smoke when using this product.
P271	Use only outdoors or in a well-ventilated area.
P272	Contaminated work clothing should not be allowed out of the workplace.
P273	Avoid release to the environment.
P280	Wear protective gloves/protective clothing/eye protection/face protection.
P281	Use personal protective equipment as required.
P282	Wear cold insulating gloves/face shield/eye protection.
P283	Wear fire/flame resistant/retardant clothing.
P284	Wear respiratory protection.
P285	In case of inadequate ventilation wear respiratory protection.

Identifier	Statement
P231 + P232	Handle under inert gas. Protect from moisture.
P235 + P410	Keep cool. Protect from sunlight.
P301	IF SWALLOWED:
P302	IF ON SKIN:
P303	IF ON SKIN (or hair):
P304	IF INHALED:
P305	IF IN EYES:
P306	IF ON CLOTHING:
P307	IF exposed:
P308	IF exposed or concerned:
P309	IF exposed or if you feel unwell:
P310	Immediately call a POISON CENTER or doctor/physician.
P311	Call a POISON CENTER or doctor/physician.
P312	Call a POISON CENTER or doctor/physician if you feel unwell.
P313	Get medical advice/attention.
P314	Get medical advice/attention if you feel unwell.
P315	Get immediate medical advice/attention.
P320	Specific treatment is urgent (see ... on this label).
P321	Specific treatment (see ... on this label).
P322	Specific measures (see ... on this label).
P330	Rinse mouth.
P331	Do NOT induce vomitting.
P332	If skin irritation occurs:
P333	If skin irritation or rash occurs:
P334	Immerse in cool water/wrap in wet bandages.
P335	Brush off loose particles from skin.
P336	Thaw frosted parts with lukewarm water. Do not rub affected area.
P337	If eye irritation persists:
P338	Remove contact lenses, if present and easy to do. Continue rinsing.

Identifier	Statement
P340	Remove victim to fresh air and keep at rest in a position comfortable for breathing.
P341	If breathing is difficult, remove victim to fresh air and keep at rest in a position comfortable for breathing.
P342	If experiencing respiratory symptoms:
P350	Gently wash with plenty of soap and water.
P351	Rinse cautiously with water for several minutes.
P352	Wash with plenty of soap and water.
P353	Rinse skin with water/shower.
P360	Rinse immediately contaminated clothing and skin with plenty of water before removing clothes.
P361	Remove/Take off immediately all contaminated clothing.
P362	Take off contaminated clothing and wash before reuse.
P363	Wash contaminated clothing before reuse.
P370	In case of fire:
P371	In case of major fire and large quantities:
P372	Explosion risk in case of fire.
P373	DO NOT fight fire when fire reaches explosives.
P374	Fight fire with normal precautions from a reasonable distance.
P375	Fight fire remotely due to the risk of explosion.
P376	Stop leak if safe to do so.
P377	Leaking gas fire: Do not extinguish, unless leak can be stopped safely.
P378	Use … for extinction.
P380	Evacuate area.
P381	Eliminate all ignition sources if safe to do so.
P390	Absorb spillage to prevent material damage.
P391	Collect spillage.
P301 + P310	IF SWALLOWED: Immediately call a POISON CENTER or doctor/physician.

Appendix

Identifier	Statement
P301 + P312	IF SWALLOWED: Call a POISON CENTER or doctor/physician if you feel unwell.
P301 + P330 + P331	IF SWALLOWED: rinse mouth. Do NOT induce vomitting.
P302 + P334	IF ON SKIN: Immerse in cool water/wrap in wet bandages.
P302 + P350	IF ON SKIN: Gently wash with plenty of soap and water.
P302 + P352	IF ON SKIN: Wash with plenty of soap and water.
P303 + P361 + P353	IF ON SKIN (or hair): Remove/Take off immediately all contaminated clothing. Rinse skin with water/shower.
P304 + P340	IF INHALED: Remove victim to fresh air and keep at rest in a position comfortable for breathing.
P304 + P341	IF INHALED: If breathing is difficult, remove victim to fresh air and keep at rest in a position comfortable for breathing.
P305 + P351 + P338	IF IN EYES: Rinse cautiously with water for several minutes. Remove contact lenses, if present and easy to do. Continue rinsing.
P306 + P360	IF ON CLOTHING: Rinse immediately contaminated clothing and skin with plenty of water before removing clothes.
P307 + P311	IF exposed: Call a POISON CENTER or doctor/physician.
P308 + P313	IF exposed or concerned: Get medical advice/ attention.
P309 + P311	IF exposed or if you feel unwell: Call a POISON CENTER or doctor/physician.
P332 + P313	If skin irritation occurs: Get medical advice/ attention.
P333 + P313	If skin irritation or rash occurs: Get medical advice/attention.
P335 + P334	Brush off loose particles from skin. Immerse in cool water/wrap in wet bandages.
P337 + P313	If eye irritation persists: Get medical advice/ attention.

Identifier	Statement
P342 + P311	If experiencing respiratory symptoms: Call a POISON CENTER or doctor/physician.
P370 + P376	In case of fire: Stop leak if safe to do so.
P370 + P378	In case of fire: Use … for extinction.
P370 + P380	In case of fire: Evacuate area.
P370 + P380 + P375	In case of fire: Evacuate area. Fight fire remotely due to the risk of explosion.
P371 + P380 + P375	In case of major fire and large quantities: Evacuate area. Fight fire remotely due to the risk of explosion.
P401	Store …
P402	Store in a dry place.
P403	Store in a well-ventilated place.
P404	Store in a closed container.
P405	Store locked up.
P406	Store in corrosive resistant/… container with a resistant inner liner.
P407	Maintain air gap between stacks/pallets.
P410	Protect from sunlight.
P411	Store at temperatures not exceeding °C/°F.
P412	Store at temperatures not exceeding 50 °C/ 122 °F.
P413	Store bulk masses greater than kg/lbs at temperatures not exceeding °C/°F.
P420	Store away from other materials.
P422	Store contents under …
P402 + P404	Store in a dry place. Store in a closed container.
P403 + P233	Store in a well-ventilated place. Keep container tightly closed.
P403 + P235	Store in a well-ventilated place. Keep cool.
P410 + P403	Protect from sunlight. Store in a well-ventilated place.
P410 + P412	Protect from sunlight. Do not expose to temperatures exceeding 50 °C/122 °F.
P411 + P235	Store at temperatures not exceeding °C/°F. Keep cool.

continues on next page

Identifier	Statement
P501	Dispose of contents/container to …

D Statistical Methods

Bootstrapping

Bootstrapping describes a technique to create statistical data based on only one set of data [538]. It is used when the real distribution of data points is not known. With bootstrapping, the variability of the mean can be estimated. As shown in Figure 1, new sets of data are created by randomly choosing data from the original data set. The mean $\bar{x}_{b,i}$ is calculated each time and can be used to show how much the mean varies over each sample/set of data.
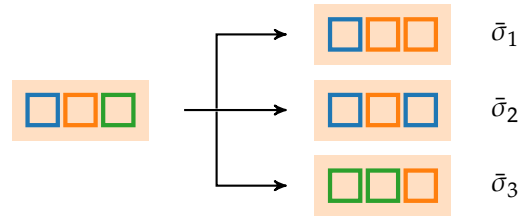
Figure 1: Schematic representation of the bootstrapping technique.

The total mean $\bar{x}_b$ obtained by bootstrapping is given by

$$\bar{x}_b = \frac{1}{N_b} \sum_{i=1}^{N_b} \bar{x}_{b,i}, \tag{1}$$

where N_b is number of re-sampling iterations. The variance is given by

$$Var(x) = \frac{1}{N_b} \sum_{i=1}^{N_b} \bar{x}_{b,i}^2 - \bar{x}^2. \tag{2}$$

Jackknife
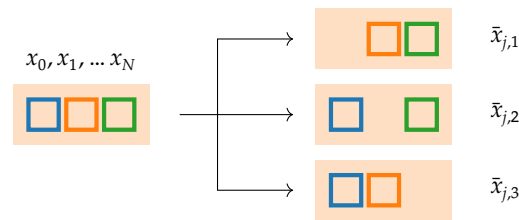
Figure 2: Visualization of the Jackknife technique.

A special case of bootstrapping is *jackknife*, which can be used to estimate the bias of a set of data. For the jackknife-technique, a sample x of a set of data is removed from the set and the mean recalculated by

$$\bar{x}_i = \frac{1}{n-1} \sum_{j=1, j \neq i} x_j. \tag{3}$$

The mean of the sampling distribution can be calculated from all the $\bar{x}_i$ by

$$\bar{x} = \frac{1}{n} \sum_{i=1}^{n} \bar{x}_i. \tag{4}$$

The variance of the estimator can be calculated by

$$\mathrm{Var}(\bar{x}) = \frac{n-1}{n} \sum_{i=1}^{n} (\bar{x}_i - \bar{x})^2 . \tag{5}$$

In this work, the Jackknife analysis was used to quickly identify measurements in a large set of data, which deviate strongly from the rest of the data set. This was done by performing the Jackknife analysis and comparing the obtained values of $\bar{x}_i$.

E Supplementary Material for Chapter 3

XYZ Coordinates of the Molecular Junction

Coordinates for the Fe(II)Pophyrin Junction

N	−1.357511	−0.000000	3.817648
C	−2.718846	−0.025528	4.025817
C	−3.421873	−0.100345	2.768976
C	−2.476929	−0.137686	1.790178
C	−1.189157	−0.065349	2.448086
C	−3.348499	0.004573	5.261987
C	−2.716392	0.037175	6.498012
C	−3.415168	0.119580	7.755132
C	−2.467033	0.160682	8.733021
C	−1.181588	0.078014	8.075239
N	−1.353099	0.024228	6.703617
C	0.054713	0.032842	8.733752
S	0.000000	0.000000	10.520434
Fe	0.050369	−0.039451	5.261911
N	1.457102	−0.014498	3.816566
C	2.821628	−0.012807	4.023804
C	3.521008	0.053036	2.768046
C	2.571731	0.085775	1.788001
C	1.286958	0.018166	2.443669
C	3.450900	−0.050449	5.260985
C	2.820698	−0.066982	6.497528
N	1.459905	−0.007654	6.706482
C	1.291695	−0.052382	8.076646
C	2.575025	−0.159596	8.732418
C	3.521936	−0.156363	7.752523
C	0.046653	−0.036303	1.788283
S	−0.000000	0.000000	0.000000
N	0.066992	2.064432	5.244243
C	−0.679780	2.920611	6.031121
C	−0.383904	4.220640	5.705729
N	0.560955	4.142835	4.702105
C	0.806838	2.830030	4.451049
C	0.032366	−1.783003	5.270781
O	0.018023	−2.941983	5.273819
H	−0.751324	5.165296	6.086968
H	0.997746	4.924329	4.227470
H	1.508800	2.478589	3.704746
H	−1.375332	2.547027	6.771846
H	−4.438969	−0.001363	5.263560
H	4.541269	−0.076015	5.260459
H	−4.496086	0.155796	7.861727
H	−2.608863	0.245143	9.805038
H	2.722795	−0.257125	9.802395
H	4.602195	0.081708	2.661020
H	2.720001	0.166167	0.716633
H	−4.503031	−0.137336	2.665160
H	4.601325	−0.228207	7.856489
H	−2.618535	−0.218414	0.717981

Au	0.000000	−1.662766	12.835107
Au	−1.440000	0.831384	12.835107
Au	1.440000	0.831385	12.835107
Au	0.000000	−1.662766	−2.314673
Au	1.440000	0.831384	−2.314673
Au	−1.440000	0.831384	−2.314673

Coordinates for the CN–Substituted Biphenyl Junction

S	0.000000	−0.000000	18.352069
C	0.116576	0.046877	16.679465
C	0.076260	0.076007	15.456771
C	0.048314	0.099046	14.042743
C	1.245897	0.154258	13.301810
C	1.222166	0.164627	11.903883
C	−0.015934	0.119797	11.195814
C	−0.051710	0.117223	9.786878
C	−0.087276	0.106392	8.564875
C	−0.107514	0.089055	7.155688
C	1.094830	0.136739	6.415005
C	1.088104	0.117104	5.029958
C	−0.128819	0.047929	4.308307
C	−0.133774	0.028713	2.893944
C	−0.151063	0.013098	1.670447
S	0.000000	0.000000	0.000000
C	−1.180012	0.061818	13.338336
C	−1.207602	0.072071	11.953319
C	−1.334337	0.020570	6.430557
C	−1.336897	−0.000000	5.032377
H	2.203034	0.187509	13.820162
C	2.454848	0.218552	11.183122
H	−2.112893	0.022423	13.900268
H	−2.159568	0.040584	11.423958
H	2.038048	0.189784	6.958181
H	2.028832	0.154882	4.481217
C	−2.577773	−0.027756	7.132935
H	−2.285850	−0.053698	4.500886
N	3.465314	0.263066	10.603428
N	−3.597518	−0.066724	7.696549
Au	0.000000	−1.662766	20.666742
Au	−1.440000	0.831384	20.666742
Au	1.440000	0.831385	20.666742
Au	0.000000	−1.662766	−2.314673
Au	1.440000	0.831384	−2.314673
Au	−1.440000	0.831384	−2.314673

Coordinates for the Meta–Substituted Benzene Junction

C	−1.467744	−0.000000	4.926826
C	−2.132742	0.002769	6.167722
C	−3.545443	0.006568	6.191293
C	−4.261447	0.007211	4.995730
C	−3.605304	0.004406	3.766402
C	−2.193081	0.001130	3.720308
C	−1.391239	0.001591	7.378865

C	−0.740514	0.000257	8.414041
S	−0.000000	0.000000	9.922666
C	−1.509786	−0.000360	2.475279
C	−0.938838	−0.000798	1.393998
S	−0.000000	0.000000	−0.000000
H	−4.063910	0.008812	7.149626
H	−5.352041	0.010126	5.022958
H	−4.170404	0.004551	2.834765
H	−0.378884	−0.003080	4.899829
Au	0.000000	−1.662766	12.237339
Au	−1.440000	0.831384	12.237339
Au	1.440000	0.831385	12.237339
Au	0.000000	−1.662766	−2.314673
Au	1.440000	0.831384	−2.314673
Au	−1.440000	0.831384	−2.314673

Coordinates for the Meta–Substituted Pyridine Junction
(Nitrogen in Shorter Path)

C	−2.235637	−0.000000	5.972657
C	−3.644969	−0.007448	6.052976
C	−4.374730	−0.016379	4.867706
C	−3.701997	−0.017213	3.649121
C	−2.290426	−0.006815	3.662336
N	−1.563341	0.001586	4.800800
C	−1.454726	0.004058	7.164712
C	−0.792048	0.002785	8.191455
S	−0.000000	0.000000	9.670446
C	−1.564319	−0.005284	2.435814
C	−0.978465	−0.004083	1.363068
S	−0.000000	0.000000	−0.000000
H	−4.135464	−0.007341	7.025636
H	−5.465350	−0.023231	4.893598
H	−4.238502	−0.026203	2.701098
Au	0.000000	−1.662766	11.985119
Au	−1.440000	0.831384	11.985119
Au	1.440000	0.831385	11.985119
Au	0.000000	−1.662766	−2.314673
Au	1.440000	0.831384	−2.314673
Au	−1.440000	0.831384	−2.314673

Coordinates for the Meta–Substituted Pyridine Junction
(Nitrogen in Longer Path)

C	−1.965184	−0.000000	6.235711
C	−3.380946	−0.009853	6.205505
N	−4.091915	−0.014751	5.074983
C	−3.438469	−0.010694	3.910437
C	−2.026160	−0.000371	3.808964
C	−1.287527	0.005806	5.004482
C	−1.268495	0.002518	7.469030
C	−0.667849	0.001901	8.534361
S	−0.000000	−0.000000	10.075217
C	−1.389629	0.002110	2.543474

C	−0.871170	0.002112	1.435787
S	0.000000	0.000000	0.000000
H	−3.942450	−0.014068	7.142689
H	−4.046152	−0.015767	3.002507
H	−0.198619	0.014309	4.976525
Au	0.000000	−1.662766	12.389891
Au	−1.440000	0.831384	12.389891
Au	1.440000	0.831385	12.389891
Au	0.000000	−1.662766	−2.314673
Au	1.440000	0.831384	−2.314673
Au	−1.440000	0.831384	−2.314673

Visualizations of the molecular vibrations
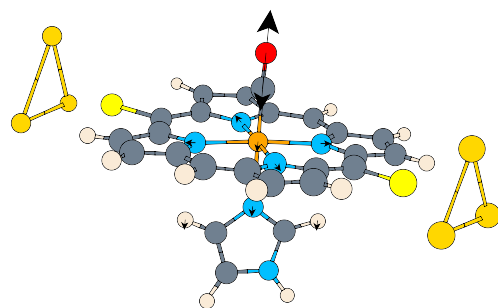
Figure 3: CO stretching mode obtained with MoViPaC and the modetracking algorithm for the Fe-prophyrin.
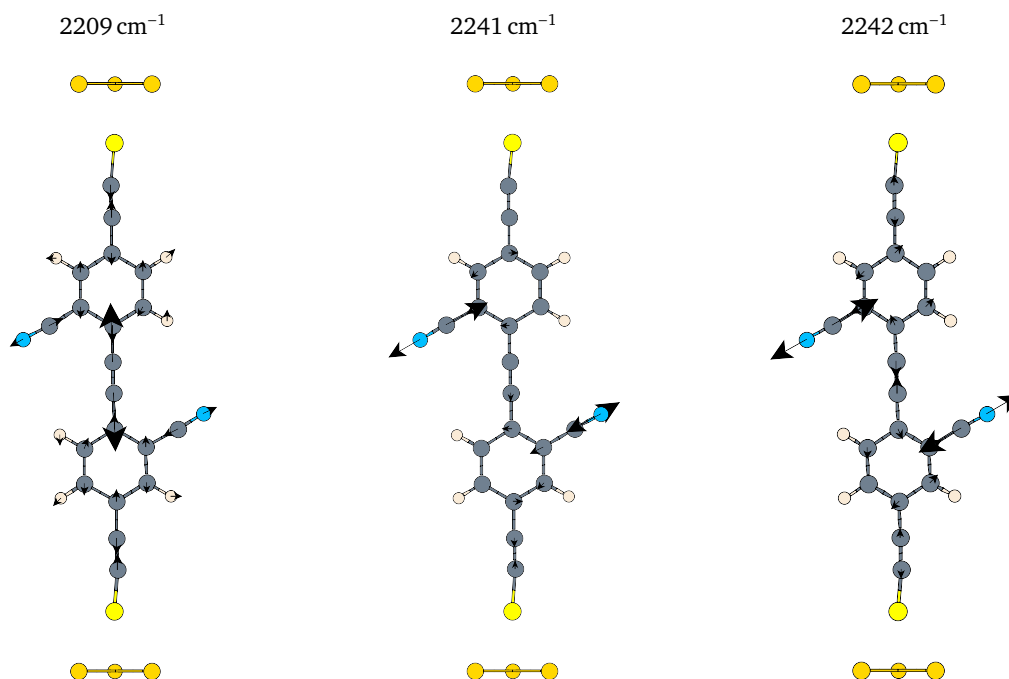
Figure 4: Stretching modes of the central CC bond (left) and the antisymmetric (middle) and symmetric (right) stretching vibration of the CN groups.
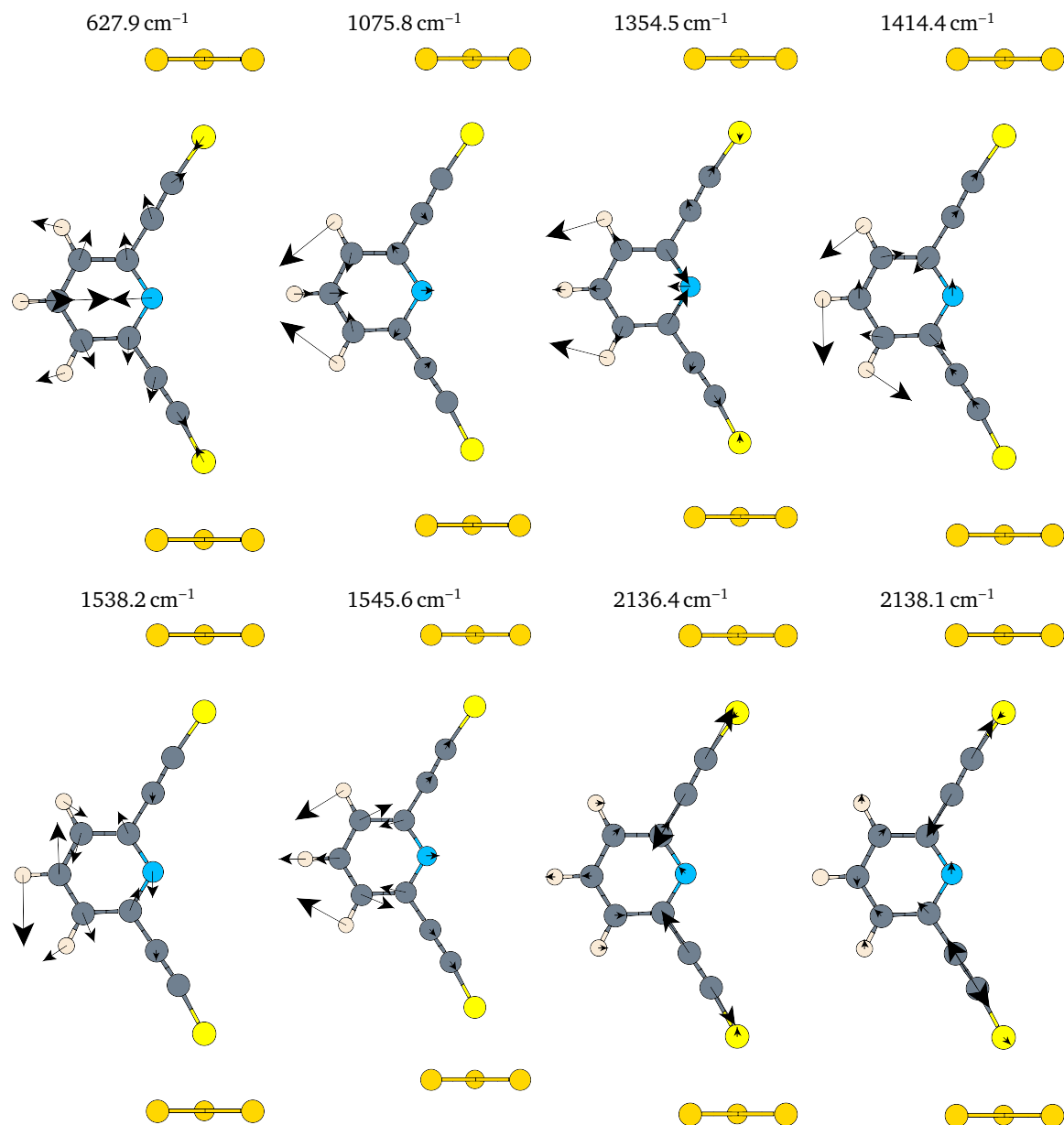
Figure 5: Collection of vibrational modes of the the meta-substituted pyridine junction, including the strongest vibrations found in the IET spectrum.

IET Spectra
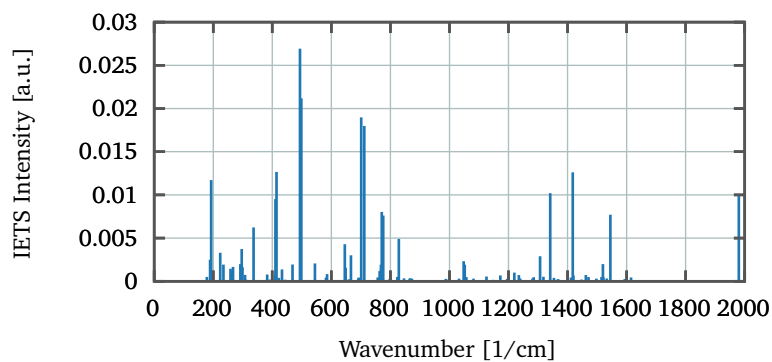
Figure 6: IET Spectra of the Fe(II)Porphyrin junction evaluated at $E_F = -5$ eV.
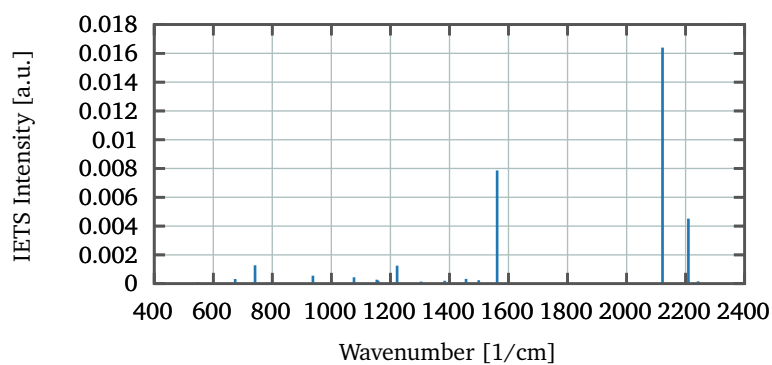
Figure 7: IET Spectra of the CN–substituted biphenyl junction evaluated at $E_F = -5$ eV.

Figure 8: IET Spectra of the three meta–substituted benzene/pyridine junctions evaluated at $E_F = -5\,\mathrm{eV}$.
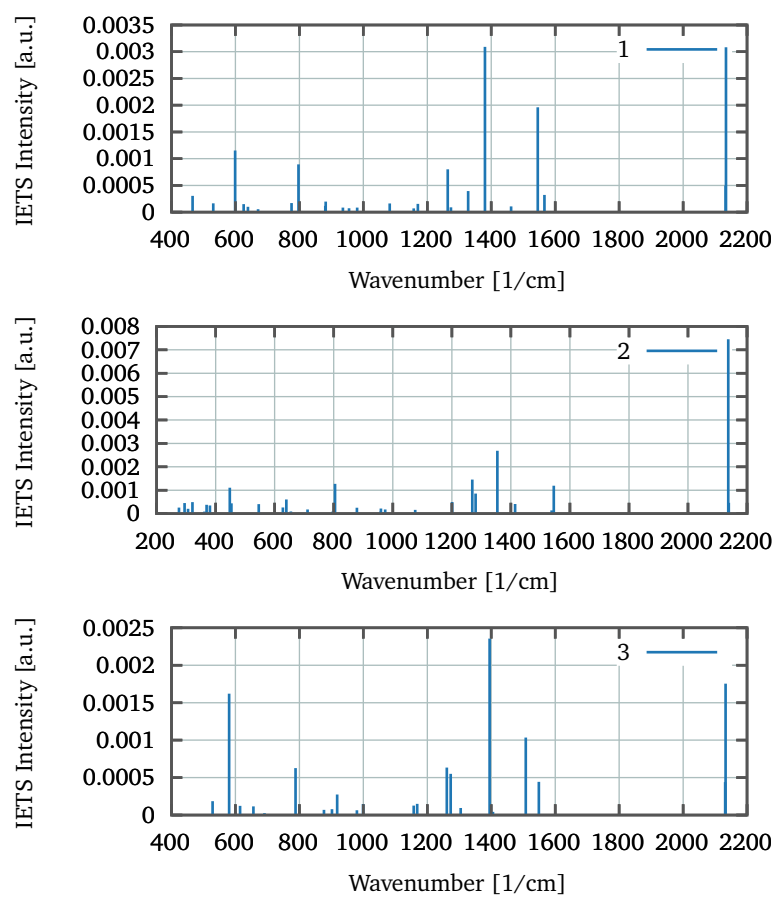
F Supplementary Material for Chapter 9

Fits of the CIS Decay Dynamics

In the following, bi- or triexpoential fits for the $\int \Delta E^2(\tau)$ dynamics of the CIS samples are shown. While for CIS-OAm and CIS-AMTD biexpoential decay fits given by

$$\epsilon_{\text{fit}}(\tau) = \text{Heavi}(\tau - t_0)\left[A_0 e^{-\frac{\tau-t_0}{\tau_1}} + (1 - A_0)e^{-\frac{\tau-t_0}{\tau_2}} +\right] \quad (6)$$

are sufficient, a triexpoential decay has to be used for the CIS-DMTD samples:

$$\epsilon_{\text{fit}}(\tau) = \text{Heavi}(\tau - t_0)\left[A_0 e^{-\frac{\tau-t_0}{\tau_1}} + A_1 e^{-\frac{\tau-t_0}{\tau_2}} + (1 - A_0 - A_1)e^{-\frac{\tau-t_0}{\tau_3}}\right]$$
$$(7)$$
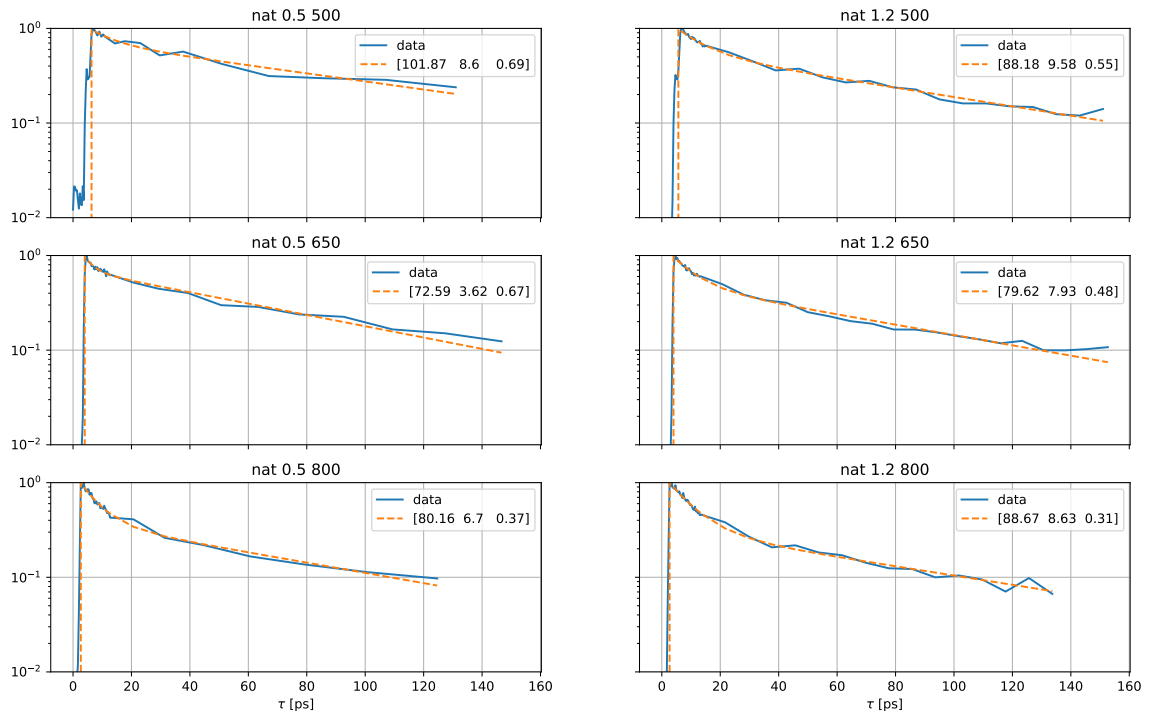
Figure 9: Biexponetial fits of the decay dynamics ($\int \Delta E^2(\tau)$) of CIS-OAm. The title of the individual graphs shows the excitation power in µJ (0.5 or 1.2) and wavelength in nm. The values given for the orange dotted lines correspond to the fitting parameters, ordered as τ_1, τ_2, A_0.
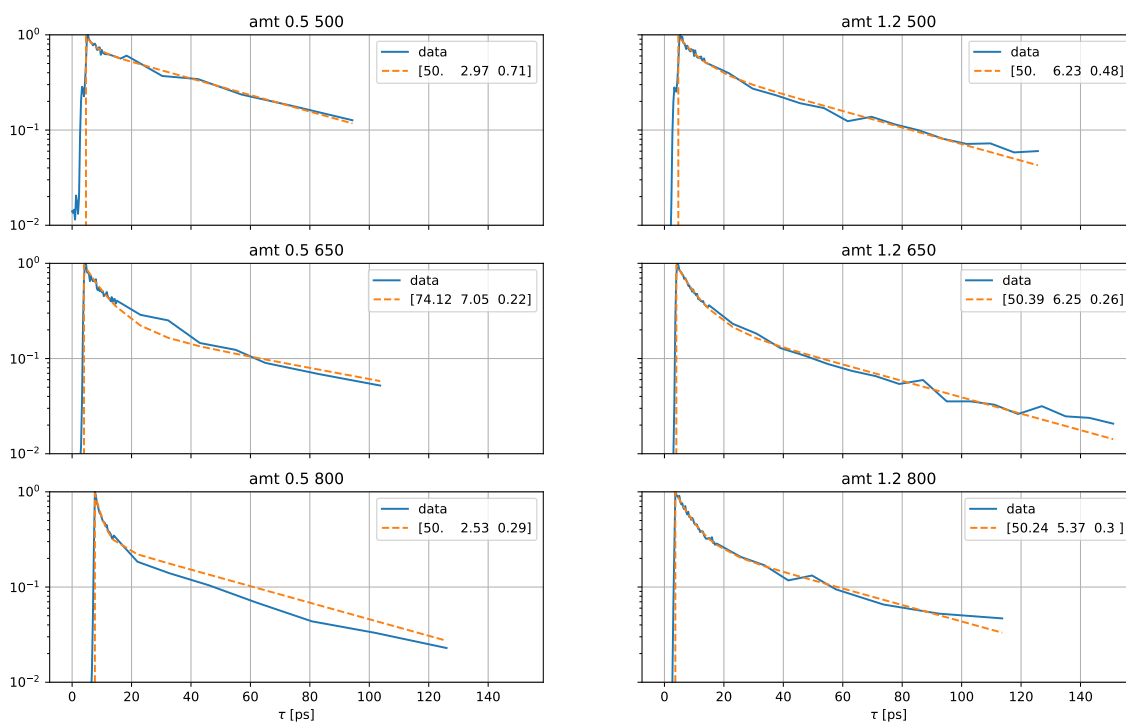
Figure 10: Biexponetial fits of the decay dynamics ($\int \Delta E^2(\tau)$) of CIS-AMTD. The title of the individual graphs shows the excitation power in µJ (0.5 or 1.2) and wavelength in nm. The values given for the orange dotted lines correspond to the fitting parameters, ordered as τ_1, τ_2, A_0.
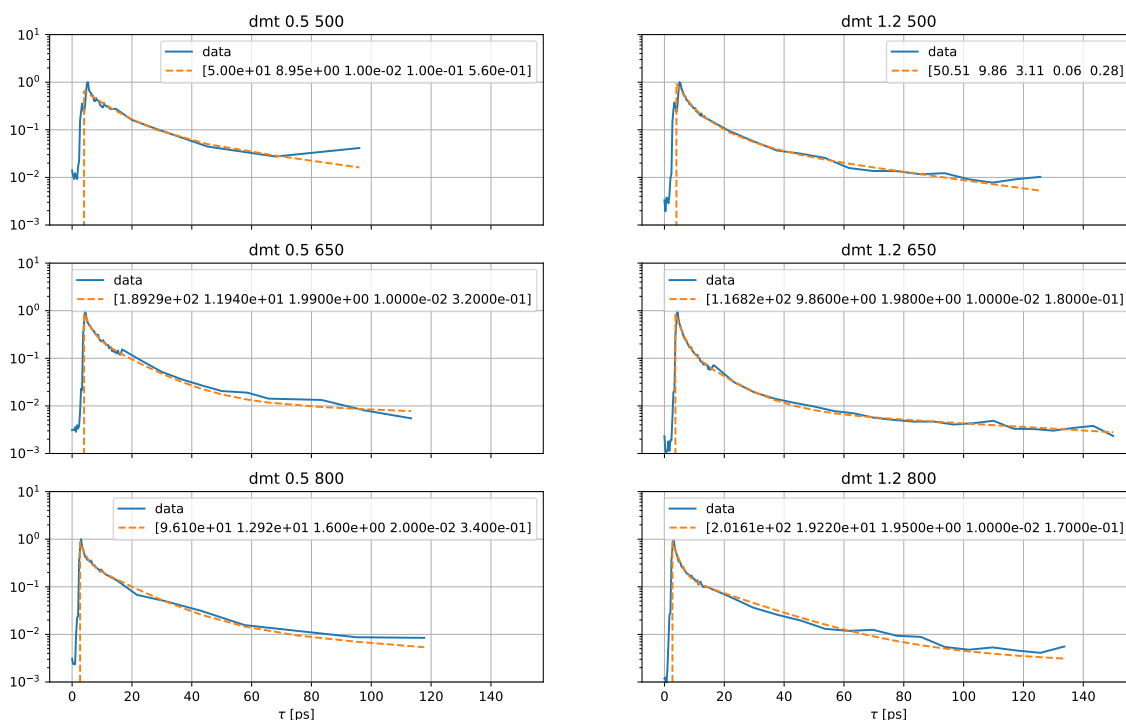
Figure 11: Triexponetial fits of the decay dynamics ($\int \Delta E^2(\tau)$) of CIS-DMTD. The title of the individual graphs shows the excitation power in µJ (0.5 or 1.2) and wavelength in nm. The values given for the orange dotted lines correspond to the fitting parameters, ordered as $\tau_1, \tau_2, \tau_2, A_0, A_1$

G Analysis of Cited Literature

Using a `python` script, the cited literature in this work could be analyzed regarding the years of the publication. Figures 12 shows the number of publications with respect to their your of publication, filtered by specific keywords in the title of the paper.
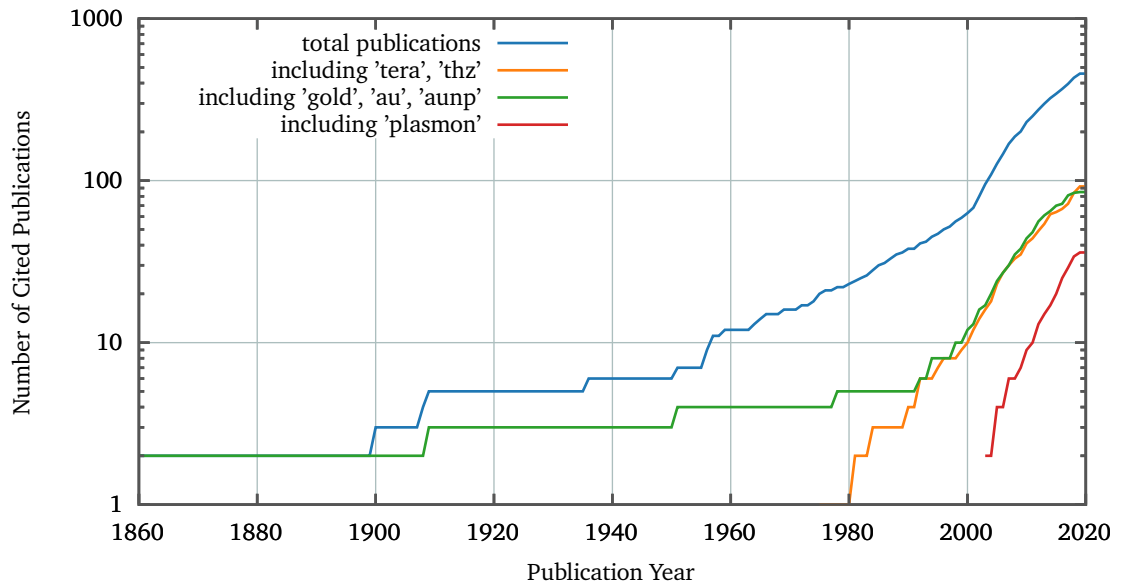
Figure 12: Total publications and publications filtered with specific keywords with respect to their year of publication.

Eidesstattliche Erklärung

Hiermit versichere ich, Michael Deffner, an Eides statt, die vorliegende Dissertation selbst verfasst und keine anderen als die angegebenen Hilfsmittel benutzt zu haben. Die eingereichte schriftliche Fassung entspricht der auf dem elektronischen Speichermedium. Ich versichere, dass diese Dissertation nicht in einem früheren Promotionsverfahren eingereicht wurde.

Hamburg, den 23.04.2020

Michael Deffner